Creep Behavior of a Zirconium Diboride-Silicon Carbide Composite and Preliminary ZrB_2-WC Quasi-Binary Alloy Development for Long Duty Cycle Aerosurfaces and Structural Propulsion Applications

A Dissertation

Presented to
the Faculty of the Department of Materials Engineering
University of Houston

In Partial Fulfillment
of the Requirements for the Degree
Doctor of Philosophy
in Materials Engineering

by
Marc William Bird

December 2013

Creep Behavior of a Zirconium Diboride-Silicon Carbide Composite and Preliminary ZrB_2-WC Quasi-Binary Alloy Development for Long Duty Cycle Aerosurfaces and Structural Propulsion Applications

Marc William Bird

Approved:

Chair of the Committee
Kenneth W. White, PhD, Professor,
Mechanical Engineering

Committee Members:

Paul F. Becher, PhD, Research Professor,
Materials Science and Engineering
University of Tennessee

Pradeep Sharma, PhD, Professor,
Mechanical Engineering

Li Sun, PhD, Associate Professor,
Mechanical Engineering

Lewis Wheeler, PhD, Professor Emeritus,
Mechanical Engineering

Kaspar J. Willam, PhD, NAE, Professor,
Civil and Environmental Engineering

Suresh K. Khator, Associate Dean,
Cullen College of Engineering

Dmitri Litvinov, PhD, Professor and
Director of the Materials Engineering
Program

Acknowledgments

I would like to thank the Air Force Office of Scientific Research and Dr. Ali Sayir for providing funding for this research under grant #FA9550-09-1-0200. Special appreciation is extended to my advisor, Professor Kenneth White, Ph.D., for his continual support throughout my Ph. D. research. Our constructive technical conversations and his guidance were the driving force for successfully completing this piece of novel research and initiating the development of next generation UHTC alloys. Special thanks are given to Paul Becher, Ph.D. for his guidance and advice for completing creep experiments and understanding creep behaviors. I would also like to thank Professor Pradeep Sharma, Ph. D. for his technical insight and nomination for a graduate fellowship under NSF grant #0840889. Extended appreciation is given to my fellow graduate and undergraduate UHTC research team, under Professor Kenneth White, for their collective assistance in completing creep experiments, quantitative metallography and room temperature property testing.

My deepest gratitude goes to my wife, Dr. Jennifer Bird, for her continual support, motivation and love throughout this research. She has and continues to support my educational and professional endeavors for which I cannot be grateful enough. I am also proud of her new found ceramic creep knowledge after countless one-sided conversations regarding UHTC creep behavior. I would like to thank my parents-in-law, Mike and Kathy Brahm for their support and love. Also, appreciation is owed to my brother Matthew Bird and extended family members for their support. Special consideration is given to my parents, Jean and Gordon Goodnough, for their support and love and most of all teaching me the value of strong work ethic for which I will always be grateful.

Creep Behavior of a Zirconium Diboride-Silicon Carbide Composite and Preliminary ZrB_2-WC Quasi-Binary Alloy Development for Long Duty Cycle Aerosurfaces and Structural Propulsion Applications

An Abstract

of a

Dissertation

Presented to

the Faculty of the Department of Materials Engineering

University of Houston

In Partial Fulfillment

of the Requirements for the Degree

Doctor of philosophy

in Materials Engineering

by

Marc William Bird

December 2013

Abstract

The mechanical behavior of select ultra-high temperature ceramics were studied for extreme environment aerospace applications. Hot-pressed ZrB_2-20 vol% SiC composites and ZrB_2-WC quasi-binary alloys were developed for assessing room temperature mechanical properties and creep behavior. A thermochemical model describing alloy phase stability and reaction equilibria, for promoting WC dissolution, is presented. Room temperature structure-property relationships were developed correlating fracture strength and K_{IC} with microstructure constituent size.

Flexural creep studies of ZrB_2-20 vol% SiC were conducted over the range of 1400°C to 1820°C assessing the macroscopic creep behavior using power-law stress and temperature dependent constants. Inert environment creep experiments were conducted for probing the local grain deformation mechanism in anticipation of bridging the deformation length scales. A two decade increase in creep rate, between 1500 and 1600°C, suggests a clear transition between the low temperature (1400-1500°C) diffusion creep and high temperature (>1600°C) grain boundary sliding creep having stress exponents of unity and $1.7<n<2.2$, respectively.

A novel indentation deformation mapping experiment clearly defined the local ZrB_2 grain boundary sliding event with its components of 80% grain translations and rotations and 20% grain deformation. EBSD and texture theory confirmed the direct observation of ZrB_2 grains deforming by dislocation flow, confined to near-grain boundary (mantle) zones, accommodating the grain rotation and translation events. A transition from the grain core to mantle deformation deviated from single crystal behavior as a result of extra geometrically necessary dislocations accommodating the deformation gradient. Microstructure observations shows evidence of <5% and <20% SiC grain deformation, contributing to the macroscopic creep

strain, for tension and compression bending fibers, respectively. Cavitation accounts for less than 5% contribution to the accumulated creep strain.

Preliminary ZrB_2-WC quasi binary alloy creep experiments reveal a decade decrease in the steady state creep rate with a 1.1 mol% increasing WC composition. Improved creep behavior is discussed in the context of solute interactions with accommodation dislocations from grain boundary sliding. Alloy creep rates of 10^{-7}-10^{-6} s^{-1} were measured contrasting with 10^{-5}-10^{-4} s^{-1} for the ZrB_2-SiC composite approaching the design creep rate of $10^{-8}s^{-1}$ for long duty cycle aerospace applications.

Table of Contents

Acknowledgements v

Abstract vii

Table of Contents ix

List of Figures xii

List of Tables xxiv

Chapter 1: Introduction 1

Chapter 2: Literature Review 5

2.1: Metal Diboride Motivation 5

2.2: Monolithic and Composite UHTC Development 7

2.2.1: Processing 7

2.2.2: Mechanical Properties 18

2.3: High Temperature Mechanical Behavior 25

2.3.1: Creep Deformation 27

2.3.1.1: Diffusion Mechanisms 30

2.3.1.2: Grain Boundary Sliding Creep 39

2.3.1.3: Lattice Mechanisms 47

2.3.1.4: Cavitation Mechanisms 51

2.3.2: ZrB_2 and ZrC Creep Behavior 56

Chapter 3: Experimental Setup and Procedures 62

3.1: Material 62

3.1.1: Powder Processing 64

3.1.2: Densification 66

3.1.3: Heat Treatment 67
3.2: Characterization 68
3.2.1: Analytical Methods 68
3.2.2: Microscopy 70
3.2.2.1: Sample Preparation 70
3.2.2.2: Electron Backscatter Diffraction 71
3.2.2.3: Quantitative Metallography 74
3.2.2.3.1: Grain Size and Inter-particle Spacing 74
3.2.2.3.2: Cavitation 75
3.2.2.4: Optical Beam Curvatures 76
3.2.2.5: Indentation Deformation Mapping 78
3.3: Mechanical Properties 79
3.4: Creep Experiments 85
3.4.1: Constant Load and Displacement 85
3.4.2: Vacuum Inert Environment 89
Chapter 4: Processing and Room Temperature Mechanical Behavior 92
4.1: Results 92
4.1.1: Microstructure and Densification 94
4.1.2: Mechanical Properties 104
4.2: Analysis and Discussion 105
4.2.1: Microstructure 105
4.2.2: Room Temperature Mechanical Behavior 115
Chapter 5: Creep Behavior 127
5.1: Results 127

5.1.1: Bending Creep 127
5.1.2: High Strain Creep 142
5.2: Analysis and Discussion 153
5.2.1: Low Temperature 154
5.2.2: High Temperature 159
5.2.2.1: Cavitation 161
5.2.2.2: Grain Deformation 166
5.2.2.3: Grain Boundary Sliding 174
5.2.2.4: Theoretical Interpretation 184
5.2.2.5: Creep Strengthening by Solid Solution 189
Chapter 6: Conclusions and Future Work 199
6.1: Processing and Room Temperature Mechanical Behavior 199
6.2: Creep Behavior 201
6.3: Future Work 203
References 208
Appendix A: Thermochemical Formulations and Data 230
Appendix B: Electron Backscatter Diffraction (EBSD) 237
Appendix C: Random Orientation Texture Analysis 241
Appendix D: Pseudo Fourier Transform Method 244
Appendix E: Solute-Dislocation Interaction Model 247

List of Figures

Figure 1- 1: Melting point comparison of select refractory metals and ceramic material systems (Fahrenholtz, Hilmas and Talmy, et al., 2007). 1

Figure 1- 2: Heat transfer schematic detailing (A) leading edge component with general heat flow considerations (B) energy balance along leading edge surface and (C) heat flux decay away from leading edge stagnation point (Squire and Marschall 2010)..... 3

Figure 2- 1: Strength of select monolithic ZrB_2 densified by Hot Pressing (HP), Reactive Hot Pressing (RHP), Spark Plasma Sintering (SPS) and Pressureless Sintered (PS) taken from Fahrenholtz, et al., (2007). 19

Figure 2- 2: Flexure strength for various ZrB_2 composites with reinforcement phase compositions 0-30 vol%. Apparent flexure strength increases with reinforcement phase taken from Fahrenholtz, et al., (2007). 22

Figure 2- 3: Room temperature and strength variations with temperature for HfB_2 and ZrB_2 based composites with SiC as the reinforcement taken from (Leohman, et al., 2006). 26

Figure 2- 4: Examples of activation energies detailing creep mechanism transitions from (A) independent operating parallel processes and (B) sequential processes. 29

Figure 2- 5: Single grain under an applied uniaxial stress. Contour flow lines indicate the mass transport direction from grain boundaries under local compression to boundaries under local tension..... 31

Figure 2- 6: Plastic flow of a polycrystalline material detailing three regions of deformation according to Ashby and Verrall (1973). 39

Figure 2- 7: Scribe offset revealing grain boundary sliding in a polycrystalline crept material from Bell and Langdon (1967). 40

Figure 2- 8: Soap film snap shot during deformation showing neighbor switching and grain translation deformation event (following grain G, H, L, M). Grain shapes remain near constant during grain movement from (a) to (c). 41

Figure 2- 9: Grain switching model proposed by Ashby and Verrall (1973) showing diffusion accommodating grain translation and subsequent neighbor switching under an applied stress. 45

Figure 2- 10: Grain switching event described by Gifkins (1978), following Ashby and Verrall (1973). Grain rotation is required for maintaining a continuous microstructure. 47

Figure 2- 11: Diffusive lenticular shaped cavity nucleation and growth schematic following Hull and Rimmer (1957) along a grain boundary. boundary stress relaxation occurs by diffusion along the grain boundary (JB) and along the cavity surface (J_S) 51

Figure 2- 12: Polycrystalline cavitation model proposed by Evans and Rana (1979). (A) details cavity nucleation at a triple junction and (B) growth of the equilibrium shaped cavity to full facet length. 53

Figure 3- 1: Molar Gibb's free energy curves, with WC mole fraction, at four temperatures describing possible solubility limits in the quasi-binary ZrB_2- WC system. 63

Figure 3- 2: c-axis (Top) and a-axis (Bottom) lattice parameter determination for ZrB_2 polycrystalline phase. Dark hashed line represents linear regression fit of Equation (3-6) and the dotted lines represent 95% confidence interval. 71

Figure 3- 3: EBSD reconstruction map highlighing the SiC phase (black) and ZrB_2 phase (grey) (left) and the actual SEM image (right). RD, TD and ND are sample space default directions with TD parallel to the bending stress axis (bottom). 72

Figure 3- 4: Intercept lines overlaid on polished and etched ZrB_2 grains (dark grey) and SiC grains (light grey) micrograph. Z20SB was final polished using 0.05µm SiO2 colloidal solution and etched with 1:1 H2O2:HNO3. 74

Figure 3- 5: Creep bar cross-section detailing cavity analysis location for both tensile and compressive creep zones..... 75

Figure 3- 6: Simple beam theory model showing geometric relationships between NA, Compressive arc length (BC) and Tensile arc length (AB)..... 77

Figure 3- 7: Un-crept state (left) and crept state (right). Vertical dotted and solid lines are indent shape boundaries based on threshold imaging and the average indent shape position, respectively. 79

Figure 3- 8: Nano-indentation load-displacement (top) and indentation collapse due to the presence of a pore (bottom). The hardness-depth calculations (right) indicate collapse contrasting with the observed hardness plateau. 84

Figure 3- 9: Protective creep setup showing flowing capsule arrangement and the four point bending fixture, sample and deflectometer (white arrow). 86

Figure 3- 10: Extensometer-deflectometer setup. 87

Figure 3- 11: Extensometer assembly calibration curve taken from Aune (2011). 88

Figure 3- 12: Loading assembly fixture and vacuum furnace setup for dead load creep experiments. Graphite load plate and support posts are shown in black. 89

Figure 4- 1: Backscatter Electron SEM micrographs for the Z20SB (a) and Z20S (b) composites. The large black inclusions are phases other than SiC (grey) and ZrB_2 (Light). 93

Figure 4- 2: Electron back scatter micrograph of ZSB composite. 93

Figure 4- 3: XRD patterns for the Z20SB and Z20S microstructures. 94

Figure 4- 4: Backscatter Electron SEM micrographs for the ZCWC (a), ZWC1 (b), ZWC2 (c) and ZWC3 (d) alloys. 95

Figure 4- 5: XRD patterns for the as sintered ZCWC, ZWC1 and ZWC3 alloys. 97

Figure 4- 6: High magnification image of the ZCWC alloy detailing the ZrB_2 (1), WB (2), Unknown (3), B-N-C (4) and C-rich (5) phase. 98

Figure 4- 7: ZWC1 micrograph and complementary EDS mapping revealing elemental distribution. Zr and B are depleted at O-rich regions while the phase difference is not readily observed in backscatter; the light phase is WB. 99

Figure 4- 8: Secondary electron SEM micrograph of as-received ZWC1 (a) and ZWC2 (b) showing the decreasing ZrO2 volume fraction. The carbon phase (black) appears minimal in ZWC2. 99

Figure 4- 9: Optical micrographs showing C-rich HAR phase in the as-sintered microstructure (a) and the near complete dissolution with solution treating for 90 minutes at 2100°C (b). 100

Figure 4- 10: ZWC3 alloy 2100°C solution treatment for 60 min showing little microstructure change from the as-sintered condition. 101

Figure 4- 11: 2300°C anneals for ZCWC (a) and ZWC3 (b). The light multi-grain junction phase is a Zr-W alloy phase with elongated ZrB_2 grains and a black carbon-rich phase (a). Globular WB phase and ZrB_2 grains (grey) are shown in the ZWC3 alloy (b). 101

Figure 4- 12: XRD patterns showing the crystalline phase character of the ZCWC and ZWC3 alloys after a 2300°C heat treatment. 102

Figure 4- 13: Zr-W-B ternary phase diagram after Chang (ref) detailing a ternary phase solid solution phase of composition ~ 26Zr-41W-33B at 1400°C, taken from (Chang 1966). 108

Figure 4- 14: Excess carbon concentration effects on WC dissolution and WB reaction equilbiria at T=2700K. The dissolution factor, y, has a significant effect on the critical carbon concentration (ΔG<0) for promoting WC dissolution. 110

Figure 4- 15: W-B-C ternary diagram from Rudy (ref) at 2150°C detailing starting nominal WB compositions for ZCWC (Black) and ZWC3 (Grey) circles, taken from (E. Rudy 1969). 112

Figure 4- 16: W-B-C ternary diagram at 2320°C detailing starting (filled circles) and final (open circles) nominal WB compositions for ZCWC (Black) and ZWC3 (Grey), taken from (E. Rudy 1969). 113

Figure 4- 17: Backscattered electron SEM image of the mapped area showing WB phase (light) surrounded by small (Zr,W,C,B)ss phase (grey) and the W elemental mapping showing regions of W-depletion near the WB grain boundaries. 115

Figure 4- 18: Intrinsic flaw size correlation with presumably strength limiting microstructure constituents. Hashed boxes represent Griffith. 117

Figure 4- 19: HAR Carbon phase (dark) embedded in a ZrB_2 matrix, from a ZCWC alloy MOR fracture face, illustrating the fibrillated morphology and the volume defects observed at the interphase boundary. 119

Figure 4- 20: Fractographs of the Z20S (a) and ZWC1 (b) materials illustrating transgranular matrix fracture. 120

Figure 4- 21: ZWC3 AR alloy fractograph detailing an apparent increase in ZrB_2 grain facets.... 121

Figure 4- 22: Residual stress from thermal expansion anisotropy transformation from the c-axis for ZrB_2 122

Figure 4- 23: Substitutional solute concentration model (lines) with experimentally measured composite and alloy hardness (circles). The error bars represent the hardness variation from crystallographic orientation slip dependencies. 124
Figure 5- 1: Low temperature (1400 - 1500°C) smoothed Z20SB creep curves through 97MPa. Dotted arrow breaks indicate experiment terminated based on time prior to failure. Samples did not fail during creep experiments. 128
Figure 5- 2: High temperature (1600 - 1800°C) high stress (>30 MPa) Z20SB creep curves. Solid arrow breaks indicate experiment terminated based on displacement limitations and dotted arrows indicate creep curve terminated based on time. 129
Figure 5- 3: High temperature (1600 - 1800°C) low stress (<30 MPa) Z20SB creep curves. Solid arrow breaks indicate experiment terminated based on displacement limitations and continuous arrows show creep curves extend beyond the time axis. 130
Figure 5- 4: As-crept Z20SB specimens illustrating macroscopic creep behavior under protective environment and constant load creep conditions. 131
Figure 5- 5: Creep rate-stress dependent plot for the Z20SB flexure creep experiments. 132
Figure 5- 6: Creep rate-temperature dependence for the Z20SB flexure creep experiments. Dotted lines illustrate apparent stress dependent behavior..... 133
Figure 5- 8: As-crept Z20SB specimens illustrating macroscopic creep behavior under protective environment and constant load creep conditions. 134
Figure 5- 7: ZWCAR and HT alloy creep curves at 1800°C and 30 and 97 MPa constant stress. Dotted arrow breaks indicated experiment terminated based on time prior to failure and vertical solid arrow indicates specimen rupture. 135

Figure 5- 9: 1800°C, 97MPa creep compressive zone (left); Corresponding creep tensile zone (right). Cavitation is absent along compressive creep zones contrasting with noticeable cavitation along the tensile creep zone. 136

Figure 5- 10: 1500°C, 97 MPa cavitation free compressive zone (left) and tensile zone (right). Tensile stress zone shows no triple point cavitation. 137

Figure 5- 11: 1800°C, 97MPa polished and thermal etched section viewing the flexure tensile zone cavitation. Black arrows indicate ZrB_2-SiC cavitation and white arrows ZrB_2-ZrB_2 cavitation. 138

Figure 5- 12: ZWC3AR alloy crept at 1800°C, 30 MPa showing negligible cavitation along the compressive region (top) and small cavities, pointed out by the solid arrows along the tensile zone (bottom). 139

Figure 5- 13: ZWC3AR alloy crept at 1800°C, 97 MPa showing cavitation (solid arrows) along the tensile zone (top). ZWC3HT alloy crept at 1800°C, 30 MPa in inert environment (bottom). Mild oxidation was observed. 140

Figure 5- 14: High strain Z20SB creep specimen tested at 1800C, 16MPa for 7.75 hrs under 3 psi pressurized Ar gas. Outer-fiber strains of 15.6% and 6.5% for tensile and compressive sides, respectively, using optical methods. 141

Figure 5- 15: Optical beam curvature strain distribution (dotted line) with SiC spacing strain measurements (circles), Horizontal and vertical error bars represent the strain interval from the average SiC spacing distribution and micrograph locations. 142

Figure 5- 16: Grain size (top) and Grain aspect ratio (Bottom) for ZrB_2 (left) and SiC (right) grains measured using EBSD method for compressive and tensile deformation regions.. 143

Figure 5- 17: Inverse pole figure (IPF) maps of the tensile (a), Hot-pressed (b) and compression (c) deformation zones of a Z20SB crept composite for ZrB_2 (left) and SiC (right). The Hot-pressed condition is provided as a reference for the initial conditions. 145

Figure 5- 18: Inverse Pole Figure (IPF) texture plots for ZrB_2 (left) and SiC (right) for the tension (a), hot-pressed (b) and compression (c) bending zones. Greek letters correspond to Schmid angle pairs for predominant fiber texture orientations. 146

Figure 5- 19: Compression bending region KAM (left) and HREBSD GND concentration rendering (right) regions. SiC particles are labeled for reference and the GND color map is in log10 m-2 units. 148

Figure 5- 20: Tension bending region KAM (left) and HREBSD GND concentration rendering (right) regions. SiC particles are labeled for reference and the GND color map is in log10 m-2 units. 148

Figure 5- 21: Local creep strain distribution based on indent-to-indent horizontal creep displacement changes from the un-crept reference frame. 149

Figure 5- 22: Partitioned strain distributions for (a) Rotational, (b) Grain interior and (c) Translational. 150

Figure 5- 23: Local creep strain probability (dashed line) and PDF's (left) and maximum likelihood (right). The fractional probability of individual strains (i.e. rotational, translation and grain interior) identify the local creep contributions (shapes). 151

Figure 5- 24: IDM crept specimen comparison with those conducted in the flowing argon setup. Creep experiments were conducted at 1800°C and stresses of 30 MPa and 30 and 40MPa for the protective and inert conditions, respectively. 152

Figure 5- 25: IDM results for the crept (right) and un-crept (left) condition. The solid arrow highlights a cavity formed during creep. 152

Figure 5- 26: Low temperature creep models with the open circles representing experimental data, the solid line represents known prediction range and the hashed line indicates model predicted intervals 159

Figure 5- 27: Strain due to cavitation (%) contribution to overall creep strain independent of temperature. Vertical error bars show standard deviations for all creep experiments; horizontal error bars show error in creep strain measurement. 161

Figure 5- 28: Cavity number density, independent of temperature, as a function of stress for T>1500°C (Left). Vertical error bars are standard deviations for 1600 -1800°C creep experiments. 163

Figure 5- 29: 1600C 16 MPa (left) and 97 MPa (right) post creep fracture faces showing cavitation primarily at Z-S boundaries. White arrows indicate Z-S full facet cavitation and black arrows indicate isolated triple point cavitation. 164

Figure 5- 30: (0001) $< 1120 >$ or $< 1010 >$ slip systems (Left) with Schmid factors 0.488-0.500 (light grey) and 0.400-0.488 (black) and $1010 < 1120 >$ system (right) with Schmid factors 0.488-0.500 (white) and 0.400-0.488 (light grey to black). 167

Figure 5- 31: SiC IPF plots; compression creep (left) having solid (22°, 68°), dotted (90°, 0°) and dashed (49°, 41°) orientations. Tension creep (right) having solid (22°,68°), dotted (64°,36°) and dashed (32°,55°) orientations. 168

Figure 5- 32: SiC texture orientation distribution change. 169

Figure 5- 33: Strain limits for starting grain shapes of 0.20≤AR<1.0. The bold dotted line respresents the 99% confidence interval from ZrB_2 EBSD grain shape measurement intervals and the outer dotted line representing a starting aspect ratio of 1. 171

Figure 5- 34: ZrB_2 IPF plots; Compression creep (left) having solid (32°,60°) and dotted (66°,36°) orientations. Tension creep (right) having solid (39°,51°) and dotted (69°,25°) orientations. 172
Figure 5- 35: ZrB_2 texture orientation distribution change. 173
Figure 5- 36: Pole figures of the (0001) pole projection for the tensile (a), Hot-pressed (b) and Compression (c) ZrB_2 zones. The ND direction is normal to the polish plane. The TD and RD directions are parallel and normal to the bending stress axis. 175
Figure 5- 37: As-crept micrograph of observed grain rotation (Top) and un-crept condition (Bottom). Indent alignments, between grains, noticeably deviate from the un-crept array positions. 176
Figure 5- 38: 1800°C and 54 MPa outer-fiber tensile creep zone on polished and etched surface. Black arrows indicate Z-S triple point cavitation and white arrows indicate the appearance of damage free Z-S triple points. 176
Figure 5- 39: Revised tensile zone featuring ZrB_2 GND density spatial distributions. 178
Figure 5- 40: Orowan model (solid line) with the 95% confidence bounds (dashed lines) overlaid with GND-distance quantities calculated using HREBSD rendering (circles). Error bars represent the standard deviations. 179
Figure 5- 41: Orowan model (solid line) with the 95% confidence bounds (dashed lines). IDM calculated and theoretical GND densities (filled shapes). HREBSD GND densities (open circles). Error bars represent the standard deviations. 182
Figure 5- 42: 1600°C creep model comparison for diffusion and grain boundary sliding creep at low stresses. Intermediate stresses: grain boundary sliding accounts for majority of creep. High stress: grain boundary sliding and cavitation dominate. 185
Figure 5- 43: 1800°C Z20SB flexure creep comparisons with existing creep theory. 187

Figure 5- 44: Flexure creep model comparison at 1800°C. The hashed line represents Equation (5-17) and (5-19) operating sequentially. The black hashed line represents Ashby and Verrall (1973) creep model. 189

Figure 5- 45: Deformation Mechanism Schematic for Z20SB composite. Grey grain represents a place holder for a SiC or ZrB_2 grain. 189

Figure 5- 46: Solute drag model derived by Cottrelll and Jaswon (solid line) with 95% CI bounds (hashed lines) compared with normalized creep rates for the ZrC-WC (circles) and ZrB_2-WC (Squares). 194

Figure 5- 47: Breakaway stress model illustrating alloy constitution, cs, effectiveness. 195

Figure 6- 1: ZrB_2-SiC composite strength assessment illustrating volume fraction reinforcement and critical grain/agglomerate size relationships. 205

Figure A- 1: Calculated molar free energy-composition curves for the ZrB_2 and WC phases. 221

Figure A- 2: Calculated ZrB_2-WC solvus line with temperature. Exprimental WC solute concentrations (circles) and the composition variation (hashed line) are shown for reference. 221

Figure A- 3: Activity coeficients for non-standard state W, C and B in solution with either a ternary or binary Zr based solution. 223

Figure B- 1: EBSD setup in an SEM chamber illustrating the sample, beam and diffraction camera positions (left) and a representative Kikuchi diffraction pattern produced from an accelerating voltage (right). Images taken from EDAX (2011) 227

Figure B- 2: ROI selections (rectangles) illustrating the approach for determining the Kikuchi pattern center. 228

Figure C- 1: Pole plot orientation data from EBSD pattern analysis along three arbitrary crystallographic directions 230

Figure C- 2: Theoretical orientation distribution profiles for tensile strains illustrating lattice rotations towards the stress axis indicated by small misalignment angle peak development recreated from ref ((Hosford 1993)). 232

Figure C- 3: Experimental orientation distribution plot compared with the model fit for an average lattice deformation strain of -1.40%. The stress axis is oriented 69° and 25° from the(0001) pole and [$11\bar{2}0$] crystal direction. 232

Figure D- 1: Example KAM image with a profile line overlaid. 233

Figure D- 2: Example lattice misorientation-distance profile across the ZrB_2 grain structure illustrating the harmonic signal nature 234

Figure D- 3: FFT plot illustrating the maximum frequency corresponding to the profile Fourier length, d. 235

List of Tables

Table 2- 1: Select physical, chemical and mechanical properties for ZrB_2 and HfB2 polycrystalline ceramics. 6

Table 2- 2: Select elastic and thermal property temperature dependence for ZrB_2. The polycrystalline Young's modulus is reported for 1400K. The subscripts a and c represent the [1 1 -2 0] and [0 0 0 1] hexagonal lattice directions. 7

Table 2- 3: Room temperature mechanical properties for select ZrB_2 monolith and composites microstructures. 20

Table 2- 4: Summary of creep model parameters and rate-controlling mechanisms 28

Table 3- 1: Material and experiment designations and processing descriptions for the composites and alloys used in this study..... 62

Table 3- 2: Raw powders used for materials processing with starting particle sizes. 64

Table 3- 3: Nano-indentation experimental parameters. 82

Table 4- 1: As-Received ZrB2 based ceramic alloys and composite density comparison 92

Table 4- 2: ZrB2 based monolithic alloy and composite grain sizes for matrix (ZrB_2) and reinforcement (SiC) phase. Errors are grain size distribution standard deviations.... 92

Table 4- 3: : ZSB composite phase analysis via electron probe (WDS)..... 94

Table 4- 4: EDS average phase compositions observed with corresponding material designations. 96

Table 4- 5: Lattice Parameter comparisons for select as-received and heat treated billets..... 103

Table 4- 6: Room temperature mechanical properties for SiC containing ZrB_2 composites and monolithic WC bearing alloys. All materials were tested in the as-received condition. 104

Table 4- 7: Room temperature hardness and elastic modulus for select heat treated ZrB_2-WC alloys. 104
Table 4- 8: WC composition comparisons vs. nominal compositions assuming all WC impurities are included in the initial powder charge. 106
Table 4- 9: Optically measured WB phase quantities for the as-sintered alloys. 111
Table 5- 1: Measured activation energies and errors based on 95% confidence interval of the data for Z20SB composite. 131
Table 5- 2: ZWC3 alloy creep results. 136
Table 5- 3: High temperature cavitation - strain data. 137
Table 5- 4: High strain optical and intercept strain measurements over the sampled total micrograph area for each normalized bar height positon. 142
Table 5- 5: Fiber Texture Directions from Figure 5- 18 and the equivalent stress vector positions relative to the (0001)-Pole and $\mathbf{2\ 1\ 1\ 0}$ cyrstallographic directions. 147
Table 5- 6: Low temperature grain boundary diffusion model inputs for 1400°C and 1500°C creep. 157
Table 5- 7: SiC Texture Strain Results for fiber texture peaks developed in the hot-pressed (HP), tension (T) and compression (C) deformation configurations. 168
Table 5- 8: Texture Strain Results for fiber texture peaks developed in the hot-pressed (HP), tension (T) and compression (C) deformation configurations. 173
Table 5- 9: Grain boundary sliding and cavitation model parameters. 187
Table 5- 10: Normalized experimental creep rates for ZWC3AR (1.4 mol% WC) and HT (2.5 mol% WC) 195
Table 6- 1: ZrB_2 based composite and alloy property comparison. 203

Table A- 1: Thermochemical data used for phase diagram and reaction equilibria development 224

Table A- 2: Activity coefficients for select ternary and binary Zr based systems for T= 2500 and 2700K. 225

Table E- 1: Model parameters for the breakaway stress calculation. 240

Chapter 1

Introduction

Ultra High Temperature Ceramics (UHTC's) are a class of materials specifically developed for extreme environment structural applications (T>1500°C). Figure 1- 1 is a compilation of melting points for classifying candidate refractory metals and compounds.

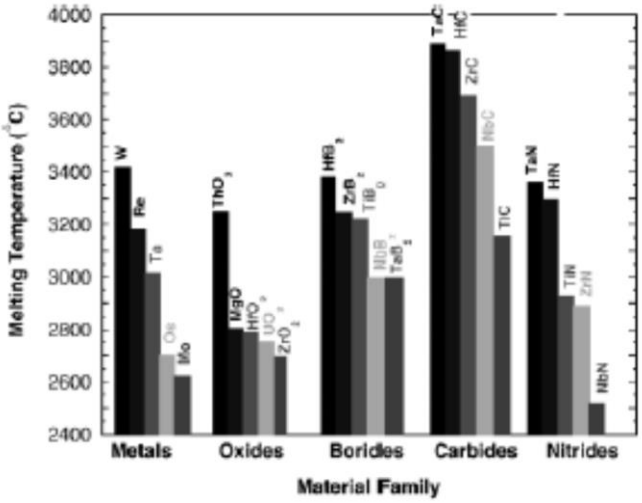

Figure 1-1: Melting point comparison of select refractory metals and ceramic material systems (Fahrenholtz, Hilmas and Talmy, et al., 2007).

It is immediately apparent the group IV borides, select group IV and V carbides and nitrides meet these criteria. The fundamental considerations existing include: high temperature strength behavior, oxidation resistance, low toughness, and creep behavior (Courtright, et al., 1992). Diboride materials offer excellent strength retention as a result of the strong covalent bonding characteristics despite accelerated oxidation beyond T=1400°C (Courtright, et al., 1992). The Low fracture toughness (~3 $MPa\sqrt{m}$), of monolithic diborides, inhibits reliable service life in applications involving thermal shock and foreign body impact damage. Therefore, diboride based composites, with refractory reinforcements such as SiC show improved

mechanical strength, toughness and oxidation characteristics (Courtright, et al., 1992). For example, HfB_2 composites containing SiC showed reduced oxidation rates at 2000°C suggesting possible short-duty cycle applications over the monolithic variety despite the high material density (11.20 g/cc) (Courtright, et al., 1992). Although, the introduction of interphase boundaries may have a deleterious effect on creep behavior, as a result impurities, driving the creep rate above the design threshold of $< 10^{-8}\ s^{-1}$ for long duty cycle turbine applications (Courtright, et al., 1992). Presently creep of diboride-based monoliths and composites are not well known in inert and oxidizing environments.

UHTC applications include hypersonic flight ((Courtright, et al., 1992), (Leohman, et al., 2006), (Opeka, Talmy and Wuchina, et al., 1999) and (Squire and Marschall 2010)) winged atmospheric re-entry and low earth orbiting vehicles ((Courtright, et al., 1992) and (Levine, et al., 2002)) , refractory linings ((Kislyi and Kuzenkova 1966) and (Kuzenkova and Kislyi 1966)), electrodes, microelectronics and cutting tools (Fahrenholtz, Hilmas and Talmy, et al., 2007). Most notably, the aerodynamic surfaces of hypersonic, winged atmospheric re-entry vehicle designs, and structural propulsion components require improved material performance under long exposure to ultra-high temperatures, convective heating and extreme oxidation conditions. Squire and Marschall (2010) have completed a review of select material properties most critical for hypersonic and re-entry vehicle designs. From Figure 1- 2, the aerodynamic surface design example shows the energy balance expected at the leading edge and exponentially heat flux decay away from the stagnation point. Ahead of the design leading point lays a thermal shock zone accompanied by primary heat conduction through the material volume and additional heating and cooling from oxidation reactions and subsequent evaporation. Hence, high thermal conductivity, excellent thermal shock properties, and oxidation resistance are required for best performance (Squire and Marschall 2010).

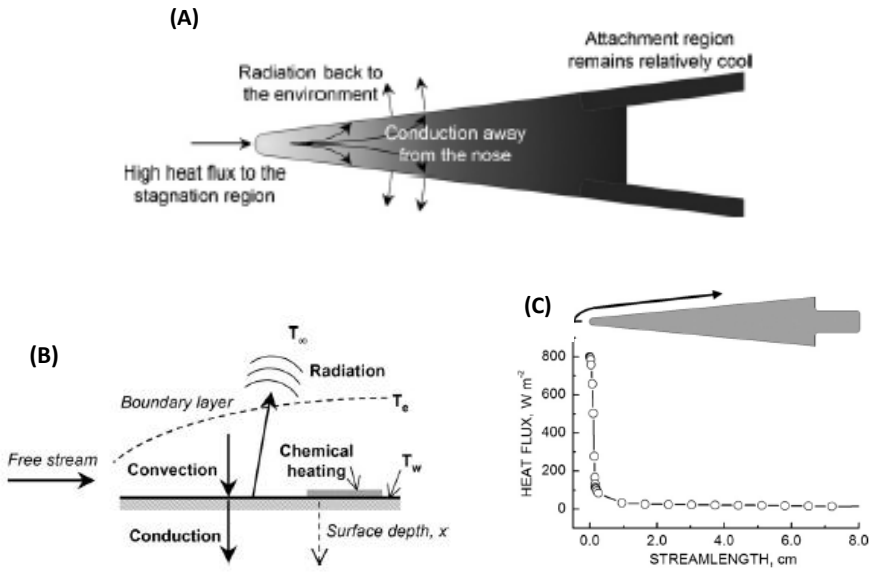

Figure 1-2: Heat transfer schematic detailing (A) leading edge component with general heat flow considerations (B) energy balance along leading edge surface and (C) heat flux decay away from leading edge stagnation point (Squire and Marschall 2010).

The present study seeks to provide the following characterization of physical, chemical and mechanical properties in the context of relevant microstructural influences, in particular, behavior transitions with temperature are discussed from a mechanistic viewpoint. For convenience processing and room temperature physical and mechanical properties are discussed separately from the assessed composite and alloy creep behavior.

ZrB_2-20% SiC composites were processed for characterizing room and high temperature mechanical behavior. Additionally, a preliminary alloy development program was launched for investigating WC solubility in ZrB_2 with the anticipation of forming improved creep resistant materials. Material characterization was attempted using a combination of X-ray diffraction, electron dispersive spectroscopy and optical and scanning electron microscopy. Room temperature fracture strength and toughness, hardness and elastic modulus were measured for property comparison. Approximate thermochemical descriptions of reaction equilibria and phase stability were provided for understanding the microstructure evolution

amongst varying processing parameters including high temperature annealing (T=2300°C). Structure-property relationships were developed on the foundation of linear elastic fracture theory.

Attempt was made to characterize the temperature and stress dependence of the creep behavior for a ZrB_2-20% SiC UHTC through 1820°C. Protected atmosphere flexure creep experiments were conducted for determining the predominate temperature and stress dependent deformation mechanisms, based on experimental Norton constants. To consider the global question of what rate-controlling mechanisms operate and how the microstructure accommodates the strain, first the optical scale was examined, in particular, comparing grain boundary intercept quantities at bend radius traces near the tensile surface to those along the compressive surface. When combined with grain aspect ratio data, details emerge regarding the structure evolution manifested as grain extension or grain rearrangement. Second, deformation mapping using and Electron Back Scatter Diffraction (EBSD) methods characterized the bulk micro-deformation of the ZrB_2-20% SiC composite. Finally, a version of the earlier scribe experiments, indentation deformation mapping (IDM), under inert conditions, was conducted for assessing bulk micro and grain-to-grain deformation. Attempt was made to bridge the deformation length scales from local grain movements through macroscopic creep behavior. Rate-controlling creep deformation and accommodation mechanisms were discussed in the context of existing creep and single crystal deformation theory, respectively. Based on these findings, preliminary creep experiments were conducted providing valuable insights to creep reduction by solid solution strengthening. Solute-dislocation interactions were considered based on dislocation creep theory and dislocation breakaway stresses for understanding alloying effectiveness.

Chapter 2

Literature Review

This literature review is a comprehensive overview of active UHTC research spanning six decades. Topics cover metal diboride systems and motivation as candidate high temperature materials and considered applications, monolithic and composite zirconium diboride development, zirconium diboride room and high temperature deformation phenomena including an extensive review of creep theory.

2.1. Metal Diboride Motivation

Metal boride compounds offer a unique combination of high melting points, high thermal conductivity and thermodynamic stability which make such materials candidates for ultra-high temperature oxidizing environments. A comprehensive study conducted by MANLABS, Inc. identified HfB_2 and ZrB_2 monoliths, based on oxidation and vapor pressure research, as most suitable diboride compounds for high temperature applications requiring oxidation resistance (Kaufman and Clougherty 1963). Table 2- 1 is a review of select material properties for both the Hf and Zr boride systems revealing a unique blend of metallic-refractory material behavior.

The hexagonal lattice is comprised of metal (Me) basal plane atomic arrangement with an inserted boron (B) half plane (Lawson, et al., 2012), (Okamoto, et al., 2010) and (Fahrenholtz, Hilmas and Talmy, et al., 2007). Therefore, a combination of covalent, ionic and metallic bonding exists where Me-Me bonding occurs within the basal plane and covalent/ionic bonding between B-B and Me-B atoms. These bonding states have been confirmed by *ab initio* calculations performed by Lawson, et al., (2012). Temperature dependent physical material

Table 2- 1: Select physical, chemical and mechanical properties for ZrB_2 and HfB2 polycrystalline ceramics.

Property - 25°C	ZrB_2	HfB_2
Crystal system	Hexagonal†	Hexagonal†
Space group/Structure	P6/mmm AlB2†	P6/mmm AlB2†
a (Å)	3.169‡	3.142‡
c (Å)	3.531‡	3.475‡
Density (g-cm^{-3})	6.09*	11.2*
Melting Temperature (°C)	3256*	3402*
Young's modulus (GPa)	440**	480†
Bulk Modulus (GPa)	215†	212†
Hardness (GPa)	21**	24**
Linear Coefficient of thermal expansion (K^{-1})	6.29x 10-6‡	6.72 x10 -6‡
Heat Capacity (J-mol^{-1}K^{-1})	48.2‡	49.7‡
Electrical Resistivity (Ω-m)	5.7x10-8‡	13.5 x10-8‡
Thermal conductivity W-m^{-1}K^{-1}	60†	104†
Heat of Formation (KJ-mol^{-1})	-320.9‡	-310.5‡

† (Fahrenholtz, Hilmas and Talmy, et al., 2007)
‡ (Kaufman and Clougherty 1963)
* (Kaufman and Clougherty 1965)
** (Shackelford, Alexander and Park 1995)

properties have been investigated by Okamoto, et al., (2010) for select MeB_2 monoliths through 723°C. Table 2- 2 is a compilation of elastic and thermal expansion properties as a function of lattice direction and temperature.

Okamoto, et al., (2010) showed the elastic properties were highly anisotropic for ZrB_2 consistent with typical hexagonal lattice symmetry behavior. Additionally, Lawson confirmed the room temperature elastic properties. Inspection of the thermal expansion properties indicates a transition to isotropic behavior with increasing temperature through ~723°C. This is unusual as most hexagonal material properties are anisotropic. The C_{44}/C_{66} elastic constant ratio of ~ 1 for ZrB_2 indicates a reduction in anisotropic bonding behavior contrasting with TiB_2 and CrB_2 ratio of 0.880 and 0.614, respectively (Okamoto, et al., 2010). The covalent/ionic bonding is attributed to high modulus, low thermal expansion, high hardness and high melting points while metallic bonding improve thermal and electrical conductivity.

Table 2- 2: Select elastic and thermal property temperature dependence for ZrB_2. The polycrystalline Young's modulus is reported for 1400K. The subscripts *a* and *c* represent the [1 1 -2 0] and [0 0 0 1] hexagonal lattice directions.

Material	E_a (GPa)	E_c (GPa)	B (GPa)	G (GPa)	v
*ZrB_2 - 0 K	----	----	248	234	----
†ZrB_2 - 300K	533.3	387.7	240.1	231.7	0.135
†ZrB_2 - 1400K	475		240	210	0.151
Material	α_a (K^{-1})	α_C (K^{-1})	α_a/α_C	C_{33}/C_{11}	C_{44}/C_{66}
†ZrB_2 - 300K	$5x10^{-6}$	$6.8x10^{-6}$	0.74	0.77	0.97
†ZrB_2 - 1073K	$7x10^{-6}$	$7X10^{-6}$	1.00	0.79	1.01

† (Okamoto, et al., 2010)

* (Lawson, et al., 2012)

2.2. Monolithic and Composite UHTC Development

Many research efforts have addressed combinations of processing, sintering additive effects and composite reinforcement phase strength property relationships and short crack fracture resistance. Early research by Kuzenkova and Kislyi (1966) and Kislyi and Kuzenkova (1966) investigated pressureless sintering shrinkage of ZrB_2 and ZrB_2 – Mo particulate composites. Kaufman and Clougherty (1965) also conducted a similar sintering study while investigating the sinterability of stoichiometric and metal-rich Zr and Hf diboride systems. Three decades later S-Q, Guo (2009) and Fahrenholtz, et al., (2007) provided a comprehensive overview of ceramic processing techniques, sintering aid and composite reinforcement effects on final microstructure. The forth coming section provides an in-depth treatment of the sinterability of ZrB_2 monoliths and composite compositions and the effect on mechanical properties.

2.2.1. Processing

Processing additives and milling procedures have been explored in efforts to reduce sintering temperatures and improve final ceramic density. Pressureless densification of

nominally pure Me-borides has been reported to only occur near their melting points. As a result of impeded diffusion from strong covalent bonding between B-B and Me-B atoms, significant porosity maybe present without the addition of sintering aids. Kuzenkova and Kislyi (1966) and Kislyi and Kuzenkova (1966) explored the shrinkage nature of ZrB_2 monolith using high temperature dilatometry for elucidating the densification mechanisms. In their study single phase ZrB_2 was pressureless sintered between 1800 and 2100°C. At all temperatures a minimum of 30% porosity was present along with two distinct densification stages: transient stage 1 (< 30 min isothermal holding) and quasi-steady state stage 2 (>30 min isothermal holding). During stage 1 interface slip is thought to control the shrinkage behavior as viscous flow could not accommodate the rapid length change. However, approaching stage 2, densification proceeds by viscous flow. From their relative density change data, a characteristic shear viscosity (η) was calculated according to Equation (2-1),

$$\eta = \frac{3}{2}\frac{\sigma\Pi(3-\Pi)(1-\Pi)^2}{r_0(1-2\Pi)\frac{d\Pi}{dt}}, \qquad (2\text{-}1)$$

where σ is the surface tension, Π porosity, r_0 mean particle size and t sintering time. The shear viscosity is considered an activated process where the densification energy of 678 +/- 114 KJ/mol represents diffusion controlled quasi-steady state densification (Kuzenkova and Kislyi 1966).

Similar sintering studies were conducted by (Kaufman and Clougherty 1965) for Zr-rich boride monolith structures including 1% ZrC, Si and W additions at temperatures of 2000 - 2200°C for 1-16 hours. Relative density changes were measured as a function of sintering temperature and time for describing the sintering kinetics where pressureless sintering models were derived. All sintered microstructures were observed to have a second phase originating from a liquid film which promoted densification. In specimens sintered at 2300°C and

containing tungsten accelerated densification behavior, as a result of eutectic phase formation, occurred at tungsten compositions of 6 wt%. For specimens with additions of silicon and zirconium densification rates were inhibited resulting in low densities. Using intermediate stage diffusion models, for bulk (Equation (2-2)) and grain boundary (Equation (2-3)) paths, the $ZrB_{1.89}$ sintering mechanisms were determined along with approximations for valuable diffusion coefficients and activation energies.

$$\frac{d\rho}{dt} = \frac{AD_L\gamma\Omega}{G^3kT} \tag{2-2}$$

and

$$\frac{d\left(\rho^{3/2}\right)}{dt} = \frac{BD_bW\gamma\Omega}{G^4kT}, \tag{2-3}$$

where ρ is the relative density, A and B are constants, D_L lattice diffusion coefficient of rate-controlling species, D_b grain boundary diffusion of rate-controlling species, W grain boundary width, γ surface energy, Ω is the ZrB_2 lattice volume, k Boltzmann's constant, T temperature, t time, and G is grain size. From Equation (2-2), a sintering activation energy and lattice diffusion coefficient, between 2000 and 2200°C, of 644 KJ/mol and 1.6 – 30 $x10^{-10}$ cm^2/sec were approximated. The grain boundary diffusion coefficient and boundary product (D_bW) are 5.4-105 $x10^{-7}$ cm^2/sec and 5.4 – 105 x 10^{-14} cm^3/sec, respectively, assuming a boundary width of 10^{-7} cm (monolayer) suffices for rapid sintering (Kaufman and Clougherty 1965). Inspection of the D_0 values for each mechanism shows lattice diffusion kinetics are excessive for any realistic intrinsic diffusion process ((Porter and Easterling 2004) and (Kaufman and Clougherty 1965)) and grain boundary or liquid interphase diffusion as the dominant sintering mechanism between 2000 – 2200°C.

From Kaufman and Clougherty (1965) a grain boundary or liquid phase densification mechanisms was tentatively concluded from the assessed diffusion coefficient analysis. A

similar observed sintering mechanism was reported by Kuzenkova and Kislyi (1966) for commercial grade ZrB_2 where ZrB_{12} impurity phase was reported on grain surfaces. This was thought to activate sintering by the presence of precipitated secondary ZrB_2 and boron-rich phases along the grain facets, when sintered, promote intergranular diffusion as the secondary ZrB_2 homogenizes leaving boron-rich ZrB_2 grain boundaries. As evidence of this mechanism the approximate shear viscosity activation energy for commercial ZrB_2 of 416 +/- 174 KJ/mol noting a 100% decrease in activation energy with associated sintering mechanism (Kuzenkova and Kislyi 1966).

Sintering additives have been proven to enhance sintering by reduction in the activation barrier promoting mass transport along either liquid phase or clean grain boundaries driving the densification temperature down. The former has been explored for high temperature sintering of ZrB_2 with W impurities (Kaufman and Clougherty 1965) and ZrB_2 – Si_3N_4 (Monteverde, Guicciardi and Bellosi 2003) based ceramics and composites. Kaufman and Clougherty (1965) reported rapid densification of $ZrB_{1.89}$ containing 6 wt% W impurities sintering at 2300°C. Metallographic inspection revealed eutectic phase formation at grain boundary triple points suggesting liquid phase enhanced sintering kinetics. A W-ZrB_2 eutectic point of 2250°C for ~28 wt% W and a solubility limit of 10 wt% in ZrC has been reported for the W-Zr-B ternary (Chang 1966). Considering Zr-rich diboride compounds the equilibrium eutectic and W solubility limit in stoichiometric ZrB_2 would shift toward the ZrB_2 side of the quasi-binary diagram rendering a supersaturated 6 wt% W-ZrB_2 composition where excess W promotes liquid phase formation of eutectic composition. Additional metallic sintering additives have been used such as Ni, Fe, Cr and Mo where addition in excess of 2 wt% were required for liquid phase formation during sintering of fully dense ZrB_2 ((S. K. Mishra, S. K. Das, et al., 2002) and (Monteverde, Bellosi and Guicciardi 2002)). Kislyi and Kuzenkova (1966) showed < 15% Mo additions to ZrB_2 lowered the

shear viscosity activation from 678±55 KJ/mol to 379±46 KJ/mol suggesting Mo additions promote particle rearrangement and subsequent diffusion based densification.

The ZrB_2- Si_3N_4 system relative densities were found to increase through 98% contrasting with 87% relative density for nominally pure ZrB_2 at 1900°C (Monteverde, Guicciardi and Bellosi 2003). The low densification behavior of pure ZrB_2 was attributed to boron oxide formation and subsequent evaporation-condensation kinetics impeding densification and resulted in ZrB_2 grain growth. For improving densification and reducing the activation barrier, a reaction of Si-O-B compounds on the particle surfaces form a liquid amorphous layer concentrated at the triple points. Research has shown that Si_3N_4 does not remain as a particulate phase but completely reacts concentrating glass-like phases at the grain triple points (Monteverde, Guicciardi and Bellosi 2003). Similar effects have been shown for TiC-Si_3N_4 systems where liquid phase formation enhances grain boundary diffusion ((Park, Lee, et al., 2000) and (Park, Koh, et al., 1999)). AlN additions have been used for accomplishing similar oxide glass forming grain boundary phases enhancing densification (Monteverde and Bellosi 2003). However, the low refractory behavior of the grain boundary glass phase causes structural instabilities when approaching application temperatures ((S.-Q. Guo 2009) and (Monteverde, Guicciardi and Bellosi 2003)). Similarly reduction of oxides residing on ZrB_2 particle surfaces increases boron activity (suppresses B_2O_3 formation) and improves grain boundary diffusion. Additional non-metallic sintering additives such as B_4C, WC and C have been investigated for reactively cleaning ZrB_2 particle surfaces and promoting densification.

A review of pressureless sintering aids has shown B_4C, WC and C reduce ZrB_2 particle surface oxides promoting densification for temperatures as low as 1800°C under vacuum, ((Fahrenholtz, Hilmas and Zhang, et al., 2008), (Zhang, Hilmas and Fahrenholtz 2006) and (Zhu, Fahrenholtz, et al., 2007)). ZrB_2 reacts spontaneously with oxygen at room temperatures

forming ZrO_2 and amorphous B_2O_3; B_2O_3 removal can be achieved by maintaining a mild vacuum (110 mTorr) through 1650°C during sintering. Zhang, et al., (2006) reported a B_2O_3 boiling point of ~1340°C at 150 mTorr external pressure. However, ZrO_2 is a low vapor pressure oxide through sintering temperatures and requires chemical oxide reduction by the following reactions:

$$ZrO_{2(cr)} + 2WC_{(cr)} \rightarrow ZrC_{(cr)} + 2CO_{(g)} + 3W_{(cr)}\,, \qquad (2\text{-}4)$$

$$7ZrO_{2\,(cr)} + 5B_4C_{(cr)} \rightarrow 7ZrB_{2\,(cr)} + 2CO_{(g)} + 3B_2O_{3\,(l)}, \qquad (2\text{-}5)$$

and

$$ZrO_{2\,(cr)} + B_2O_{3\,(l)} + 5C_{(cr)} \rightarrow ZrB_{2\,(cr)} + 5CO_{(g)}, \qquad (2\text{-}6)$$

where the minimum favorable temperature of 1945°C, 1219°C and 1140°C for reactions (2-4), (2-5) and (2-6) respectively (Fahrenholtz, Hilmas and Zhang, et al., 2008); the minimum favorable reaction temperature was calculated for a Gibb's free energy of zero at standard pressure. Additionally, under vacuum conditions the partial pressure of $CO_{(g)}$ was considered equal to the chamber pressure (~110 mTorr) thus further reducing the minimum favorable reaction temperature to 1298°C, 787°C and 775°C for reactions (2-4), (2-5) and (2-6), respectively (Fahrenholtz, Hilmas and Zhang, et al., 2008). All three reactions are thermodynamically feasible, however, reactions involving B_4C and C occur at much lower temperatures than WC. Zhang, et al., (2006) found reaction (2-4) did not go to completion and suggested disassociation of WC into W_2C near 1500°C and subsequent reaction of W_2C with ZrO_2 from reaction (2-7),

$$ZrO_{2\,(cr)} + 3W_2C_{(cr)} \rightarrow ZrC_{(cr)} + 6W_{(cr)} + 2CO_{(g)}, \qquad (2\text{-}7)$$

where the reaction rate of W_2C was sluggish, reaching a kinetic limitation for ZrO_2 consumption. However, the overall weight loss measurements were consistent with those calculated based on reaction (2-4) thus proving that WC can promote densification by oxide film reduction.

Reaction (2-5) has a minimum favorable temperature well below 1000°C, under vacuum, and is reported to completely react with ZrO_2 forming ZrB_2 as the final microstructure where B_2O_3 and CO gas is removed by the mild vacuum. Zhang, et al., (2006) had shown that ~97% relative densities of raw ZrB_2 powder, from oxide removal, was achieved for B_4C compositions of 2 wt% and 4 wt%. Residual B_4C clusters were observed for microstructures sintered with 4 wt% B_4C additive while single phase ZrB_2 was observed for 2 wt% B_4C. This research considered complete consumption of 2 wt% B_4C microstructures according to reaction (2-5) and non-reacted B_4C remaining as a ZrB_2 grain growth inhibitor. Calculated quasi-binary phase diagrams, from Kaufman (1986), indicate limited solubility of B_4C in ZrB_2 of 0.5-1 wt% through temperatures of 2200°C suggesting the possibility of un-reacted B_4C dissolution for the 2 wt% B_4C-ZrB_2 composition rendering a single phase ceramic alloy. Additions of Carbon have a similar effect on particle surface oxide reduction according to reaction (6) where ZrB_2 and CO gas are produced. A thermochemical study of reactions (2-4)-(2-6) showed ZrO_2 – B_2O_3 –C reduction is most favorable through 1700°Cat standard pressure. The differences between other non-metallic additives mentioned is both particle surface oxides can be reduced forming stable ZrB_2 while the CO gas is removed by a mild vacuum. Zhu, et al., (2007) suggested an additional ZrO_2-C reduction reaction of

$$ZrO_{2\,(cr)} + 3C_{(cr)} \rightarrow ZrC_{(cr)} + 2CO_{(g)}, \qquad (2\text{-}8)$$

where oxide reduction to ZrC is thermodynamically favorable above 1166°C under 110mTorr pressure. The formation of fine ZrC phase on ZrB_2 particle surfaces would likely dissolve into solid solution with ZrB_2 as the solubility limit is approximately 4.5wt% ((L. Kaufman 1986) and (Zhu, Fahrenholtz, et al., 2007)). Zhu, et al., (2007) also reported carbon aggregation along ZrB_2 grain boundaries due to the limited solubility in ZrB_2. Kaufman (1986) reported a maximum solubility of 0.20 wt% in ZrB_2 through 2390°C suggesting the possibility of carbon segregation at

the grain boundaries which may reduce grain growth at 1900°C. With an increase in sintering temperature through 2100°C, Zhu, et al., (2007) observed grain growth and large triple point carbon rich sites from the same starting carbon composition. A separate study showed grain growth for carbon compositions of 2, 5 and 10 wt% (Mishra and Pathak 2008). Following a similar phase stability argument, an increase in carbon dissolution would be expected where an apparent grain pinning threshold had been reached. Additionally, lack of mixing has shown to promote abnormal grain ZrB_2 grain growth (Mishra and Pathak 2008). Primary ZrO_2 reduction reactions involving B_4C and C are thermochemically preferred for sintering because of the favorable reaction kinetics and minimum thermodynamic temperature. Furthermore, ZrO_2 –C reduction appears as the preferred non-metallic sintering additive because of the uniform distribution of carbon on particle surfaces contrasting with isolated B_4C particles (Fahrenholtz, Hilmas and Zhang, et al., 2008) and a reduction in oxide reduction temperature for equivalent relative densities.

Oxide growth on particle surfaces and subsequent chemical reduction is required to promote densification. However, this procedure is governed by oxygen concentration and particle size. Oxygen concentration is comprised of dissolution during powder synthesis and/or absorption during powder size reduction. From pressureless sintering studies oxygen concentration effects on densification were measured for attrition milled ZrB_2 powders in air and under argon ((Fahrenholtz, Hilmas and Zhang, et al., 2008) and (Zhang, Hilmas and Fahrenholtz 2006)). Monolith ZrB_2 milled in argon resulted in a near 150°C depression in densification temperature as a result of decreasing oxygen concentrations. Furthermore, both milled argon and air compositions reached a maximum relative density of ~84% at 1850°C and 2100°C for 1 hour, respectively, suggesting densification was inhibited by particle surface oxides. Oxygen concentration reductions of ~1-2 wt% for milling in argon were reported ((Fahrenholtz,

Hilmas and Zhang, et al., 2008) and (Zhang, Hilmas and Fahrenholtz 2006)). Attrition milling of ZrB_2- 4 wt% B_4C resulted in a 750% increase in particle surface area and 1.0 wt% O concentration increase from the similar as-received composition. A reduction in particle size increases the driving force for densification according to Equations (2-2) and (2-3). For example, monolithic attrition milled ZrB_2 had a 10% increase in relative density with respect to the as-received monolith at 1900°C for 2 hours (Zhu, Fahrenholtz, et al., 2007). In a separate study, monolithic ZrB_2 densities increased by 5% at 2100°C with attrition milling despite an increase of 2 wt% O concentration. Fahrenholtz, et al., (2008) described the increase in density is primarily due to (1) reduction in starting particle size and (2) incorporation of WC from the milling media wear resulting in particle oxide reduction according to reaction (2-4). For the ZrB_2-C ceramic system (milled and as-received) a limiting carbon concentration was observed where the increased oxygen concentration, due to increasing particle surface area from attrition milling, proved to not completely remove an equivalent amount of particle surface oxides compared to the as-received ceramic alloy. The as-received ceramic alloy relative density of 89.5% was measured contrasting a 72.4% relative density for the attrition milled alloy. Doubling the carbon concentration resulted in complete particle oxide removal and improved densification from powder size reduction as measured by ~99% relative densities as compared to 90% relative density for the as-received equivalent composition (Zhu, Fahrenholtz, et al., 2007).

Hot-pressing powder compacts is another type of sintering process where quasi-steady state densification behavior includes an effective stress or “Driving Force” (D.F.) (R. L. Coble 1970). The advantage of hot pressing includes reduced time and temperature to achieve an equivalent relative density over pressureless sintering. However, billet dimensions are confined to the hot press die geometry limiting the complexity of sintered components. The initial stages of hot pressing include particle rearrangement by grain boundary sliding, particle fracture or

grain shape changes by plastic flow (R. L. Coble 1970). Intermediate stages typically describe predominately mass shrinkage due to densification facilitated by diffusion mass transfer. Coble (1970) proposed a physical interpretation of the fundamental driving force for hot-pressing differing from the surface energy (γ) driving force for pressureless sintering. The effective driving force for early stages of fusion by neck growth, shrinkage and densification is given by

$$DF = [\gamma + P_a R/\pi], \tag{2-9}$$

where P_a is the applied pressured between the die punches projected upon the particle of radius R. The addition of the projected stress upon the powder bed neck growth and initial shrinkage is enhanced. Transitions into the intermediate and final densification stages include changes in the driving force for densification. Coble (1970) found the total driving force for densification follows

$$DF = \left[\frac{P_a}{D} + \frac{\gamma}{r}\right], \tag{2-10}$$

where D is the density a and r is the pore radius. Again, the effective stress, $\frac{P_a}{D}$, applied from the die punch is included enhancing densification, however, addition of the pressure difference across the pore surfaces must be included as a result of entrapped gas in pores. This suggests the final densification rate prediction requires procedures using experimental density observations as the densification rate as a function of density is dependent upon the pore radius and vacancy sinks. This assessment provides fundamental insight to the role of applied pressure (Equation (2-9) and (2-10)) and the effective stress on powder compact densification (R. L. Coble 1970).

Two phase UHTC composites have been developed for improved densification, during hot pressing, mechanical behavior and oxidation behavior above 1200°C ((Monteverde, Guicciardi and Bellosi 2003) and (Fahrenholtz, Hilmas and Talmy, et al., 2007)). Typical second

phase additions are SiC, $MoSi_2$, $ZrSi_2$, TiC, ZrN , ZrC in quantities of 5-50 vol%. These composites show limited to no mutual solubility in ZrB_2 ((E. Rudy 1969) (Eckert 1966), (L. Kaufman 1986)). Early investigations of compositional effects on densification were conducted by Kats, et al., (1981) and Spivak, et al., (1974). Considering the ZrB_2-ZrN system, varying ZrN compositions from 0-100% showed maximum densification of 77-80% near compositions of 40-60% were achieved (Kats, Ordan'yan and Unrod 1981). Additionally, for the ZrB_2-ZrC system, a reduction in final porosity with increasing ZrC composition was observed having a porosity minimum near 50:50 ZrC:ZrB_2 composition ratio (Spivak, et al., 1974). Their results come from pressureless sintered pellets at 2100°C for 1 hr. Similarly for ZrB_2-SiC composites many have shown obvious improvements in composite densification by additions as small as 2% SiC ((Leohman, et al., 2006), (A. Chamberlain, et al., 2004), (S.-Q. Guo 2009) and (Fahrenholtz, Hilmas and Talmy, et al., 2007)). TiC-ZrB_2 sintering studies showed additions of TiC through 5 vol% to ZrB_2 were accompanied by a relative density increase of 86% to 94% contrasting with TiC compositions of 10 vol% having 86% relative density (Mishra and Pathak 2008). From this study, the 5 vol% TiC composition was found to completely dissolve into the ZrB_2 where 10 vol% TiC composition formed (Zr,Ti)B_2 solid solution phase and TiB_2. Mishra and Pathak (2008) concluded the reduction in molar volume from TiC to TiB_2 resulted in pore formation during sintering, lowering the relative density. Hot-pressed (Mizuguchi, Guo and Kagawa 2009) and spark plasma sintered (Mizuguchi, Guo and Kagawa 2010) ZrB_2-10% $MoSi_2$ composites showed improved densification over ZrB_2 monolith. From these studies the introduction of interphase boundaries appears to have lowered the activation barrier for densification and agrees with the activation energy reduction calculated by Kislyi and Kuzenkova (1966) for < 15% Mo additions to ZrB_2 (Mizuguchi, Guo and Kagawa 2009).

2.2.2. Mechanical Properties

Room temperature mechanical properties vary considerably for both monolithic and composite based ZrB_2 ceramic systems as final density, reinforcement shape and quantity determine fracture strength and toughness. Table 2- 3 is a compilation of typical room temperature fracture strengths and toughness for a variety of monolithic and composite ZrB_2 based ceramic systems.

Considering monolithic ZrB_2 fracture strengths and toughness are rather low compared to the composite counterparts. Fahrenholtz, et al., (2007) compile the effect of matrix metal-diboride grain size on fracture strength for various processing methods, Figure 2- 1. With an increase in matrix grain size the fracture strength decreases with an approximate $GS^{-1/2}$ dependence suggesting typical ceramic strength-grain size relationship contrasting with the traditional Hall-Petch relationship ((Hertzberg 1996), (Hull and Bacon 2001))

$$\sigma = \sigma_0 + K_Y d^{-1/2}, \tag{2-11}$$

where σ_0 and K_Y are constants dependent on the yield point and d is grain size. For ceramics systems where slip is traditionally restricted due to narrow dislocation cores and subsequent large Peierls force (Hull and Bacon 2001) and lack of interpenetrating slip systems (Hull and Bacon 2001) dependence is based on a Griffith fracture criterion given by (Anderson 2005)

$$\sigma = KYd^{-1/2}, \tag{2-12}$$

where K is stress intensity, Y is a constant and d is grain size. Fabrication of fine grain sized monolithic ZrB_2 can result in maximum strengths approaching 1 GPa. However, as reviewed by S-Q Guo (2009) and observed by others ((Fahrenholtz, et al., (2007) and Leohman, et al., (2006)) obtaining sufficiently small grain sizes for monolithic ZrB_2 is difficult based on the lack of grain growth inhibitors and sintering conditions favoring grain growth. Therefore, upper limit

monolithic fracture strength 565 ± 53 MPa (A. L. Chamberlain, et al., 2004), are expected for relative densities of 99% and average matrix grain size of ~ 6 μm according to Equation (2-12); assuming σ = 565 MPa, $K = K_{IC}$ = 3.5 MPa√m and Y = 0.400; the calculated grain size is in agreement with the measured average grain size and fracture toughness for the ZrB_2 used in Chamberlain, et al., (2004).

Fabrication of ZrB_2 ceramics with second phase additions of SiC, $MoSi_2$, ZrC and ZrN improve densification, inhibit grain growth and improve fracture strengths and toughness. Figure 2- 2 shows the volume fraction of second phase composite reinforcement on fracture strength for ZrB_2 based composites.

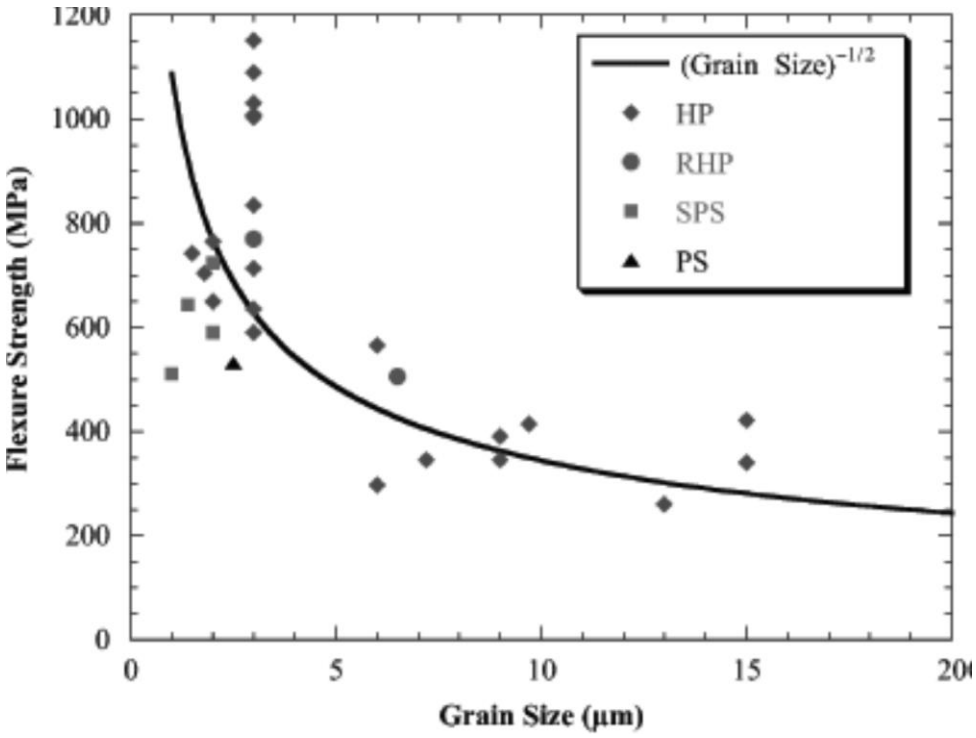

Figure 2-1: Strength of select monolithic ZrB_2 densified by Hot Pressing (HP), Reactive Hot Pressing (RHP), Spark Plasma Sintering (SPS) and Pressureless Sintered (PS) taken from Fahrenholtz, et al., (2007).

A general trend of increasing the volume fraction of second phase reinforcement has a dramatic increase in fracture strengths through 30 vol% additive. Loehman, et al., (2006) observed disagreement with the above trend as 2 vol% SiC – ZrB_2 composites had ~200 MPa higher fracture strength than 5 and 20 vol% SiC-ZrB_2 composites. The milling processes selection (i.e. attrition vs. ball milling) proved to influence SiC particle agglomeration, thus, SiC cluster size varied between the different composites and larger clusters reduced the fracture strength despite higher volume fractions of SiC. Rezaie, et al., (2007) observed composite fracture strength was limited by the maximum SiC particle and cluster size for 30 vol% SiC by varying the hot-pressing temperature and time. A separate study varied the as-milled SiC particle size and found the maximum SiC particle/cluster size-strength effect where >6μm particles/clusters had a ~300 MPa decrease in fracture strength for 30vol% SiC – ZrB_2 composite (Zhu, Fahrenholtz and Hilmas 2007). Bird, et al., (2012) showed both maximum SiC particle/cluster size and residual B_4C sintering aid limited strength for 20 vol% SiC-ZrB_2 composite. ZrB_2-20 vol% SiC composites processed with (ZSB) and without (ZS) B_4C had reported average strengths of 734 and 456 MPa, respectively, where the >10μm B_4C inclusion size limited strength despite larger matrix grain sizes for the ZS composite. Fahrenholtz, et al., (2007) reports the residual stresses between the SiC and ZrB_2, from thermal expansion mismatch, where estimated tensile hoop stresses of 4.2 GPa exist at the ZrB_2-SiC interface are responsible for SiC-strength interplay. A similar procedure was adopted for assessing TiC particle interactions in a SiC matrix (Wei and Becher 1984). Watts, et al., (2011) quantified these residual stresses upon cooling from 1750°C to room temperature, using neutron diffraction, and compared the sintered compact d-spacing change relative to the starting powder. Accumulated residual stress development was observed near 1400°C, increasing to a maximum average 450 MPa tensile residual matrix stress at room temperature (Watts, et al., 2011). The matrix residual stresses were assumed as thermal

Table 2- 3: Room temperature mechanical properties for select ZrB_2 monolith and composites microstructures.

Material	Densification	Relative Density (%)	Modulus (GPa)	Strength (MPa)	K_{IC} (MPa*$m^{1/2}$)	Reference
ZrB_2-20% SiC-B_4C	HP	99.7	519	456 ± 66	3.9 ± 0.2	(Bird, Aune and Thomas, et al., 2012)
ZrB_2-20% SiC	HP	98.6	515	734 ± 60	4.5 ± 0.9	(Bird, Aune and Thomas, et al., 2012)
ZrB_2	HP	99.8	489	564 ± 53	3.5 ± 0.3	(A. Chamberlain, et al., 2004)
ZrB_2-10% SiC	HP	93.2	450	713 ± 48	4.1 ± 0.3	(A. Chamberlain, et al., 2004)
ZrB_2-20% SiC	HP	99.7	466	1003 ± 94	4.4 ± 0.2	(A. Chamberlain, et al., 2004)
ZrB_2-30% SiC	HP	99.4	484	1089 ± 152	5.3 ± 0.5	(A. Chamberlain, et al., 2004)
ZrB_2-2%B_4C-1%C	PS	100	507	473	3.5	(Fahrenholtz, et al., 2008)
ZrB_2	HP	100	489	565	3.5	(Fahrenholtz, et al., 2008)
ZrB_2 – 4%B_4C	PS	94	500	489	3.3	(Fahrenholtz, et al., 2008)
ZrB_2-Ni	HP	98	496	371 ± 24	3.38±0.42	(Monteverde, et al., 2002)
ZrB_2-TiB_2-Ni	HP	100	439	599 ± 167	4.09±0.14	(Monteverde, et al., 2002)
ZrB_2-B_4C-Ni	HP	99.6	448	643 ± 86	4.53±0.24	(Monteverde, et al., 2002)
ZrB_2-SiC	RHP	97.6	---	506 ± 43	4.0	(Zhang, et al., 2000)
ZrB_2-5% $MoSi_2$	PS	96	---	570±50	2.9±0.1	(Sciti, et al., 2011)
ZrB_2-5$MoSi_2$-20%SiC	PS	98.1	---	350±80	4.7±0.1	(Sciti, et al., 2011)
ZrB_2	HP	87	346±4	350±30	2.35±0.15	(Monteverde, et al., 2003)
ZrB_2-S_3N_4	HP	98	419±5	600±90	3.75±0.10	(Monteverde, et al., 2003
ZrB_2-30%SiC	HP	97-99.5	501-516	720-1060	3.9-5.5	(Rezaie, et al., 2007)
ZrB_2-30%SiC	HP	97-99	479-520	389-909	4.2-4.6	(Zhu, et al., 2007)
ZrB_2-15%SiC	HP	99	480±4	887±125	4.07±0.03	(Monteverde, Bellosi and Scatteia 2008)
ZrB_2-SiC-HfB_2	HP	98	506±4	763±73	4.08±0.75	(Monteverde, Bellosi and Scatteia 2008)

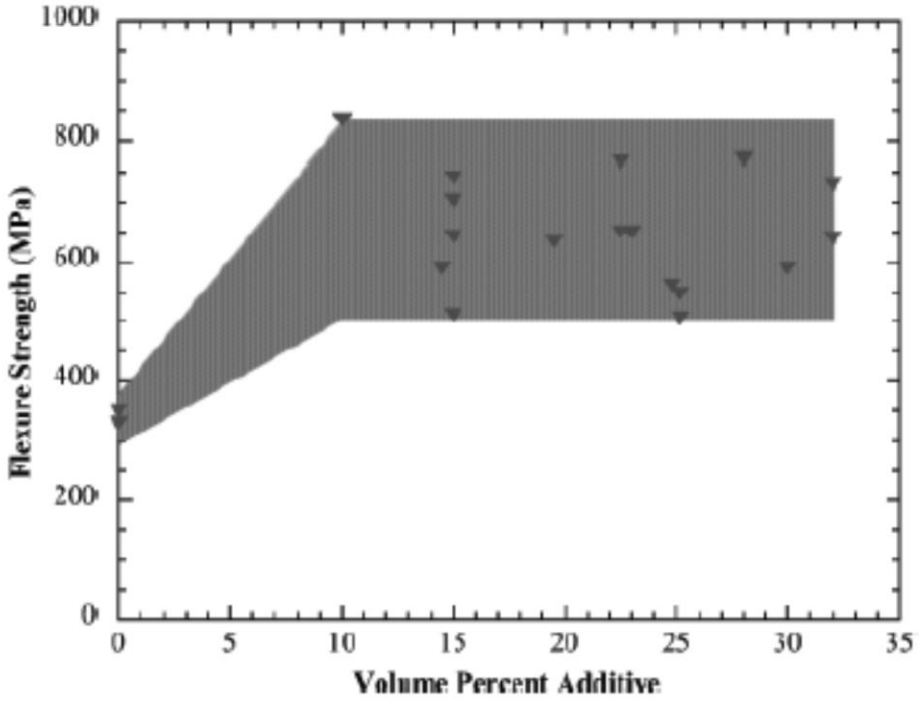

Figure 2- 2: Flexure strength for various ZrB_2 composites with reinforcement phase compositions 0-30 vol%. Apparent flexure strength increases with reinforcement phase taken from Fahrenholtz, et al., (2007).

expansion mismatch between SiC and ZrB_2 and no consideration to the stresses developed from thermal expansion anisotropy from the ZrB_2 non-cubic lattice structure ((Bird, Aune and Thomas, et al., 2012) and (Okamoto, et al., 2010)). Other reported structural effects on room temperature strength include precipitation of solid solution ZrB_2-WC phase by introduction of favorable residual stresses (A. Chamberlain, et al., 2004). However, in TiB_2-W_2B_5 solid solution alloys, strength increased from reduced porosity (hence improved densification) and grain growth inhibition, not residual stress (Watanabe and Kouno 1982).

Similar to fracture strength increases, short crack fracture toughness (K_{IC}) tend to increase with addition of composite reinforcements. From monolithic ZrB_2 fracture toughness varies with and without sintering additives. The lowest reported ZrB_2 fracture toughness strongly correlated with transgranular fracture modes contrasting with predominantly

intergranular fracture modes producing the largest fracture toughness. Larger grain sizes and intergranular fracture increases fracture toughness by process zone crack deflection which is dependent on number of deflections and deflection angle ((S.-Q. Guo 2009) and (S. M. Wiederhorn 1984)). Addition of refractory second phase particles generally improves fracture toughness over monolithic ZrB_2 ceramics where a transgranular fracture mode is predominant. The second phase particles act to deflect cracks as a means of process zone toughening ((Wei and Becher 1984) and (S. M. Wiederhorn 1984)). Reported indent fracture paths for ZrB_2 – SiC and ZrB_2-SiC-$MoSi_2$ composites show predominately transgranular ZrB_2 fracture with reinforcement deflection. Additionally, long crack room temperature DCB studies revealed very little wake zone toughening phenomena, however, SiC particles stabilized crack growth by wake zone crack face interactions ((Bird, Aune and Thomas, et al., 2012), Kurihara, et al., 2010) and (Thomas 2011)). Fracture toughness, like strength, saturates with SiC composition. Monteverde, et al., (2003) observed mixed mode intergranular and transgranular fracture with SiC additions to ZrB_2. SiC particles were assumed to strengthen the ZrB_2 grain boundaries, promoting transgranular ZrB_2 fracture. Additionally, large SiC particles and clusters did not participate in the crack deflection process but rather form intragranular cracks (Monteverde, Guicciardi and Bellosi 2003). According to Figure 2- 2 a minimum of 10 vol% additives may be required to achieve maximum fracture toughness. The plateau can be explained by increasing additions of large or clustered second phase particles may not participate in the deflection toughening mechanism.

An alternative approach to toughening was incorporating a high aspect ratio additive such as SiC whisker or rod for improved toughening. From Sciti, et al., (2011) in situ formed SiC platelet reinforced ZrB_2 composites were investigated for mechanical behavior by varying the sintering additives (i.e. S_3N_4 and $MoSi_2$). Short crack fracture toughness was compared amongst

particulate, platelet, whisker and fibers revealing high aspect ratio second phases improve toughness based on geometric arrangement and crack deflection. However, crack tip shielding from grain bridging, arising from both geometric and thermal expansion anisotropy, may also contribute to mode one fracture toughness ((Steinbrech, Reichl and Shaarwachter 1990), (Grimes, et al., 1990), (Hay and White 1994) and (Becher 1991)). Measured fracture toughness of the composites containing platelets increased with additions of SiC over the baseline composites, but varied considerably with choice of sintering aid. $MoSi_2$ – SiC – ZrB_2 additive composites had improved fracture toughness of 5.0 MPa√m contrasting with Si_3N_4 – SiC – ZrB_2 composite toughness of 3.8 MPa√m. Indentation-Microscopy experiments revealed two distinct fracture mechanisms contributing to the overall crack deflection mechanism. For the $MoSi_2$ based composites ZrB_2 intergranular cracking and SiC deflection of favorably oriented platelets contributed most to toughening contrasting with primarily transgranular ZrB_2 cracking and negligible deflection toughness contributions. Interphase and grain-boundary cohesive strength were assumed as a primary fracture path modifier where local variations in chemistry from impurity segregation or presence of grain boundary second phases (Sciti, et al., 2011). ZrB_2 like grain boundaries were occasionally observed to have Si-O based amorphous films (~2 nm thick) differing in composition between $MoSi_2$ and Si_3N_4 additives, however, the majority of grain boundaries were considered clean. Grain boundary chemistry modifications appeared to promote primary intergranular fracture improving both monolithic and composite room temperature toughness. However, the high temperature strength retention may be adversely affected (Monteverde, Guicciardi and Bellosi 2003) with the addition of low melting point impurities.

2.3. High Temperature Mechanical Behavior

High temperature mechanical strength and toughness are of interest for these ZrB_2 monoliths and composites as application temperatures are expected to be greater than $0.5T_m$ suggesting mechanical behavior transitions to include creep. From MOR studies, Monteverde, et al., (2003) showed the influence of sintering aids and reinforcement phase addition on flexure strength through 1200°C. Monolithic ZrB_2 had average strengths of ~330 MPa through 1200°C with a consistent linear elastic behavior. However, ZrB_2-SiC-Si_3N_4 and ZrB_2-Si_3N_4 showed decreasing flexure strength through 1200°C. Electron Dispersive X-ray Spectroscopy (EDS) measurements revealed a siliceous grain boundary glass phase in both composites suggesting softening through 800°C and strength reductions of 180 MPa and 110 MPa for ZrB_2- Si_3N_4 with and without SiC additions, respectively. Additions of Al_2O_3 and Y_2O_3 proved to modify the composition of the glassy grain boundary phase as the strength transition temperature was increased through 1000°C followed by a 350 MPa strength decrease through 1200°C. In all composites with glass forming aids non-linear loading behavior was observed (Monteverde, Guicciardi and Bellosi 2003). Strength retention through 1200°C was observed for ZrB_2 – $MoSi_2$ – SiC and ZrB_2 – $MoSi_2$ composites (Sciti, et al., 2011). Despite additions of glass forming $MoSi_2$ the couple action of oxide-particle reduction and carbo-thermo reduction in a CO-rich furnace atmosphere produced clean or partially wetted grain boundaries. The lack of strength decrease shows the importance of an extensive amorphous network required for a temperature dependent strength reduction. Bird, et al., (2012) measured a similar strength and stiffness transition temperature for ZrB_2-20 vol% SiC composite. The observed normalized stiffness transition temperature was ~1100°C accompanied by a brittle-to-ductile transition strength temperature of 1000°C. Measured load-displacement strength curves showed linear-elastic behavior through 1200°C where the bending compliance increased beyond 1100°C. Beyond

1200°C a non-linear response was observed for all specimens indicating a viscous response to the applied strain-rate. Grain boundary composition was not reported and oxygen concentrations were not measured. Similar brittle-to-ductile transition temperatures were reported for HfB_2 (Opeka, Talmy and Wuchina, et al., 1999). A compilation of select composite and monolithic diboride strength variations with temperature are shown in Figure 2- 3. by a characteristic viscosity which is rate-sensitive. Under constant displacement conditions, a corresponding flow stress (viscosity) will determine the deformation mechanisms. The strain rate sensitivity of ZrB_2-20 vol% SiC – B_4C composite was characterized by a four-fold critical load increase over a decade of applied strain-rates at 1600°C (Bird, Aune and Thomas, et al., 2012). Similar strain-rate effects were indirectly measured during MOR experiments through 1800°C (Hu and Wang 2010). Hu and Wang (2010) showed that doubling the grain size of both ZrB_2 and

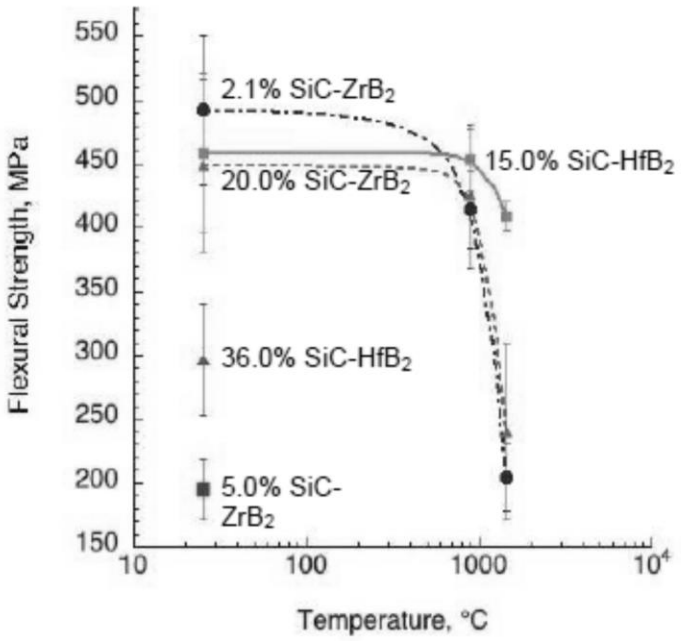

Figure 2-3: Room temperature and strength variations with temperature for HfB_2 and ZrB_2 based composites with SiC as the reinforcement taken from (Leohman, et al., 2006).

Approaching and exceeding temperatures of 0.5 T_m non-linear deformation is described SiC grains suppressed plastic deformation and raised the flexure strength ~50%. The effect of larger grains enhanced the creep resistance thus decreasing the corresponding steady state creep rate substantially below the applied strain-rate. Departures from linear elastic mechanical behavior, with temperature, have been observed during DCB fracture experiments beyond 1200°C ((Bird, Aune and Thomas, et al., 2012) and (Thomas 2011)). Measured crack lengths were 86-95% of those predicted based on linear-elastic compliance assumptions for 1400 and 1200°C, respectively (Bird, Aune and Thomas, et al., 2012). This suggests creep zone development ahead of the crack tip where reported steady state creep rates (Talmy, Zaykoski and Martin, Flexural Creep Deformation of ZrB_2/SiC Ceramics in Oxidizing Atmosphere 2008) for these temperatures were consistent with the applied strain rate of 3.75 x $10^{-7}s^{-1}$.

2.3.1. Creep Deformation

Creep deformation is defined as time-dependent deformation where a characteristic strain-rate is dependent upon the applied stress. From a continuum approach classical creep is commonly characterized by the generalized power-law function of the form ((Norton, The Creep of Steel at High Temperatures 1929) and (Dunne and Petrinic 2005)),

$$\dot{\varepsilon}_{ij}^{cr} = \frac{3}{2}\frac{S_{ij}}{\sigma_e}\dot{\varepsilon}_0 exp\left(\frac{-Q}{KT}\right)\left(\frac{\sigma_e}{\sigma_0}\right)^n, \qquad (2\text{-}13)$$

where $\dot{\varepsilon}_{ij}^{cr}$ is the creep strain rate tensor, S_{ij} is the deviatoric component of stress, σ_e is the Von Mises stress, σ_0 a threshold stress, $\dot{\varepsilon}_0$ a threshold strain rate, *Q* the activation energy, *n* a stress exponent and k and T the Boltzmann's constant and absolute temperature, respectively. Under uniaxial conditions Equation (2-13) reduces to the classical form known as Norton's equation (Norton, The Creep of Steel at High Temperatures 1929),

$$\dot{\varepsilon} = \dot{\varepsilon}_0 exp\left(\frac{-Q}{KT}\right)\sigma^n, \qquad (2\text{-}14)$$

Table 2- 4: Summary of creep model parameters and rate-controlling mechanisms

Model	Rate-Controlling mechanism	n	P	Q	Reference
Diffusion	G.B. diffusion	1	3	Q_{gb}	(R. L. Coble 1963)
Diffusion	Lattice Diffusion	1	2	Q_l	(C. Herring 1950)
Diffusion	Glass phase diffusion	1	3	Q_g	(Raj and Chyung 1981)
Diffusion	Glass phase interface	1	1	Q_g	(Raj and Chyung 1981)
Diffusion	Interface reaction , fine grains	2	1	Q_{gb}	(Ashby and Verrall 1973)
G.B. Sliding	G.B. dislocation climb	2	2	Q_{gb}	(Ball and Hutchinson 1968)
G.B. Sliding	G.B. dislocation climb	2	1	Q_l	(T. G. Langdon 1970)
Lattice	Dislocation climb	4.5	0	Q_l	(Weertman 1957)
Lattice	Dislocation glide	3	0	Q_l	(Weertman 1957)
Lattice	Dislocation climb	3	0	Q_l	(F. N. Nabarro 1967)
Lattice	Coarse grain climb	1	0	Q_l	(T. Langdon 2002)
Cavitation	Viscous flow boundary glass	1	3	Q_g	(Dryden, et al., 1989)
Cavitation	G.B. sliding	>1	0	Q_c	(Evans and Rana, High Temperature Failure Mechanisms in Ceramics 1979)
Cavitation	Boundary diffusivity	1	0	Q_{gb}	(Needleman and Rice 1980)

where $\dot{\varepsilon}$ is the measured strain rate, $\dot{\varepsilon}_0$ pre-exponential term, *R* the universal gas constant, σ the uniaxial applied stress and *n, Q,* and, *T* there usual significance. From experimental ceramic and metals creep studies, Q and n provide insights to the rate-controlling creep mechanism. Modeling creep behavior consists of either a phenomenological approach or a micromechanical approach. The phenomenological approach is convenient, but lacks generality as it only describes the creep behavior of a single microstructure. Taking a micromechanical approach attempts to integrate the microstructural behavior with the macroscopic behavior measured. Table 2- 4 is a compilation of rate-controlling creep mechanisms and the corresponding stress exponent and activation energies ((Cannon and Langdon 1983), (Cannon and Langdon 1988) and (Hynes and Doremus 1996)). Interpretation of measured activation energies can be misleading and has been pointed out by Cannon and Langdon (1983) as a possible measurement of the

apparent activation energy. These differ from the true activation energy because the variation in shear modulus with temperature and the term 1/KT from Equation (2-13) are not included. However, for n =1 to 2 this difference is negligible and the apparent activation energy can be useful for determining the rate-controlling creep mechanism. Hynes and Doremus (1996) provide a schematic representation of activation energy evolution with temperature, Figure 2-4.

The rate controlling process is defined by

$$\dot{\varepsilon} = \sum \dot{\varepsilon}_i, \tag{2-15}$$

where the i^{th} component represents each creep mechanism operating either simultaneously (i.e. parallel) or sequentially. Equation (2-15) represents a parallel process representing the faster creep mechanism dominates and the measured creep rate is a summation of all operating mechanisms. Furthermore, Figure 2- 4 (A) shows an increase in activation energy (slope of $\dot{\varepsilon} - {}^{1}/_{T}$ plot) indicates a faster creep mechanism operates over a higher temperature interval suggesting the observed creep behavior is a summation of the lower temperature and high temperature processes. Conversely, sequential operating creep is identified by a reduction in

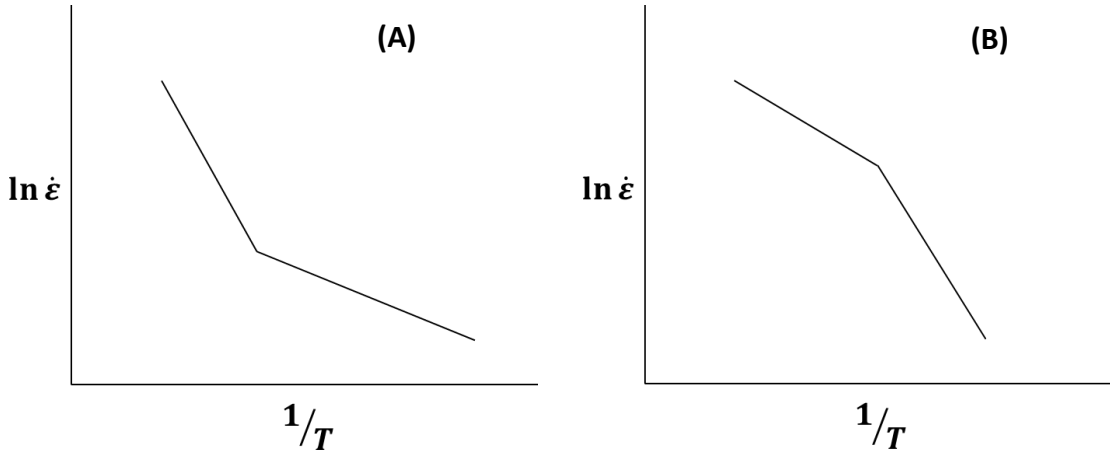

Figure 2-4: Examples of activation energies detailing creep mechanism transitions from (A) independent operating parallel processes and (B) sequential processes.

activation energy with increasing temperature Figure 2- 4 (B) suggesting the slower process is rate-controlling. This is obvious for a sequential creep processes in the form of Equation (2-16)

$$\dot{\varepsilon} = \sum \frac{1}{\dot{\varepsilon}_i}, \tag{2-16}$$

where the slower operating creep mechanism is rate controlling. From Table 2- 4 creep data it is immediately evident the overlap between stress exponents and mechanisms and consequently a clear interpretation of experimental creep data can be difficult without precise knowledge of n, Q and extensive microstructure evaluation. The forthcoming sections are a review of a variety of creep mechanisms, often encountered during ceramics and metals creep, subdivided into diffusion, grain boundary sliding, and cavitation and lattice mechanisms. The latter section specifically focuses on the role of dislocations during time-dependent deformation.

2.3.1.1. Diffusion Mechanisms

Diffusion creep can be considered as Newtonian or viscous creep from a common linear strain-rate- stress response (n=1). However, such diffusion models can be further subdivided into those pertaining to the path of mass transport in response to an external stress i.e. grain boundary, lattice (bulk), interphase or amorphous phase diffusion. Furthermore, debate exists focusing on diffusion as an accommodation processes and not the creep mechanism. Such discrepancies compare classical diffusion models with those formulated focusing on creep involving array of space filling grains with irregular grain boundaries.

Classical diffusion mechanisms include vacancy diffusion (or mass transfer) from grain boundaries perpendicular to the applied stress, coupled with the slowest atomic species finding the most likely diffusion path (i.e. grain boundary or lattice), Figure 2- 5. Grain elongation accounts for accumulated strain while grain boundary sliding accommodates this process as suggested by Coble (1963), Nabarro (1948), Herring (1950) and Cannon and Langdon (1988).

Creep rates are defined by' (Cannon and Langdon 1988), (R. L. Coble 1963), (C. Herring 1950), (F. R. Nabarro 1948), (Hynes and Doremus 1996):

$$\dot{\varepsilon} = \frac{AbG^n D}{KT}\left(\frac{b}{d}\right)^p \left(\frac{\sigma}{G}\right)^n, \tag{2-17}$$

where A, n and p are constants, *b* the Burger's vector, *D* the respective diffusion coefficient (D_{gb} for grain boundary and D_l for lattice), *G* is shear modulus, *d* grain size, σ applied stress and *KT*

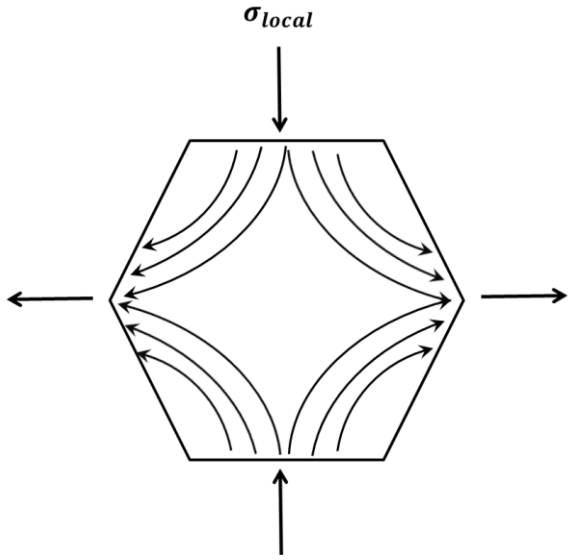

Figure 2-5: Single grain under an applied uniaxial stress. Contour flow lines indicate the mass transport direction from grain boundaries under local compression to boundaries under local tension.

has the usual significance. Coble (1963) proposed a model detailing creep of spherical grains and vacancy transport along grain boundaries in response to an applied stress as the dominant mechanism. From the derivation there exists a chemical potential gradient, or driving force, for increasing the local vacancy concentration above the equilibrium vacancy concentration,

$$\frac{\Delta C}{C_0} = \frac{\sigma\Omega}{kT}, \tag{2-18}$$

where C_0 is the equilibrium vacancy concentration at temperature *T* in a stress-free crystal, σ is the local grain boundary normal stress and Ω is the atomic volume occupied by a vacancy. Thus under a local normal component of stress on a grain boundary the maximum vacancy

concentration change occurs. Hence mass transfer occurs from boundaries under local compression to boundaries under tension, Figure 2- 5. From these arguments and the assumption (1) the vacancy source and sink are not uniform and (2) the distribution of normal stress along the grain boundary has reached a quasi-steady state the predicted creep rate has the form of Equation (2-17) with n=1, p=3, D=Boundary and A= 148 (R. L. Coble 1963). The final formulation takes into account creep rate from grain shape change (diffusion controlled) and from shear stress relaxation at the grain boundaries. The shear stress relaxation promotes grain boundary sliding, hence grain boundary sliding accommodates the grain shape change and is a requirement for maintaining a continuous microstructure. Analogous to grain boundary diffusion, Nabarro (1948) and Herring (1950) independently derived formulations for creep rate dependent on bulk vacancy diffusion.

Herring (1950) proposed a similar theory involving a simplified case of self-diffusion transport on a spherical particle with a surface normal traction equivalent to that proposed by Coble (1963) and a composition gradient similar to Equation (2-18). Two theories were proposed by Herring (1950) detailing only the diffusion component of a single spherical particle contrasting with the incorporation of coupled quasi-steady state diffusion and boundary shear stress relaxation in an array of spherical grains. The latter theory is more consistent polycrystalline viscous behavior, however, differing from Coble (1963), distinct differences are apparent as $D=L_{attice}$, p = 2 and A = 13 from ((Hynes and Doremus 1996), (Cannon and Langdon 1988)) Equation (2-17). Incorporating boundary shear relaxation into the model and accelerated creep rate by a factor of 5/2 was calculated showing excellent agreement with Coble (1963) on the coupled effects of diffusion and boundary movement due to grain sliding. Nabarro (1948) derived the same creep rate grain size dependence as Herring (1950) for a single crystal undergoing self-diffusion in response to an external stress. Additionally, Nabarro (1948)

considered the relative motion of grains during viscous deformation from a simple two atom thick “liquid” grain boundary. Noting the proximity of atomic positions relative to a common axis between two grains an edge dislocation may be present to accommodate the misfit. Under a flux of vacancies from regions under tension to compression, where the region below the dislocation half plane acts as a vacancy sink, the edge dislocation will move along the common boundary by one atomic position thus moving the atomic positions of one grain relative to the other. This process of vacancy diffusion relaxes the shear stress at the grain boundary promoting movement by dislocation climb within the grain boundary. Nabarro (1948) predicted a creep-rate increase under these conditions showing creep by diffusion necessitates grain boundary sliding for maintaining microstructural continuity.

From review of both boundary and lattice theories a linear stress dependence is preserved where the grain size and diffusion path are most critical for assessing the applicability of these models to experiments as the constant A is strongly dependent on n, p and Q (Cannon and Langdon 1983). The grain size dependence (p) and numerical constant differ between both diffusion mechanisms where Coble (1963) creep is favored at low temperature and fine grain sizes contrasting with high temperatures and large grain sizes favoring Nabarro (1948)-Herring (1950) creep. However, under constant grain size conditions, the transition to Nabarro (1948)-Herring (1950) creep can occur because of lower grain boundary diffusion activation energy as represented by the diffusivity equation

$$D = D_0 exp\left(\frac{-Q}{RT}\right), \tag{2-19}$$

where D is the diffusion coefficient, D_0 is a constant dependent on the atom vibration and jump frequencies having an activation barrier Q at temperature T. Both grain boundary and lattice diffusion paths may operate in parallel where the resulting creep rate follows Equation (2-15). For ceramics, cation and anion diffusion must occur in stoichiometric quantities and can have

different diffusivities thus complicating the diffusion process. Under such steady state conditions both cation and anion diffusion along grain boundaries and lattice diffusion may operating forming a complex or effective diffusion flux. The slowest species along the fastest path becomes rate controlling ((Cannon and Langdon 1988), (Hynes and Doremus 1996)).

For the case of polycrystalline creep, diffusion as an accommodation process where grain boundary sliding is the creep mechanism seems appropriate. The following models are considered as "Diffusion Mechanisms" as the creep-rate linearly scales with stress and accommodation mechanisms are similar to those presented earlier. Creep deformation by diffusion accommodated viscous flow was considered by Lifishitz (1963) where an array of space filling grains were assumed to undergo self-consistent displacement and subsequent deformation aligning parallel with the major stress axis with a restriction that deformation proceeds in a compatible way (i.e. no discontinuities) ((L. M. Lifshitz 1963) and (Raj and Ashby 1971)). Using similar formulations for the diffusion driving force (Equation (2-18)) the total grain motion was given as

$$v = v^{\alpha} + D_0 \nabla c, \tag{2-20}$$

where the velocity, *v*, is comprised of a diffusive flux $D_0 \nabla c$ and grain velocity v^{α}. For two opposing grains, α and β, the total relative grain motion is equal producing a self-consistent grain boundary sliding-diffusion deformation couple. Furthermore, both normal and tangential components of boundary stress were considered for amorphous (free sliding) and insufficiently amorphous boundaries controlled by slip (L. M. Lifshitz 1963). Boundary viscosities were approximated under free-sliding conditions where the tangential stress relaxed to zero and the normal component remaining constant across the boundary under quasi-steady state conditions similar to the sliding conditions of Coble (1963), Nabarro (1948) and Herring (1950). However, increasing boundary viscosities are expected in the presence of boundary discontinuities

(insufficiently amorphous) where slip is greatly impeded and the characteristic boundary viscosity is much greater than the free sliding condition. Hence the boundary tangential stress does not tend to zero and is scaled relative to the fractional change in boundary viscosity. Resulting diffusion fluxes are much smaller than the free sliding case and overall creep deformation is governed by grain boundary sliding (Raj and Ashby 1971). Grain elongation is merely the result of diffusion accommodated grain boundary relaxation in a continuous network of grains.

This process of "Lifshitz" grain boundary sliding has been termed for all polycrystalline creep where diffusion accommodates the boundary sliding creep strain contribution ((Hynes and Doremus 1996), (Cannon and Langdon 1988)). Raj and Ashby ((1971) and Ashby, Raj and Gifkins (1970) later expanded on the notions of Lifshitz and postulated the grain boundary sliding rate correlates with the macroscopic creep rate of bicrystals. They considered irregular grain boundary profiles contrasting with classical atomically smooth planar boundaries, having a common sinusoidal, step-ledge profile (Raj and Ashby 1971) or serrated grain boundary (Ashby, Raj and Gifkins 1970). Diffusion accommodated sliding rate follows the format, for an arbitrary grain boundary shape (Raj and Ashby (1971)),

$$\dot{U} = \frac{2}{\pi}\frac{\tau_a \Omega}{kT}\frac{\lambda}{h^2} D_v \frac{1}{\sum_1^\infty \left\{ \frac{h_n^2/h^2}{\left(\frac{1}{h}+\frac{\pi\delta D_B}{\lambda\ D_v}\right)} \right\}}, \tag{2-21}$$

where D_v is the self-diffusion coefficient, D_B is the boundary diffusion coefficient, δ is the thickness of the grain-boundary diffusion path, λ is the grain boundary periodicity, h_n are the grain boundary shape descriptions from the Fourier coefficients, and h is the total height of the grain boundary topography. From the sliding-rate formulation the topographical height and diffusivity flux paths limit the sliding rate under a shear stress. This agrees well with Lifshitz (1963) findings as the sliding rate exponentially decays with boundary irregularity (amorphous

quality) where relative grain motion is impeded. Comparisons of the above theory with those of Coble (1963), Nabarro (1948) and Herring (1950) one finds excellent agreement in predicted creep rates between the theories despite foundational differences from which each theory was derived. Assuming viscous deformation following Equation (2-17), Raj and Ashby (1971) predict quasi-steady state creep constants of n = 1, p=3, A = 44 for boundary diffusion and n = 1, p=2 and A= 14 for self-diffusion; correcting Coble's (1963) grain boundary diffusion constant, A, by a factor of π yields A= 48. Later, Ashby and Verrall (1973) proposed a diffusion accommodated mechanism focusing on sliding of grain groups in effort to explain observed strain rates one order of magnitude larger than those predicted by classical diffusion models. The mechanical aspects of this theory are identical to those for Lifshitz (1963) sliding and classical models where constants n = 1, p=2 and A =98. The pre-exponential factor is much larger than those predicted by Lifshitz (1963), Raj and Ashby (1971), Herring (1950), and Coble (1963). This can be explained by three competing factors (1) diffusion is accelerated because of a reduction in path length (2) increased number of diffusive paths accelerating mass transport and (3) a restriction on grain group orientation effectively reducing the work done by an applied stress if not oriented favorably (Ashby and Verrall 1973). The final theoretical picture includes grains with relatively unchanged shape contrasting with grain elongation scaling with the macroscopic creep strain at an accelerated creep rate.

From these classical diffusion and diffusion accommodated micromechanical models there are several similarities despite the theoretical assumption differences. As a result all of the above models, with exception to Ashby and Verrall (1973), predict similar creep rates on the basis that creep deformation is controlled by a diffusion-viscous sliding couple. However, as noted by Nabarro (1948), boundary shear stress relaxation by vacancy transport, under an applied stress, promotes movement of geometrically necessary grain boundary dislocations and

hence sliding occurs. This mimics that of Lifshitz (1963) and later Raj and Ashby (1971) that boundary relaxation must occur for promoting grain boundary sliding. Coble (1963) and Herring (1950) indirectly derived the requisite of grain boundary sliding as a means to maintain a continuous microstructure. Furthermore, Langdon (1970) pointed out grain boundary sliding makes no direct contribution to the overall creep strain and therefore is an accommodating process to diffusion dominated creep.

Another diffusion-type creep deformation mechanism is solution-precipitation creep deformation in materials possessing an amorphous intergranular "glass-like" phase. This creep mechanism has become popular with the development of Si_3N_4 engineered ceramics containing an extensive amorphous film network. Solution-precipitation creep occurs if the matrix and/or reinforcement phase is partly soluble in the liquid grain boundary phase; rate of dissolution and diffusion into and through the liquid grain boundary phase accounting under an applied stress accounting for the macroscopic creep strain (Raj and Chyung 1981) (Pharr and Ashby 1983). Atoms are transported from regions of high local compressive stresses to regions of high local tensile stresses similar to tradition diffusivity paths mention earlier. However, solution-precipitation is limited by the slower of the two reaction rates: the interface reaction and mass transport within the amorphous phase. Interface controlled solution-precipitation occurs when the rate of dissolution of atoms and subsequent precipitation is slower than the diffusion of atoms through the liquid phase ((Raj and Chyung 1981) (Wakai 1994)). This process commonly occurs at line defects in grain boundaries (e.g., screw dislocations, 2-D growth ledges) (Wakai 1994). Raj and Chyung (1981) derived the island model assuming a distribution of grain boundary ledges (islands) that transmit the boundary normal traction with the liquid film residing in the valleys of such islands acting as a fast diffusion path. A more rigorous treatment, step model, assumes that line defects in the form of kinks or crystal growth ledges created by

nucleation process or screw dislocations are the sites for solution-precipitation (Wakai 1994). Creep deformation is controlled by the density and velocity of these steps. The general creep rate formulation follows the form of (Wakai 1994),

$$\dot{\varepsilon} = \frac{\rho_s a v_s}{d}, \tag{2-22}$$

where ρ_s is the density of surface step, v_s is the velocity of step, d is grain size and a is height of step. The step velocity may be described as having three rate controlling components: rate of diffusion in liquid film, rate of diffusion in adsorption layer to the step and reaction at the step. Slower kinetics of the three will be the controlling rate for step velocity. In all cases the necessary concentration gradients to drive diffusion are developed from the applied stress. However, under interface reaction controlled step velocity, two conditions may apply: constant step density within the grain boundary or steps in the form of ledges. For the case of steps in the form of ledges, additional constant interface stress is required to nucleate additional steps to enhance deformation. Below is the general velocity step formulation (Wakai 1994),

$$v_s = \frac{C_0 \sigma_n \Omega}{KT} [R_1 + R_2 + R_3]^{-1}, \tag{2-23}$$

where C_0 is the initial concentration, R_1, R_2, and R_3 are the step reaction resistance, adsorption layer diffusion resistance and liquid film diffusion resistance, respectively. Furthermore, R_1 and R_2 may be treated as the total interface reaction resistance. Considering diffusion controlled deformation the creep rate is proportional to $1/d^3$ from the following equation (Wakai 1994),

$$\dot{\varepsilon} = C \frac{C_0 \sigma \Omega \delta D_l}{KT d^3}, \tag{2-24}$$

where solute C_0 diffuses through the amorphous boundary of thickness δ. Similar to Raj and Chyung (1981) and Pharr and Ashby (1983), with extension to Lifshitz (1963), Coble (1963) and Raj and Ashby (1971), the grain size dependence is consistent for boundary diffusion only.

However, under interface reaction controlled the creep rate follows,

$$\dot{\varepsilon} = C\frac{C_0\sigma\Omega}{KTd}x, \tag{2-25}$$

with *x* representing the volume fraction of glass. Immediately a 1/d grain size dependence is observed and consistent with Raj and Chyung (1981). Further, Ashby and Verrall (1973) found the same grain size dependence for reaction rate-controlled diffusion accommodated grain boundary sliding. The 1/d dependence has been observed experimentally for fine grained materials where diffusion creep dominates ((Ashby and Verrall 1973)) contrasting with $1/d^2$ or $1/d^3$ for medium to coarse grain sizes.

2.3.1.2. Grain Boundary Sliding Creep

Grain boundary sliding, as an individual creep mechanism, has been suggested by many authors as a dominant creep mechanism in metal and ceramic systems with a stress exponent n = 2 – 3 (Hynes and Doremus 1996). Often grain boundary sliding models are associated with superplastic deformation behavior. From Figure 2- 6, creep (or superplastic) deformation can be divided into three regions governed by diffusion, grain boundary sliding and dislocation mechanisms (Ashby and Verrall 1973). A review of small deformation, "Lifshitz" type sliding, has been considered and pertains to Region I deformation contrasting with larger creep strains and negligible concomitant grain shape change, Region II deformation. Rachinger (1952) attempted experiments for measuring the relative grain translations during plastic flow of Aluminum to 50% strain. Using transverse and parallel markings, relative to the stress axis, grain deformation strains were measured against the macroscopic creep strains under the condition of a starting equiaxed grain structure. Similar markings experiments have been conducted on various ceramics and metals for quantifying grain boundary sliding strain contributions, Figure 2- 7((Bell and Langdon 1967), (T. G. Langdon 1974)). Moreover, scribe experiments have been used for

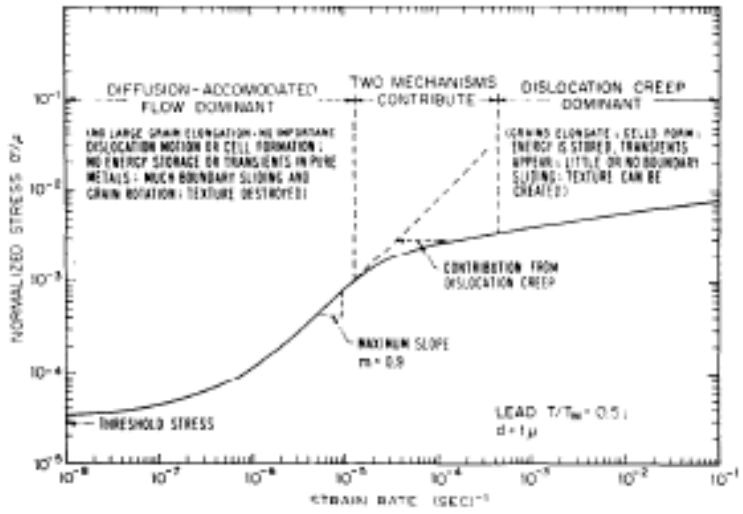

Figure 2-6: Plastic flow of a polycrystalline material detailing three regions of deformation according to Ashby and Verrall (1973).

distinguishing between mechanisms involving grain shape change ((Rachinger 1952), (T. Langdon 2002), (T. G. Langdon 2006)). With increasing temperature the ratio of grain deformation strain to macroscopic strain approach unity at room temperature and rapidly decreased to ~0.10 through 350°C; the transition temperature of ~250°C was observed where grain deformation ratio dropped from ~ 0.88 to ~0.10. From these findings, room temperature grain deformation agrees with traditional plasticity as deformation is controlled by dislocation slip as the grain shape change nearly accounts for all of the macroscopic strain. Approaching high temperatures the grain boundary markers exhibited offset discontinuities at presumably sliding grain boundaries (Rachinger 1952). Langdon (1974), (2002) and (2006) later showed such marker line offsets are expected for grain translations both of the Lifshitz (1963) and Rachinger (1952) type, while grain deformation should not produce such offsets, Figure 2- 7. Using a soap film analogy Figure 2- 8, Rachinger (1952) showed relative grain translations require continual grain shape adjustments for accommodating the sliding process and preserving a continuous microstructure. Furthermore, aluminum deformation was sensitive to temperature where slip dominated deformation transitioned to grain boundary sliding under creeping conditions.

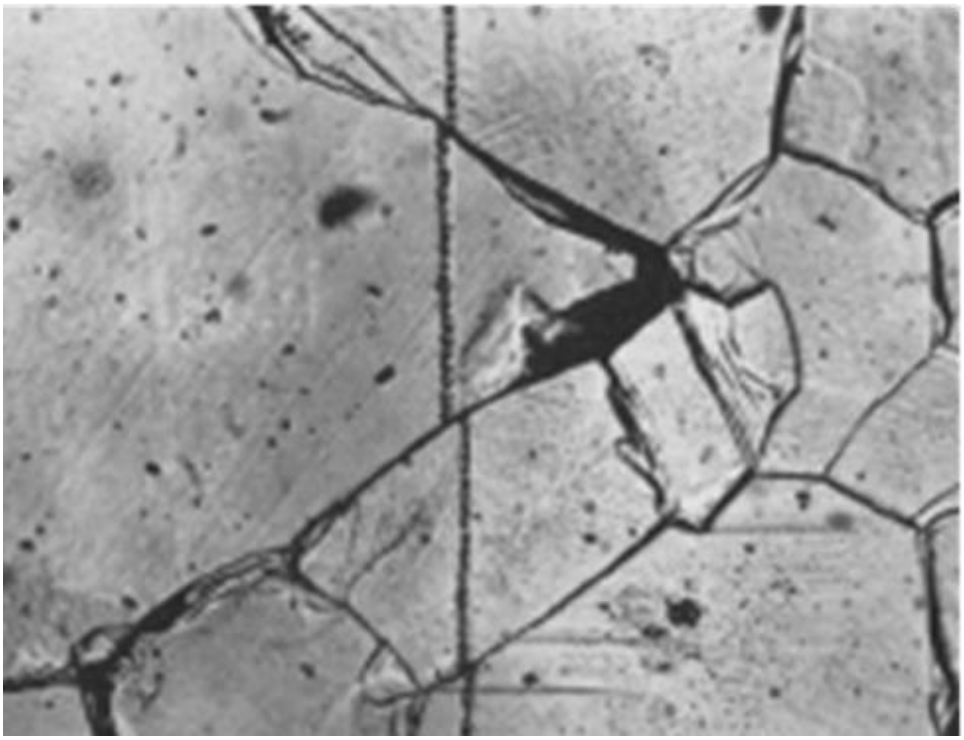

Figure 2-7: Scribe offset revealing grain boundary sliding in a polycrystalline crept material from Bell and Langdon (1967).

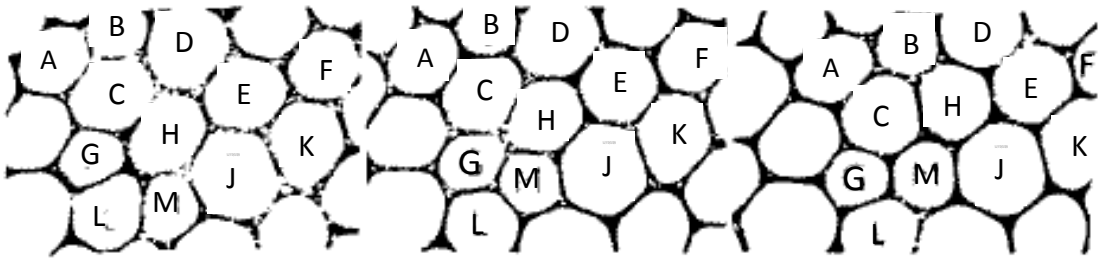

(a) (b) (c)

Figure 2-8: Soap film snap shot during deformation showing neighbor switching and grain translation deformation event (following grain G, H, L, M). Grain shapes remain near constant during grain movement from (a) to (c).

Grain boundary sliding creep where grain shape change is considered negligible has been considered Rachinger (1952) type grain boundary sliding where the accommodation process is typically grain boundary deformation. Rachinger (1952) type creep models have been reviewed by Hynes and Doremus (1996) and Cannon and Langdon (1988) for purposes of explaining ceramics creep behavior. From these reviews grain boundary sliding creep show symptoms of metals superplastic deformation at much lower overall strains. Ball and Hutchinson (1968) developed a model for describing creep deformation under large strains (>400%) for Aluminum-Zinc eutectoid alloys. From transmission electron microscopy (TEM) very low dislocation densities were observed within the 2.5μm grain size interior with few observed extended dislocation pileups at impurities and few grain boundaries for specimens deformed to 400% strain under creeping conditions. With increasing displacement, failure elongations decreased to 80% and low angled dislocation structures were formed, suggesting grain deformation controlled macroscopic deformation (Cannon and Langdon 1988). From these observations of (1) the preservation of a stable-equiaxed grain structure and (2) large relative motions of grains the deformation rate was described by

$$\dot{\varepsilon} = \frac{A\sigma^2}{L^2} exp\left(\frac{-Q_{gb}}{KT}\right), \tag{2-26}$$

where A is a constant, L is the grain diameter, Q_{gb} is the activation energy describing grain boundary diffusion and σ, and K and T hold their usual significance. Ball and Hutchinson (1968) considered grain boundary sliding deformation as rate-controlling and dependent on grain boundary vacancy diffusion forming the basis of a σ^2 strain-rate dependence contrasting with diffusion accommodated models by Lifshitz (1963), Raj and Ashby (1971), (1973) and Verrall (1973). Grain dislocation accommodated grain boundary sliding was suggested, where grain boundary vacancy diffusion controls the rate of dislocation climb into the grain boundary network. From this hypothesis Equation (2-26) describes relative movements of grain groups

whose boundaries are orientated favorably for sliding. In the presence of grains or grain boundary protrusions (i.e. un-favorably oriented grains, ledges), concentrated shear stresses may nucleate dislocations which glide and subsequently pile-up at the opposite boundary until the back-stress is sufficient to halt dislocation generation and further sliding. Further sliding may commence upon the relaxation of the boundary stress from climb of the leading dislocation into or along the grain boundary from vacancy diffusion along grain boundary paths (Ball and Hutchinson 1968). This model requires the grain size to be smaller than the equilibrium dislocation cell size as sliding is accommodated by dislocation glide across locked grains and subsequent climb into the opposite boundary. Cannon and Langdon (1988) described the subgrain size-stress dependence given by (Bird, Makherjee and Dorn 1969)

$$\frac{\lambda}{b} = \xi \left(\frac{\sigma}{G}\right)^{-1}, \tag{2-27}$$

where λ is the dislocation cell size normalized by, b, the Burger's vector; ξ is a constant of magnitude ~20 for metals and 20-30 for ceramics and σ is the applied stress normalized by the shear modulus G. This measure provides an indication of a limiting grain size where dislocation cell structures cannot be supported. Therefore, applicability of grain boundary sliding deformation using Equation (2-26) is restricted to fine grain sizes exhibiting these local deformation behaviors.

Langdon (1970) proposed a grain boundary sliding creep model considering sliding as an independently operating mechanism governing creep at low stresses and fine grain sizes. The proposed grain boundary sliding model consisted of alternating dislocation glide and climb, within grain boundary dislocation networks or along adjacent zones, where dislocation climb was rate-controlling. Langdon (1970) derived the following relationship describing grain boundary sliding deformation,

$$\dot{\varepsilon} = \beta \frac{b^2\sigma^2}{dGKT} D_L, \tag{2-28}$$

with b the Burger's vector, d the grain size, D_L the self-diffusion coefficient, β a constant dependent on the probability of locating a jog along a dislocation line and the lattice coordination number. As observed this model shows a 1/d dependence contrasting with $1/d^2$ dependence from Ball and Hutchinson (1968) and other grain boundary sliding models. Langdon (1970) assumed dislocations move in a zone adjacent to the grain boundary where creep is a climb process but producing strain through glide. The shear strain is then a function of the volume of grain boundaries ($\sim 1/d^3$), area swept by mobile dislocations ($\sim d^2$) and the climb rate (1/s) producing a 1/d dependence. Similar 1/d relationships have been shown for grain boundary sliding models where the grain size is larger than the equilibrium dislocation size (T. G. Langdon 1994). However, this model considers dislocation pile-up lengths on the order of the sub-grain size and having a stress dependence of n =3. Langdon (1970) showed good correlation for experiments involving materials with grain sizes of 25 -100μm. Mukherjee (1971) also considered such dislocation interaction as deformation enters region III of Figure 2- 6 and dislocation tangles and low angle cell boundaries impede dislocation glide across the grain.

Mukherjee (1971) proposed a grain boundary sliding model following the path of Langdon (1970), as grain neighbor sliding is not a requirement. Additionally, the model considered the dislocation climb distance was equivalent to the grain size because grain boundary pile-up groups have the same sign. Furthermore, the model considers a $1/d^2$ regardless of activation energy correlations with grain boundary or lattice diffusion. From this assessment, and similar to Ball and Hutchins (1968), it is apparent that the rate-controlling climb process is treated as a limiting velocity and the time requirement of climb introduces a length parameter. Langdon (1970) treated this time requirement based on a climb frequency parameter dependent on the probability of locating a jog along the dislocation line (β in

Equation (2-28)). Weertman (1957) used the same climb frequency relationship for derivation of climb controlled dislocation creep showing an n=4.5 stress dependency. This approach agrees well with the σ^2 and $1/d^2$ dependence commonly seen for materials exhibiting grain boundary sliding behavior ((Mukherjee 1971), (Ball and Hutchinson 1968), (T. G. Langdon 2006), (Gifkins 1976)). The following equation describes the behavior of grain boundary sliding where climb –controlled dislocation glide accommodates the strain (Mukherjee 1971), (Bird, Makherjee and Dorn 1969)

$$\dot{\varepsilon} = K' \frac{b^3 \sigma^2}{d^2 GKT} D_{gb}, \tag{2-29}$$

where K' is a constant ≈2 and D_{gb} is the grain boundary diffusion coefficient. Equation (2-29) is a simplification from Ball and Hutchinson that sliding of grain groups was not required and the ratio between freely sliding grains-to-obstructed grain parameter eliminated. Additionally, the climb distance is equivalent to the grain size as dislocation pile-ups, along the boundary, have the same sign. However, the requirement of grain boundary relaxation (e.g. sliding) by leading pile-up dislocation annihilation by climb was similar. This yields a final microstructure consisting of near equiaxed grains undergoing large relative translations and rotations as a requirement for preserving microstructural continuity.

Gifkins (1976) proposed the core-mantle theory for grain deformation similar to Mukherjee (1971) and Ball and Hutchinson (1968) and Langdon (1970) model with the sole difference that grain deformation is confined to the near grain boundary zone. Gifkins (1976) outlines three modes of grain boundary sliding accommodation (1) triple point folds (2) grain boundary diffusion around triple points and ledges and (3) dislocation motion by climb and glide in the mantle region. Considering grain switching event ((Ashby and Verrall 1973)) in Figure 2- 9, Gifkens (1976) showed this deformation mode may be accommodated by grain boundary

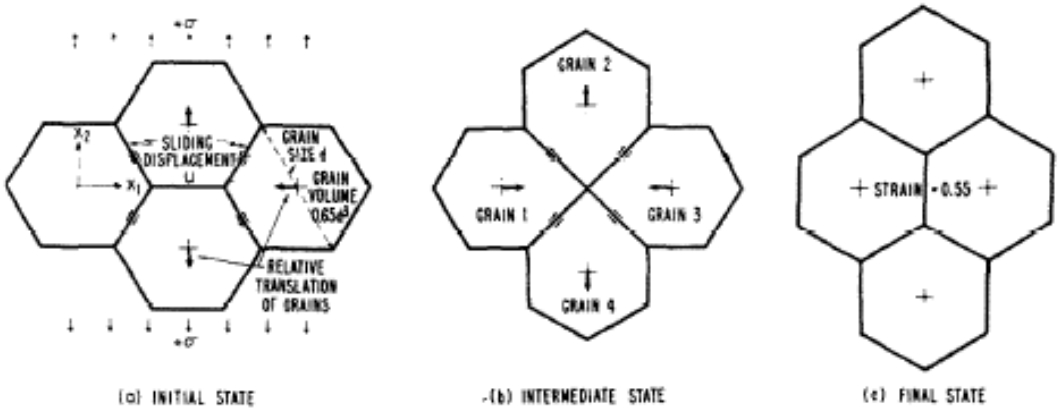

Figure 2-9: Grain switching model proposed by Ashby and Verrall (1973) showing diffusion accommodating grain translation and subsequent neighbor switching under an applied stress.

dislocation motion and subsequent pileup at triple points. The model considers grain boundary dislocations disassociate into lattice dislocations moving along the mantle by a combination of glide and climb in the sliding grain causing a net rotation until annihilating causing grain boundary relaxation, promoting sliding, Figure 2- 10 ((Gifkins 1976), (Hynes and Doremus 1996)). Similar to Equation (2-28), Gifkins (1976) derived

$$\dot{\varepsilon} = K\frac{4lb^3\sigma^2}{dh^2GKT}D_{gb}, \tag{2-30}$$

where K is geometrical constant = 1,the dislocation pile-up length, l, taken as d/2 with a total climb height h = d/√32. This formulation yields a Mukherjee (1971) constant K' of 64 compared to 2 from Equation (2-29). The characteristic climb height is based on the mantle region width y, given by (Gifkins 1978),

$$y = \left(\frac{d}{2}\right)\left(1 - \frac{\sqrt{3}}{2}\right), \tag{2-31}$$

where y is the total mantle region where climb occurs. Equation (2-30) eloquently describes region II deformation from Figure 2- 6 taking into account neighbor switching from grain boundary sliding accommodated by mantle deformation ((Gifkins 1978), (Gifkins and Langdon 1978)). Ashby and Verrall (1973) proposed this mechanism of deformation for explaining

materials deforming to large strains under creeping conditions. Furthermore, they argued the combination of their diffusion accommodated flow model with dislocation dominated creep model could predict region II deformation by neighbor switching while preserving the initial grain geometry through large deformations.

2.3.1.3. Lattice Mechanisms

Intragranular dislocation creep mechanisms typically require large homologous stress and temperatures where dislocation climb or glide are rate-controlling. Cannon and Langdon (1988) review these lattice dominated mechanisms and subdivide them into mechanisms yielding n =3 and n = 5 stress exponents. The former stress exponents are predominant in dislocation dominant creep of ceramics and solid solution alloys contrasting the latter as a fully ductile process which is common in metals of high purity and few ceramics. One exception of lattice dominated mechanisms is Harper-Dorn creep of large grained materials at high homologous temperatures and low stresses where the creep-rate is linearly proportional to stress ((T. Langdon 2002), (Hynes and Doremus 1996)).

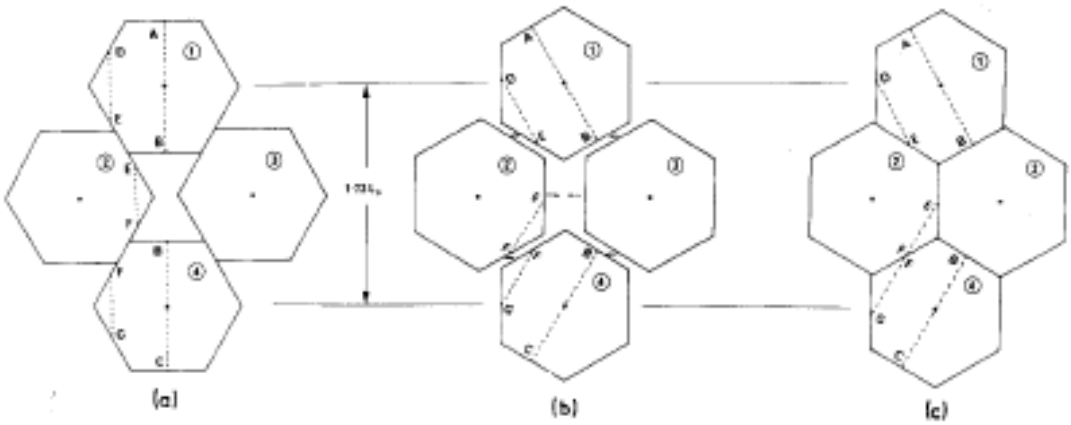

Figure 2-10: Grain switching event described by Gifkins (1978), following Ashby and Verrall (1973). Grain rotation is required for maintaining a continuous microstructure.

Considering dislocation creep mechanism with n=5 stress exponent, Weertman (1957) showed dislocation pile-up can occur between dislocations in the same slip system and subsequent leading dislocation annihilation from climb. Steady-state creep is achieved by replacing the newly annihilated leading dislocation from a Frank-Read source. This model considers dislocation glide to occur with ease and climb is rate-controlling. The creep rate at low stresses was obtained from Weertman (1957),

$$\dot{\varepsilon} = \frac{Bb^{1.5}D_l\sigma^{4.5}}{M^{0.5}G^{3.5}KT}, \tag{2-32}$$

with B a numerical constant and M is the density of Frank – Reed sources. Cannon and Sherby (1973) note that solid solution and select non-metals exhibit the fifth-power stress dependence (class I alloys). Additionally, they comment on binary alloy constituent atom size differences can be used to classify alloys as class I or II alloys. Similarities in ceramic systems has been observed where ionic or covalent radii ratios (i.e., r_{cation}/r_{anion}) < 2 correlate with n= 5 stress dependence contrasting with ratios >2 for n=3 (Cannon and Sherby 1973). Furthermore, creep rates with n= 5 stress dependence suggests fully ductile behavior (Cannon and Langdon 1988). The Von Mises criterion for polycrystalline deformation requires a minimum of five independent slip systems operating for accommodating an arbitrary shape change (Hull and Bacon 2001). Under conditions of n=3 stress dependence, Cannon and Langdon (1988) note these materials either lack the sufficient number or interpenetration of independent slip systems. Additionally, creep behavior transitions have been observed from n = 5 to n=3 with increasing stress. Cannon and Langdon (1988) discuss these transitions occur in metal solid solutions, however, nonmetals such transitions would require a shift in charge defect concentration from weak to strong interactions where vacancies and impurity atoms are usually fixed (Mohamed and Langdon 1974). Considering the influence of defects on dislocation creep, two theories were derived considering viscous nature of dislocation glide and third-powder climb creep.

Weertman (1957) treated metallic solid solution creep exhibiting a n=3 stress dependence as a viscous dislocation drag process. The creep-rate was calculated by (Weertman 1957)

$$\dot{\varepsilon} = \frac{2\pi(1-\nu)\sigma^3}{AG^2}, \tag{2-33}$$

with *v* as the Poisson's ratio and A as a constant representing a micro-creep mechanism. According to Mohamed and Langdon, the constant A represents the physical viscous drag process which include solute segregation to moving dislocations, chemical interactions with extended dislocations and local ordering of solute atoms. The constant A is given by (Cottrell and Jaswon, Distribution of solute Atoms Round a Slow Dislocation 1949)

$$A = \frac{e^2 c b^5 G^5}{\widetilde{D}KT}\ , \tag{2-34}$$

where *e* is the solute-solvent size difference, c is the solute concentration and $\widetilde{D}$ is Darken's interdiffusivity ((Reed-Hill and Abbaschian 1994), (Mohamed and Langdon 1974)). A second theory was proposed where the microcreep mechanism was solute – solvent size and concentration independent (Mohamed and Langdon 1974). However, as indicated by Cannon and Sherby (1973), the solvent-solute size is important and therefore must be included. Nonmetallic material systems exhibiting n=3 stress dependence do not necessarily follow the specific microcreep mechanism of solute drag on dislocation glide as suggested by Equations (2-33) and (2-34) ((Cannon and Sherby 1973), (Cannon and Langdon 1988)). Cannon and Langdon (1988) point out that most ceramic systems contain little or no solute and thus Equation (2-32) must incorporate drag via a charged defect such as anion or cation vacancy clouds, interstitials or impurity atoms (Cannon and Sherby 1973). An alternative creep mechanism having n=3 stress dependency includes dislocation climb from Bardeen Herring sources (Cannon and Langdon 1988). According to Nabarro (1967) the creep rate takes the follow form:

$$\dot{\varepsilon} = \frac{\beta D b \sigma^3}{\pi K T G^2}, \tag{2-35}$$

with D representing the self-diffusion coefficient and β a constant typically ~ 0.1. Cannon and Langdon and Sherby (1973) have shown excellent agreement in ceramics creep following Equation (2-36). The mechanistic difference between viscous glide creep is the dislocation source and the requirement for operating slip system(s) (F. N. Nabarro 1967). Creep by Equation (2-35) requires no operating slip system and Bardeen-Herring dislocation source dependent on local vacancy supersaturation (Hull and Bacon 2001). For example, experiments on single crystal Al_2O_3 with the stress axis oriented normal to the basal plane (0001) showed excellent agreement with Equation (2-35). Basal and prismatic slip were restricted under such loading conditions, however, pyramidal slip was possible and evidence suggested this slip system was not active ((Cannon and Langdon 1988)).

Harper-Dorn creep, near the melting point, results in a stress exponent of unity and activation energies correlating with the self-diffusion coefficient for single and polycrystalline materials. Langdon (2002) points out the experimental creep rates were significantly faster compared to Nabarro (1948)-Herring (1950) creep and identical creep rates were measured for both the polycrystalline sample and for the single crystal. According to Equation (2-17) p=0 as there is no apparent grain size dependence. A review of this mechanism suggests dislocation movement by glide and/or climb were rate-controlling. Hynes and Doremus (1996) discussed creep occurring by slip with activated of Frank – Reed sources. Similar to Weertman (1957), continued deformation leads to dislocation glide, pile up at barriers and subsequent climb (rate-controlling) relieving the back stress and continuing dislocation generation from the Frank-Reed sources. Langdon (2002) proposed edge dislocation climb occurs under saturated vacancy conditions. The observed microstructure resembles grain elongation similar to diffusion creep with the exception that marker offsets would not exist for the Harper-Dorn mechanism (T.

Langdon 2002) for large grain-sized material.

2.3.1.4. Cavitation Mechanisms

Controversy surrounds cavitation creep as a source for non-linear stress responses where the exponent has been reported over a range of values n ≥ 1. Cavitation mechanism include viscous flow phenomena with Rachinger (1952)-type grain boundary sliding, diffusive cavity nucleation and growth and cavitation by grain boundary sliding or dilation. Hall and Rimmer (1959) proposed creep rupture by diffusive cavity growth along grain facets with a lenticular shape, Figure 2- 11. Under the assumption that grains remain rigid while separating, mass transport across the entire separation width is required hence the grain boundary and surface diffusivity are rapid enough for promoting cavity growth. Later Needleman and Rice (1980) expanded this notion and included dislocation enhanced cavitation where a critical length parameter was introduced as,

$$L = \left[\frac{D_b \delta_b \Omega}{KT} \frac{\sigma}{\dot{\varepsilon}}\right]^{1/3}, \tag{2-36}$$

where L is a critical length parameter on the order of the cavity half spacing, δ_b is the grain

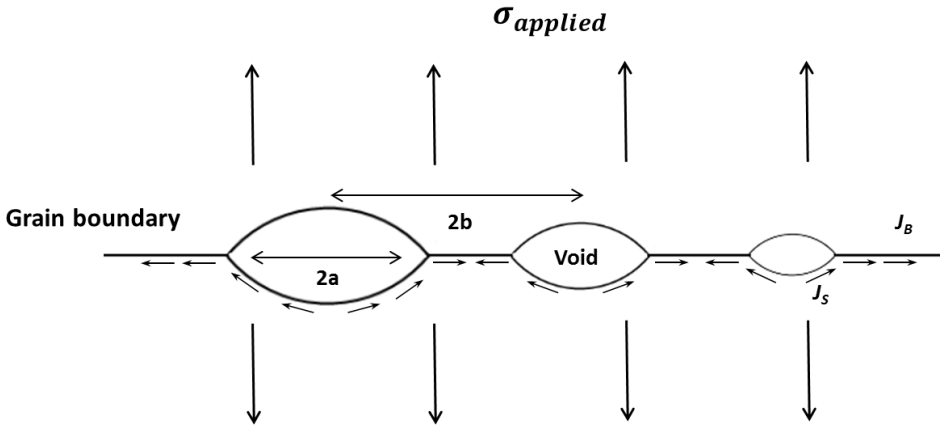

Figure 2-11: Diffusive lenticular shaped cavity nucleation and growth schematic following Hull and Rimmer (1957) along a grain boundary. Boundary stress relaxation occurs by diffusion along the grain boundary (JB) and along the cavity surface (J_S).

boundary width and $\dot{\varepsilon}$ is the steady state dislocation creep rate following Equations (2-32), (2-33) or (2-35). The cavity growth rates were significantly faster than those predicted by Hall and Rimmer (1957) as the effective diffusion distance decreased due to local deformation surrounding the cavity. According to Rice (1980), if the length parameter *L* is sufficiently large, compared to the cavity half spacing, unconstrained cavity growth occurs contrasting with constrained cavity growth where the growth rates were reduced. A similar micromechanics model was proposed taking into account plastic flow effects (Needleman and Rice 1980) for low stress diffusion dominated growth and dislocation/diffusion cavity growth under constrained conditions (Tvergaard 1984). Creep research on polycrystalline AlN revealed lenticular cavities along grain boundaries following the description of Hall and Rimmer (1957) (Jou and Virkar 1990). From a microscopy the critical length parameter "L" (Equation (36)) was found to correlate with unconstrained cavity growth conditions. Jou and Virkar (1990) considered the larger than unity stress exponent was attributed to cavitation under unconstrained growth conditions, following the format presented by Rice (1980). Cavitation was found to contribute ~30% to the overall creep strain-rate. Similar cavitation was reported in Si_3N_4 during tensile creep at 1370°C and 125 and 150 MPa applied stress (Luecke, et al., 1995). Only at low temperatures were lens-shaped cavities located along tensile boundaries. Luecke, et al., (1995) reported a higher frequency of creep failure and lower failure strains contrasting with T>1400°C creep temperatures where triple point cavitation from dilation creep dominated.

Porter, et al., (1981) investigated creep cavitation in polycrystalline Al_2O_3 with grain boundaries free from an amorphous phase. From microscopy, crack-like and full facet cavities were observed at high stresses and equilibrium cavities at low stresses and all cavities were observed at grain boundary triple junctions. A stress dependence of n = 1.8 was measured with cavitation contributing to <30% of the creep strain. Three diffusive cavitation models were

presented, with linear stress dependency, for equilibrium and full-facet cavitation (Porter, Blumenthal and Evans 1981). However, n=2 was found for crack-like cavitation at low applied stresses well below those used in creep experiments. Cavity shape transitions were found to depend on the ratio of the surface to boundary diffusion. Equilibrium-to-crack-like cavity transitions were significant with a decrease in surface diffusivity promoting cavity shape instabilities and subsequent growth across entire grain facets ((Porter, Blumenthal and Evans 1981), (Hsueh and Evans 1981)). Porter, et al., (1981) and later Hsueh and Evans (1981) showed the experimental creep non-linear stress dependence was attributed to grain-boundary sliding regardless of significant creep strain contribution from cavitation.

Evans and Rana (1979) considered a cavity nucleation and growth scenario in Figure 2-12 incorporating statistical shape distributions with n>1 stress exponents dependent upon the microstructure. Cavitation was assumed to nucleate at grain triple junctions as a result of grain boundary sliding and growth to full facet lengths under steady state conditions. The nucleation and growth even is described, under non-interacting conditions, as incorporating

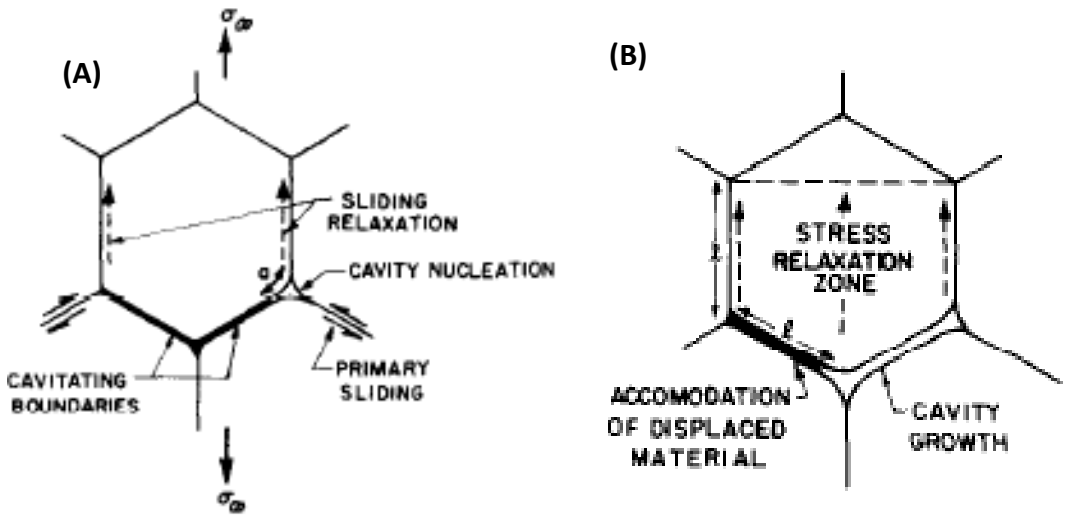

Figure 2-12: Polycrystalline cavitation model proposed by Evans and Rana (1979). (A) details cavity nucleation at a triple junction and (B) growth of the equilibrium shaped cavity to full facet length.

elastic, anelastic and viscoelastic components of strain. Under steady state conditions, the latter, was assumed to dominate because a time-dependent stress relaxation was a requirement for continuation of the primary sliding event. The statistical distribution of features was attempted to include microstructure inhomogeneities such as grain boundary dimensions, second boundary phase content and composition and boundary energies and diffusivity. The creep-rate contribution from cavitation was given as (Evans and Rana, High Temperature Failure Mechanisms in Ceramics 1979),

$$\dot{\varepsilon} = \left[{}^{3\beta\sigma^{(n+1)}}\!/_{4G} \right] \exp\left(-\frac{Q}{RT}\right), \tag{2-37}$$

where β is a constant relating the cavity facet length to the grain size and Q the activation energy for cavity growth. Equation (2-37) includes the assumption that a shape parameter, describing the statistical nature of the microstructure, is approximately unity under steady state conditions. A review of idealized single phase microstructures and microstructures consisting a continuous grain boundary second phase were modeled using these relationships. The creep-rate stress dependence varied as n=1 and n=3 for a continuous grain boundary second phase and monolithic, respectively. Contrasting from Porter, et al., (1981) and Hsueh and Evans (1981), creep-rate is modeled as a non-linear process with the extent of non-linear stress dependency varying as a function of the microstructure (Evans and Rana, High Temperature Failure Mechanisms in Ceramics 1979).

For the case of particulate composites, Biner (1995) modeled effects of grain boundary sliding anisotropy effects on cavity nucleation. An inhomogeneous distribution of sliding rates were applied to a simple particle dispersed composite microstructure where grain rotations and translations were observed resulting in discrete wedge shaped cavities at matrix-particle junctions (Biner 1995). Each model considered assumes power-law steady state creep behavior

and constant cavity nucleation and coalescence as the rupture mechanism. Using cavity growth formulations, taken form Needleman and Rice (1980), Biner (1995) calculated strain rate-stress relationships for matrix and composite creep by grain boundary sliding and concomitant cavitation. The results showed no change in the n=2 stress dependence for matrix only sliding. However, for composite grain boundary sliding with cavitation, at low stress and strain-rate the creep response maintained n=2 stress dependence contrasting with n>2 at high stress and strain-rate. Raj and Ashby (1971) considered multiple void nucleation conditions and calculated exponentially increasing failure times with a linear reduction in creep-rate for continuous cavity nucleation along a sliding boundary with distributed second phase particles. Therefore, these failure times suggest void nucleation and growth was substantially reduced for a given reduction in strain-rate despite a n=1 stress dependency which agree with the trends observed by Biner (1995) for n=2 creep.

Creep of solid embedded in a viscous glass phase has been modeled using dilatancy describing a volume expansion of densely packed grains in response to a shear stress. For example, under an applied shear stress, close-packed ensemble of ball bearings increases in volume contrasting with densification of loosely packed bearings (Wroth). (Luecke, et al., 1995) suggested the triple point creep cavitation observed during tensile creep tests in a Si_3N_4 ceramic was due to such a process accounting for ~100% of the creep strain. Rigid grain boundary sliding was thought to accommodate the volume expansion. Similar to glass redistribution models, large driving forces are created, in the presence of a cavitated pocket, for glass redistribution into pockets under hydrostatic tension. This redistribution leads to neighboring silicate pocket volume expansion, from the newly arrived glass, accommodated by grain boundary sliding and eventual cavity nucleation by dilation. The driving force for glass redistribution was modeled by Dryden, et al., (1989) using a cube mosaic separated by a viscous phase with 2/3 of the cube

surface (under compression) supplying the remaining 1/3 of the cube surface (under tension) with viscous material accounting for creep. Creep rates in tension doubled those in compression and explains the asymmetric creep behavior commonly observed in Si_3N_4 ceramics ((Chadwick, Jupp and Wilkinson, Creep Behavior of a Sintered Silicon Nitride 1993), (Wiederhorn, Hockey and French 1999), (Yoon, Wiederhorn and Luecke, Comparison of Tensile and Compressive Creep Behavior in Silicon Nitride 2000)). Lange (1975) proposed grain boundary separation or approach as opposed to sliding was rate-controlling with viscous material redistribution occurring as a transient process. Similar to Dryden, et al., (1989) asymmetric creep behavior was predicted on the basis that boundary separation was found to occur faster than any diffusion process. Additionally, separating boundaries must eventually have growth of a cavity to account for the creep strain after an equilibrium film thickness has been achieved. However, irregularities in grain boundary sliding and elastic grain contact may reduce the redistribution of viscous material, and the overall strain-rate. This is manifested in the exponential (not power-law) dependent creep behavior often exhibited by Si_3N_4 ceramics ((Krause Jr., et al., 1999) and (Lofaj and Wiederhorn 2009)). Under one constant loading condition, the creep rate would be expected to reduce as neighboring grains approach one-another until contact suggesting the dominate creep mechanism becomes exhausted (D. S. Wilkinson 1998). Krause Jr., et al., (1999) observed decreasing strain-rate with creep strain because of inter-grain contact removing the glass source supply for further strain production.

2.3.2. ZrB_2 and ZrC Creep Behavior

Early atmospheric creep investigations include those conducted by S.M. Kats (1981) and I. I. Spivak (1974) on ZrC-ZrB_2 and ZrB_2-ZrN composites, respectively. ZrB_2-ZrC investigation included low stress (5-30 MPa) compressive creep characterization and composition dependence on creep rate, between 1700°C and 2420°C. Creep rates were reported to range

between ~10^{-6} and 10^{-4} s^{-1} with corresponding stress exponent of unity and activation energy of 270 ± 29 KJ/mol for all stress and temperature combinations. A strong ZrC composition dependency on creep rate was observed having a maximum creep rate at 50 vol% ZrC. Diffusion accommodated deformation limited by carbon diffusion through ZrC (Q = 272 KJ/mol) was the rate-controlling creep mechanism (Kats, Ordan'yan and Unrod, Compressive Creep of Alloys of the ZrC-ZrB_2 and TiC-TiB_2 Systems 1981). Spivak, et al., (1974) conducted a similar investigation on flexure creep rate and ZrN composition influences. The grain sizes were significantly larger than those of Kats, et al., (1981) and hence considerable creep rate reduction was realized. However, the creep rate-ZrN composition dependencies were identical to those of ZrB_2-ZrC system with a maximum creep rate occurring at 50% ZrN. The reported large accumulated creep strains and microstructure continuity has characteristics of structural superplasticity or grain boundary sliding (Spivak, et al., 1974).

Recent ZrB_2 based atmospheric creep investigations show similar impacts of the compositional variations on the creep rates with the overall strains attributed to grain boundary sliding (Talmy, Zaykoski and Martin, Flexural Creep Deformation of ZrB_2/SiC Ceramics in Oxidizing Atmosphere 2008). Talmy, et al., (2008) studied the SiC content and grain size effect on creep rate. The studied included compositions through 50% SiC and SiC grain sizes of 2 and 10 μm between 1200°C and 1500°C with stresses through 180 MPa. They found the creep rate to increase with increasing SiC composition, stress and temperature. The creep rate was found to decrease with increasing SiC grain size. An apparent maximum in creep rate was realized at 50% SiC, consistent with Spivak, et al., (1974) and Kats, et al., (1981). The evaluated Norton stress exponent and activation energy were reported as n= 1 and n=2 for 0-25% SiC and 50% SiC compositions, associated with activation energies of 130 and 511 KJ/mol for 0% and 50% SiC, respectively. The reported dominant creep mechanisms included diffusion accommodated by

deformation and grain boundary sliding for the 0-25% SiC and 50% SiC composites, respectively. Talmy, et al., (2008) reported stress enhanced oxidation kinetics during creep testing from observed fibrillation of SiC particles sufficiently removed from the bar surface. This oxidation may have a deleterious influence on both creep behavior and experimental interpretation. Preliminary 24-135 hr. creep experiments, in air, were conducted on a ZrB_2-20% SiC composite resulting in oxide film thicknesses of ~1 mm. Further inspection of the specimen cross-sections revealed grossly irregular shaped base material at a fraction of the original cross-section (Aune 2011). Hence these findings suggest creep testing be conducted in protective or inert environments for deformation mapping and characterization.

Guo, et al., (2012) conducted limited number of inert atmosphere flexure creep experiments on ZrB_2-30% SiC composite at 1500°C and 1600°C and 19MPa for 0-100 hr. Displacement measurements were completed by beam curvature measurements and hence a discontinuous testing scheme was employed. However, their extended creep times and temperature revealed isolated wedge-shaped cavities nucleated only at ZrB_2/SiC triple points with little growth and no observable cavity coalescence. Close inspection of the micrographs reveal that continued growth of angular cavities may result in full face cavity formation as discussed by Evans and Rana (1979) and Porter, et al., (1981) at the low applied stress. Additionally, both the ZrB_2 and SiC grain shapes and size remained unchanged throughout deformation despite the 0.6% outer-fiber tensile strain. An apparent increase in cavity number density and size was observed with temperature, where cavitation sites were predominately ZrB_2-SiC grain junctions (Guo, Zhang and Lin 2012).

Other studies conducted on creep of ZrC incorporated WC solid solutions in an attempt to reduce creep rates. Solid solutions of 4-12 mol% WC in ZrC were processed from powder compacts, sintered for 1 hr. at 2100°C and annealed at 2400°C and 2500-2900°C using an

indirect high frequency furnace (Kats, Ordan'yan and Gorin, et al., 1979). Compression creep experiments were conducted at temperatures 2450 - 2900°C under applied stresses of 10-50 MPa. From the creep results two systematic studies were conducted (1) annealing temperature effects on creep rate and (2) solid solution effect on creep rate. Considering (1) increasing annealing temperature to 2700-2900°C showed a decrease in creep rate of 1-2 orders of magnitude for all solid solution compositions. Specifically, compositions > 3-4 mol% WC required high temperature and longer heat treatment time as a requirement for complete homogenization. Increasing the solid solution composition reduced creep rate by a minimum of 1 order of magnitude. Kats, et al., (1979) showed WC compositions of 4-6 mol% were required for such an improved creep response. This compositional limit is based on the measured creep response; however, melting point depression occurs with solid solution compositions greater than those above (Vil'k, Ordan'yan and Avgustinik, The possible formation of isothermal sections of Zr-W-C at 2200 and 2600C 1972). Furthermore, an accelerated creep response was observed for WC compositions greater than 6 mol% owing to an increase in homologous temperature. The Norton constants measured varied from n=2.5-2.75 between 2450 and 2650°C with activation energies of 454-652 KJ/mol were reported. Shifts in mechanism were observed between 2650 and 2800°C with n = 1.1-1.23 and activation energies of 656-803 KJ/mol. Beyond 2800°C cavitation and cracking were observed with an onset of accelerated creep rate. High temperature creep shows a stress dependency near unity however, Kats, et al., (1979) reported the grain size dependency as $p<1$ suggesting neither lattice nor grain boundary diffusion mechanisms. An alternative dislocation mechanisms operating at these temperature was concluded. Ashby and Verrall (1973) discussed diffusion creep in fine grained materials have n=1 and p =1 with the interface reaction being rate-controlling. Low temperature creep was attributed to slip and climb processes. As Weertman (1957) pointed out and later Mohamed

and Langdon (1974) and Cannon and Sherby (1973), transitions from climb controlled to glide controlled accompanies a shift form n=4.5 to n=3 creep. Furthermore, n=3 suggest viscous drag creep where dislocation glide is restricted by solute atmosphere interactions. The activation energies represent those of either Zr and/or W diffusion in ZrC (673 and 686 KJ/mol, respectively). Kats, et al., (1979) suggest a combination of grain boundary sliding following Equation (2-28) and Equation (2-33).

Continuing the work of solid solution effects on creep, compression creep and MOR experiments were conducted on ZrC based alloys with WC composition of 0.50 mol% (Gurevich, et al., 1981). Specimens were sintered for 1 hr. at 2600°C, crept at temperatures of 2250-2500°C and MOR experiments carried out at 20, 2000 and 2100°C. Diffusion creep was observed through all temperatures with activation energies of ~732 KJ/mol agreeing with those reported by Kats, et al., (1979) additionally Gurevich, et al., (1981) found no appreciable effect of sufficiently dilute solid solutions on creep behavior. Furthermore, no appreciable change in lattice constant was measured. MOR experiments revealed primarily brittle fracture through 2100°C. A ~100°C increase in the brittle-to-ductile transition temperature was observed, however, 0.5 mol% WC solid solution would have negligible effect on creep resistance and hence strength above the transition temperature. Below the transition temperature strength is controlled by structural defects and such solid solutions do not affect these defects. Only with sufficient solid solution, as reported by Kats, et al., (1979), can a sufficient increase in the transition temperature be realized.

A limited creep study was conducted on ~5 mol% WC containing ZrB_2 ceramics Hot-pressed at 1900°C for 1 hr. (Guo, Yang and Zhang 2011). Interrupted four-point flexure creep experiments were conducted at 1900°C and 25 MPa under vacuum-backfilled argon atmosphere with testing intervals between 0-60 min. From the compositional analysis, an unknown phase is

reported in the final microstructure comprising of carbon, oxygen, tungsten, cobalt and zirconium. A similar phase was reported in the room temperature strength studies for attrition milled ZrB_2-30% SiC composites (A. Chamberlain, et al., 2004). Large creep strains were iteratively measured with a maximum reported outer-fiber elastic strain of 8% and no visible macroscopic crack formation. Microstructure and TEM investigations revealed cavity nucleation, growth and coalescence along the tensile zone contrasting with negligible cavitation along the compressive zone. Additionally, the W-bearing phase was concentrated a triple points and observed to deform during creep, accommodating the ZrB_2 deformation. Close inspection of the micrographs reveal cavitation contributes very little to the macroscopic creep strain. Because of the interruptive testing style traditional Norton constants could not be derived. Considering the observed creep deformation, the W-bearing phase appeared to accommodate the ZrB_2 matrix deformation with no apparent solid solution effect on creep.

Chapter 3

Experimental Setup and Procedures

Experimental setup and procedures include the following: Material process parameters and equipment setup, microstructure characterization techniques, mechanical property equipment and analysis procedures and creep experimental details. Material processes include starting chemistries, milling procedures, sintering and heat treatment parameters. Characterization techniques are segmented into analytical and metallographic techniques comprised of electron and optical microscopy and electron backscatter diffraction (EBSD) orientation imaging microscopy (OIM). Procedures for conducting the indentation deformation mapping (IDM) experiment are also provided. Room temperature mechanical properties include Modulus of Rupture (MOR), Single Edge Notch Beam (SENB) fracture toughness, hardness, indentation and ultrasonic modulus and the necessary formulations for analysis. Finally, creep experiments include methods for conducting protective and inert dead-load and constant displacement experiments with real-time specimen displacement measurements.

3.1. Material

A combination of SiC based composites and alloyed monolithic materials were used for room temperature mechanical behavior and creep deformation studies. Table 3- 1are tabulated material compositions and experimental designations.

The Z20SB composite was selected for creep deformation and high temperature fracture research based on a combination of oxidation resistance, high temperature strength retention and room temperature mechanical properties (Fahrenholtz references). The Z20S composite, of similar composition, was processed without B_4C sintering aid for reducing the

Table 3- 1: Material and experiment designations and processing descriptions for the composites and alloys used in this study.

Material Designation	Nominal Composition (mols)	Milling	Densification	Experiments
Z20SB	ZrB_2-26SiC-2B4C	BM	HP	FC, CC, IM, HC, RM
Z20S	ZrB_2-27SiC	BM	HP	RM
ZCWC	ZrB_2-5WC-5C	BM	HP, CP	RM
ZWC1	ZrB_2-8WC	AM	HP	RM
ZWC2	ZrB_2- 4WC	AM	HP	RM
ZWC3	ZrB_2-7WC	BM	HP	IM, RM

Flexure Creep (FC), Compression Creep (CC), High-Strain Creep (HC), Indent Mapping (IM), Room-Temperature Mechanical Properties (RM), Ball Milled (BM), Attrition Milled (AM), Hot-Pressed (HP), Carbon Pyrolysis (CP)

composite flaw size in effort to boost the room temperature fracture and strength and toughness. The ZrB_2-WC ceramics were developed in effort of obtaining a solid solution alloy of WC in ZrB_2 for providing creep property tailoring based on deformation findings on the Z20SB composite. The WC compositions were selected based on a preliminary, and limited, thermodynamic study of the quasi binary ZrB_2-WC system.

From the work of Kaufman (1986) and Nesor (1978) and Uhrenius, et al.,(1984), Kaufman and Clougherty (1963)(1965), Echert (1965) and Rudy (1969) thermodynamic potentials were developed for describing the Gibb's free energy of the binary constituents making up the quaternary system. Considering Zr, W, B and C system, six possible binary combinations and their excess free energy potentials were used for calculating phase stability based on interaction potentials following a sub-regular model. The details of the thermochemical calculations are provided in Appendix A. Applying a common tangent to each phase curve reveals virtually no solubility of ZrB_2 in WC with temperature, an expanded binary WC + ZrB_2 phase field and limited WC solubility in ZrB_2. Approximate WC solubility in ZrB_2 are 15.8+/-0.5, 7.0 +/-0.5, 1.0 +/- 0.5 and ~0 mol% for 2427°C, 2227°C, 1927°C and 1727°C, respectively. These calculated solubility limits <2000°C are significantly lower than the <8 mol%

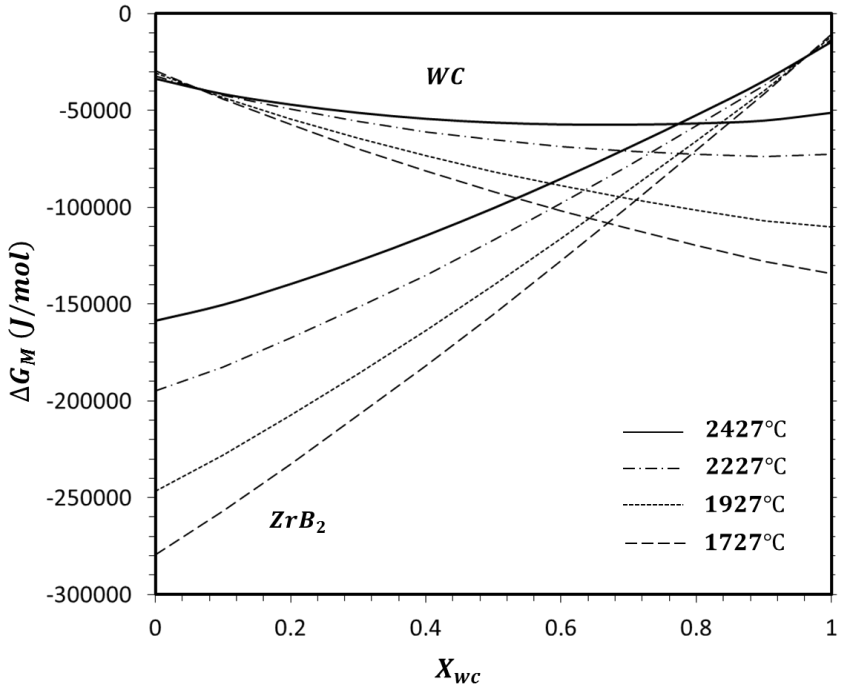

Figure 3-1: Molar Gibb's free energy curves, with WC mole fraction, at four temperatures describing possible solubility limits in the quasi-binary ZrB_2- WC system.

limit experimentally observed for ZrB_2 WC alloys sintered with an organic binder ((Zhang, Hilmas and Fahrenholtz 2011)). However, no study to-date has confirmed the extent of solid solution by lattice parameter measurements for the ZrB_2-WCsystem. For hot pressing temperatures of ≥2100°C, a minimum of ~ 4 mol% WC would dissolve into ZrB_2 provided the kinetics are favorable, leaving a maximum WC phase fraction of ~0.04 of a composition ~100% WC. Increasing the temperature through 2300°C shows improved WC solubility of ~9 mol%. Therefore, each alloy specified meets the minimum WC solubility requirement, presented in Figure 3- 1, and the composition for improved creep resistance based on ZrC-WC creep research (Kats, Ordan'yan and Gorin, et al., 1979).

3.1.1. Powder Processing

All composites and monolithic materials, for this study, were processed using standard powder mixing and size reduction processes for other UHTC materials. All raw materials were

sourced from HC-Stark (Newton, MA USA) and original particle size distributions reported (Table 3- 2); ZrB_2 starting particle size distribution was measured by Union Process (Akron, OH USA) using a Mircotrac S3000/S3500 laser diffraction system (Largo, Fl USA) with Microtrac 10.5.2 particle analyzer software and databases.

Table 3- 2: Raw powders used for materials processing with starting particle sizes.

Powder	Starting Particle Size	Measured Particle Size (μm)
ZrB_2: Grade B	d50% = 1.5 -3.0, d90% = 4-6	d50% = 3.1, d90% = 4.5
SiC: Grade UF-10	d50% = 0.70, d90% = 1.8	----
B_4C: HD-20	d50% = 0.3-0.6, d90%=0.9-1.5	----
WC: DS-60	0.60 -0.70 (Fisher Number)	----

Z20SB were produced by Missouri University of Science and Technology in a manner similar to that reported by Chamberlain, et al., 2004. Raw powders were ball milled in acetone, at a 1:5 powder solvent ratio, with ½" WC-6Co satellites (Union Process) for 24 hours at 60 rpm. DISPERBYK-110 dispersant (BYK Chemie , Wallingford, CT USA) was added at 0.5 mg/m^2 for the SiC and B_4C and 0.4 mg/m^2 for ZrB_2 to reduce agglomeration during mixing. Powders were rotary evaporated at 60°C at 60 rpm under a mild vacuum. Once dried, the powder was lightly ground with a mortar and pestle to -50 mesh. Prior to die loading, 50-80 cc (enough powder for quantity 2, 2.5" square billets) of the milled and dried powder was ball milled with 1/8" WC-6Co satellites for 1 hour at 60 rpm and rotary evaporated and lightly ground to -50 mesh with a mortar and pestle.

Z20S, and ZWC3 materials were produced by Advanced Ceramics Manufacturing, Inc. (Tucson, AZ). The Z20S material was ball milled (Labmill 8000 ACM Inc. Tucson AZ) for 24 hrs at 74 rpm, in Isopropyl alcohol, at a 1:4 powder solvent ratio, with 1/8" WC-6Co satellites. BYK-100 dispersant was added at 0.5 mg/m^2 for the SiC and B_4C and 0.4 mg/m^2 for ZrB_2 and WC powders. Batched powders were dried using a 300 rpm stir hot plate within a temperature range of 80-125°C Prior to die loading. Dried powder was lightly ground with a mortar and

pestle to -50 mesh and then die loaded. The ZCWC composite was ball milled using the same conditions as the Z20S and ZWC3 composite with 1.22 wt% (based on ZrB_2 powder weight charge) phenolic resin (Type GP 2074, Georgia Pacific, Atlanta, GA, USA) and acetone solution. The phenolic resin solution is the carbon precursor for particle oxide reduction and the quantity is based on 41% carbon yield after pyrolysis ((Zhang, Hilmas and Fahrenholtz 2011)). 500 ml of acetone was used for dissolving 2.268 g of phenolic resin for a standard powder batch of 100 ml total powder volume. The powders were dried using the same methods as the Z20S and ZWC3 and lightly ground to -50 mesh prior to die loading. The final particle sizes were not measured for all ball milled materials, however, previous research suggests negligible particle size reduction using the prescribe parameters.

ZWC1 and ZWC2 alloys were attrition milled by Union Process, Inc. (Akron, OH USA) in a Lab 01-HD attritor mill with a stainless-steel rotation spindle and WC arms in a 750 ml Teflon coated tank. 1:1 powder to solvent ratio (by weight) was milled using 1/8" WC-5Co satellites at 600 rpm for 2 hrs and 1 hr milling times, in Isopropyl Alcohol (IPA) solvent, for ZWC1 and ZWC2, respectively. Powders were dried using 300 rpm stir hot plate at 80 - 125°C. Dried powders were lightly pulverized with a mortar and pestle and sieved through a -50 mesh prior to die loading.

3.1.2. Densification

Batched powders were loaded in graphite dies coated in Boron Nitride (BN) and lined with Grafoil (Graftek Inc.), for reducing powder-die interactions, prior to hotpressing. Z20SB billets were Hot-pressed at 1950°C for 10 min under a uniaxial pressure of 32 MPa in a flowing Ar atmosphere. Initial hot-pressing heating cycle included a 30°C/min heating rate to 1450°C and 1 hour soak to recover the 100 mTorr vacuum. Heating commenced through 1650°C at a rate of 30°C/min and soak for 1 hour at 100 mTorr. The furnace chamber was backfilled with

99.999% Ar, the uniaxial load applied to the powder compact and furnace heating continued through 1950°C at a rate of 90°C/min. After hot-pressing, the furnace was allowed to naturally cool through 1450°C and the uniaxial load removed below 1650°C.

The Z20S, ZWC1-3 alloys were hot-pressed at 2100°C for 30 min under a uniaxial pressure of 32 MPa in flowing Ar or vacuum atmosphere. The heating cycle included ramping through 1650°C at a rate of 10-15°C/min under a 100 mTorr vacuum with a hold cycle of 1 hr for vacuum recovery. The maximum uniaxial load was reached at 1650°C and heating commenced through 2100°C at a rate of 10-15°C/min. After hot-pressing the furnace was allowed to naturally cool and the uniaxial load removed below 1850°C. The ZCWC alloy was hot-pressed under the conditions state above with an additional "Pyrolysis" heat treatment, prior to the load application, for converting the phenolic resin to carbon-black and promoting densification by particle oxide reduction. The phenolic covered packed powder bed was heated to 700°C at a rate of 1°C/min and a soaking period of 2 hr under 100 mTorr vacuum. The remaining hot-pressing schedule was unchanged.

3.1.3. Heat Treatment

Alloy heat treatments were conducted under inert atmosphere conditions in effort to promote solute dissolution and homogenization. Select heat treatments were conducted at 2100°C and 2300°C for 30, 60, 90 or 120 minute soaking periods. The 2300°C furnace runs were completed by AVS Inc. (Avery, MA USA) in a resistance heated furnace capable of 2350°C temperatures with an integral gas quenching system for optimizing the cooling rate. Alloys were heated through 500°C at a rate of 12°C/min and stabilized for 30 minutes under a 20 mTorr vacuum. The furnace was back-filled with 10 psig 99.999% Ar overpressure and then heated through 2300°C at a rate of 12°C/min for the desired soaking period. The billet was gas quenched by backfilling to 13.00 bar to achieve a quench rate sufficient to hold the dissolved

species in solution without cracking, through 1800°C, and then naturally cooled to removal temperature. 2100°C heat treatments were conducted in a vacuum furnace capable of 2150°C with low pressure gas backfilling capabilities. Heating treating schedules are similar to those for 2300°C heat treatments with exception to a flowing argon (~2-3 psi overpressure) backfill for facilitating quenching through 1800°C and naturally cooling through the removal temperature.

3.2. Characterization

3.2.1. Analytical Methods

Specimen density was measured using Archimedes' method using water as the immersing fluid (ASTM 2013). Based on initial powder charges and the rule of mixtures, a theoretical density was calculated and compared with those measured. Porosity and nominal compact compositions were determined using the relative density and the rule of mixtures given as

$$\rho_{Total} = \sum_i V_{f,i}\rho_i, \tag{3-1}$$

where the total density, ρ_{Total}, is dependent on the volume fraction, $V_{f,i}$, and density, ρ_i, of each constituent.

Phase composition, alloying and spatial analysis was completed using both Energy Dispersive Spectroscopy (EDS) and X-ray Diffraction (XRD). EDS was carried out at 15 and 5 KV accelerating voltages at working distances between 12 and 18 mm with a probe current of 14 µA. Reducing the acceleration voltage decreases the excitation volume and improves image resolution and isolates the desired area for analysis, however, the number of excited energy states are reduced. For example, at 5 KV only the W-Mα energy bands is excited contrasting with 15 KV accelerating voltage exciting both W-M and W-L energy bands improving elemental quantification with an increasing excited volume. A combination of point analysis and elemental

mapping were conducted for semi-quantification of phase composition and spatial distribution of elemental components.

XRD was used for identifying crystalline phases present in each composite or monolithic using a fixed-slit, D-5000 (Siemens Co.) diffractometer with Cu-Kα radiation. Diffraction experiments were conducted over a 2-theta range of 20-130° at 0.02° increments. Diffraction patterns were indexed using powder diffraction software and diffraction database (X'Pert HighScore V2.2b PANalyticical 2007 and PDF-2 Release 2011 V4.11.3.3 Database 2.1102). Phase identification was completed by identification of top three diffraction peaks and intensity matching (Cullity and Stock 2001). Lattice parameter measurements were performed on surface relief polished specimens in effort to characterize solid solution behavior of ZrB_2-WC alloys. Following Bragg's law (Cullity and Stock 2001),

$$\lambda = 2d_{hkl} \sin\theta, \tag{3-2}$$

where λ is the source x-ray wavelength, d_{hkl} the inter-planar spacing and θ the Bragg angle. From the diffractometer, diffraction peak intensities are measured with respect to 2θ positions for a given material. Application of Equation (3-2), with knowledge of the x-ray source, the inter-planar are calculated with respect to the 2θ positions. Considering the hexagonal lattice geometry, the lattice parameters were calculated from ((Cullity and Stock 2001) (Kaufman and Clougherty 1963))

$$a^* = \lambda \left(\frac{h^2+hk+k^2}{3}\right)^{1/2} \frac{1}{\sin\theta_{hk0}} \tag{3-3}$$

and

$$c^* = \frac{\lambda l}{\sin\theta_{00l}}, \tag{3-4}$$

where a* and c* represent the true lattice parameter parallel and perpendicular to the basal

plane, respectively, and *h, k,* and l are the Miller indicies. The a-parameter is dependent only on planar reflections along the basal planes as indicated by the hk0 designation contrasting with the c-parameter dependent only on the 00l reflections. However, diffraction of polycrystalline materials tends to show an observed d-spacing deviation from the theoretical d-spacing, for a given reflection, due to x-ray absorption and specimen alignment. The systematic error can be expressed in the form of

$$\frac{\Delta d}{d} = Kf(\theta) \tag{3-5}$$

and

$$f(\theta) = \frac{1}{2}\left(\frac{\cos^2\theta}{\sin\theta} + \frac{\cos^2\theta}{\theta}\right), \tag{3-6}$$

where $f(\theta)$ is an extrapolation function and $\frac{\Delta d}{d} = \cot\theta\,\Delta\theta$ is the relative uncertainty in the d-spacing associated with a shift Bragg angle ((Cullity and Stock 2001), (Kaufman and Clougherty 1963)). The error function, $f(\theta)$, is minimized when approaching Bragg angles of 90° (2θ=180°). Therefore, high angle plane reflections show the least d-spacing deviation and the calculated a-parameter approaches a*at $f(\theta) = 0$, Figure 3- 2.

3.2.2. Microscopy

3.2.2.1. Sample Preparation

Specimen preparation was completed for all composite and monolithic materials prior to characterization. A combination of mechanical grinding and polishing, chemo-mechanical polishing and etching procedures were implemented for achieving desired surface properties. All epoxy mounted specimens were ground with bonded diamond coarse grit diamond pads followed by SiC grit hand grinding to achieve a flat surface. Mechanical polishing was completed using 0.25 and 0.10µm diamond suspension followed by chemo-mechanical polishing using 0.05

μm colloidal SiO_2 on a vibromat. The colloidal SiO_2 final polish etches deformed surface material resulting in a stress-free state. Etching procedures included both chemical and thermal etching. Chemical etching was completed using equal volumes of concentrated H_2O_2 and HNO_3, submerged and agitated in an ultrasonic bath for 20-30 minutes. Additionally, relief etching was achieved from the final colloidal SiO_2 lightly exposing grain boundaries after 30-40 minutes.

Composite thermal etching was completed by heat treating polished specimens, wrapped in Grafoil (GrafTech Int. Lakewood, OH) under 2-3 psi 99.999% Argon over pressure after achieving a vacuum < 20 mTorr and 1600°C for 1 hour. An alternative composite thermal etching procedure included flowing argon over a graphite crucible, containing each polished specimen wrapped in Grafoil, at 1550°C for 1 hour under atmospheric pressure. ZrB_2 alloy etching, specimens were heated to 1800°C for 1 hr under a similar vacuum and argon over pressure. Alloys containing appreciable free carbon were not thermally etched because the surfaces were to reactive at the maximum obtainable vacuum.

3.2.2.2. Electron Back Scatter Diffraction

Electron Back Scatter Diffraction (EBSD) was conducted using a Hikari EBSD camera mounted on a Philips XL-30 FEG SEM. Orientation Imaging Microscopy (OIM) was completed with data collection and analysis of ZrB_2 and 2-H α-SiC Kikuchi patterns (TSL OIM Data Collection/Analysis V5.3) using an Octane EDS detector (EDAX Inc.) with a survey window of approximately 100μm x 100 μm at a step size 0.2 μm, surveying approximately 1500 ZrB_2 grains, and 4x4 binning for the coarse scans. Fine scans were collected over a 15μm x 15μm window at a step size of 0.050μm, surveying approximately 30 ZrB_2 grains, and 1x1 binning. (Humphreys 2004) All scans were run with an accelerating voltage of 20kV at a working distance of 12 mm and a take-off angle of 70° from horizontal; theoretical details are considered in Appendix B. Typical OIM image reconstruction is shown in Figure 3- 3 and provides the necessary Euler angle

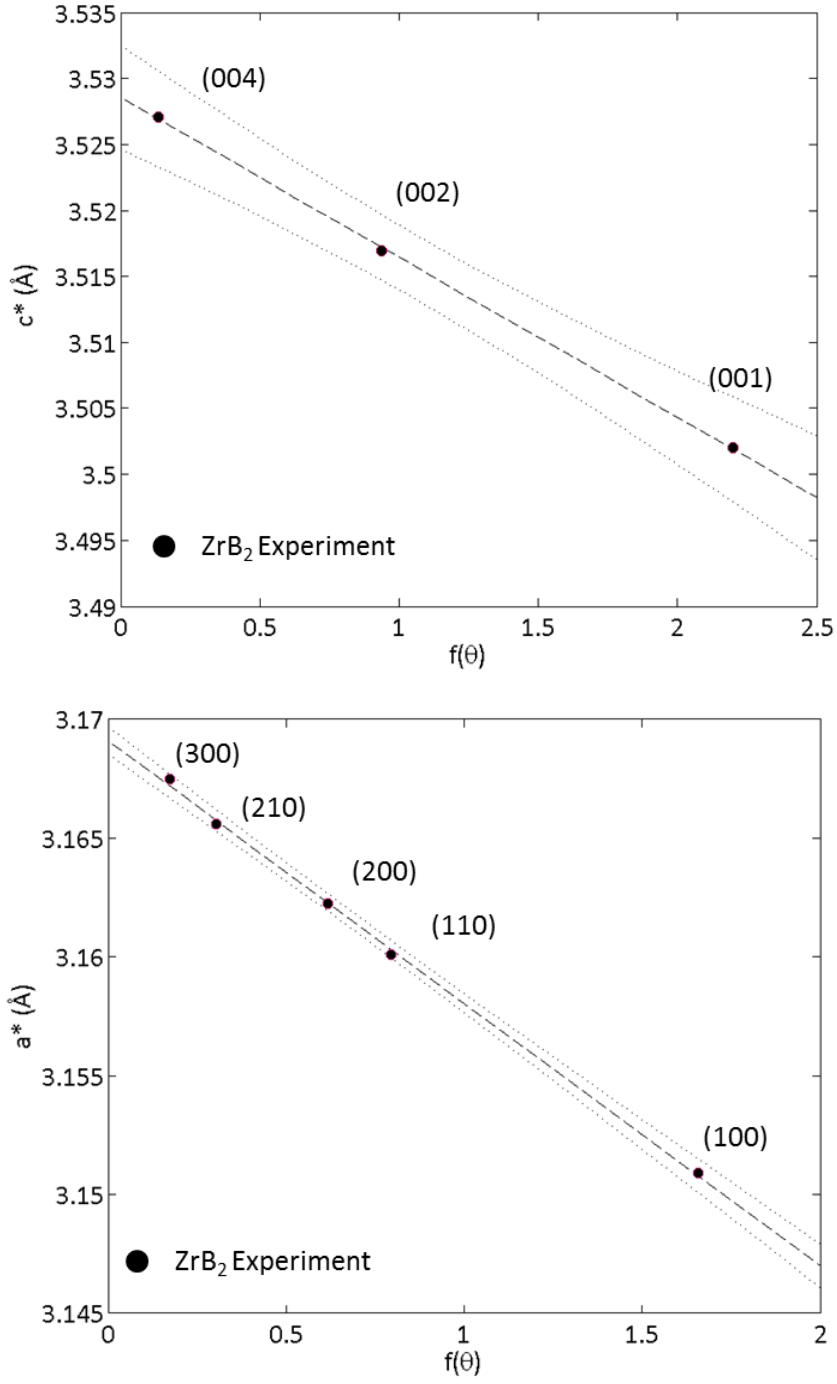

Figure 3-2: c-axis (Top) and a-axis (Bottom) lattice parameter determination for ZrB_2 polycrystalline phase. Dark hashed line represents linear regression fit of Equation (3-6) and the dotted lines represent 95% confidence interval.

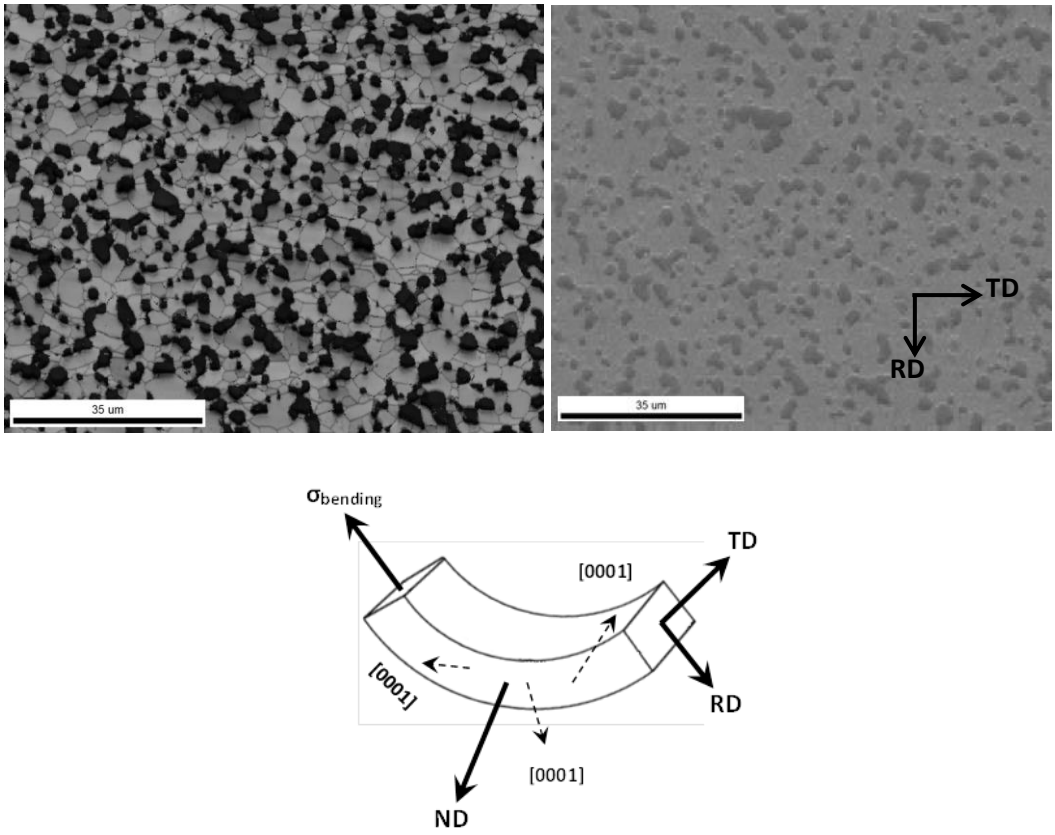

Figure 3-3: EBSD reconstruction map highlighting the SiC phase (black) and ZrB_2 phase (grey) (left) and the actual SEM image (right). RD, TD and ND are sample space default directions with TD parallel to the bending stress axis (bottom).

descriptions for crystallographic real space interpretation with respect to orthogonal sample space providing grain size, shape and crystal direction statistics. Furthermore, the sample reference frame with respect to the loading axis and crystallographic real space are shown, Figure 3- 3.For the EBSD texture analysis, the Orientation Distribution Function (ODF) was calculated using a harmonic series expansion, proposed by Bunge (EDAX 2011), (Bunge 1982), of rank 16 with a Gaussian Half-Width of 2.0° for all texture plots. Choice of the series rank and Gaussian half-width affect the texture plot smoothing (EDAX 2011); the chosen parameters are considered sufficient for describing texture of these materials. Kernel Average Misorientation (KAM) analysis was used for qualitatively assessing the spatial distribution of regions containing local lattice misorientations. This analysis provides insight to the location and relative density of

geometrically necessary dislocation density relative to the microstructure ((Hualong, Emilie and Szpunar 2008) and (Petrov, et al., 2007)). Second nearest neighbor, inclusive, kernel averaging was implemented for 0-2° of local misorientation with an angular resolution of 0.5°. Improvements in angular misorientation resolution were made by incorporating cross-correlation Kikuchi pattern analysis in effort for quantifying the geometrically necessary dislocation density. Each Kikuchi pattern, per measured point, was post-processed for obtaining lattice displacements. The theoretical details are included in Appendix B for reference.

3.2.2.3. Quantitative Metallography

3.2.2.3.1. Grain Size and Interparticle Spacing

Quantitative inter-particle spacing statistics were collected using the linear intercept method on crept and un-crept specimens utilizing grey-scale binary threshold imaging (Nikon Nis-Elements Documentation V3.22.00). A series of lines, of known, length were overlaid on a micrograph parallel to the direction of the applied stress, Figure 3- 4. SiC grain interfaces were counted for each test line within a single micrograph and compiled for each micrograph analyzed; a total micrograph area greater than >10260μm^2 were analyzed for each bending fiber. Center-to-center particle mean particle spacing, σ, was calculated from ((Underwood 1995))

$$\sigma = \frac{1}{N_L}, \tag{3-7}$$

where N_L is the number of particle intercepts per test line length. Center-to-center SiC spacing distributions were compiled for multiple positions along each bar height in effort to compare the change in SiC particle spacing with creep strain. Grain size was also measured using Equation (3-7) with each SiC particle treated as a grain boundary. However, this method tends to overestimate the grain size, and direct measurement or EBSD are more suitable methods.

Considering the direct measurement method, on a suitably etched (either chemically or thermally) ZrB_2 and SiC grain sizes were measured by inscribing a circle of diameter equivalent to the maximum ferret dimension. A minimum of 100 grains were measured from randomly selected micrographs for constructing size distributions. A comparison of all three grain size measurement methods shows no statistical difference for ZrB_2 or SiC grains.

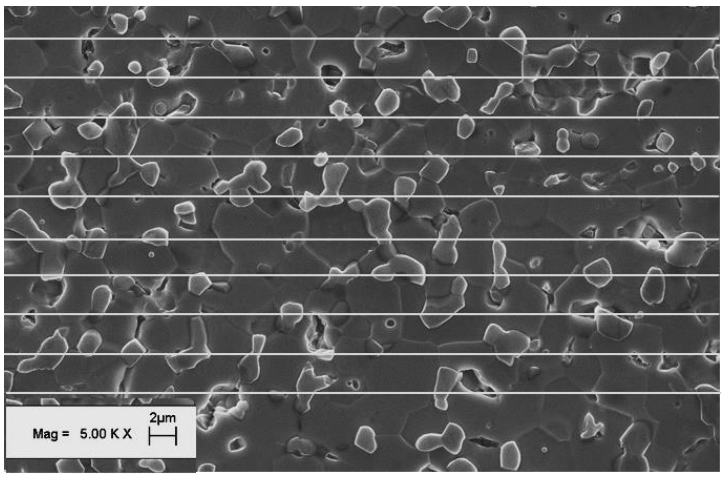

Figure 3-4: Intercept lines overlaid on polished and etched ZrB_2 grains (dark grey) and SiC grains (light grey) micrograph. Z20SB was final polished using 0.05µm SiO2 colloidal solution and etched with 1:1 H2O2:HNO3.

3.2.2.3.2. Cavitation

Creep cavitation image analysis was completed using binary threshold image analysis techniques. Specifically, cavitation analysis included cavity size, distribution and quantity information. Such an analysis requires assumptions about cavity uniformity and reported values are only unique to a designated viewing window because of the inherent strain gradient from flexure creep. Figure 3- 5 schematically details a standardized viewing window, ~50µm from specimen edge, for acquiring cavitation data for both compressive and tensile sides. These locations were chosen to adequately represent cavitation processes with respect to measured outer-fiber tensile strain. Cavity statistics including cavity diameter and area were compiled using binary thresholding image analysis **(**Nikon Nis-Elements Documentation V3.22.00) for each

crept specimen. Cavity volume fraction was calculated by the following relationship

$$\frac{\sum_{i=1}^{N} A_{C_i}}{\sum_{i=1}^{N} A_{M_i}}, \tag{3-8}$$

where $A_{C,I}$ and $A_{M,I}$ are the i-th components of the area measured for each cavity and micrograph, respectively. Equation (3-8) assumes cavity depth and a total volume element thickness of one average cavity diameter and a uniform distribution beyond the fracture face.

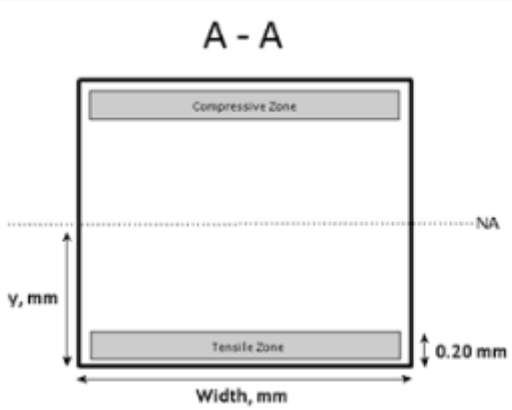

Figure 3-5: Creep bar cross-section detailing cavity analysis location for both tensile and compressive creep zones.

3.2.2.4. Optical Beam Curvatures

Optical beam curvature measurements were completed for (Nikon Nis-Elements Documentation V3.22.00) for acquiring a tensile and compressive curvature plot. Following Jakus and Wiederhorn (1988), measured beam curvatures and subsequent curvature radii were calculated based on a second order polynomial

$$y = p_1 x^2 + p_2 x + p_3, \tag{3-9}$$

where p_1, p_2 and p_3 are fitted constants by means of non-linear regression analysis. Curvature radii were calculated based on

$$\rho = \left[1 + \left(\frac{dy}{dx}\right)^3\right] / \frac{d^2y}{dx^2} \ , \tag{3-10}$$

where $\frac{dy}{dx}$ and $\frac{d^2y}{dx^2}$ are first and second derivatives of the characteristic 2nd order polynomial for both tensile (ρ_T) and compressive (ρ_C) sides, Figure 3- 6. The corresponding arc lengths were calculated based on the relationship:

$$S = \rho 2\theta \tag{3-11}$$

and

$$\theta = \sin^{-1}\left(\frac{x}{\rho}\right), \tag{3-12}$$

where S is the arc length having a curvature radius of ρ, angle of θ in radians and the half chord length x. The outer-fiber tensile and compressive strains were calculated using $\varepsilon = \left(\frac{S-L}{L}\right)$, where L is the original reference length. From Figure 3- 6 the tensile ((AB-NA)/NA) and compressive ((BC-NA)/NA) strains were calculated where the NA length is equivalent to the inner load span length. An alternative approach later implemented for neutral axis determination, calculates BC or AB arc length directly from (The MathWorks, Inc. 2009)

$$S = \int_0^{2x} \sqrt{1 + f'(x)^2}\, dx, \tag{3-13}$$

where $f'(x)$ is the first derivative of Equation (3-9) and 2x is the chord length from Figure 3- 6. Under four-point bending, the majority of strain develops within the inner span, hence, the calculated strain differs between the arc length (Equation (3-10)) and the original bar length over the inner span length. The calculated strain is within 9% of those predicted by Equations 3-9 to 3-12.

Neutral axis positions were initially estimated based on the assumption $\varepsilon = {}^{y}/_{\rho}$ for viscoelastic behavior (Finnie 1966). However, this provides a relative position as the optical

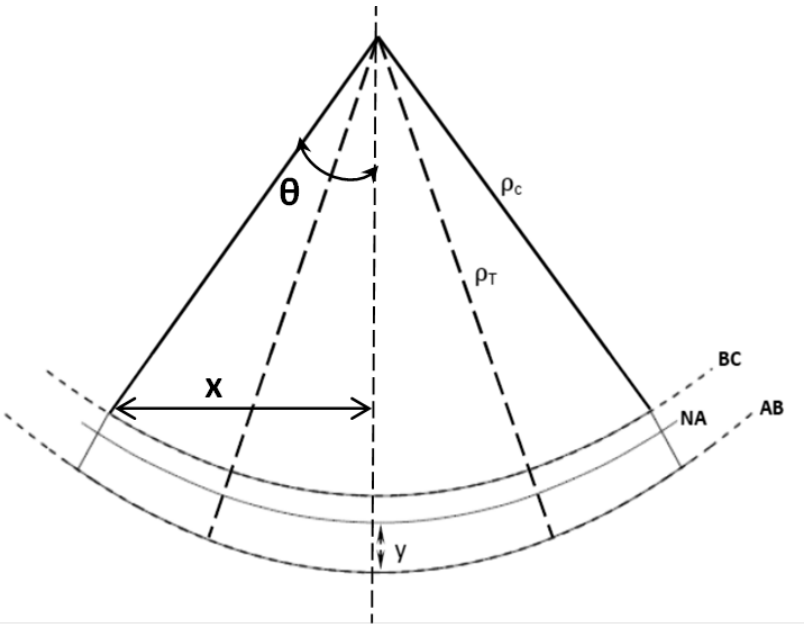

Figure 3-6: Simple beam theory model showing geometric relationships between NA, Compressive arc length (BC) and Tensile arc length (AB).

beam curvatures have a random error of 5% from measurement. An objective approach includes a modification to Figure 3- 6 where the beam is divided in equal sections along the outer-compressive fiber and the neutral axis. If the compressive side curvature (ρ_C) and arc-length (BC) are known than the following describes the neutral axis position

$$y = \rho_C \left(\frac{S_C}{l} - 1\right), \tag{3-14}$$

where the neutral axis is positioned, y, from the compressive edge and the outer-fiber compressive arc length, S_c, equivalent to BC in Figure 3- 6 and l is the initial bar length equivalent to NA. The neutral axis position, from the tensile outer-fiber, is then 1-y.

3.2.2.5. Indentation Deformation Mapping

Local creep deformation events were mapped using a line of nano-indentations positioned within a maximum of 250µm from the bending outer-fibers. A minimum of 100 indentations, of 200 nm depth and 1.50µm spacing using a cube-corner diamond tip indenter, were placed using the MTS Nano Indenter XP (MTS, Eden Prairie, MN) using Testworks4 control

software under displacement control CSM mode. The indentation array, aligned parallel to the bending stress axis served as markers for mapping deformation. Cracking, from indentation, was not observed in penetration depths ≤ 200 nm for this composite. The indentation array was imaged before and after creep using either secondary (Figure 3- 7a) or backscatter electron SEM detectors and high resolution backscatter electron SEM detector, respectively. Four classes of measurements were made, with aid the of binary threshold image analysis, in the crept and un-crept conditions, for determining indentation position and hence local strain calculations: The total strain distribution, grain deformation strains, grain rotation strains, and grain translation strains. The total strain distribution was measured by assessing the horizontal displacement change between each indentation in the crept and un-crept condition, Figure 3- 7a. The grain deformation strains were calculated based on the indentation displacement change, for a single grain while grain translations were calculated from indentation displacement changes between two grains, Figure 3- 7b. Grain rotations were measured from two construction lines intersecting the indent average center positions, Figure 3- 7c, for indentations within the same grain. The angle between the construction line and the micrograph horizontal was recorded and the corresponding displacement changes from the angular rotation used for the strain calculation.

3.3. Mechanical Properties

Room temperature mechanical properties were assessed for all composites and monoliths using 4-pt and 3-pt bending fixtures under displacement controlled. Modulus of Rupture (MOR) and K_{IC} Single Edge Notched Beam (SENB) experiments were conducted using screw driven Instron (Instron, Norwood, MA) loading frames controlled by Merlin II software (Instron (1996)). Load application rods and bending fixtures are made of α-SiC (Hexoloy-St. Gobain Ceramics, Niagra Falls, NY). MOR experiments use a combination of 4-pt and 3-pt

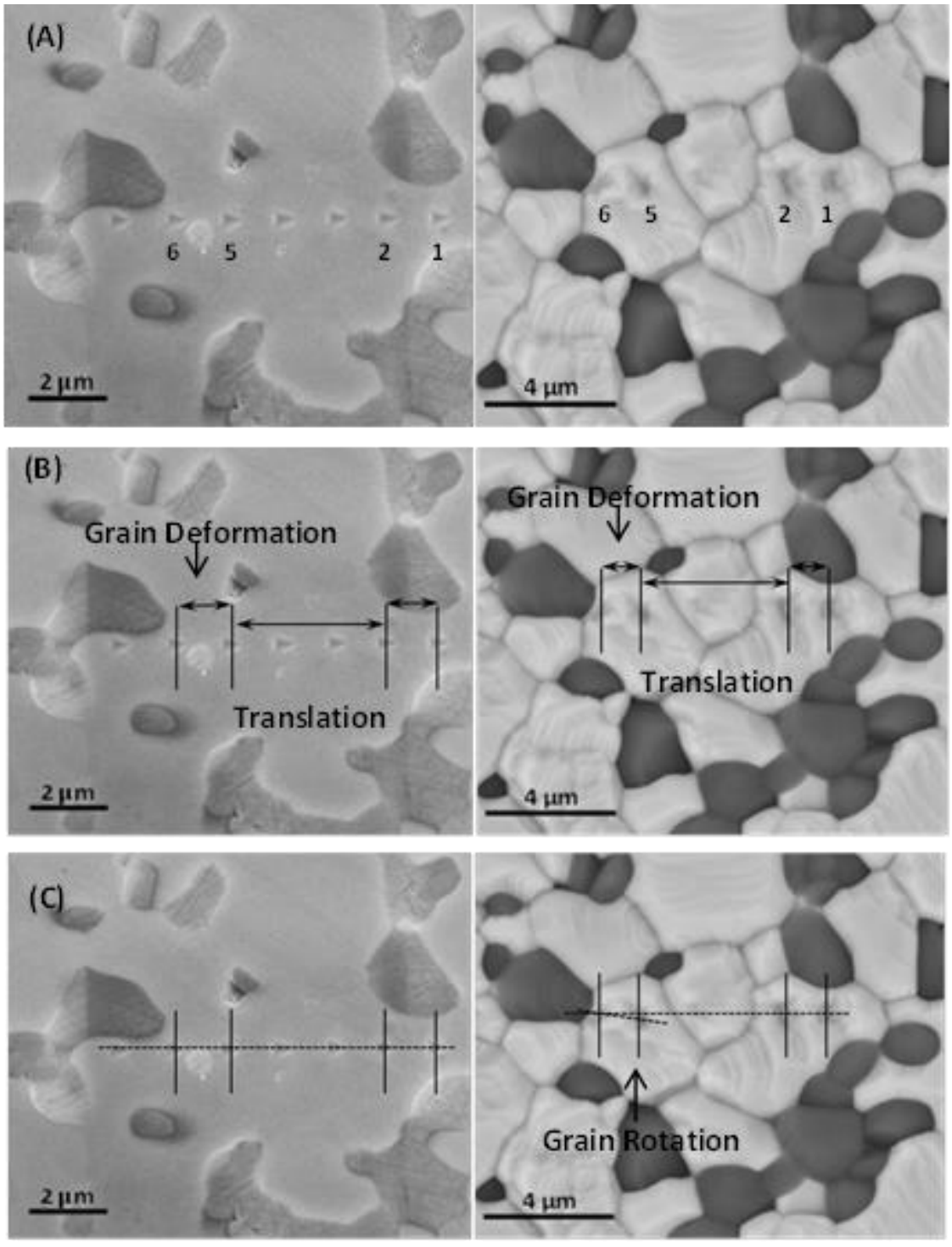

Figure 3-7: Un-crept state (left) and crept state (right). Vertical dotted and solid lines are indent shape boundaries based on threshold imaging and the average indent shape position, respectively.

bending with inner and outer spans of 20/40 mm and 40 mm, respectively; SENB experiments used 10/20 mm 4-pt bending and 20 mm 3-pt. bending fixtures. Fracture stresses were calculated using linear elastic beam theory equations of the form

$$\sigma_{fracture} = \frac{3}{2}\frac{PL_o}{BH^2}, \tag{3-15}$$

for three point bending, and four point bending,

$$\sigma_{fracture} = \frac{3P(L_o - L_i)}{2BH^2}, \tag{3-16}$$

under an the maximum load, P, for a bar of width B and height H over an outer span of length L_o (3-pt.) or the difference between the inner and outer load span, L_o-L_i (4-pt.). Experiments were conducted at cross-head displacement rates of 0.10 -0.15 mm/min. Fracture toughness, K_{IC}, was calculated according to (Anderson 2005)

$$K_{IC} = \frac{3}{2}\frac{PL_o}{BH^{3/2}}\left(\frac{a}{H}\right)^{0.5} * f\left(\frac{a}{H}\right) \tag{3-17}$$

and

$$f\left(\frac{a}{H}\right) = \frac{1.99 - \frac{a}{H}\left(1-\frac{a}{H}\right)\left[2.15 - 3.93\frac{a}{H} + 2.7\left(\frac{a}{H}\right)^2\right]}{\left(1+2\frac{a}{H}\right)\left(1-\frac{a}{H}\right)^{1.5}}, \tag{3-18}$$

where a/H = 0.2-0.3 for a crack length a and P, L_o, H and B hold the usual significance for three-point bending. Considering four-point bending the fracture toughness is represented by (Gogotsi 2004)

$$K_{IC} = \frac{3}{2}\frac{P(L_o - L_i)}{BH^{3/2}}\left[\frac{3\left(\frac{a}{H}\right)^{0.5}}{2\left(1-\frac{a}{H}\right)^{0.5}}\right] * f\left(\frac{a}{H}\right) \tag{3-19}$$

and

$$f\left(\frac{a}{H}\right) = 1.9887 - 1.326\frac{a}{H} - \frac{\frac{a}{H}\left(1-\frac{a}{H}\right)\left[3.49 - 0.68\frac{a}{H} + 1.35\left(\frac{a}{H}\right)^2\right]}{\left(1+\frac{a}{H}\right)^2}, \tag{3-20}$$

where a/H = 0.4-0.6 for a crack length a. SENB experiments were completed using cross-head displacement rates of $1x10^{-4}$ – 5 x 10^{-4} mm/min. Starting notches were cut using a 0.4 mm thick diamond wafering blade and then sharpened using 1µm diamond paste and a razor blade yielding a starting notch radius of 0.070 +/- 0.02 mm. Crack lengths were measured post mortem, using stereomicroscope and image analysis software (Nikon Nis-Elements Documentation V3.22.00)**,** taking the average and standard deviation of 10 measurements spaced evenly across the fracture face.

Hardness and Elastic modulus were measured using a Nano Indenter XP (Nano Instruments, Inc. Oak Ridge, TN USA) and Testworks4 version 4.06A control software under displacement control CSM mode. Additionally, Elastic modulus was also measured using the Resonant Ultrasound Spectroscopy (RUS) method at Oak Ridge National Labs (Oak Ridge, TN USA). Moduli measurements were conducted on 240 grit ground composite tiles of dimensions 15 x 15 x 4 mm, +/-0.02 mm on each dimension, rectangular parallelepipeds. This shape was chosen for simplifying the relationship between the resonance frequencies and the modulus tensor through Lagrangian minimization techniques (Migliori and Maynard 2005). Nano-indentation mechanical properties were measured using a Berkovich indenter tip for applying uniform indent loads, to sufficient depths, without cracking for hardness and elastic modulus measurement. Each specimen was ground and polished using the procedures outlined in section 3.2.2.1. Using a diamond scribe, cross-marks were placed onto the polished surface for indentation position referencing. Indentation arrays of 2 x 25 or 2 x 15 were used with indentation spacing of 5 µm in both vertical and horizontal directions sufficiently away from the neighboring indentation. The indentation loading experimental parameters are summarized in Table 3- 3. Elastic modulus was calculated based on the relationship ((Oliver and Pharr 2004)

Table 3- 3: Nano-indentation experimental parameters.

Parameter	Value
Load	1.5 gf
# Load/Unload Cycles	5
Unload %	90%
Surface approach distance	1000 nm
Surface approach velocity	10 nm/s
Surface approach sensitivity	25%
Peak load holding time	30 sec
Drift rate	0.05 nm/s
Surface find, ΔX and d ΔY	-50 µm

$$\frac{1}{E_r} = \frac{(1-\nu^2)}{E} + \frac{(1-\nu^2{}_i)}{E_i} \tag{3-21}$$

and

$$\frac{dP}{dh} = \frac{2}{\sqrt{\pi}} E_r \sqrt{A}, \tag{3-22}$$

where a reduced modulus, E_r, is calculated from the unloading slope , $\frac{dP}{dh}$, at the maximum load and displacement and the projected area of elastic contact A. Finally, the Young's modulus, E, can be determined with knowledge of the material Poisson's ratio, ν, and the indenter Elastic modulus and Poisson's ratio E_i and ν_i, respectively. Hardness is measured from the maximum load, P_{max}, and the projected indentation area following

$$H = \frac{P_{max}}{A}, \tag{3-23}$$

with the projected area as a function of the indenter depth under load, $A = f(h)$.

Both hardness and moduli are reported for the same load displacement curve, unique to the individual indentation. For polycrystalline monoliths and composites there exists a high probability of an indentation falling on a second phase, grain boundary or other defect rather than the grain proper of the phase of interest. Therefore, a selection criterion was implemented combining load-displacement data review, optical microscopy and statistical methods for

filtering indentations that are assumed as outliers. Metallographic inspection of the indent array allows for numbering and filtering out indents that do not fall within the phase of interest. Additionally, any indents on or within 0.5 um of a grain boundary were thrown out as they do not represent the grain interior and any indent in contact with a preexisting defect were also discarded. Subsequent inspection of each load-displacement curve for irregularities was completed for each selected indent. For polycrystalline materials, there exists preexisting defects that might reside below the plane of polish and, therefore, require inspection of the load displacement curves for insights to the indentation depth behavior. For example, Figure 3-8, represents a load and unloading curve for an indent centered within a grain contrasting with the same pair plots for an indent centered over a preexisting defect. Any remaining indentations, which have passed both metallographic and load-displacement inspection, and appear as outliers are further filtered using Chauvenet criteria for data selection based on the distribution and sample population (Chauvenet 1868). An acceptable scatter, about the mean, can be determined based on the probability of rejection form normal probabilities based on the relationship

$$\tau_{max} = \frac{d_{max}}{S_x}, \tag{3-24}$$

where τ_{max} is a nondimensional maximum deviation, S_x a precision index and d_{max} the maximum deviation from the mean. Based on this statistical filtering, all remaining outliers, with no apparent explanation, can be discarded leaving only those which approach the true ZrB_2 grain hardness.

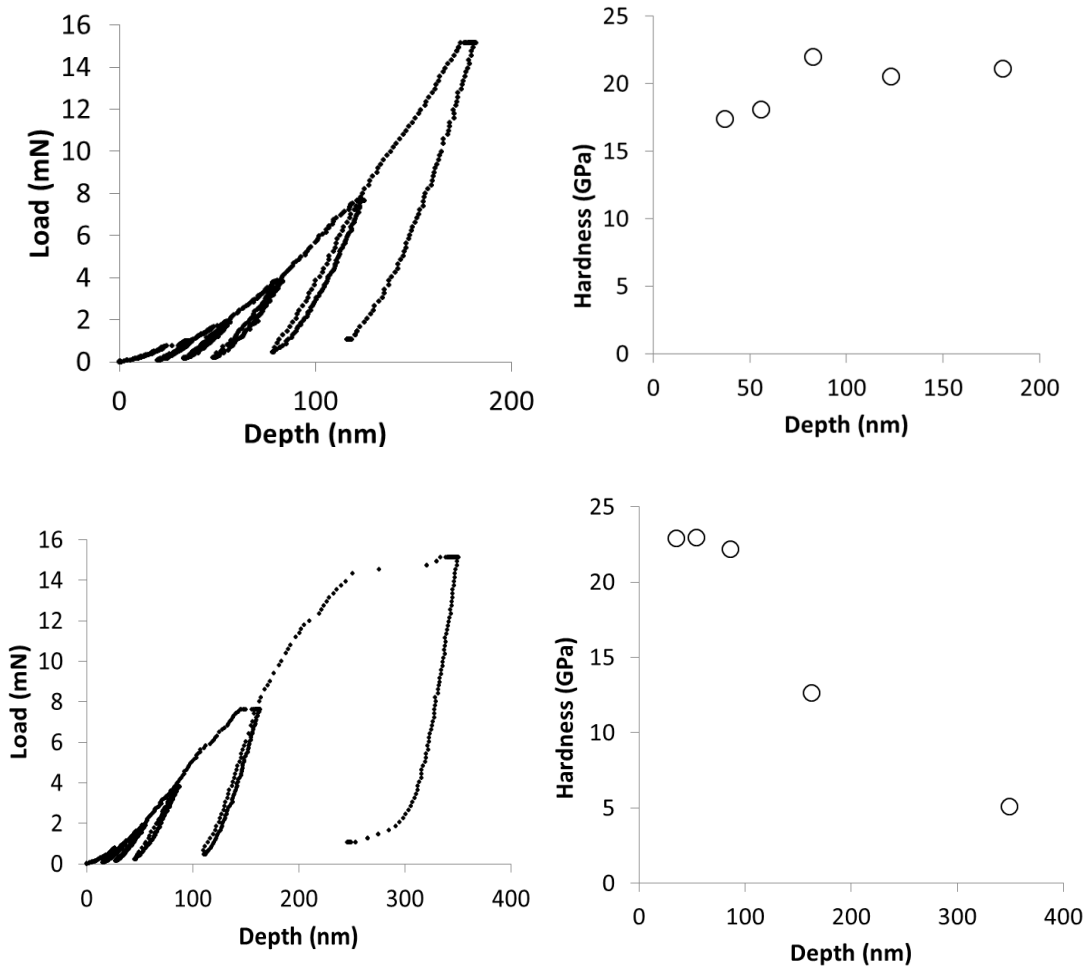

Figure 3-8: Nano-indentation load-displacement (top) and indentation collapse due to the presence of a pore (bottom). The hardness-depth calculations (right) indicate collapse contrasting with the observed hardness plateau.

3.4. Creep Experiments

3.4.1. Constant Displacement and Load

Protective environment creep experiments were conducted for measuring and assessing creep deformation based on the Norton constants from Equation (2-14). A flowing argon apparatus was essential for reducing excessive oxidation which was found to consume >1/3 the area of base material (Aune 2011). Creep testing used α-SiC 20/40 mm and 10/20 mm four-point bend fixtures in a vertical, clamshell furnace (DT-33-55, Deltech, Inc., Denver, CO)

equipped with Super Kanthal (Kanthal, Inc.) molydisilicide elements capable of reaching 1800°C. Protected atmosphere was achieved by flowing 99.999% Argon through an internal enclosure, containing the sample and fixtures, made from a ~7" long alumina tube with ~12" long porous (90%) alumina refractory plugs on each end. A dead weight load applicator equipped with water cooled junctions was implemented with appropriate weights, guided by linear bearings, to apply creep loads, Figure 3- 9.

For the case of constant displacement, the linear bearing dead load alignment fixtures were replaced with a load cell. Under constant displacement conditions, cross-head displacement rate and load were measured as a function of time using a custom LabView VI. For all creep testing conditions the specimen (nominal 4 x 4 x 45 mm and 3 x 3 x 25 mm bars) outer-fiber displacement was captured, within 1-2 μm, using a video extensometer (Messphysik, Austria) coupled with a custom built spring-loaded linear displacement dashpot and SiC extension probe rod contacting the tensile midpoint of each bar, Figure 3- 10. The dashpot-extensometer assembly was calibrated using a 5500 Instron load frame with Merlin software monitoring the cross head displacement (Aune 2011), Figure 3- 11.

Preliminary outer-fiber creep strains were calculated following linear elastic beam assumptions (Talmy, Zaykoski and Martin 2008)

$$\varepsilon = \left[\frac{12h}{\left(3L_o^2 - 4a^2\right)}\right]\delta, \tag{3-25}$$

where h is beam height, δ is outer-fiber displacement, L_o= outer span and a = distance between outer and inner span. Strain rate was calculated taking the point-slope of each strain-time creep curve. Direct differentiation of Equation (3-25) was also used as the beam and fixture dimensions are independent of time. Norton stress exponents were calculated based on the preliminary data analysis curve fit followed by further refinement of the strain rate.

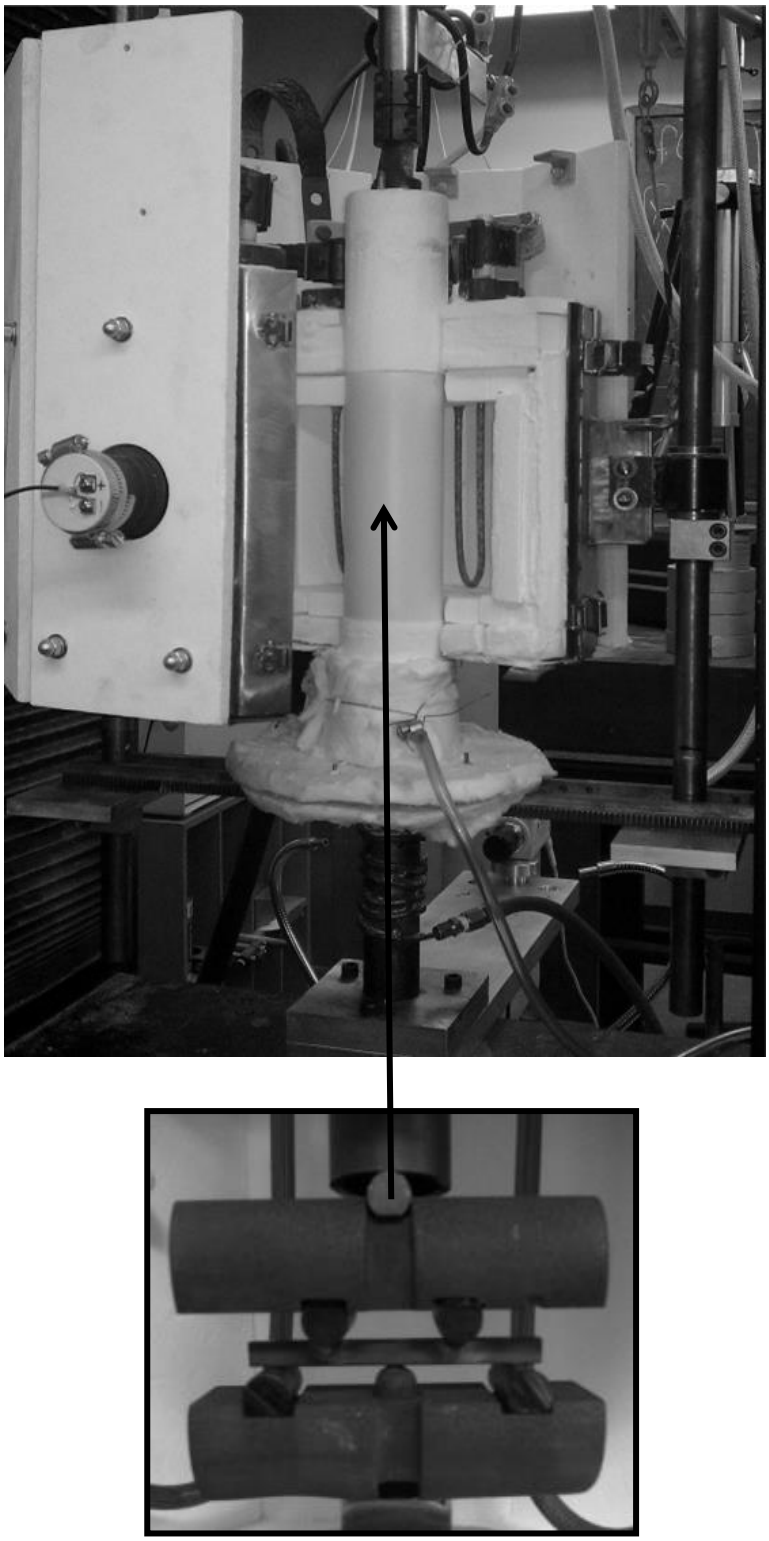

Figure 3-9: Protective creep setup showing flowing capsule arrangement and the four point bending fixture, sample and deflectometer (white arrow).

Hollenberg, et al., (1971) proposed a modified bending outer-fiber strain function including viscoplastic assumptions in the form of

$$\varepsilon_{max} = \frac{2h(n+2)}{(L-a)[L+a(n+1)]} y. \quad (3\text{-}26)$$

The strain is dependent on the beam, h , the Norton stress exponent, n, the distance between the outer and inner loading points, a, L the outer span and y the deflection. The time derivative of Equation (3-26) provides the strain rate as a function of displacement rate. In the limit n= 1 Equation (3-26) is 20% greater than the elastic format used in Bird, et al., (2013) and Talmy, et al., (2008). This theory still carries the assumption creep in compression and tension is identical, however, Equation (3-26) offers a better approximation of the true bending strain rate.

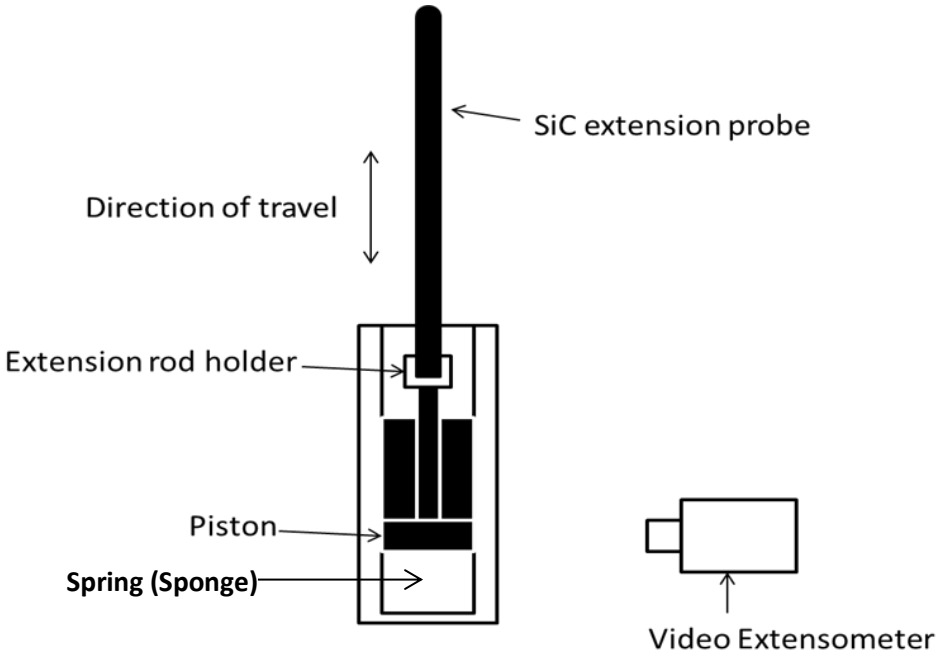

Figure 3-10: Extensometer-deflectometer setup.

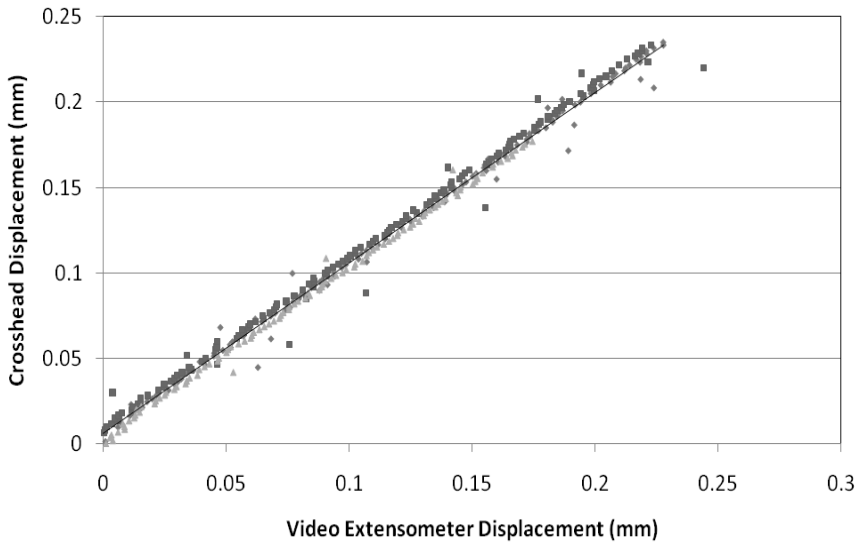

Figure 3-11: Extensometer assembly calibration curve taken from Aune (2011).

3.4.2. Vacuum-Inert Environment

Vacuum-inert environment experiments were conducted for preserving specimen surfaces as a means to map the deformation events. However, direct specimen displacement measurements are difficult for this setup and no attempt was made to iteratively measure displacement and hence no traditional creep curves were constructed. All macro and microscopic strain measurements were conducted on un-crept and as-crept specimens at room temperature. Dead load creep testing used α-SiC 10/20 mm four-point bend fixtures with 6.35 mm diameter α-SiC rollers in a graphite lined resistance vacuum furnace (Centorr Vacuum Industries, Nashua, NH) equipped with graphite heating elements and a Trivac vacuum pump capable of temperatures and pressures of 2150°C and 2 mTorr, respectively, Figure 3- 12**.** Inert atmosphere was achieved by back filling 99.999% Argon through a pressure manifold to an overpressure of < 3 psig after the vacuum pressure fell below 30 mtorr. The dead load application was achieved by placing a drawn Tantalum cup (MTI, Albany, OR USA) filled with Tungsten metal chips on a graphite pedestal directly over the inner-span bending fixture. For

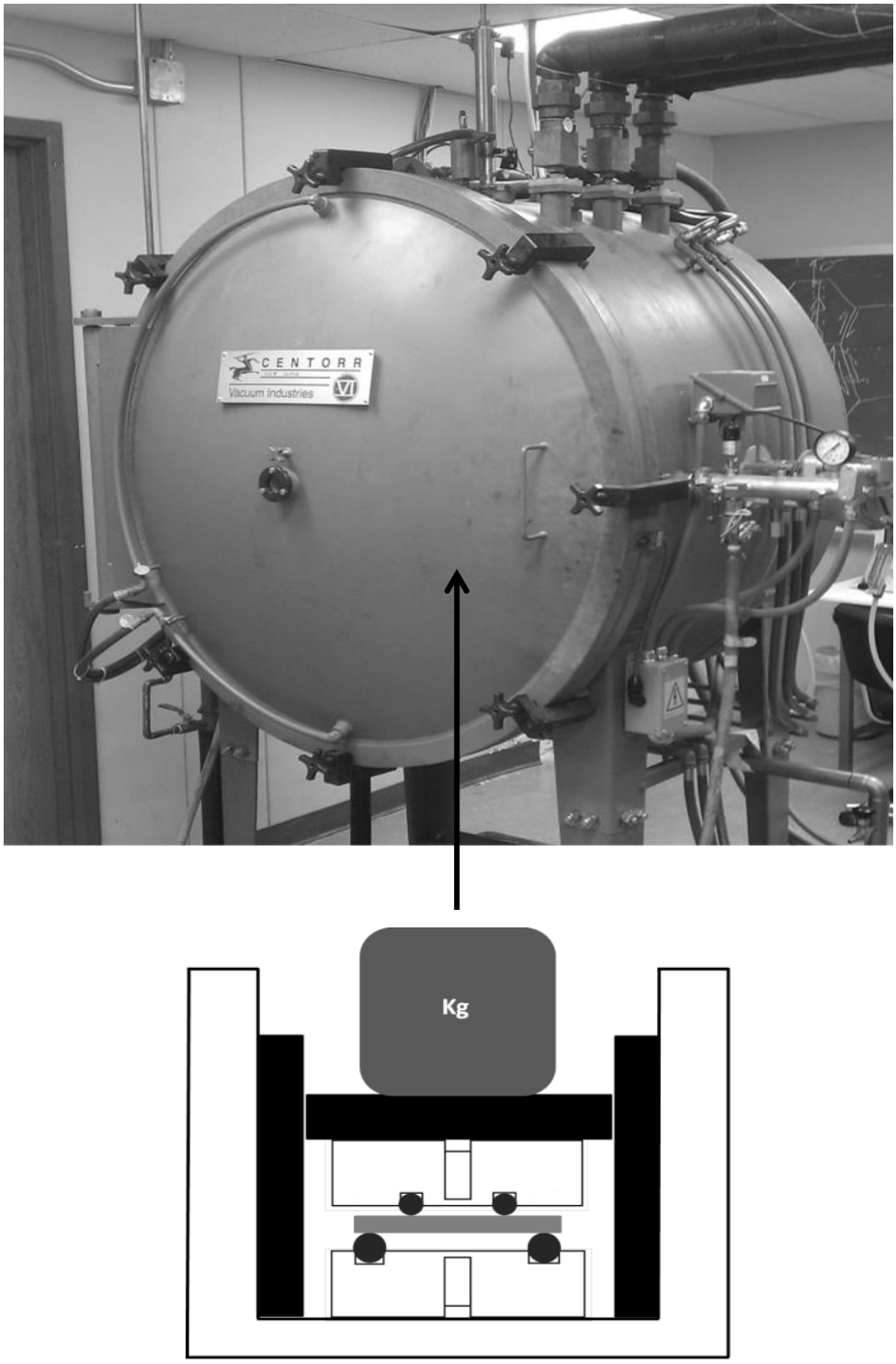

Figure 3-12: Loading assembly fixture and vacuum furnace setup for dead load creep experiments. Graphite load plate and support posts are shown in black.

stresses > 20MPa a 12” long 3” diameter SiC tube was placed in a 3.25” ID graphite cup and filled with tungsten chips. A distributed load was transmitted to the bending fixture pins and the specimen (nominal 1.75 x 3.5 x 25 mm) and the assembly was stabilized by two graphite posts with sufficient clearance to avoid binding, Figure 3- 12. Creep experiments were carried out at 1800°C and applied stresses of 13-40 MPa for 5-10 hr holding times.

Chapter 4

Processing and Room Temperature Mechanical Behavior

This chapter discusses the experimental program for understanding the microstructure evolution and room temperature structure property relationships ZrB_2 based SiC composites and ZrB_2-WC solid solution alloys. Hot-pressed composites and alloys had near 100% relative density confirmed by metallography. The solid solution alloys showed a monotonic decreasing lattice parameter for 1.4-4.2 mol% W concentrations. The interplay between WC dissolution and WB phase formation are discussed showing the possible effect of excess carbon on reaction equilibria and effects of starting particle size on reaction kinetics. Structure property relationships were developed using linear elastic fracture theory correlating maximum microstructure defect size with experimental K_{IC} and MOR results. Process zone crack deflection from crack interaction with reinforcement particles appear as the dominant composite fracture toughening mechanism along a primarily transgranular matrix fracture path. Alloy modifications showed increasing intergranular fracture raising the possibility of wake zone crack face interactions, such as grain bridging. Non-cubic crystallographic anisotropy is discussed in the context of residual stress development for improved fracture toughness and crystal plasticity.

4.1. Results

4.1.1. Microstructure and Densification

Measured densities and microstructures varied based on composite/monolithic composition, milling procedure and hot pressing conditions. Table 4- 1 summarizes the theoretical and measured densities for each material. For each material, with exception to the

ZCWC alloy, showed a relative density less than 100% suggesting a maximum of ~1.5% porosity may exist in these compacts. For those alloy with relative densities >100% suggests possible deviations from the nominal compositions, assuming a fully dense compact. Furthermore, the hot-pressing procedures implemented were adequate in producing near fully dense compacts.

Table 4- 1: As-Received ZrB_2 based ceramic alloys and composite density comparison

Material	Measured (g/cc)	Theoretical (g/cc)	Relative (%)
Z20SB	5.52+/0.01	5.5	99.8
Z20S	5.52+/-0.02	5.6	98.6
ZCWC	6.44 +/-0.04	6.42	100.3
ZWC1	6.52+/-0.09	6.62	98.5
ZWC2	6.29+/-0.02	6.34	99.3
ZWC3	6.57 +/-0.04	6.57	99.9

The grain size was measured for each material for assessing matrix effects on room temperature strength and creep properties, Table 4- 2. As-received microstructures were observed to contain several additional phases beyond the nominal compositions. The Z20SB and Z20S composites looked similar and the SiC was well distributed, Figure 4- 1. The primary difference between these composites was the existence of a large bulky phase present only in the Z20SB.

Table 4- 2: ZrB_2 based monolithic alloy and composite grain sizes for matrix (ZrB_2) and reinforcement (SiC) phase. Errors are grain size distribution standard deviations

Material	ZrB_2 (µm)	SiC (µm)
Z20SB	3.1 +/- 0.9	1.5 +/- 0.5
Z20S	3.8 +/- 1.1	2.2 +/- 0.6
ZCWC	4.1 +/- 0.6	----
ZWC1	3.5 +/-0.5	----
ZWC2	3.0 +/- 0.4	----
ZWC3	4.6 +/- 0.7	----
ZWC3HT	5.6 +/- 1.0	----

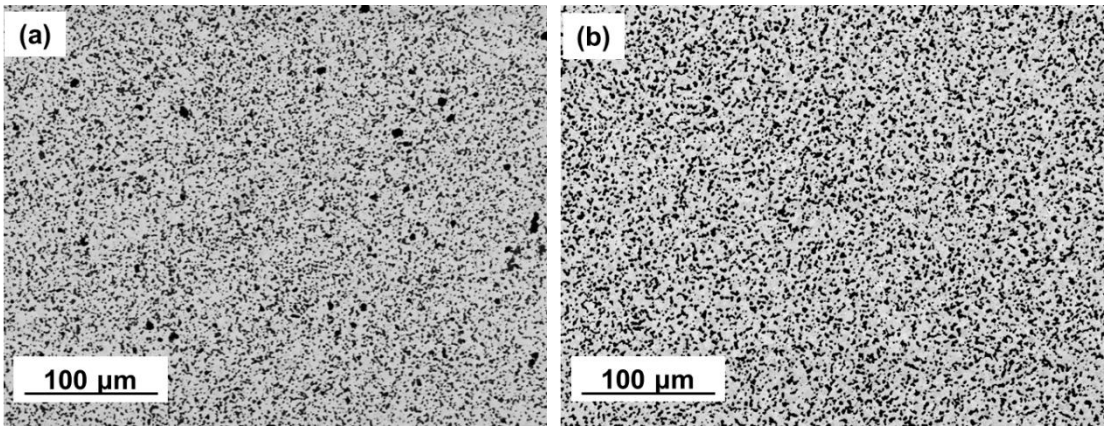

Figure 4-1: Backscatter Electron SEM micrographs for the Z20SB (a) and Z20S (b) composites. The large black inclusions are phases other than SiC (grey) and ZrB_2 (Light).

Electron probe analysis was conducted for quantitatively assessing the chemistry of the bulky phase present in the Z20SB composite, Figure 4- 2 and Table 4- 3. Two chemistries were measured for the bulky phase with one containing a carbon deficient boron carbide phase (black) and the second a Si-rich carbide phase (dark-grey). The remaining smaller particles and matrix were confirmed as SiC and ZrB_2, respectively. XRD was completed, for the Z20SB composite, and ZrB_2 and SiC primary peaks are indexed, Figure 4- 3.

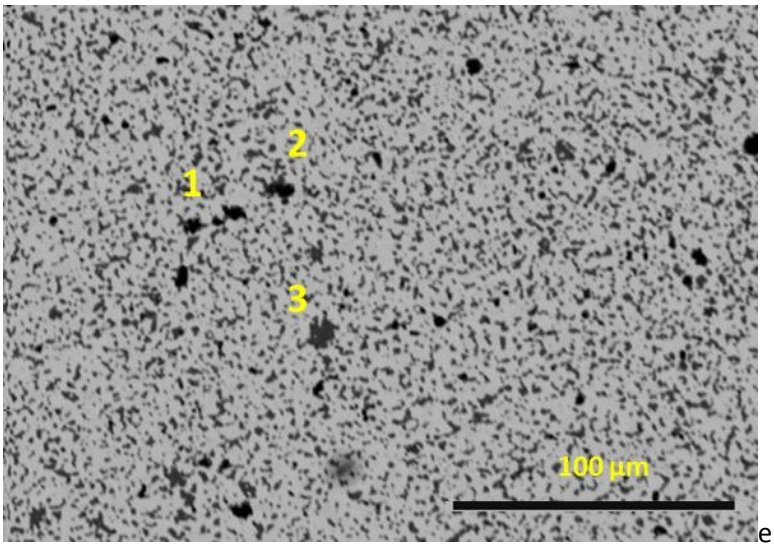

e

Figure 4-2: Electron back scatter micrograph of ZSB composite.

Table 4- 3: : ZSB composite phase analysis via electron probe (WDS).

Element at%	Zr	Si	B	C
1	0.14	3.35	89.76	6.75
2	0.11	0.50	92.49	6.91
3	0.24	71.24	0.00	28.52

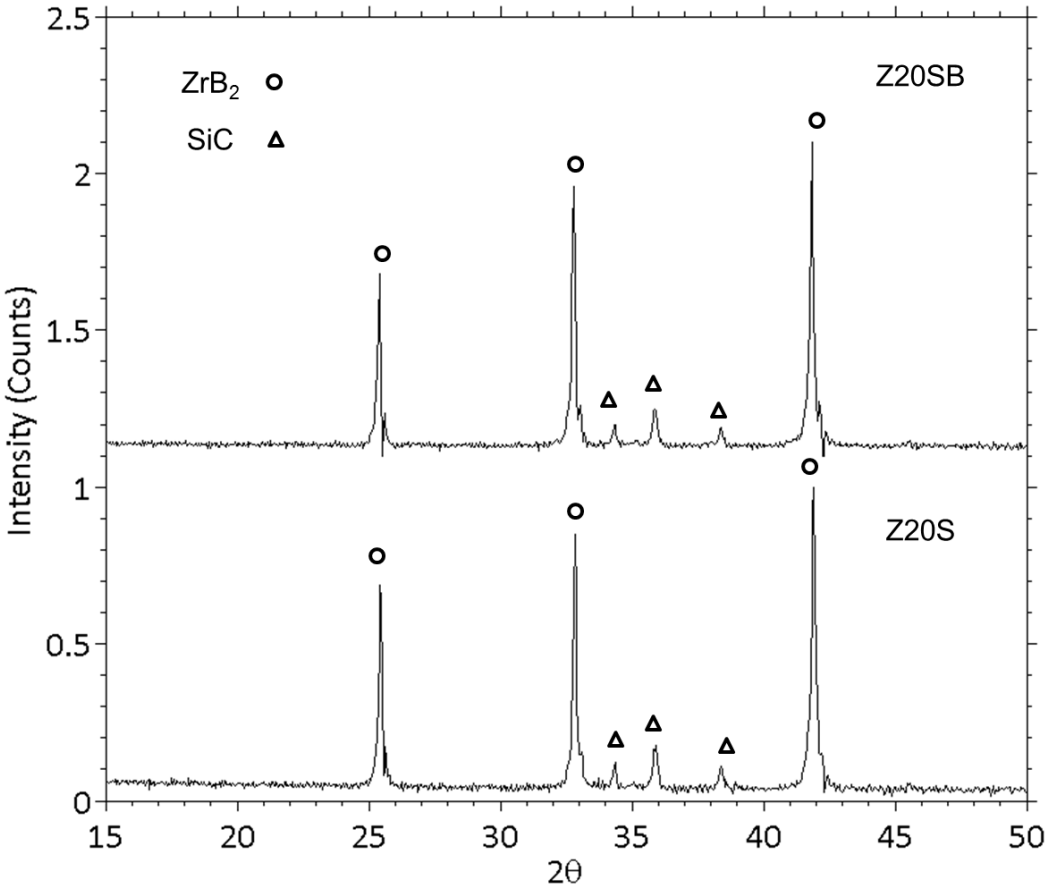

Figure 4-3: XRD patterns for the Z20SB and Z20S microstructures.

The boron-carbide and Si-rich carbide phase reflections were not observed as a result of low concentrations. W concentrations of 0.40 mol% were measured using EDS and XPS techniques for both SiC containing composites.

The WC –containing alloys showed markedly different phase distributions despite the relatively simple nominal composition, Figure 4- 4. Using a combined analysis including XRD and EDS experiments, the phase character was assessed. A summary of the phases found in each microstructure and the relative composition is given in Table 4- 4; select phases were common amongst the different alloys.

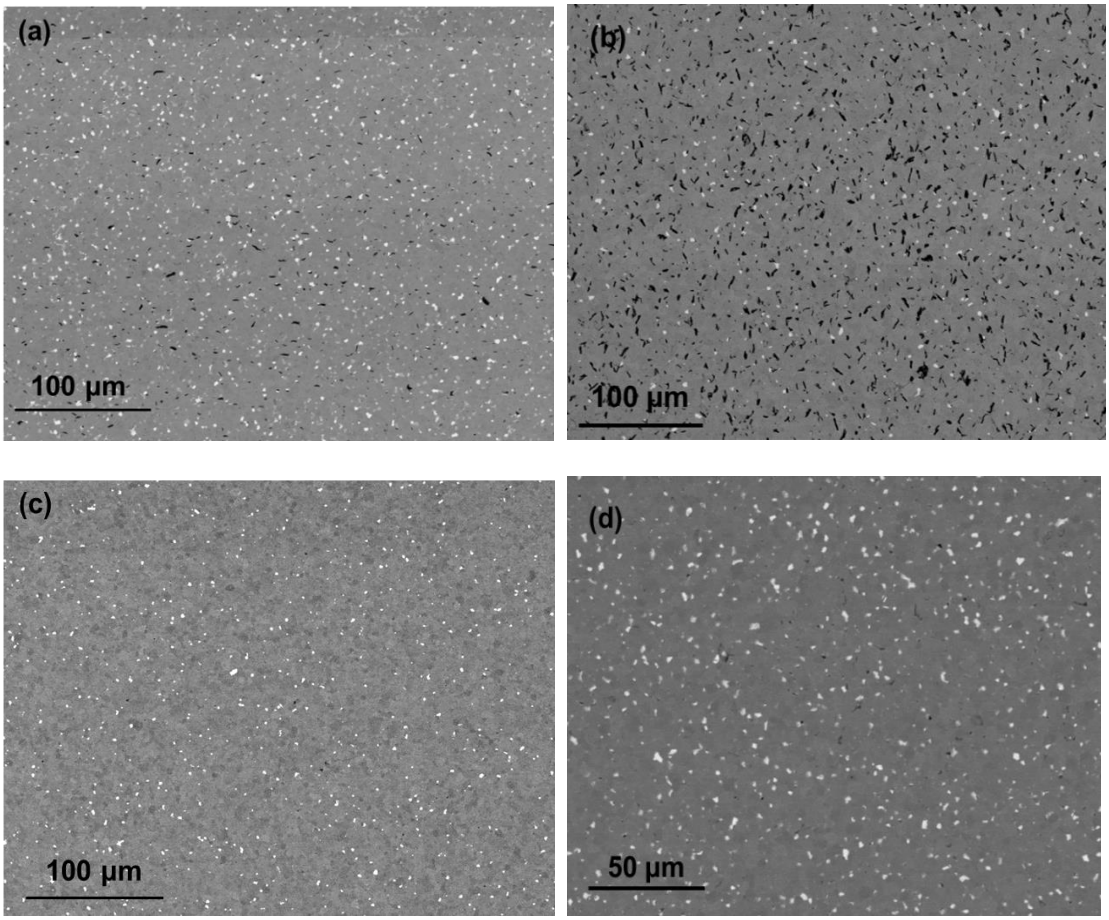

Figure 4-4: Backscatter Electron SEM micrographs for the ZCWC (a), ZWC1 (b), ZWC2 (c) and ZWC3 (d) alloys.

Table 4- 4: EDS average phase compositions observed with corresponding material designations.

	Mol% (% Error)								
Compound	**B**	**C**	**N**	**O**	**W**	**Zr**	**Hf**	**Co**	**Alloy**
ZrB2	73 (7)	6 (37)	2 (66)	1 (25)	0.3 (14)	16 (10)	1 (62)	0	All
ZrO_2	22 (15)	7 (36)	4 (40)	46 (11)	0.1 (28)	20 (2)	0.5 (12)	0	ZWC1, ZWC2
WB	44 (19)	15 (19)	0.5 (42)	6 (16)	33 (7)	0.8 (74)	0.08 (62)	0.4 (35)	ZCWCAR, ZWC1, ZWC2 ,ZWC3AR,ZWC3HT
WB_2	59 (15)	8 (35)	0.6 (100)	5 (31)	19 (3)	7 (12)	0.32 (66)	0.5 (22)	ZWC2, ZWC3AR, ZWC3HT
P $(Zr\text{-}W\text{-}C\text{-}B)_{ss}$	26 (14)	42 (14)	0.04 (100)	0.6 (20)	4 (15)	27 (10)	0.1 (58)	0	ZCWCAR, ZWC3AR, ZWC3HT
S $(Zr,W,C,B)_{ss}$	21 (14)	43 (14)	0	3 (20)	8 (4)	23 (5)	0.8 (59)	0	ZCWCHT
B-C-N	16 (12)	68 (8)	14 (42)	0.8 (75)	0.05 (100)	0.5 (72)	0	0	ZCWC
C-rich	7 (14)	74 (10)	0	14 (12)	0.04 (36)	5 (3)	0.1 (15)	0	ZCWCAR, ZWC1
BN	43 (9)	3 (34)	47 (11)	2 (17)	0.3 (20)	4 (13)	0.2 (60)	0	ZCWCAR, ZWC2

P = Primary, S = Secondary

All compositions are nominal

Subsequent XRD experiments on the select alloys provided the necessary crystal phase information. XRD spectrums were indexed for the as-sintered (AS) ZWC1, ZWC3 and ZCWC alloys and the crystal phase results are shown with the corresponding spectrums, Figure 4- 5. Coupling the two analytical experiments allows for the phase identification and spatial distribution. There exist two primary phases, in each alloy, of ZrB_2 and WB and, for the ball milled alloys, an unknown solid solution phase. A closer look at a representative micrograph shows each of these phases which are not readily apparent from the low magnification images, Figure 4- 6.

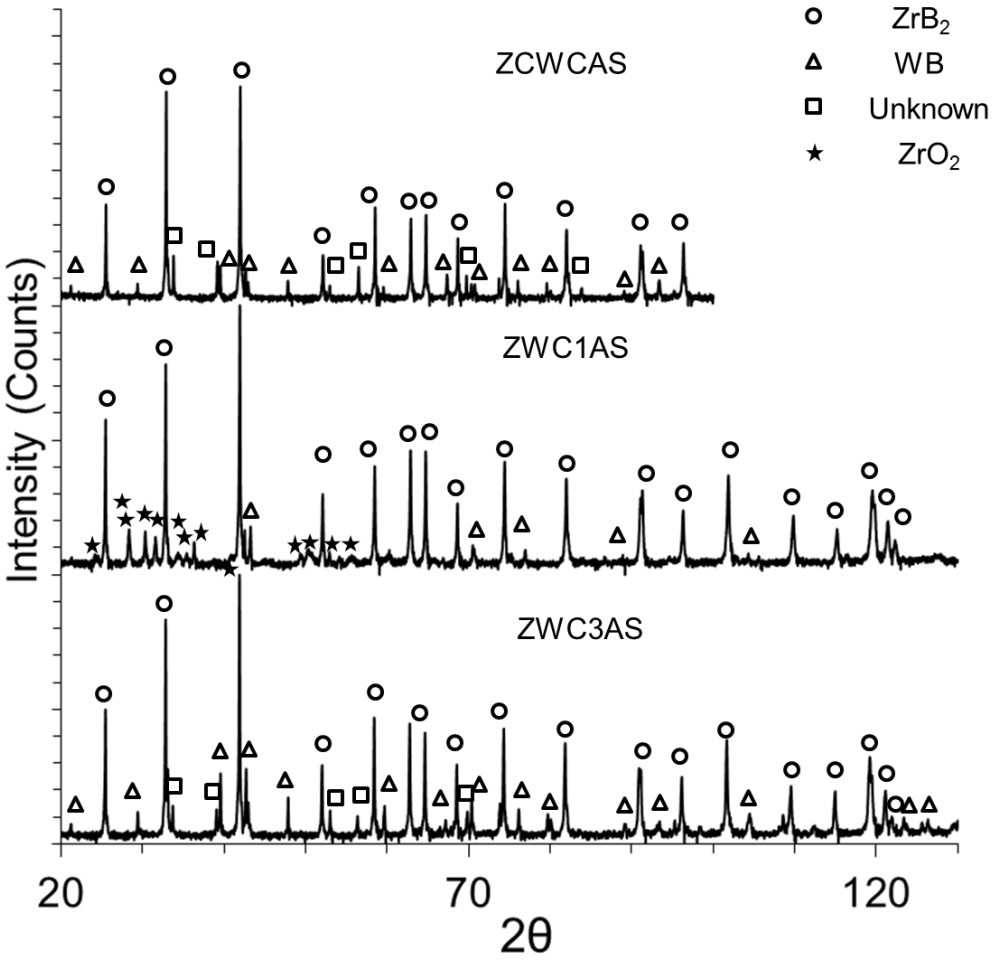

Figure 4-5: XRD patterns for the as sintered ZCWC, ZWC1 and ZWC3 alloys.

For the ZWC1 and ZWC2 alloys, ZrO_2 was indexed as a phase constituent which was included as an impurity from powder processing. From Figure 4- 4 it is difficult to see any additional phases, beyond those common to all alloys, due to the varying contrast of the ZrB_2 grain structure. EDS mapping of a high magnification ZWC1 region reveals O-rich regions depleted of B corresponding to the ZrO_2 particles in a matrix of ZrB_2, Figure 4- 7.
Using the secondary electron detector the ZrO_2 phase is readily observed protruding from the surface as a result of the colloidal SiO_2 polishing, Figure 4- 8. Between the two ZWC1 and ZWC2 alloys, the amount of ZrO_2 decreases in volume fraction from 0.23 to 0.09, respectively. Additionally, the carbon-rich phase quantity is negligible for the ZWC2 composite contrasting with the 5.43 vol% measured for the ZWC1 composite. The ZCWC alloy had a residual amount of 1.39 vol% carbon phase after pyrolysis and sintering.

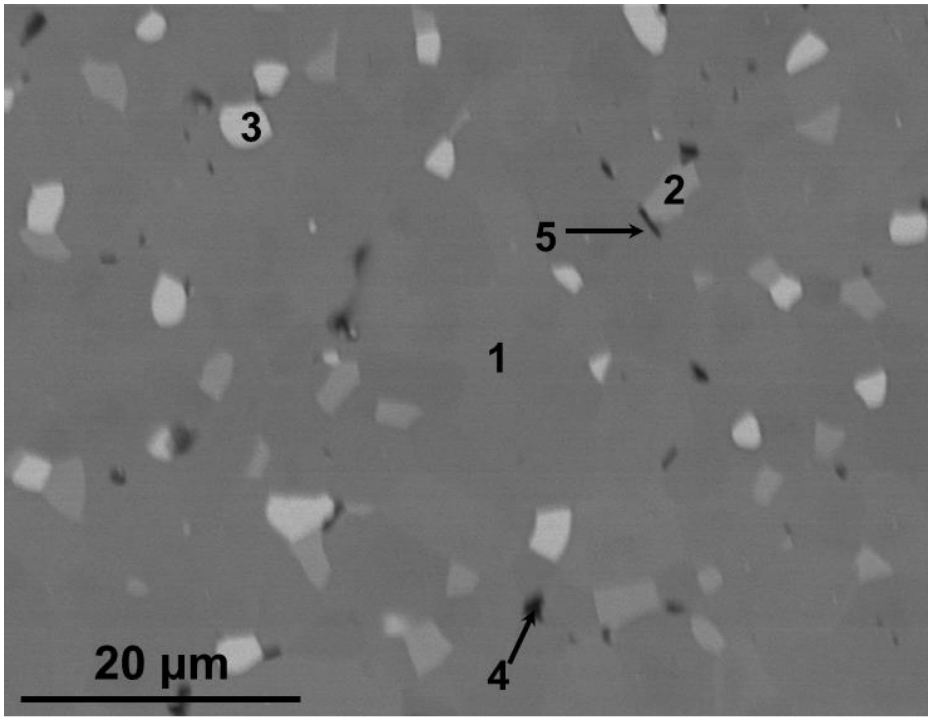

Figure 4-6: High magnification image of the ZCWC alloy detailing the ZrB_2 (1), WB (2), Unknown (3), B-N-C (4) and C-rich (5) phase.

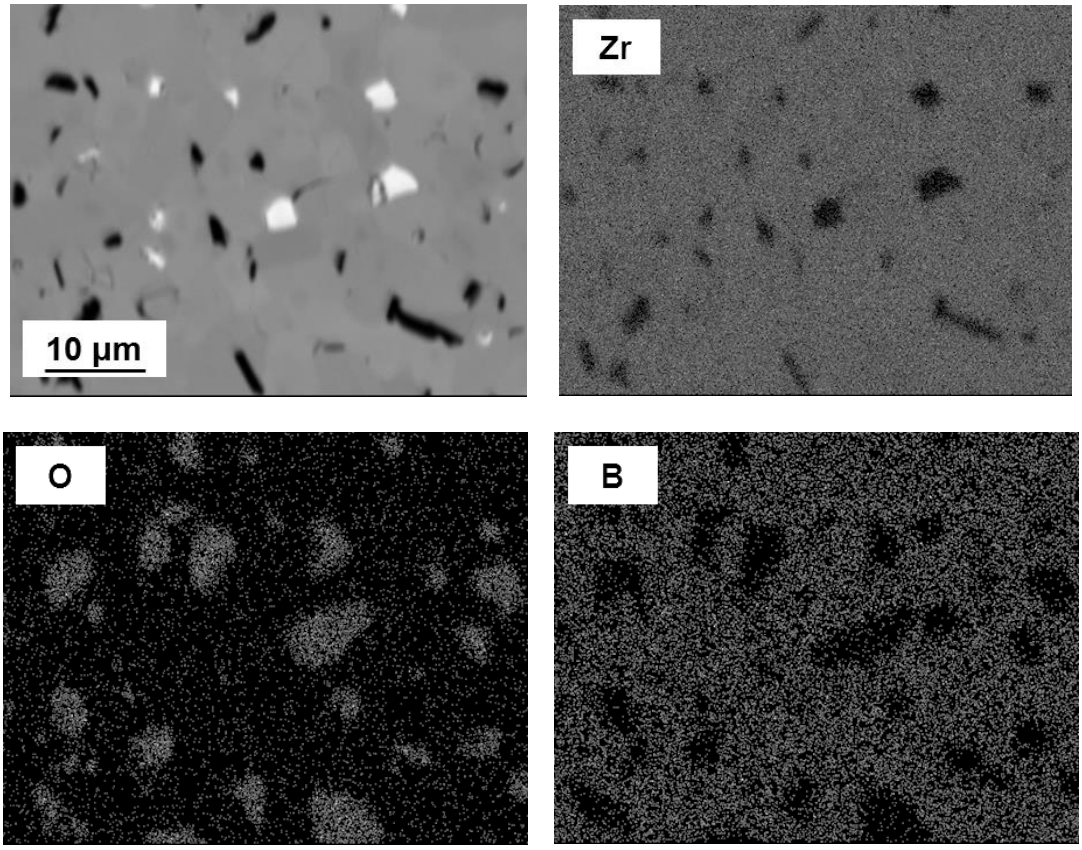

Figure 4-7: ZWC1 micrograph and complementary EDS mapping revealing elemental distribution. Zr and B are depleted at O-rich regions while the phase difference is not readily observed in backscatter; the light phase is WB.

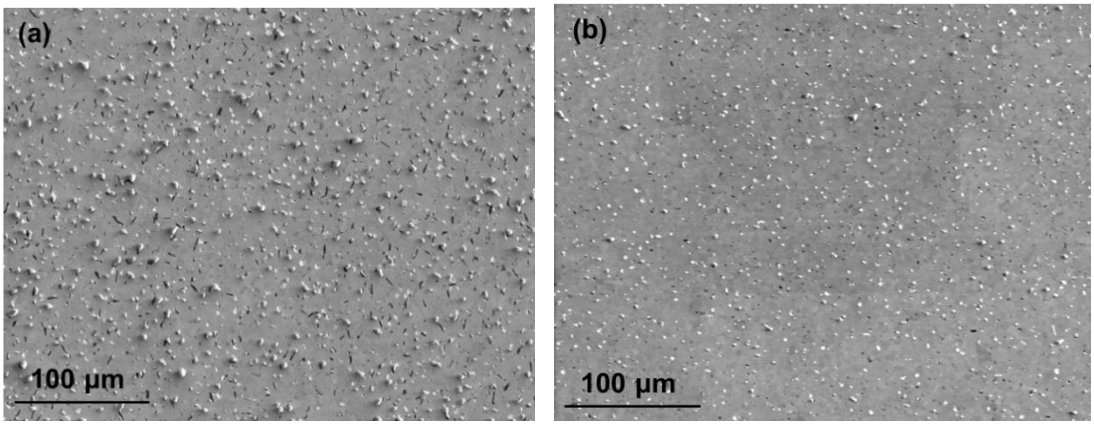

Figure 4-8: Secondary electron SEM micrograph of as-received ZWC1 (a) and ZWC2 (b) showing the decreasing ZrO2 volume fraction. The carbon phase (black) appears minimal in ZWC2.

Two heat treatments were conducted on ZrB_2-WC alloys with the anticipation of altering microstructures in favor of carbon-rich phase and/or W dissolution. Heat treatments were conducted at 2100°C (ST) and 2300°C (HT) for varying soaking periods. For prolonged solution treatments of the ZCWC alloy, the high-aspect ratio carbon-rich phase preferentially dissolved in solution with the remaining globular C-B-N and WB phases remaining unchanged. Statistically fewer HAR phases were observed with corresponding area percentages of 1.39+/- 0.22 and 0.57 +/- 0.07 for the as-received and ST heat treatment for 90 minutes, Figure 4- 9. A similar solution treatment with a 60 minute holding period was conducted on the ZWC3 alloy yielding negligible microstructural and phase composition changes, Figure 4- 10. Furthermore, the a*-lattice parameter remained constant through the heat treatment, Table 4- 5. High temperature heat treatments revealed two thermochemical behaviors in the presence of excess carbon, Figure 4-11. For the ZCWC alloy, the grains grew in excess of 5x the original diameters as a result of preferential growth along one direction. The elongated grains correspond with the appearance of a solidified melt near multigrain junctions replacing the once WB phase. XRD patterns show a decreasing WB reflection intensity with the heat treatment and the phase character of the multigrain junctions was similar to the as sintered unknown with an increasing W/Zr ratio of

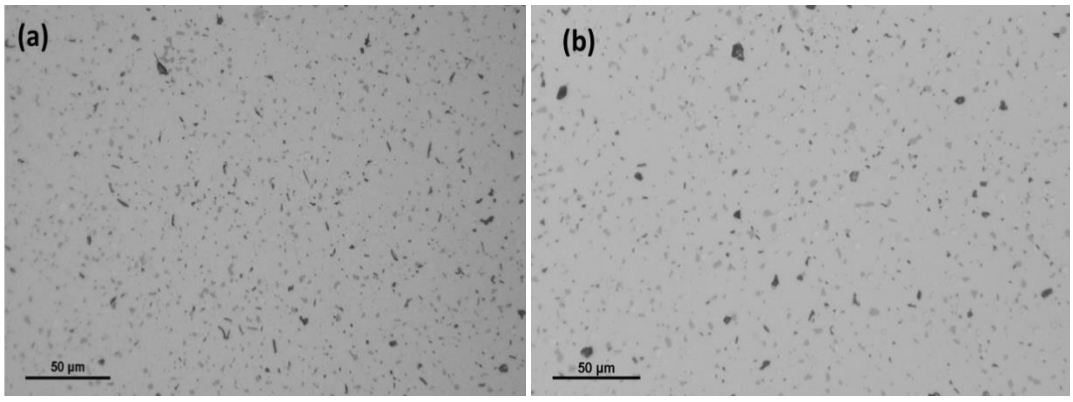

Figure 4-9: Optical micrographs showing C-rich HAR phase in the as-sintered microstructure (a) and the near complete dissolution with solution treating for 90 minutes at 2100°C (b).

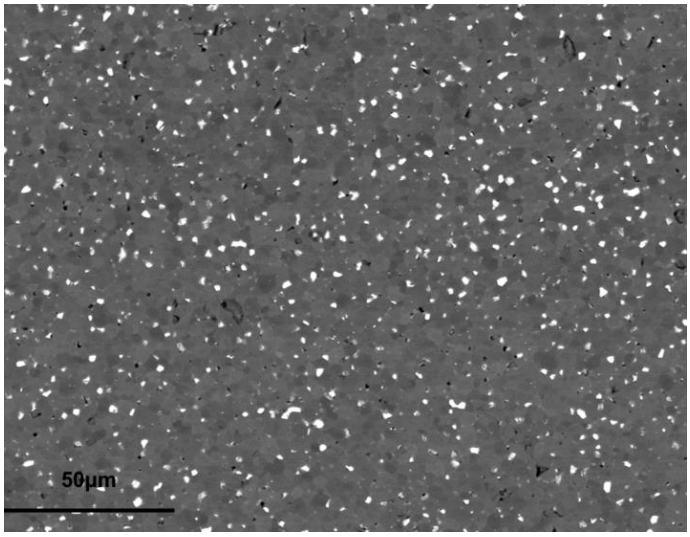

Figure 4-10: ZWC3 alloy 2100°C solution treatment for 60 min showing little microstructure change from the as-sintered condition.

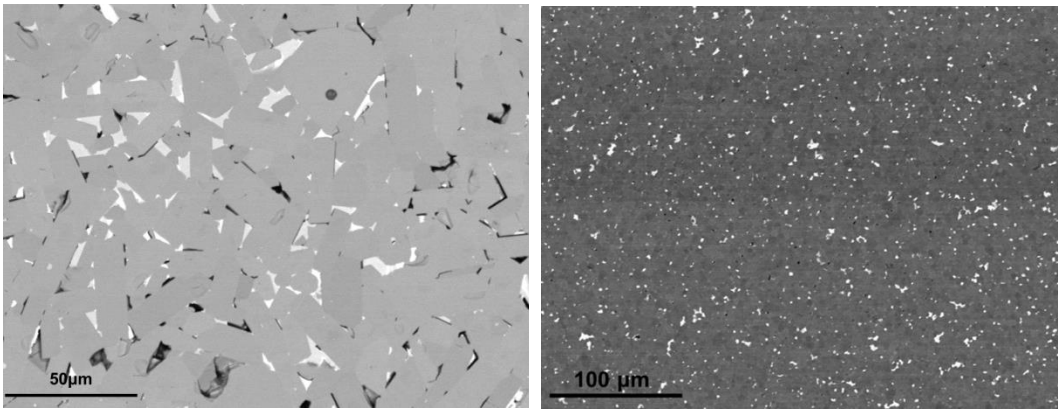

Figure 4-11: 2300°C anneals for ZCWC (a) and ZWC3 (b). The light multi-grain junction phase is a Zr-W alloy phase with elongated ZrB_2 grains and a black carbon-rich phase (a). Globular WB phase and ZrB_2 grains (grey) are shown in the ZWC3 alloy (b).

~0.35. The ZWC3 2300°C anneal caused minor microstructural changes including 20% increase in average ZrB_2 grain size, an increase in W dissolution of 1.1 mol%, and a reduction in WB average particle size. However, the distribution of WB remained statistically unchanged. The formation of an unknown Zr-W-B-C alloy phase was observed from the XRD patterns with reflections centered over similar 2-theta positions as the ZCWC alloy, Figure 4- 12.

Lattice parameter measurements were calculated for select composites in effort to characterize the extent of solid solution in addition to W and Zr mol ratio measurements using

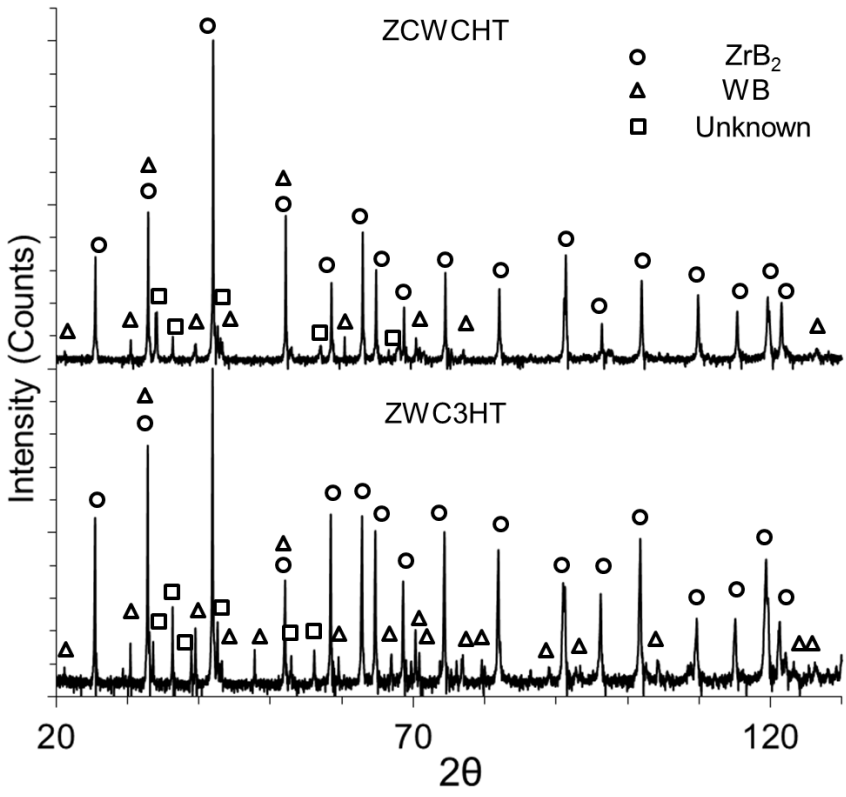

Figure 4-12: XRD patterns showing the crystalline phase character of the ZCWC and ZWC3 alloys after a 2300°C heat treatment.

EDS, Table 4- 5. Following the methods described in Chapter 3, a* and c* parameters were measured with precisions of <0.002Å and <0.006Å, respectively. The c*-parameter precision was not within those reported in the literature because of the uncertainty in the (003) reflection 2θ position. Examination of PDF 00-034-0423 shows the (003) reflection is masked by the (112) reflection making the absolute peak position difficult to determine. For the purpose of the solid solution study, the a*-parameter should be sufficient for analysis as the W atom is likely to substitute with Zr atoms on the basal plane; W is known to have an atomic radius ~ 12% less than the Zr atom and too large to occupy interstitial sites (Teatum, Gschneidner, Jr. and Waber 1960). The a*- parameter precision was improved and within those reported in the literature (Kaufman and Clougherty 1963). The lattice parameter was found to monotonically decrease with increasing W (WC) composition indicating the presence of a solid solution. From these

results ~1.4 mol% W dissolution does not affect the lattice parameter and a maximum W solubility of ~4 mol% was observed for this study for heat treatments at 2300°C and 120 minutes. Furthermore, the starting ZrB_2 particle size seems to have an effect on the W-dissolution as the attrition milled ZWC1AR shows an increase in W composition contrasting with the ball milled ZWC3AR material.

Table 4- 5: Lattice Parameter comparisons for select as-received and heat treated billets.

Alloy	a* (Å)	c* (Å)	WC mol%
ZWC3_AR	3.1690 +/- 0.0004	3.5286 +/- 0.0028	1.4 +/- 0.5
ZWC3_ST	3.1690 +/- 0.0006	3.5286 +/- 0.0039	1.4 +/- 0.4
ZWC3_HT1	3.1663 +/- 0.0020	3.5247 +/- 0.0030	2.5 +/- 0.5
ZWC1_AR	3.1644 +/- 0.0010	3.5233 +/- 0.0059	3.5 +/- 1.7
ZCWC_HT2	3.1621+/- 0.0012	3.5201+/- 0.0123	4.2 +/- 0.9
PDF00-034-0423	3.1687	3.530	----

AR = As Received, ST = 2100°C-60min, HT1 = 2300°C-60min, HT2 = 2300°C-120min
(Ekbom and Amundin 1981)

4.1.2. Mechanical Properties

Average room temperature flexure strengths, K_{IC} fracture toughness, elastic modulus and hardness are summarized in Table 4- 6. A substantial decrease in fracture strength, with identical modulus and fracture toughness, for the Z20SB was observed compare with the Z20S composite. The WC containing alloys showed consistent fracture strength, modulus and hardness with a statistical fracture toughness change. Elastic modulus measurements between the Berkovich nano-indentation method and the RUS method are in good agreement. The change in variance for the nano-indentation measurement corresponds to either the proximity of the reinforcement phase or local W-composition variations between indented grains.

Room temperature Berkovich nano-indentation hardness was conducted on select heat treated samples for determining solid solution (if any) effects on the ZrB_2 plasticity, Table 4- 7. Elastic modulus and hardness remained statistically unchanged from resulting heat treatments with respect to the as-received condition. The lack of distinguishable hardness increase for

increasing solid solution appears masked by either local compositional variations or crystallographic orientation anisotropy on the room temperature ceramic plastic behavior.

4.2. Analysis and Discussion

4.2.1. Microstructure

Measured composite densities for both ZSB and ZS materials are identical, but lower than those reported by A. Chamberlain, et al., (2004) study. Previous studies attributed these density differences to WC/Co impurities from precursor powder milling ((A. L. Chamberlain, et al., 2004), (Rezaie, Fahrenholtz and Hilmas 2007) and (Zhu, Fahrenholtz and Hilmas 2007)). The density of the ZSB composite exceeds the calculated value, presumably due to these WC/Co impurities. Boron-rich carbide (B_xC_y) concentrations in the ZSB material, identified using WDS, were measured using image analysis and the theoretical density adjusted accordingly.

Table 4- 6: Room temperature mechanical properties for SiC containing ZrB_2 composites and monolithic WC bearing alloys. All materials were tested in the as-received condition.

	σ_f [Mpa]	K_{IC} [MPam1/2]	E [GPa]	H [GPa]
Z20SB	456 +/- 66	3.9 +/- 0.2	492 +/- 41 (519 +/- 3.6)	21.6 +/- 0.7
Z20S	734 +/- 60	4.5 +/- 0.9	492 +/- 65 (515 +/- 3.6)	20.0 +/- 1.6
ZCWC	371 +/- 39	2.7 +/- 0.5	514 +/- 67	21.4 +/- 1.4
ZWC1	486 +/- 101	3.8 +/-0.5	503 +/- 53	20.6 +/- 1.4
ZWC2	404 +/- 55	3.2 +/- 0.2	506 +/- 50	20.4 +/- 1.2
ZWC3	401 +/- 61	4.2 +/- 0.2	478 +/- 38	20.7 +/- 0.5

E = Nano-indentation-Value (RUS-Value)

Table 4- 7: Room temperature hardness and elastic modulus for select heat treated ZrB_2-WC alloys.

	H [GPa]	E [GPa]
ZWC3_ST1	21.0 +/- 2.0	519 +/- 56
ZWC3_HT1	20.6 +/- 2.0	514 +/- 57
ZCWC_ST2	19.9 +/- 1.4	494 +/- 43
ZCWC_HT2	20.9 +/- 1.6	482 +/- 42

ST1 = 2100°C, 60min, ST2=2100°C, 90min, HT1 = 2300°C, 30min, HT2 = 2300°C, 120min

Measured residual concentrations of ~2.60 vol% (~1 wt%) is less than initial B_4C powder concentrations, from particle oxide reduction reactions, but compare favorably with initial B_4C powder composition. WDS analysis of three characteristic particles (Table 4- 3) indicates either a carbon-deficient two phase compound or solid solution of metastable $B_{50}C_2$ in $B_{13}C_2$ (Ekbom and Amundin 1981) Additionally, a relatively large Si-rich irregular phase was observed and is detailed below. Exact stoichiometry determination for both B-rich and Si-rich carbides was not attempted. Optical and SEM microstructural evidence of as-received composite shows minimal porosity as predicted by our density measurements.

Similar density variations were observed for the ZrB_2-WC alloys suggesting small final composition changes from nominal. Theoretical densities were calculated based on the assumption all WC impurities, from milling media wear, were mixed with the initial powder precluding *a priori* knowledge of additional impurities (e.g. carbon, zirconia). Initial relative densities reveal and maximum of ~1.5% porosity despite the absence of the carbon and ZrO_2 impurities from the milling process. The alloys containing ZrO_2 were expected to have slightly lower measured densities compared to the theoretical values determined from the starting nominal composition. When accounting for the volume fraction of ZrO_2 the adjusted theoretical densities become 6.41 g/cc and 6.27 g/cc for the ZWC1 and ZWC2 alloys respectively, yielding new relative densities of >100%. The micrographs for all alloys confirm the relative density magnitudes showing negligible porosity concentrations distinguishable from polishing damage. Alloys with relative densities >100% appear having an excess of WC from the nominal starting compositions, Table 4- 8. The ball milled alloys showed the minimum difference between nominal and calculated WC compositions contrasting with the attrition milled alloys. Large

Table 4- 8: WC composition comparisons vs. nominal compositions assuming all WC impurities are included in the initial powder charge.

WC-Based Density	WC-Density	Nominal+Impurity	**Difference**
ZWC1- 100% dense	9.75	7.74	23.3%
ZWC2-100% dense	4.25	3.58	17.4%
ZWC3 - 100% dense	6.97	7.04	-1.0%
ZCWC-100% dense	5.93	5.31	11.1%

compositional differences were apparently from the different milling media cleaning procedures prior to weighing before and after milling. From this observation additional WC impurity was incorporated in the three alloys exhibiting >100% relative density. The ball milled alloys exhibit consistent WC concentrations from a reduced amount of WC contamination and the addition of a known quantity of WC. Variability of WC impurity concentration has been observed from similar powder processing techniques ((A. L. Chamberlain, et al., 2004), (S.-Q. Guo 2009) and (Fahrenholtz, Hilmas and Zhang, et al., 2008)). Continual wear of the WC milling ball and WC rotating shaft arms were the impurity sources affecting final density. A. L. Chamberlain, et al., (2004) and Rezaie, et al., (2007) used Helium pycnometry on ground sintered composite for accurately determining the WC impurity concentration with those measured using buoyancy methods. However the initial assumptions for the introduction of WC impurities exist and do not account for other impurities (e.g., carbon-based and zirconia). Therefore, density measurements by Archimedes method and impurity calculations, using a rule-of-mixtures approach, was suitable for confirming the nominal alloy compositions provided the initial charge concentrations are well known.

Initial predictions of WC solubility in ZrB_2 proved larger than those observed for all alloys in the as-sintered or heat treated conditions. Measured average W concentrations in solid solution 1.5 -4.2 mol% were well below the calculated solubility of 4 – 9.25 mol% for temperatures of 1927-2300°C. Additionally, these are below those reported by (Zhang, Hilmas

and Fahrenholtz 2011) for ZrB_2-WC alloys having a solubility <8 mol% WC below T>2000°C. The ΔG-X_{WC} curves, shown in Chapter 3, were approximated without accurate knowledge of the higher order alloy interaction terms which, if included, would shift the ZrB_2 tangent point to a higher WC concentrations yielding larger solubility. For the current presentation, the lack of WC dissolution suggests a solubility limit much less than those observed (Zhang, Hilmas and Fahrenholtz 2011) and calculated. Moreover, WB and apparently a primary quaternary solid solution phase were observed suggesting other W-Zr-B-C reaction equilibria. Guo, et al., (2011) observed an unknown primary $(Zr,W,C,B)_{SS}$ phase with ~ 5 mol% WC added as a milling impurity. XRD peak positions were observed along 2θ positions near those peak reflections indexed to WB for the current work. The current WB peak reflections were offset to lower 2θ values suggesting lattice strain from solid solution formation within the WB. E. Rudy (1969) presented a limited W_2C, WC, W_2B, W_2B_5 and C solubility in WB accounting for the observed 2θ shift; EDS measurements indicate appreciable carbon presumably in solution. Zhang, et al., (2011) showed the presence of $(Zr,W)B_2$ solid solution by pointing out the primary ZrB_2 plane reflection shifts to smaller 2θ positions and the emerging WB peak reflections near WC concentrations >8 mol%. A. L. Chamberlain, et al., (2004) observed both WC/WB phase and a primary $(Zr,W,C,B)_{SS}$ phase in attrition milled ZrB_2-SiC composites with WC milling impurity concentrations of 3-4 mol%. A review of the Zr-W-B phase diagram shows a ternary compound phase field centered at a nominal composition of 26Zr-41W-33B, Figure 4- 13 (Chang 1966). Chang (1966) suggested the ternary compounds react sluggishly and form in the company of ZrB_2, W and W_2B phases. For the present case, the observed solid solution phase has an adjusted composition of 45Zr-10W-45B located outside of the ternary phase field, however, the presence of carbon (~30 mol%) may promote such a reaction in the proximity of the observed WB phase. It is apparent the presence of carbon affects the WC dissolution kinetics in ZrB_2 and the formation of WB.

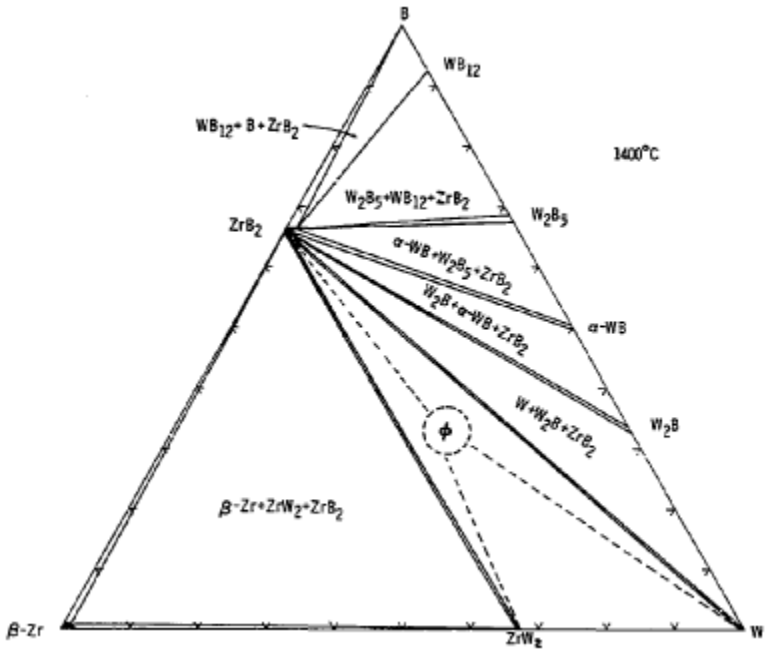

Figure 4-13: Zr-W-B ternary phase diagram after Chang (ref) detailing a ternary phase solid solution phase of composition ~ 26Zr-41W-33B at 1400°C, taken from (Chang 1966).

Amongst all microstructures the WB phase was present despite the differences in WC dissolution in ZrB_2. For all alloys two general equilibrium reactions were considered assuming WC and WB standard state

$$WC_{(cr)} \rightarrow (C)_{ZrB_2} + (W)_{ZrB_2} \ , \ \Delta G_{5\ mol\%\ WC} = 0.0768T - 63.411\ KJ/mol \quad (4\text{-}1)$$

and

$$WC_{(cr)} + (B)_{ZrB_2} \rightarrow WB_{(cr)} + (C)_{ZrB_2} \ , \ \Delta G_{5\ mol\%\ WC} = -0.0199T - 18.904\ KJ/mol, \quad (4\text{-}2)$$

where the elements in the brackets represent the dissolved species in ZrB_2 and $\Delta G_{5\ mol\%\ WC}$ is the Gibb's free energy at a nominal 5 mol% WC in ZrB_2; activity coefficients and free energy formulations are tabulated in Appendix A. Reaction (4-1) represents the complete dissolution of WC in ZrB_2, capped by the solubility limit, and reaction (4-2) detailing the WC-WB formation with dissolved boron. The latter reaction is spontaneous over the applicable processing temperature range contrasting with the former having a $\Delta G_{5\ mol\%\ WC} > 0$. Under these initial

assumptions the formation of WB is preferred over complete dissolution of WC into ZrB_2. Comparing the ZCWC and ZWC3 alloys, WB was formed at multigrain junctions despite the statistically different $(W)_{ZrB2}$ compositions of 2.7 +/- 0.6 mol% and 1.4 +/- 0.5 mol%, respectively. Both alloys were identically processed with exception to the addition of a ~4.2 mol% carbon-yield precursor binder, prior to sintering. Similarly, the carbon effect appears consistent with the identically milled ZWC1 and ZWC2 alloys having $(W)_{ZrB2}$ compositions of 3.5 +/- 1.7 mol% and 2.6 +/-0.3 mol%, respectively.

From the observed microstructures, excess carbon appears to promote WC dissolution. Reaction (4-1) was modified to include excess carbon following

$$WC_{(cr)} + XC_{(cr)}^{xs} \rightarrow (1 + yX)(C)_{ZrB_2} + 2(W)_{ZrB_2} + 2X(1 - y)C_{(cr)}^{xs} \quad , \qquad (4\text{-}3)$$

where X is any arbitrary quantity of excess carbon, $C_{(cr)}^{xs}$, having a dissolution factor of y = 0 and y=1 for incomplete and complete excess C dissolution, respectively. The presence of excess carbon drives the $\Delta G_{5\ mol\%\ WC} < 0$ for reaction (4-3) at a critical carbon concentration, Figure 4- 14. For complete dissolution, y=1, a critical excess carbon concentration of X = 2 is required for complete dissolution of 1 mol of WC suggesting the dissolution of 5 mols WC in ZrB_2 requires 10 mols of excess carbon resulting in a required ZrB_2 carbon solubility of 11.8 mol%. A reduction in WC composition changes the activity of both C and B reducing the excess carbon (x~1.5) required for complete dissolution contrasting with reducing temperature driving the excess carbon requirement to x~3 for 5 mol% WC dissolution. Kaufman (1986) conducted preliminary thermochemical calculations on the Zr-B-C system showing a maximum carbon solubility of 2 mol% in ZrB_2 which is well below that required for 5 mols of WC dissolution. However, Zhang, et al., (2011) experimentally observed ~ 14 mol% carbon solubility, at 1900°C, using the same carbon precursor and pyrolytic treatment. Therefore, a maximum WC dissolution of ~7 mol% at 2700K is possible while not violating the proposed carbon solubility limit observed by Zhang, et

al., (2011). Applying the dissolution reaction (4-3) to the ZCWC alloy, a critical C^{xs} factor of ~1.43 is required for the measured 2.7 +/- 0.6 mol% dissolved WC resulting in a theoretical C^{xs} concentration ~3.86 mol%. Taking the difference between the initial and theoretical C^{xs} yields a ΔC^{xs} of 0.34 mol% which agrees favorably with the optically measured C^{XS} of ~0.50 mol% (1.39 vol%); the un-reacted C^{xs} includes both the unstable carbon-rich high aspect ratio and apparently stable globular C-B-N phases suggesting the actual final C^{xs} < 0.50 mol%. Control over the excess carbon concentration for driving WC dissolution depends on the processing temperature and desired final WC concentration.

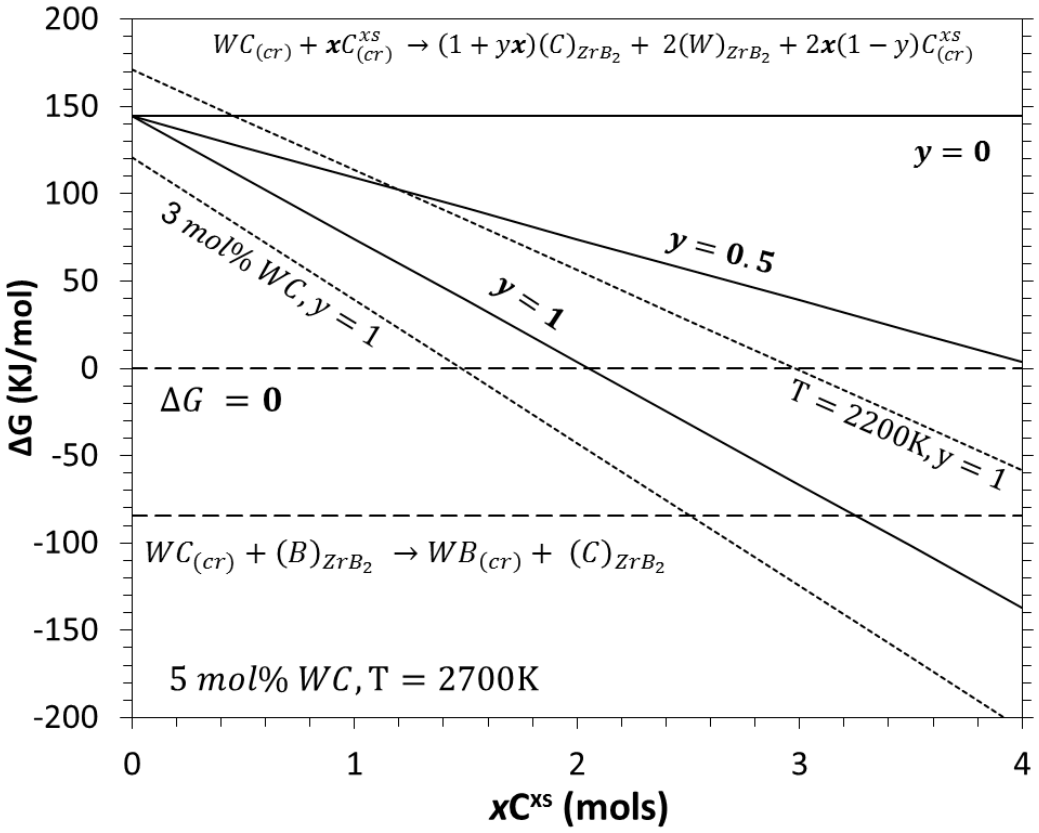

Figure 4-14: Excess carbon concentration effects on WC dissolution and WB reaction equilibria at T=2700K. The dissolution factor, y, has a significant effect on the critical carbon concentration (ΔG<0) for promoting WC dissolution.

Table 4- 9: Optically measured WB phase quantities for the as-sintered alloys.

Alloy Designation	Area % WB	Area % C-rich
ZWC1	1.10%	5.44%
ZWC2	1.18%	0.22%
ZWC3	4.34%	0.18%
ZCWC	2.36%	1.39%

The competition between reactions (4-2) and (4-3) are based on the kinetics as both are thermochemically favorable between 2000-2700K. Optically determined WB phase quantities are tabulated, Table 4- 9, showing significant difference between the ball and attrition milled alloys. ZWC1 and 2 alloys were attrition milled resulting in an increasing surface area (~factor of four) from a 75% reduction in starting ZrB_2 particle size producing a finer and more homogeneous WC distribution. Additionally, finer starting particle sizes reduces the diffusion distances promoting dissolution. Fahrenholtz, et al., (2008) found the starting particle distribution improved reaction kinetics for particle oxide reduction. The same effect is apparent as a reduction in WB phase quantity implies a more uniform distribution of the local free carbon concentration promoting uniform WC dissolution. A secondary effect may include a reduction in the required excess carbon needed for driving the dissolution reaction. Therefore, the observed increasing average $(W)_{ZrB2}$ composition of 25 and 85% for alloys ZCWC-ZWC1 and ZWC3-ZWC2, respectively, correlates with a particle size reduction and improved particle distribution due to attrition milling.

Heat treatments conducted at 2300°C for the ZCWC and ZWC3 promoting the WC dissolution in ZrB_2,, over the as-sintered compositions, had varying microstructural effects, Figure 4- 11. Excessive grain growth and observed high temperature solid solution phase were present for the ZCWC contrasting with a relatively stable microstructure for the ZWC3 alloy. The ZWC3 alloy WB particle chemistry showed slight fluctuations in carbon/boron ratios between the as-sintered and heat treated conditions along with 1μm average grain diameter increase, however,

XRD confirms no significant WB phase change occurred during heat treatment. For the ZCWC alloy, preferential grain elongation and a secondary $(W,Zr,C,B)_{ss}$ solid solution phase, replacing the WB phases at the multigrain junctions, was observed. The discontinuous grain growth appears as a result of the presence of a liquid phase, at heat treating temperature, promoting the dissolution and re-precipitation of Zr and B from the liquid contact regions towards the grain ends. Based on the proximity of the solid solution phase, the as-sintered WB phase appears to have transformed to liquid during heat treatment; the nature of the solidified phase was not determined from XRD as known PDF's were not indexed to the plane reflections. Rudy (1969) Rudy proposed a series of W-B-C ternary phase diagrams through 2320°C detailing low melting point phase formation along the W-B and B-C binaries. For this analysis zirconium was not included as negligible Zr dissolution was observed for the nominal WB phase. A survey of the ternary diagram at 2150°C shows no liquid phase formation for either the ZCWC and ZWC3 starting nominal WB compositions, Figure 4- 15.

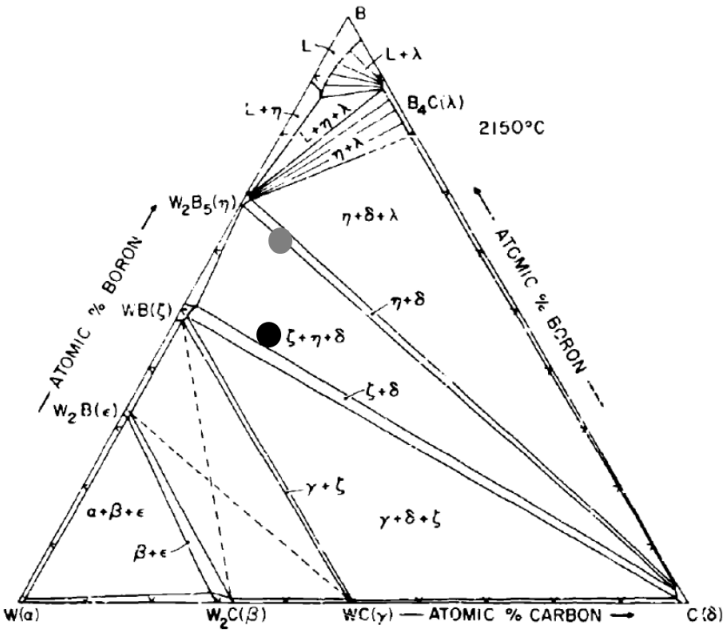

Figure 4-15: W-B-C ternary diagram from Rudy (ref) at 2150°C detailing starting nominal WB compositions for ZCWC (Black) and ZWC3 (Grey) circles, taken from (E. Rudy 1969).

Increasing the temperature through 2350°C, the ZCWC and ZWC3 starting WB compositions are well within an equilibrium liquid phase field , Figure 4- 16. The role of excess carbon in the ZCWC alloy influences the phase stability promoting liquid phase formation by driving phase composition towards the C-rich corner. In the absence of appreciable excess carbon (ZWC3 alloy), increasing W-composition drives the starting WB phase towards the stable equilibrium WB-WC-W_2C phase field away from the low melting point compositions. The starting carbon concentrations of the WB phase showed negligible change with heat treating temperature. The ZWC3 phase evolution seems counter intuitive as the W-dissolution in ZrB_2 increased while the equilibrium concentration also increased for the nominal WB phase. Qualitatively the formation of W-depleted zones near these WB phases indicates a possible explanation for the increasing W composition stabilizing the solid phase, Figure 4- 17. However, the partial dissolution of the

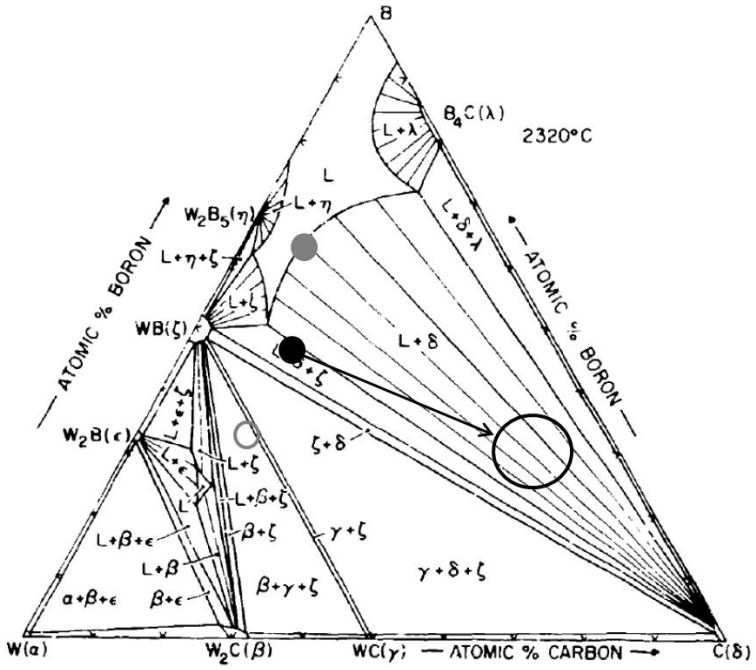

Figure 4-16: W-B-C ternary diagram at 2320°C detailing starting (filled circles) and final (open circles) nominal WB compositions for ZCWC (Black) and ZWC3 (Grey), taken from (E. Rudy 1969).

primary $(W,Zr,C,B)_{ss}$ solid solution phase, in ZrB_2, may be responsible for the increased ZrB_2 – W composition at these temperatures.

The formation of a melt between ZrB_2 grains appears to drive dissolution and re-precipitation as the final grain shape aspect ratio increased substantially from the near equiaxed starting grain shapes, Figure 4- 11. Chemical analysis of the melt shows ~20 mol% Zr dissolved contrasting with the starting WB composition having ~ 1 mol% Zr dissolution. Therefore, the melt appears as an efficient solvent for dissolving and transporting the ionic species of ZrB_2. Grain growth in the presence of a liquid occurs by grain boundary migration. For the present case (Figure 4- 11), it is assume the WB, primary $(Zr,W,C,B)_{SS}$ and small ZrB_2 grains preferentially dissolve resulting from the high interfacial energy, diffuse through the melt and precipitate along the larger ZrB_2 grains reducing the surface energy. The formation of discontinuous growth may occur as a result of enhanced growth along more accommodating crystallographic planes (i.e. non-closed packed). Discontinuous grain growth was observed in Alumina-1% anorthite having a liquid film (Kaysser, et al., 1987). Song and Coble (1990) observed similar platelet growth in Al_2O_3 obeying an Ostwald ripening model (Nikolic 1999) in the presence of an intergranular liquid film promoting dissolution and re-precipitation. Grains grew parallel to the flat boundaries as a result of insufficient nucleation sites promoting perpendicular growth (Song and Coble 1990). It is unclear the crystallographic nature of the current grain growth in the ZCWC composite, however, the appearance of flat interfaces adjacent to melt regions strongly suggests a similar growth mechanism.

4.2.2. Room Temperature Mechanical Behavior

Room temperature strength properties were found to vary considerably with the composite/alloy composition. Flexure strengths of 456 ± 66MPa and 734 ± 60MPa for ZSB and ZS composites, respectively, fell significantly below the 1003 ± 94 MPa reported for a similar

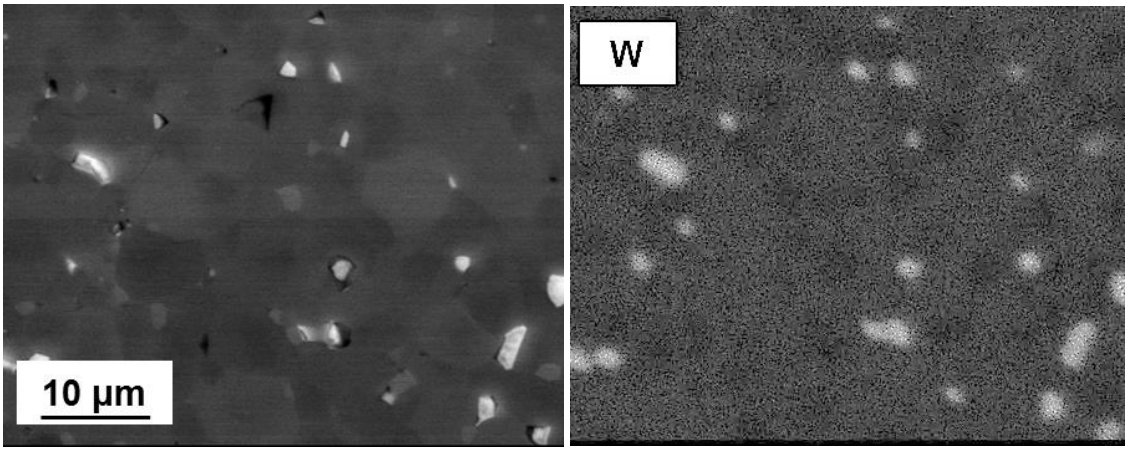

Figure 4-17: Backscattered electron SEM image of the mapped area showing WB phase (light) surrounded by small (Zr,W,C,B)ss phase (grey) and the W elemental mapping showing regions of W-depletion near the WB grain boundaries.

material (A. L. Chamberlain, et al., 2004). Furthermore, monolithic alloy strengths fell significantly below those reported for fine grained ZrB_2 monolith having a relative density of ~ 100%. The expected strength decrease between the ZSB and ZrB_2 alloys was observed due to the absence of a reinforcement; one exception exists for the ZWC1 as the presence of sufficient (~20%) non-reacting particles should boost the room temperature strength (Fahrenholtz, Hilmas and Talmy, et al., 2007). The candidate strength-limiting features include: second phase reinforcements, grain size, impurity phase and solid solution strength limitations.

The strength differences between the Z20S composite and the monolithic alloys were consistent with those tabulated in Chapter 2. The presence of > 10% reinforcement phases has been shown increase strength and fracture toughness by modifying the crack path and reducing grain sizes during sintering. Removal of the SiC phase resulted in a 76% strength reduction following the trends shown in Figure 2-2. Chamberlain, et al., (2004) reported a ~70% strength reduction from 20% to 0% reinforcement for fined grained attrition milled material. The abrupt strength decrease for the Z20SB composite does not correlate with observed strength trends based on volume fraction reinforcement or matrix grain size. Based on the Griffith strength

criteria (Equation (2-12)), for the Z20SB composite, a ZrB_2 matrix strength of ~537MPa, in excess of the observed strength, represents the minimum theoretical obtainable strength for an average ZrB_2 K_{IC} of 3.0 $MPa\sqrt{m}$, Y = 0.400 and d_{max} = 5 µm. A similar argument, for the absence of reinforcement strength increases, for the ZWC1 alloy having ~20% ZrO_2 particles, was made based on a minimum theoretical matrix strength of ~640 MPa, having a maximum grain size of 3.5 µm. Considering the ZWC2 alloy, 9% ZrO_2 was measured, marking the apparent threshold reinforcement fraction where the matrix dominates the fracture process over the reinforcement. The observed strength reduction appears as a combination of reinforcement fraction reduction and the presence of other strength limiting flaws. A review of the room temperature K_{IC} suggests the presence of the 9% ZrO_2 negligibly effects the toughening promoting the matrix for limiting strength. The strength-improving presence of sufficient reinforcement fraction was offset by other competing strength limiting mechanisms.

Composite and alloy grain growth, at sintering temperatures, may also affect composite strength. The Z20SB strength reduction does not follow this notion based on the premise the matrix grain size is smaller than the Z20S composite. Furthermore, the ZrB_2-based alloy grain sizes qualitatively show these effects on strength. Analysis of the ZCWC and ZWC3 strength-grain size relationship reveals the minimum theoretical matrix strength of 408 and 460 MPa for a d_{max} = 6.85µm agreeing with the average strengths of 371 +/- 39 and 401 +/- 61 MPa, respectively, for a typical ZrB_2 matrix toughness of 3 $MPa\sqrt{m}$. However, the statistically different K_{IC} suggests the strength limiting mechanism differs between these two alloys of similar grain size and composition.

In an effort to understand possible influences from microstructural constituents, MOR and fracture results are presented (Figure 4- 18) in the context of an intrinsic Griffith flaw size and fracture stress, σ_f, using the simple relationship between the apparent critical stress

intensity factor and critical flaw size, a^*, as

$$a^* = \frac{1}{\pi}\left(\frac{K_{IC}}{\sigma_f f(\frac{a}{w})}\right)^2. \quad (4\text{-}4)$$

Observed microstructural features were correlated with the critical flaw size range based on measured MOR fracture strength and apparent fracture toughness, from SENB results. The composites containing SiC showed the maximum B_xC_y particle size correlates well with the ZSB composite flaw size range minimum. Irregularly shaped Si-rich carbide phases were grouped with the B-rich carbide class, based upon the similar grain sizes. However, the sparse and inhomogeneously distributed Si-rich carbide phase minimizes the probability of locating B-rich carbide in high stress region. In the absence of these large carbides, the smaller critical flaw size of the higher strength Z20S microstructure correlates well with the primary SiC constituents.

The ZrB_2-based alloys showed similar flaw size correlations with residual phase constituents present as a result of sintering. The observed high aspect ratio carbon phase, in

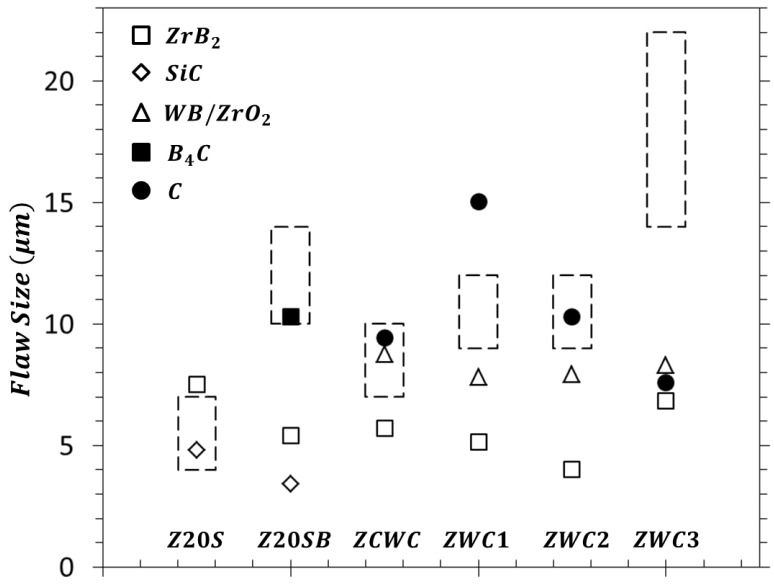

Figure 4-18: Intrinsic flaw size correlation with presumably strength limiting microstructure constituents. Hashed boxes represent Griffith.

the ZCWC alloy, correlated well with the calculated intrinsic flaw size. Detailed observation of the carbon phase, present along ZrB_2 facets, and appeared fibrillated and partially debonded suggesting a weak matrix particle interface promoting crack initiation at these sites, Figure 4-19. For the ZWC1 alloy, a similar carbon phase was observed, however, the intrinsic flaw size does not correlate with this phase as a result of possible toughening contributions from the present of ZrO_2. The ZrO_2 particles present for the ZWC1 and 2 alloys do not appear strength limiting, however they may serve as crack deflectors, Figure 4- 20.

The maximum ZrB_2 grain sizes fall below the lower flaw size bounds confirming previous studies of several microstructures having indicated a strong correlation between maximum SiC or impurity phase size and critical flaw size. Thermal expansion mismatch between SiC and ZrB_2 creates ~ 450 MPa residual matrix tensile stress suggesting SiC-ZrB_2 interfaces are likely crack initiation sites (Watts, et al., 2011). Including ZrO_2 particles are likely to exhibit a strengthening effect as the thermal expansion mismatch would promote compressive matrix residual stress. This beneficial effect can be countered by the 3-5% volumetric expansion from subsequent martensitic transformation promoting tensile residual matrix stresses (Wolten 1963). The latter is likely to occur as the ZrO_2 was indexed as predominately monoclinic structure. These results identify an argument for limiting sources of boron and compounds, such as B_4C and carbon sintering aids and the importance for minimizing particle agglomeration.

Room temperature fracture for composites containing reinforcement particles (Z20S, Z20SB, ZWC1 and ZWC2) had predominately transgranular fracture through the ZrB_2 matrix, Figure 4- 20. Process zone crack deflection has been reported for similar ZrB_2-based composites as a primary fracture mechanism (Rezaie, Fahrenholtz and Hilmas 2007). A fracture model based only on process zone crack deflection, was proposed, having the form of

$$K(\theta) = K_{IC}(\theta = 0)\sec^2\left(\theta/2\right), \quad (4\text{-}5)$$

where θ is the crack deflection angle and $K(\theta)$ and $K_{IC}(\theta = 0)$ are the fracture toughness from crack deflection and intrinsic material fracture toughness, respectively (S. M. Wiederhorn 1984). Applying this model, Rezaie, et al., (2007) found crack deflection dominated the toughening of ZrB_2-30% SiC composites having intrinsic toughness of ~3.7 $MPa\sqrt{m}$ and 4.7 $MPa\sqrt{m}$ for predominately transgranular and intergranular matrix fracture. Monolithic ZrB_2 K_{IC} of 2.3 -3.5 $MPa\sqrt{m}$ having predominately transgranular fracture have been reported (S.-Q. Guo 2009) suggesting crack deflection contributes 10-50% of the observed toughening for the Z20S, Z20SB and ZWC1 composites; the ZWC2 alloy K_{IC} agrees well with the matrix controlled transgranular

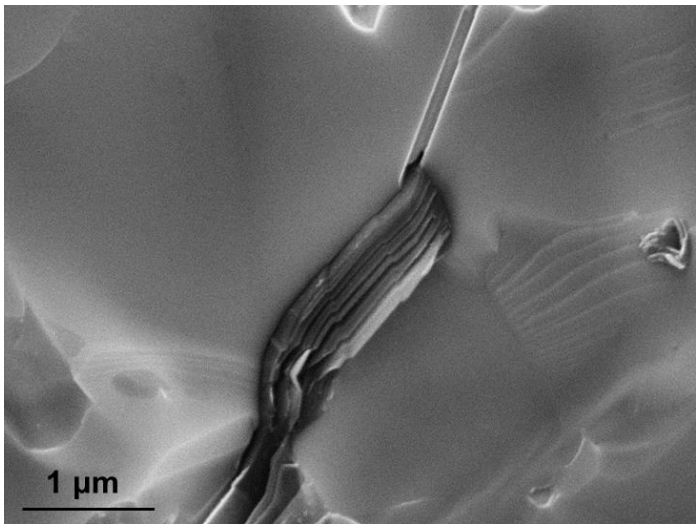

Figure 4-19: HAR Carbon phase (dark) embedded in a ZrB_2 matrix, from a ZCWC alloy MOR fracture face, illustrating the fibrillated morphology and the volume defects observed at the interphase boundary.

K_{IC} reported (S.-Q. Guo 2009). The ZWC3 alloy had a K_{IC} fracture toughness equivalent to the Z20SB, Z20S and ZWC1 alloys containing 20% reinforcements. An intrinsic K_{IC} of 2.6 $MPa\sqrt{m}$, for the average MOR strength of 400 MPa, correlating with a Griffith flaw size of 6.85 µm (d_{max}) was ~ 40% of the measured K_{IC} indicating other toughening mechanisms may dominate such as crack deflection and wake zone phenomena. The observed fracture faces shows an increasing fraction of intergranular fracture suggesting possible crack wake zone interactions improving

toughness. Thomas (2011) and Bird, et al.,(2012) investigated crack wake-zone phenomena, such as grain bridging for the Z20SB composite. Room temperature long crack behavior revealed negligible grain bridging as a result of transgranular fracture despite the stable growth throughout the experiments. Similar behavior was observed at room temperature for ZrB_2-10 vol% SiC (Kurihara, et al., 2010). However, a transition to predominately intergranular fracture was observed at 1000°C with a noticeable rise in stress intensity and increasing plateau toughness as a result of geometric interactions between neighbor grain facets along the crack wake zone ((Bird, Aune and Thomas, et al., 2012) and (Thomas 2011)).

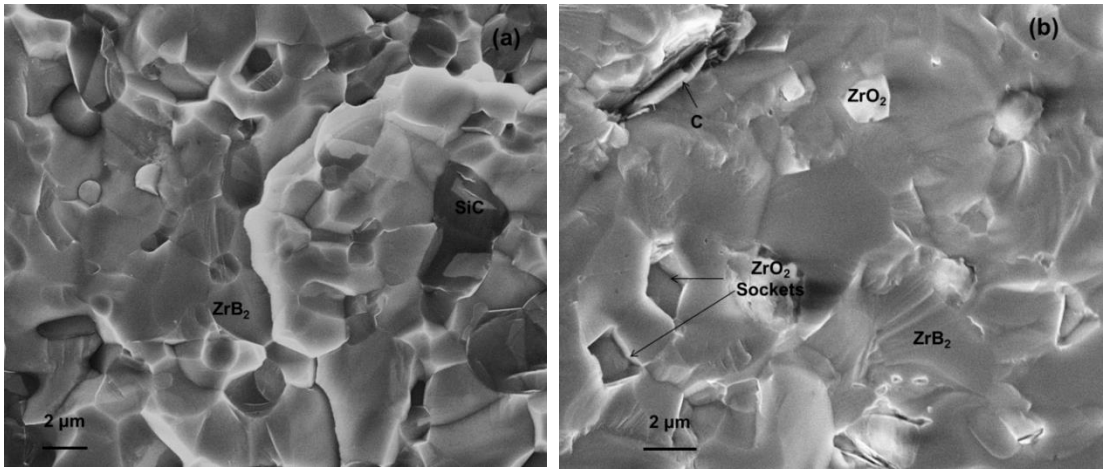

Figure 4-20: Fractographs of the Z20S (a) and ZWC1 (b) materials illustrating transgranular matrix fracture.

In ZrB_2 based ceramics thermal expansion anisotropy (Bird, Aune and Thomas, et al., 2012) may provide necessary grain tractions for possible wake-zone load support at room temperature (Hay Jr. 1995). For the present case, the increased crack face communication can exploit the substantial compressive stresses promoting grain pinching along the ZrB_2 *a*-axis, Figure 4- 22. Previous alumina studies used a locking parameter, β, for quantifying both thermoelastic (thermal expansion anisotropy (TEA) and geometric (grain shape, size, distribution) components contributing to crack bridging efficiency ((Kelkar 1989), (Hay Jr. 1995) and (Hay and White 1994)). A locking parameter was proposed having the following

relationship:

$$U^*_{COD} = \beta d_{act}, \tag{4-6}$$

where U^*_{COD} is a critical crack opening displacement for a corresponding active grain size, d_{act} scaled by β; typically ranging between 0.25 (Steinbrech, et al., (1990)) to 0.5 (Kelkar 1989) for monolithic alumina (Steinbrech, Reichl and Shaarwachter 1990). The fine matrix grain size of the ZWC3 alloy will likely limit wake zone size and load capacity resulting from a small characteristic U^*_{COD}, despite the anticipated TEA effects of the non-cubic ZrB_2 (Hay Jr. 1995). Therefore, the ZrB_2 K_{IC} increase of ~1.4 $MPa\sqrt{m}$ over the assumed calculated 2.6 $MPa\sqrt{m}$.

W-Zr-B-Co precipitates and substitutional solid solutions have been suggested for improving flexure strength of ZrB_2 – SiC composites by introduction of favorable residual stresses and solute drag processes (A. L. Chamberlain, et al., 2004). A study of TiB_2-W_2B_5-CoB reported significant strength increases with tungsten dissolution in TiB_2 (Watanabe and Kouno 1982)). Watanabe, et al., (1982) concluded reduced porosity and TiB_2 grain growth inhibition, by solid solution lattice strains, increased strength. No precipitates were observed in ZS and ZSB

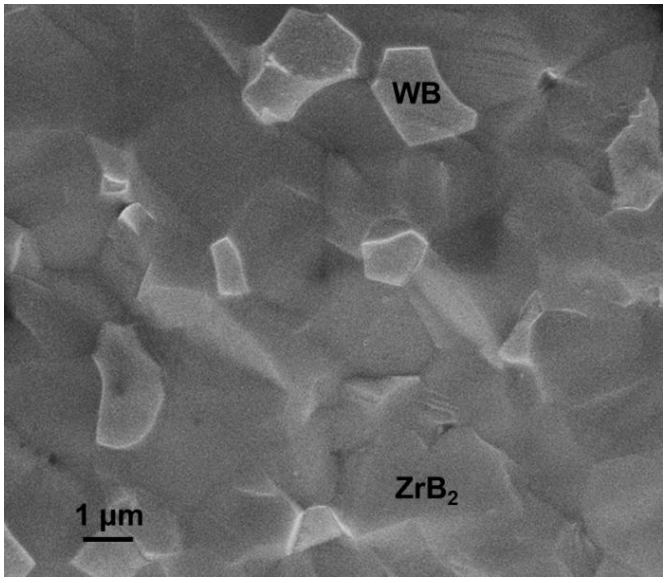

Figure 4-21: ZWC3 AR alloy fractograph detailing an apparent increase in ZrB_2 grain facets.

microstructures, however, 0.4 at% W was identified in solid solution with ZrB_2, which fell within the calculated solubility range for WC in ZrB_2. WB and quaternary alloy phases were observed, particularly, isolated at multi-grain junctions, with WC dissolution ranging from 1-3.5 mol% for as-sintered WC containing alloys. The appearance of the either the quaternary or WB may promote intergranular fracture for the ZWC3 and ZCWC alloys. Although, the strengths remained lower than those reported for ZrB_2 monoliths containing W-bearing phases despite the smaller average ZrB_2 grain size (A. L. Chamberlain, et al., 2004). Dissolved W in ZrB_2 may have compressive residual strain, by ZrB_2 lattice relaxation, shown in Table 4- 5, available to interact and inhibit ZrB_2 grain growth which appears as the cause of the observed grain size difference between the alloys from this study and those of Chamberlain, et al., (2004). Negligible solid solution MOR strength dependence was observed for each alloy and composite.

The solid solution strengthening was not expected during room temperature MOR experiments as slip would be restricted as a result of the brittle nature of ZrB_2. As a means for examining the solute effect on room temperature mechanical behavior, single ZrB_2 grain

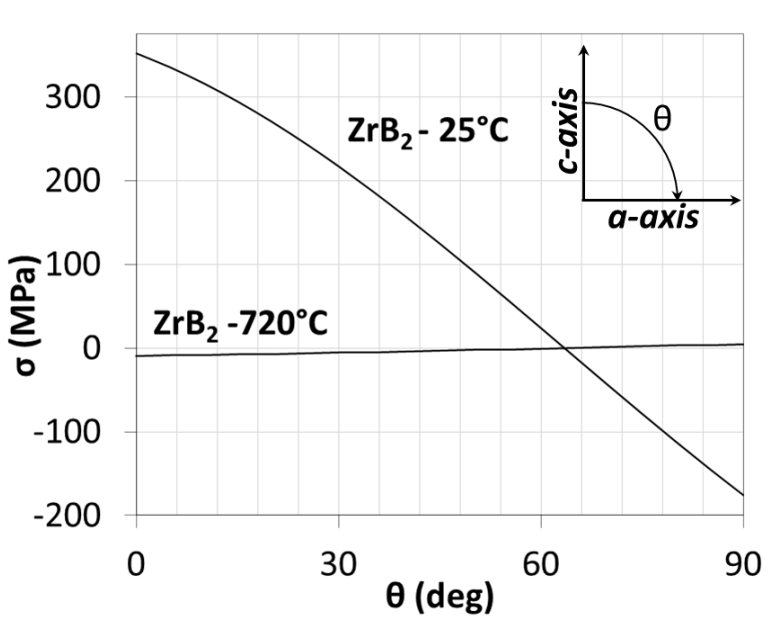

Figure 4-22: Residual stress from thermal expansion anisotropy transformation from the c-axis for ZrB_2.

hardness was measured. The hardness for each composite and alloy were not statistically different between both the as-sintered and heat treated alloys despite sufficient W-dissolution in some of the alloys. For the present case, the contributions of W-dissolution on hardness was investigated based on a substitutional strength model following (Hull and Bacon 2001)

$$\tau_{Flow} \simeq \sqrt{2} G c^{1/2} \left(\frac{1}{5}|\delta|\right)^{3/2}. \quad (4\text{-}7)$$

Equation (4-7) considers short range interactions with edge dislocations, bound by parallel planes containing substitutional solute of concentration, c_0, and atomic misfit strain, δ, raising the flow stress, τ_{Flow}, required for moving the edge dislocation. This flow stress increase corresponds to the change in hardness, assuming no work hardening under plane strain conditions, by the following (Tabor 2000)

$$\Delta H \approx 3\Delta\sigma_Y \quad (4\text{-}8)$$

and

$$\tau_{Flow} = \frac{\Delta\sigma_Y}{2}, \quad (4\text{-}9)$$

where ΔH is the change in hardness, the uniaxial yield stress, $\Delta\sigma_Y$ and the resultant flow stress based on Tresca's yield criterion following the results obtained on a LiF dislocation study (Swain and Lawn 1969). Application of Equations (4-7)-(4-9) gives an average WC concentration effect on the hardness change, for a misfit strain of 12%, G = 220 GPa (Okamoto, et al., 2010) and a starting ZrB_2 hardness of 20 +/-2.7 GPa (Kats, Ordan'yan and Unrod 1981), Figure 4- 23. No clear solute concentration effect was observed due to relatively large uncertainty presumably from crystallographic orientation differences.

Crystallographic orientation can have an effect on local mechanical properties from the non-cubic nature of ZrB_2. Local anisotropy was observed from the modulus calculations based

on single grain indentations. Large modulus variations were found for single grain measurements contrasting with the RUS bulk modulus values reported. Okamoto, et al., (2010) measured the single crystal ZrB_2 Young's modulus of 387 and 533 GPa for the $\langle 11\bar{2}0 \rangle$ and $\langle 0001 \rangle$ directions highlighting the elastic anisotropy of the ZrB_2 lattice. Nakano, et al., (1973) measured the ZrB_2 single crystal Knoop microhardness on select crystallographic orientation combinations for the $(0001)\langle 11\bar{2}0 \rangle$, $(10\bar{1}0)\langle 0001 \rangle$ and $(11\bar{2}0)\langle 0001 \rangle$ with the indent long axis parallel to the direction indices. Microhardness differences of ~2 GPa were reported between the basal and first and second order prismatic planes with average values of ~22, 20, 20 GPa, respectively. Xuan, et al., (2002) observed hardness differences between the basal and prismatic indented planes with increasing anisotropy and temperature. From the dislocation analysis of Haggerty and Lee (1971) and Gosh, et al., (2009), the $(10\bar{1}0)\langle 11\bar{2}0 \rangle$ slip

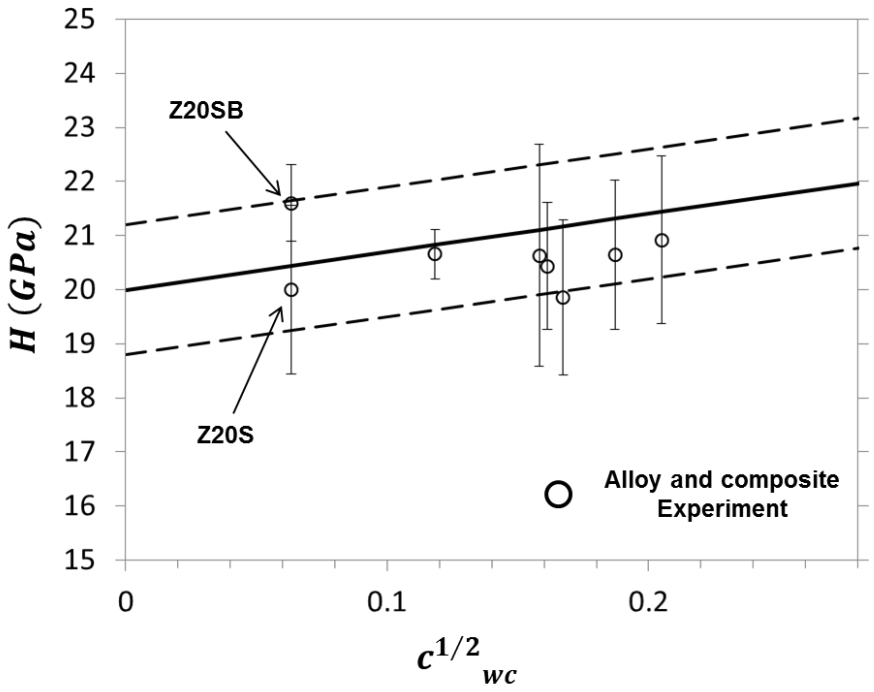

Figure 4-23: Substitutional solute concentration model (lines) with experimentally measured composite and alloy hardness (circles). The error bars represent the hardness variation from crystallographic orientation slip dependencies.

system operates preferentially over the $(0001)\langle 11\bar{2}0\rangle$, at room temperature, as a result of an increasing planar packing density and a lower critical resolved shear stress. Nakano, et al., (1973) calculated the $(10\bar{1}0)\langle 11\bar{2}0\rangle$ slip system Schmid factors of 0.156, 0.457 and 0.380 for the 22, 20 and 20 GPa hardness values, respectively. Furthermore, the $(0001)\langle 11\bar{2}0\rangle$ slip system Schmid factors of 0.331, 0.058 and 0.066 for the 22, 20 and 20 GPa hardness values, respectively. The hardness differences between the basal and prismatic indented planes suggest a lower $(10\bar{1}0)\langle 11\bar{2}0\rangle$ critical resolved shear stress then the $(0001)\langle 11\bar{2}0\rangle$ confirming the findings of Haggerty and Lee (1971) and Ghosh, et al., (2009). Therefore, the anisotropic behavior between basal and prismatic indented planes and their respective preferred slip systems accounts for the ~ 2 GPa average nano-indentation hardness difference observed over the low concentration range.

Chapter 5

Creep Behavior

This chapter covers the results and analysis of the flexure creep experimental program. Bending creep was conducted in flowing argon and inert atmosphere for assessing creep behavior forming a bridge between local grain deformation mechanisms to macroscopic behavior. Experiments were conducted between 1400 -1800°C for measuring macroscopic stress and temperature dependent creep parameters for providing mechanistic deformation insights. A novel indentation deformation mapping experiment was developed for directly observing relative grain movements during the creep event and EBSD texture analysis was completed for assessing the local deformation character. Rate-controlling and creep accommodation mechanisms were proposed in the context of existing creep theory and a deformation mechanism was proposed. Preliminary ZrB_2 –WC solid solution alloy s were designed with the deformation mechanism findings and crept with anticipation of a creep-rate reduction. Solute-dislocation interaction models are proposed and qualitatively describe the preliminary observed creep behavior.

5.1. Results

5.1.1. Bending Creep

Creep behavior was assessed over the range of 1400°C to 1820°C and stresses from 16 to 97 MPa. Each stress-temperature condition conducted to achieve steady state creep conditions. To non-objectively extract steady state creep rates, a phenomenological approach was implemented, similar to that used in silicon nitride creep studies. Following the equation (Luecke, et al., 1995)

$$\dot{\varepsilon} = \dot{\varepsilon}_S + \dot{\varepsilon}_P[exp(-\varepsilon/\varepsilon_0)], \quad (5\text{-}1)$$

$\dot{\boldsymbol{\varepsilon}}_{\boldsymbol{S}}$, $\dot{\boldsymbol{\varepsilon}}_{\boldsymbol{P}}$ and $\boldsymbol{\varepsilon_0}$ are fitted regression constants representing steady state, primary creep rates and initial strain constant, respectively. For fitting purposes all displacement-time measurements were transformed to strain-rate vs. strain coordinates by calculating point-by-point derivative from strain-time curves. Experimental creep curves are shown in Figure 5- 1, Figure 5- 2 and Figure 5- 3. Figure 5- 1 displays 1400 - 1500°C (low temperature), high stress creep curves that have been smoothed due to inherent noise from extensometry method used at low strain values.[1] The steady state strain rate increases with stress and temperature. Additionally, large strains (>4%) were achieved within short periods of time, for high temperature experiments, with no evidence of a tertiary stage. Low temperature creep data was gathered over reasonable time periods, while high temperature experiments were limited by flexure displacements imposed by the loading fixture. Examples of as-crept Z20SB specimens are illustrate the abrupt change in creep behavior by the observed gross permanent deformation over a 100°C temperature interval, Figure 5- 4. Norton creep constants were derived from stress dependence and strain-rate Arrhenius-type plots as shown in Figure 5- 5 and Figure 5- 6. The stress dependency becomes nonlinear with increasing temperature, where at low temperature $n \approx 1$, becoming $1.7 \leq n \leq 2.2$ with increasing temperatures. Stress exponents were evaluated using the F-test at a 95% confidence interval, showing them to be statistically distinct between T<1500°C, 1500°C <T<1600°C and T>1600°C. . Therefore, the observed two orders of magnitude increase in strain-rate between 1500 and 1600°C indicates a creep mechanism change. The temperature dependency plot shows two distinct slopes at low (1400 - 1500°C) and high temperatures (T > 1600°C). Table 5- 1 summarizes activation energies calculated from these

[1] Quadratic smoothing routine was employed for low temperature creep curve smoothing using a span of 250 points at each evaluation point. Smoothing does not displace actual data points about the time variable and serves to extract the average displacement value.

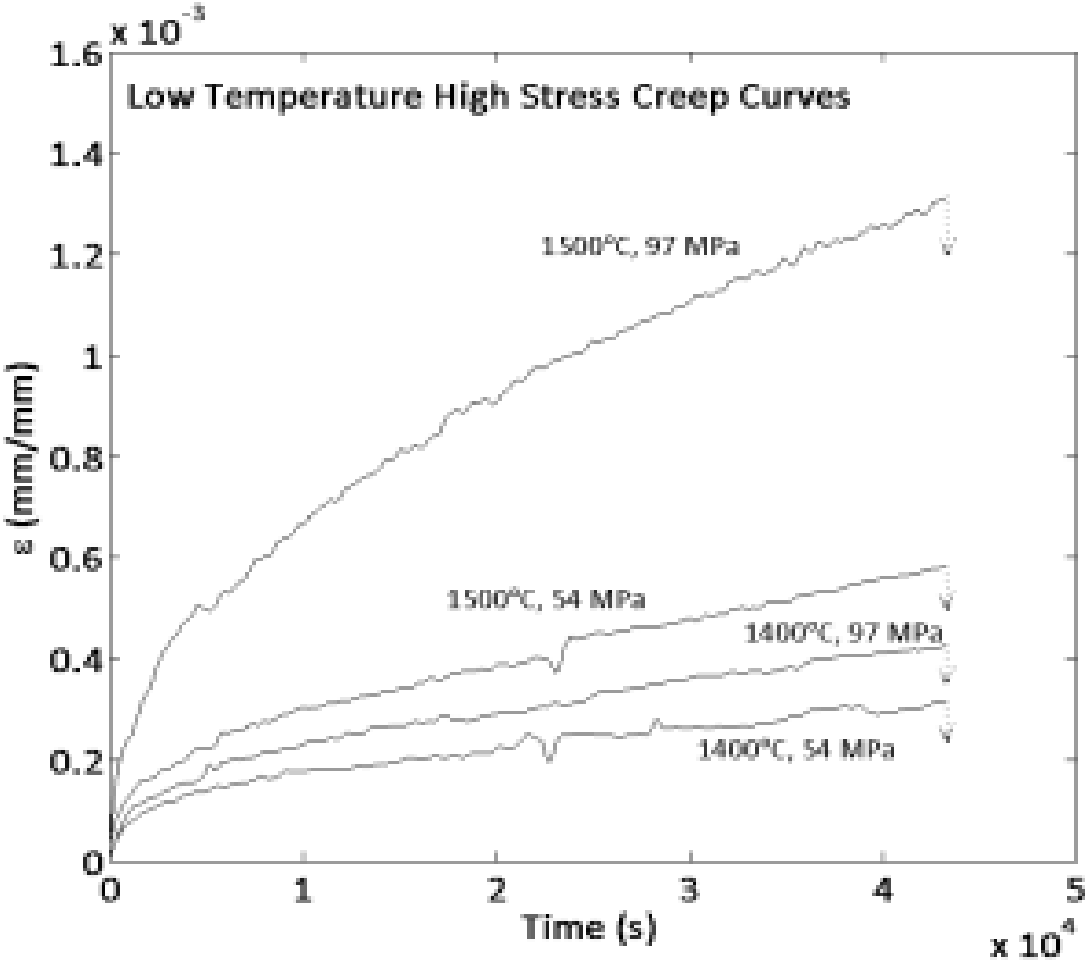

Figure 5-1: Low temperature (1400 - 1500°C) smoothed Z20SB creep curves through 97MPa. Dotted arrow breaks indicate experiment terminated based on time prior to failure. Samples did not fail during creep experiments.

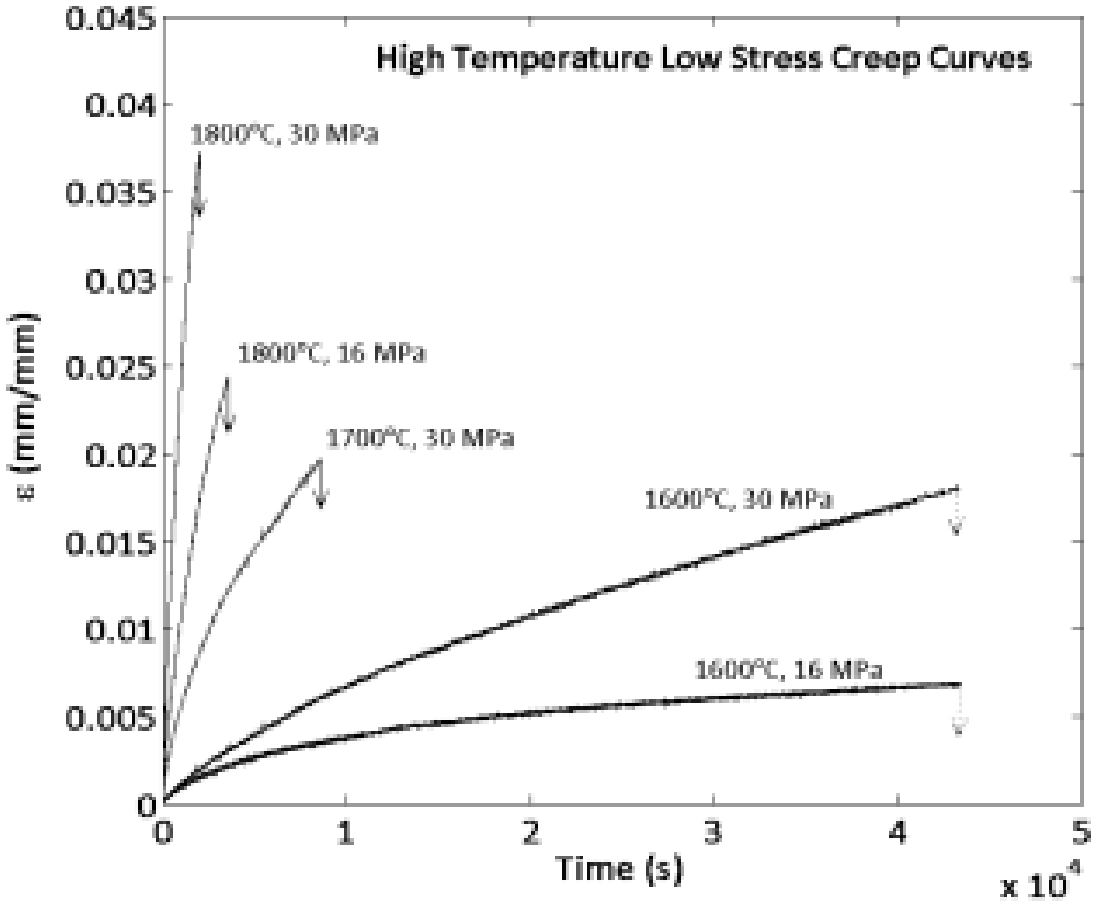

Figure 5-2: High temperature (1600 - 1800°C) high stress (>30 MPa) Z20SB creep curves. Solid arrow breaks indicate experiment terminated based on displacement limitations and dotted arrows indicate creep curve terminated based on time.

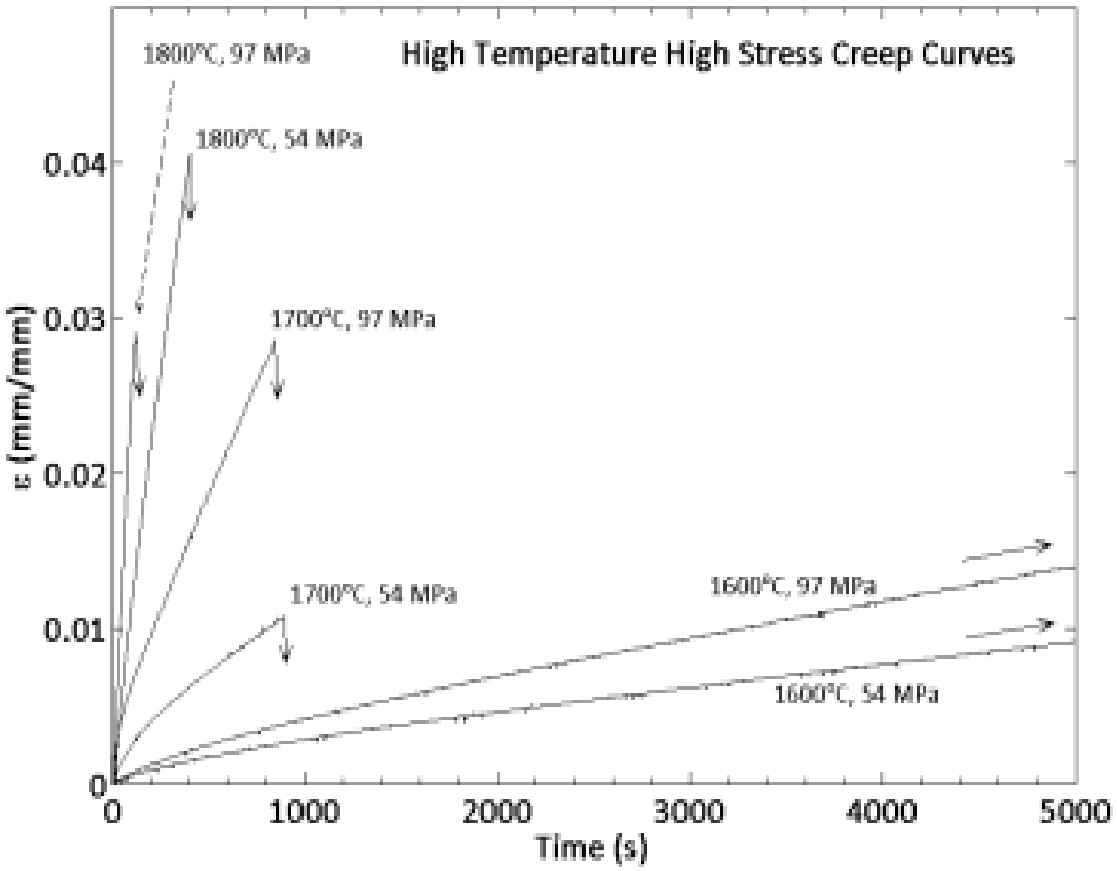

Figure 5-3: High temperature (1600 - 1800°C) low stress (<30 MPa) Z20SB creep curves. Solid arrow breaks indicate experiment terminated based on displacement limitations and continuous arrows show creep curves extend beyond the time axis.

data detailing two distinct, and statistically significant, rate limiting creep mechanisms. Furthermore, activation energies are independent of stress when greater than 54 MPa, at all temperatures, and show a statistically significant drop when approaching applied stresses near 30 MPa.

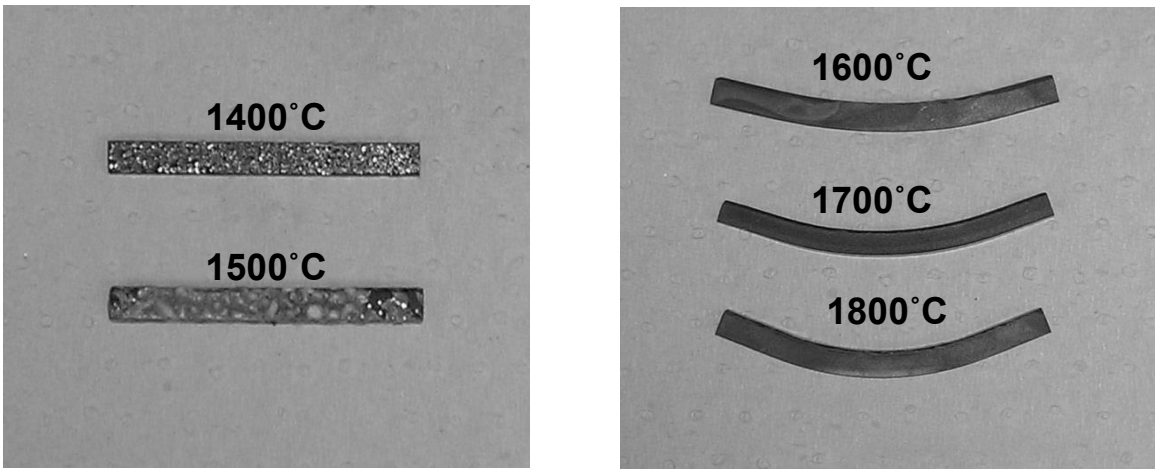

Figure 5- 4: As-crept Z20SB specimens illustrating macroscopic creep behavior under protective environment and constant load creep conditions.

Table 5-1: Measured activation energies and errors based on 95% confidence interval of the data for Z20SB composite.

Temperature	Slope #	Stress Range	Activation Energy
1600 - 1820°C	1	54-97 MPa	**639 ± 1 KJ/mol**
	2	16-30 MPa	**568 ± 10 KJ/mol**
1500 - 1600°C	3	54-97 MPa	**1608 ± 105 KJ/mol**
	4	16-30 MPa	**1321 ± 167 KJ/mol**
1400 - 1500°C	5	54-97 MPa	**364 ± 93 KJ/mol**

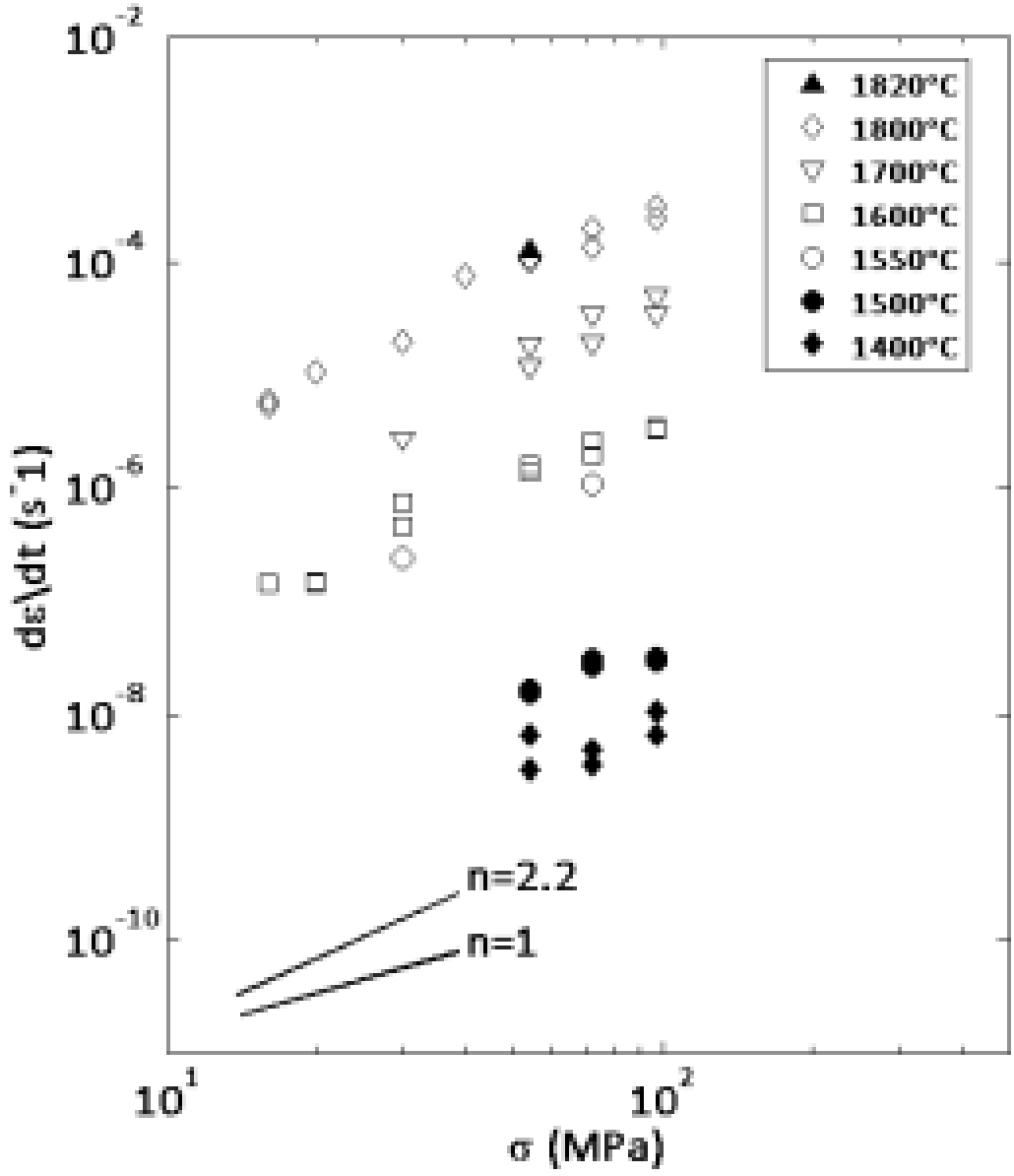

Figure 5- 5: Creep rate-stress dependent plot for the Z20SB flexure creep experiments.

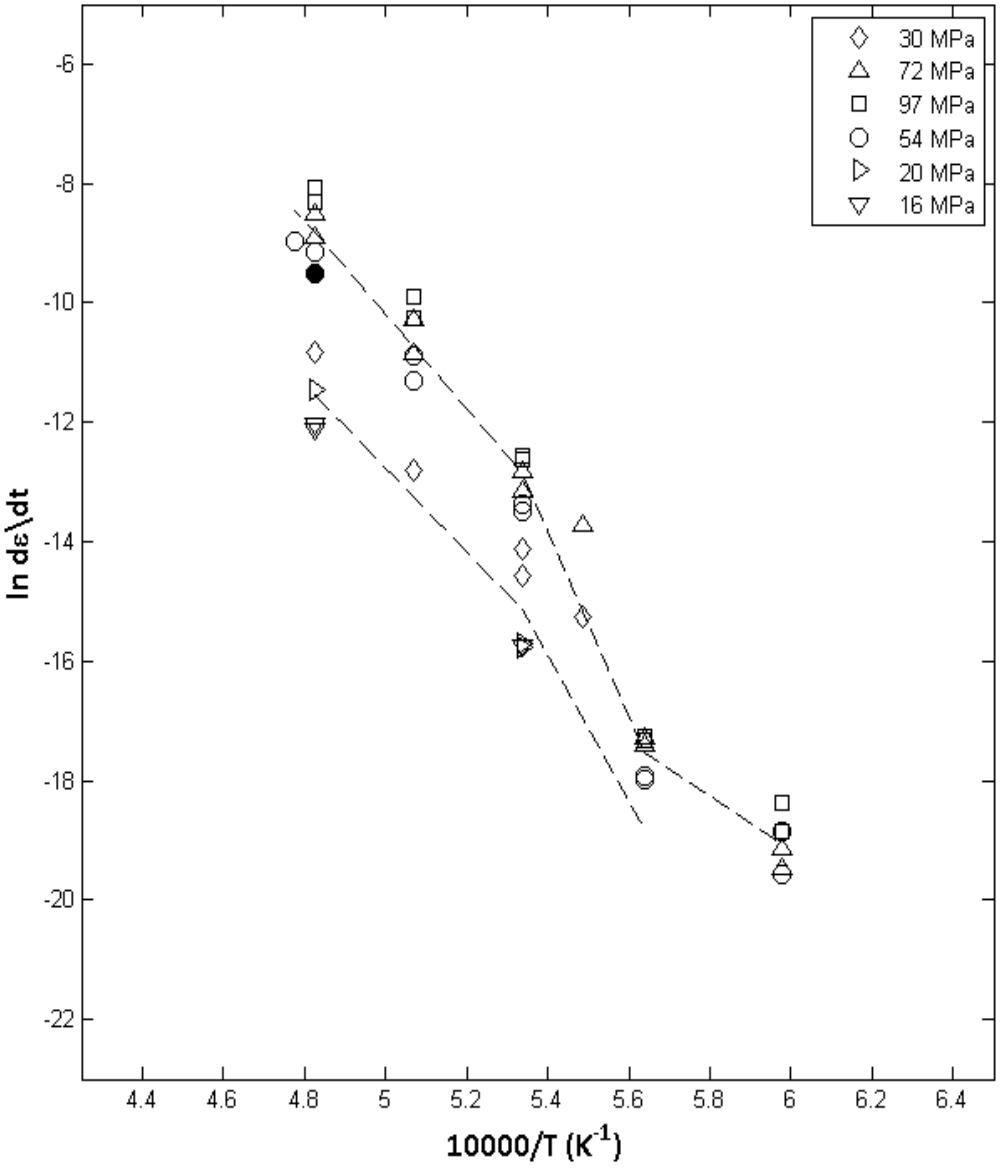

Figure 5-6: Creep rate-temperature dependence for the Z20SB flexure creep experiments. Dotted lines illustrate apparent stress dependent behavior.

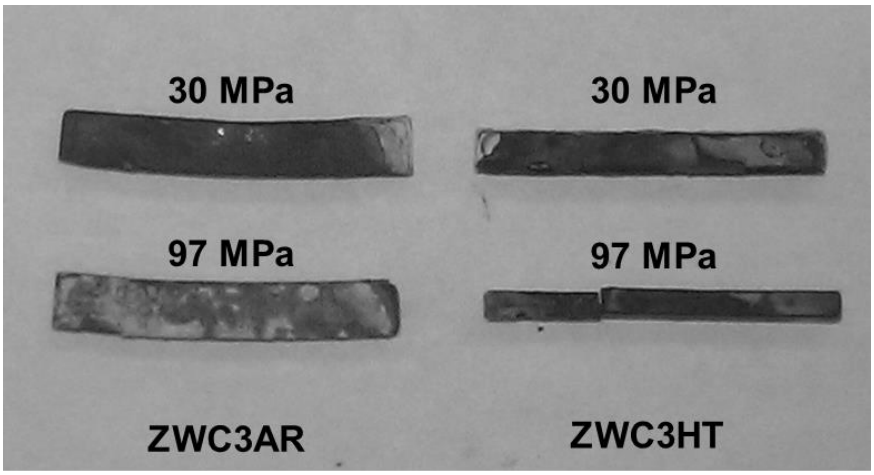

Figure 5-8: As-crept Z20SB specimens illustrating macroscopic creep behavior under protective environment and constant load creep conditions.

ZrB_2-WC alloy flexure experimental creep curves and derived steady state creep rates are shown in Figure 5- 7 and Table 5- 2 for 1800°C. Steady state creep rates were calculated based on Equation (5-1) using a similar procedure applied to the Z20SB composite creep curves. There exists a significant difference in steady state creep behavior and accumulated creep strain between the ZWC3AR and HT alloys over the stress ranges, despite a small number of experiments conducted. Examples of the as-crept specimens illustrate the creep and oxidation behavior, Figure 5- 8. Qualitatively, steady state creep rate decreases with stress and increasing WC concentration. An apparent tertiary creep stage was observed for the 30MPa ZWC3HT alloy with extended creep times, however, no evidence of surface cracks were observed underneath the oxide layer within the inner span region. Additionally, the 97MPa HT experiment ruptured underneath the loading pin after an apparent steady state behavior was achieved. The monolithic alloys show a ~two decade creep rate reduction and accumulated creep strain from the Z20SB composite for a given stress at 1800°C. Additionally, the alloy creep tests were restricted not by the deflection distance, but the oxidation rate having maximum scale thicknesses of ~0.200 mm resulting in an adjusted creep stress increase of 3MPa.

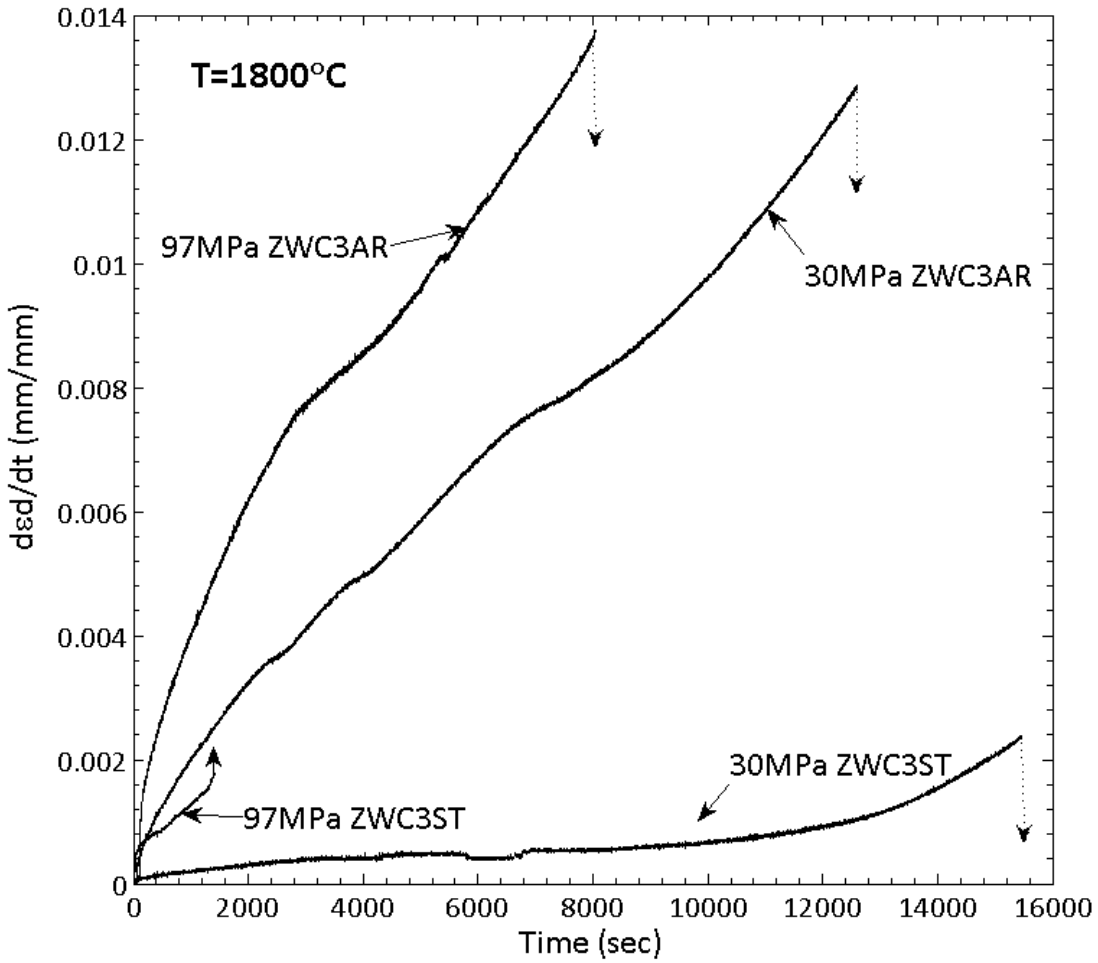

Figure 5-7: ZWCAR and HT alloy creep curves at 1800°C and 30 and 97 MPa constant stress. Dotted arrow breaks indicated experiment terminated based on time prior to failure and vertical solid arrow indicates specimen rupture.

Table 5- 2: ZWC3 alloy creep results.

Test label	Stress (Mpa)	Strain rate (s-1)
ZWC3AR_1	97	1.746E-06
ZWC3AR_2	97	1.214E-05
ZWC3AR_3	30	1.037E-06
ZWC3HT_1	97	7.980E-06
ZWC3HT_2	97	1.232E-06
ZWC3HT_3	30	1.296E-07

Cavitation was observed for all high temperature creep specimens in the tensile zone; negligible cavitation was measured in corresponding compressive creep zones, Figure 5- 9. However, unlike many ceramic creep investigations, cavitation does not show a linear relationship with strain suggesting cavitation does not solely contribute to the overall strain and strain-rate ((Luecke, et al., 1995), (Wiederhorn, Hockey and French 1999), (Lofaj and Wiederhorn 2009), (Krause Jr., et al., 1999) and (Yoon, Wiederhorn and Luecke 2000)). Cavitation was not observed in T<1500°C crept specimens, Figure 5- 10, suggesting that cavitation likely evolves along with the proposed mechanism change between 1500 and 1600°C. Table 5- 3 summarizes total strain and measured cavitation volume fractions (strain) for each T>1500°C

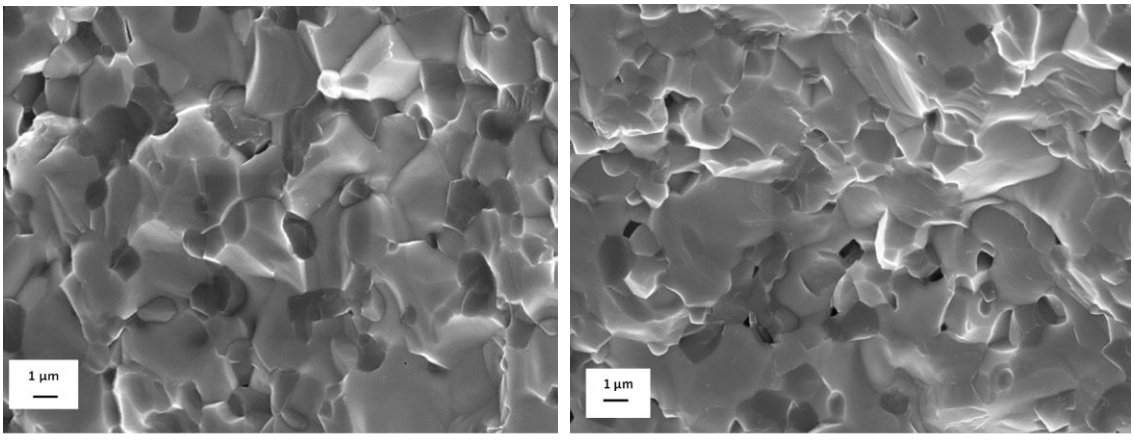

Figure 5-9: 1800°C, 97MPa creep compressive zone (left); Corresponding creep tensile zone (right). Cavitation is absent along compressive creep zones contrasting with noticeable cavitation along the tensile creep zone.

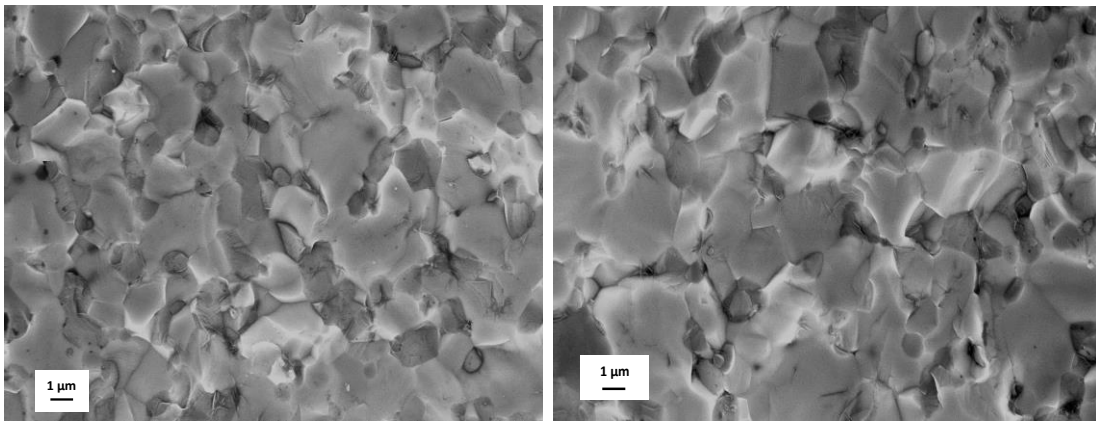

Figure 5-10: 1500°C, 97 MPa cavitation free compressive zone (left) and tensile zone (right). Tensile stress zone shows no triple point cavitation.

Table 5- 3: High temperature cavitation - strain data.

	Stress	ε_{Total}	f_v	Creep Time, ks
1800°C	16MPa	0.0430	0.0012	7.9
	20MPa	0.0429	0.0013	4.6
	30MPa	0.0408	0.0025	2.95
	54MPa	0.0480	0.0029	0.54
	72 MPa	0.0447	0.0025	0.25
	97 MPa	0.0309	0.0028	0.145
1700°C	30MPa	0.0248	0.0010	10
	54MPa	0.0226	0.0014	1.3
	72MPa	0.0354	0.0017	1.31
	97MPa	0.0351	0.0020	1.21
1600°C	16MPa	0.0070	0.0009	43.2
	20MPa	0.0060	0.0007	43.2
	30MPa	0.0244	0.0015	38
	54MPa	0.0347	0.0010	26.5
	72MPa	0.0371	0.0016	14.8
	97MPa	0.0209	0.0013	8.1
1550°C	30MPa	0.0082	0.0002	43.3
	72MPa	0.0223	0.0005	22.4

creep condition. Approaching 1550°C, negligible cavity fractions are measured for crept specimens with 2.23% tensile creep strain under 72 MPa constant stress. For T>1600°C and 54 to 97MPa, maximum strain and cavity volume fractions were achieved quickly. Microscopy studies show ZrB_2-SiC (Z-S) boundaries as preferential cavity nucleation sites, Figure 5- 11 .

1550°C specimens, regardless of stress, showed cavitation along only Z-S boundaries. Increasing temperature through 1800°C revealed increasing cavitation along ZrB_2-ZrB_2 (Z-Z) boundaries and SiC-SiC (S-S) boundaries (Figure 5- 11). Through 30 MPa, preferential cavitation along Z-S boundaries of 89% and increasing cavitation of 10% and 1% for Z-Z and S-S boundaries, respectively. Beyond 30 MPa, Z-S boundary cavitation decreased to 78% and Z-Z and S-S boundary cavitation increased to 17% and 5%, respectively.

Preliminary cavitation microscopy reveals similar spatial distributions to those found for the Z20SB composite along the tensile loading directions and negligible cavitation along the compressive loading direction, Figure 5- 12. Increasing the creep stress through 97 MPa shows a similar cavity spatial distribution to those at 30MPa. Microscopy reveals these cavities are equilibrium shaped cavities located along the ZrB_2 multi-grain junctions, Figure 5- 13.

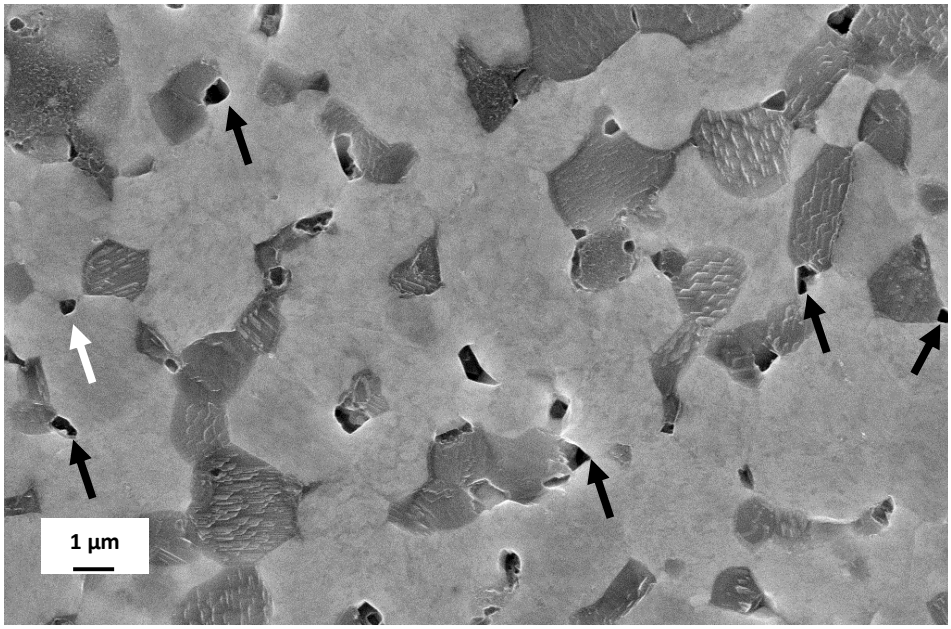

Figure 5-11: 1800°C, 97MPa polished and thermal etched section viewing the flexure tensile zone cavitation. Black arrows indicate ZrB2-SiC cavitation and white arrows ZrB2-ZrB2 cavitation.

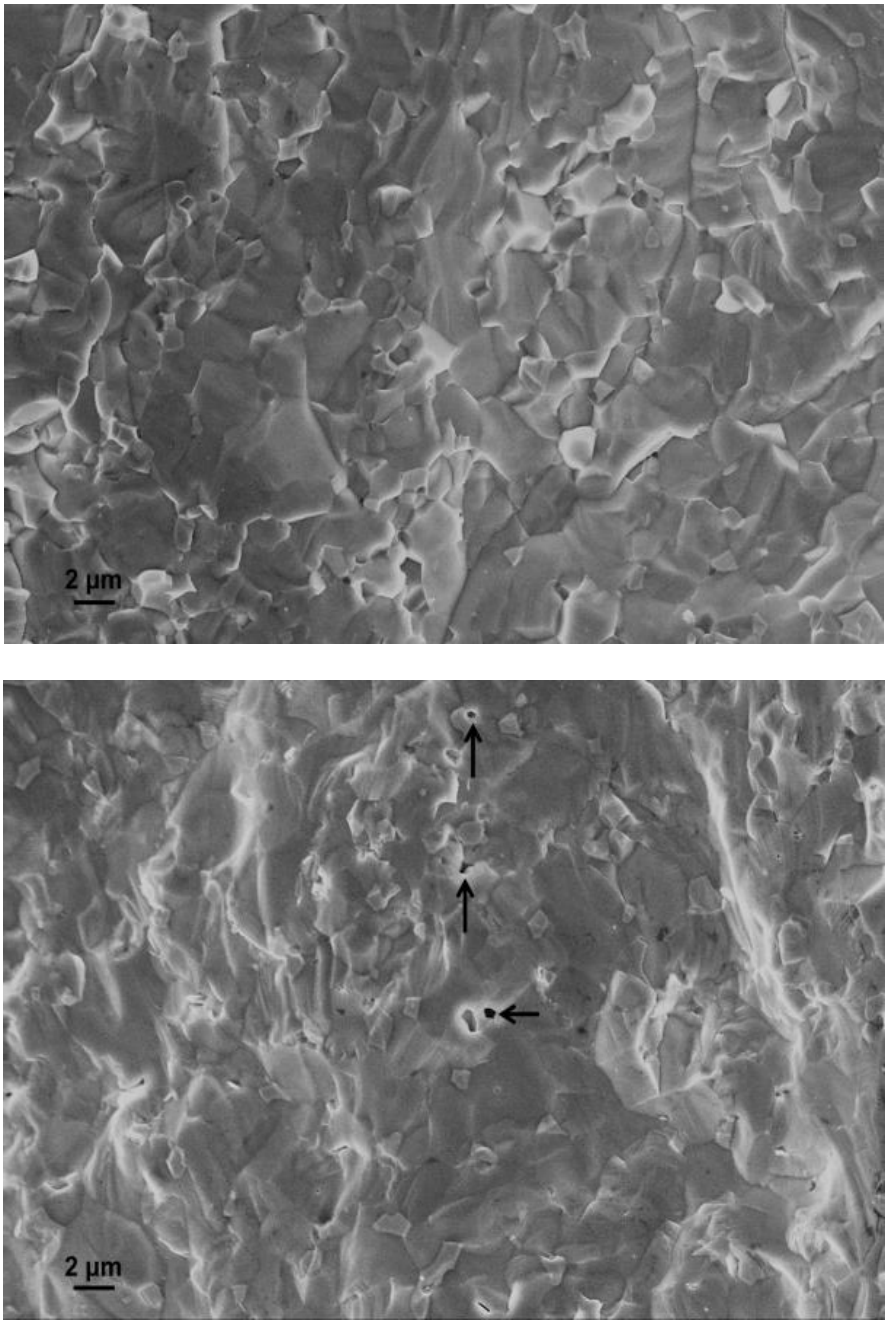

Figure 5-12: ZWC3AR alloy crept at 1800°C, 30 MPa showing negligible cavitation along the compressive region (top) and small cavities, pointed out by the solid arrows along the tensile zone (bottom).

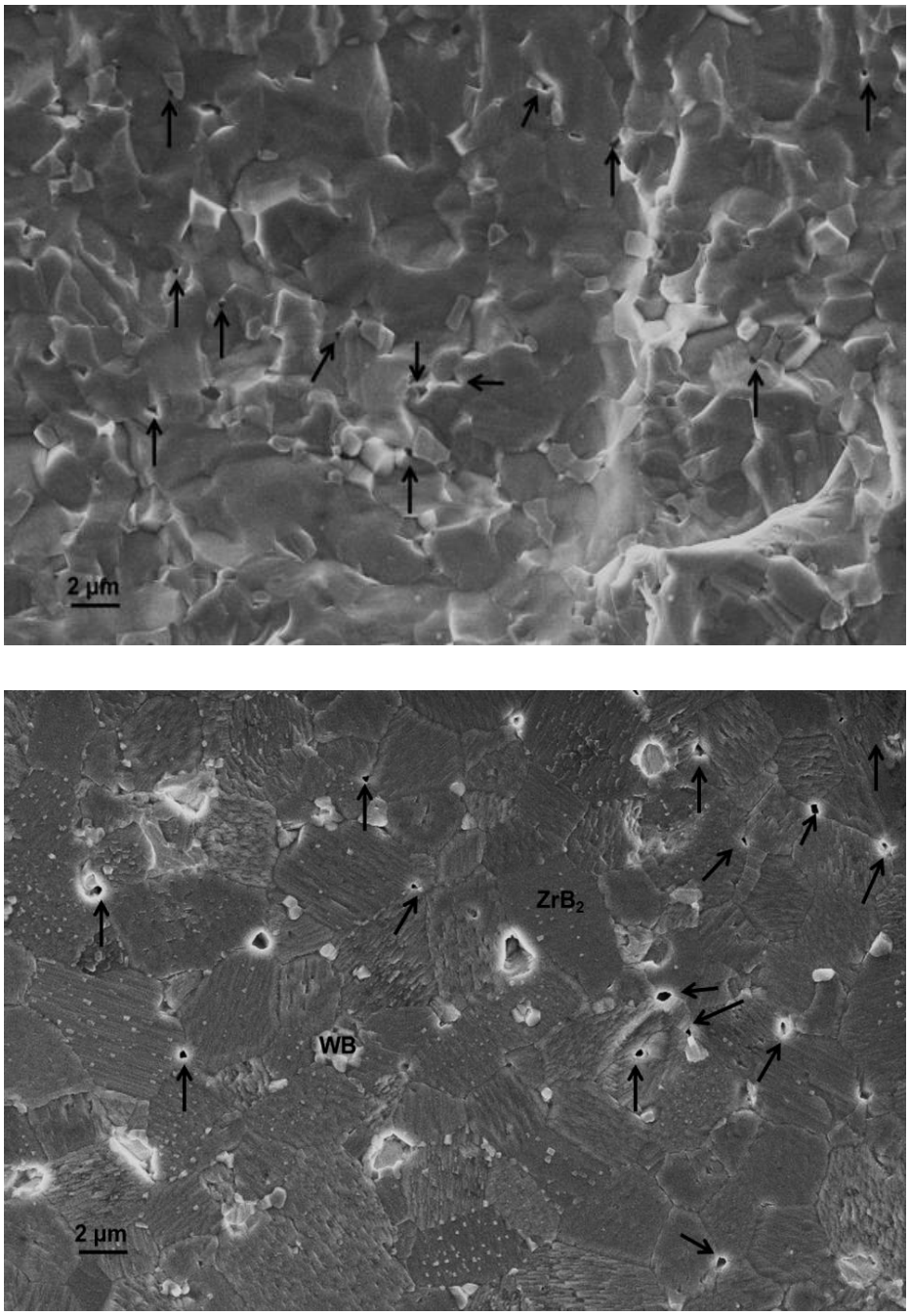

Figure 5-13: ZWC3AR alloy crept at 1800°C, 97 MPa showing cavitation (solid arrows) along the tensile zone (top). ZWC3HT alloy crept at 1800°C, 30 MPa in inert environment (bottom). Mild oxidation was observed.

5.1.2. High Strain Creep

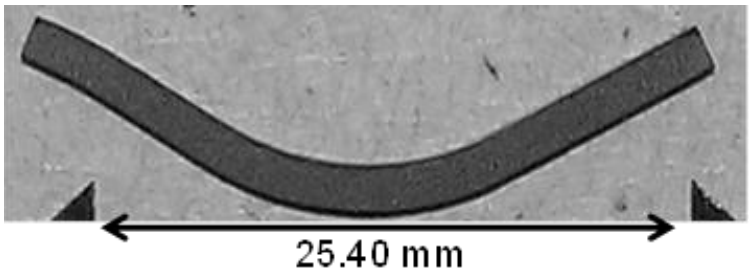

Figure 5-14: High strain Z20SB creep specimen tested at 1800C, 16MPa for 7.75 hrs under 3 psi pressurized Ar gas. Outer-fiber strains of 15.6% and 6.5% for tensile and compressive sides, respectively, using optical methods.

High temperature creep micro-mechanisms were assessed using a dead load vacuum-inert bending creep and indent tracking bending experiments on large strain (>8% strain) specimens, Figure 5- 14. The asymmetric deformation (13.5 - 15.5% tension, 6.5-7.6%, compression) shifted the neutral axis position to near 0.64-0.71. Linear intercept measurements provided comparisons with deformation modes of Lifshitz (L. Lifshitz 1963) or Rachinger (Rachinger 1952) – grain boundary sliding or lattice dominated deformations, respectively. Considering Lifshitz (L. Lifshitz 1963) grain boundary sliding, the number of interfaces would remain constant upon deformation, contrasting with an increasing number of ZrB_2 interfaces for Rachinger (Rachinger 1952) sliding. A count of ZrB_2 grain intercepts along an average intercept line length of 46 μm were 9.23 +/- 3.01 and 8.81 +/- 2.71 for normalized bar height ranges of 0.24-0.30 and 0.80 - 0.86 for tensile and compressive regions, respectively. Based on a 95% confidence level these data sets are statistically indistinguishable, suggesting the number of ZrB_2 intercepts did not change with strain. However, the metallographic measurements of the SiC particle spacing correlate well with creep strains measured from the beam curvature, Figure 5-15 and Table 5- 4. From a first inspection, Lifshitz (L. Lifshitz 1963) -type sliding may apply.

Table 5- 4: High strain optical and intercept strain measurements over the sampled total micrograph area for each normalized bar height position.

h_t/H	SiC Spacing	$\varepsilon_{Optical}$	$\varepsilon_{Intercept}$	Micrograph Area
	μm	%	%	μm^2
0.14 +/- 0.06	5.56 +/-0.25	12.48	13.12 +/- 4.88	115520.00
0.28 +/- 0.08	5.42 +/-0.33	9.39	10.14 +/- 6.80	10260.00
0.71 +/- 0.06	4.92 +/- 0.25	-0.02	0.00 +/-5.07	115520.00
0.83 +/- 0.08	4.73 +/- 0.29	-2.74	-3.86 +/- 5.94	10260.00
0.85 +/- 0.06	4.77 +/- 0.23	-3.11	-3.04 +/- 4.69	115520.00

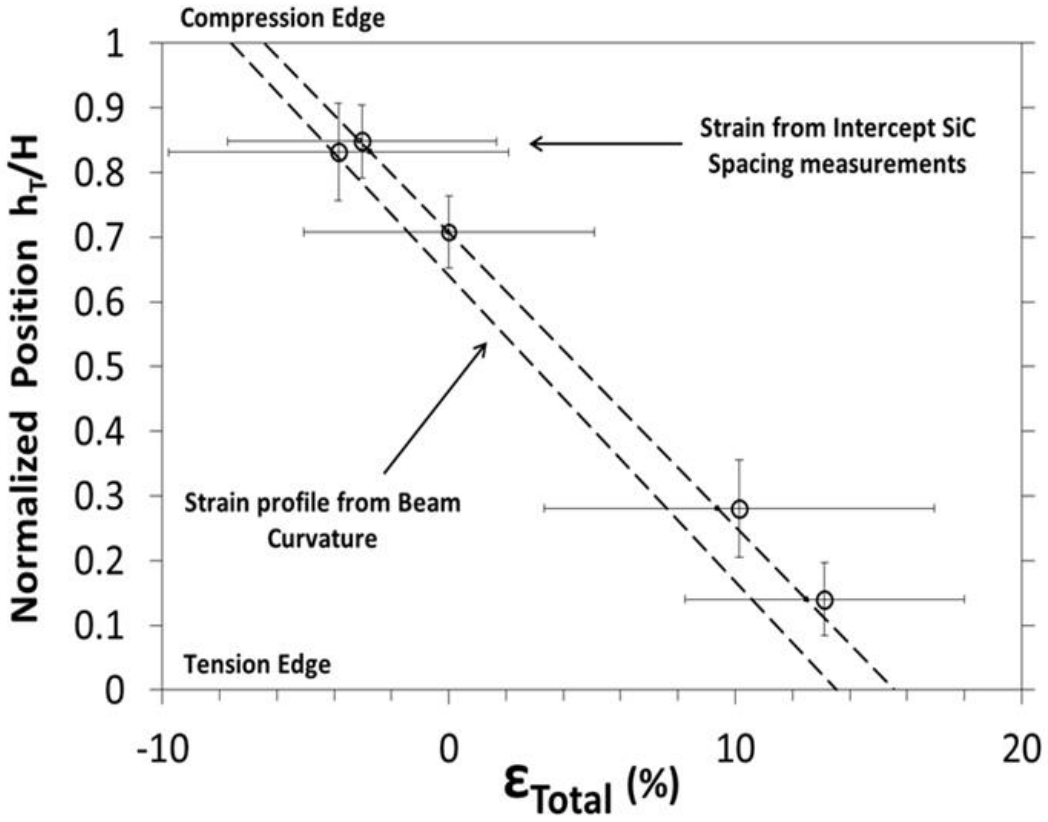

Figure 5-15: Optical beam curvature strain distribution (dotted line) with SiC spacing strain measurements (circles), Horizontal and vertical error bars represent the strain interval from the average SiC spacing distribution and micrograph locations.

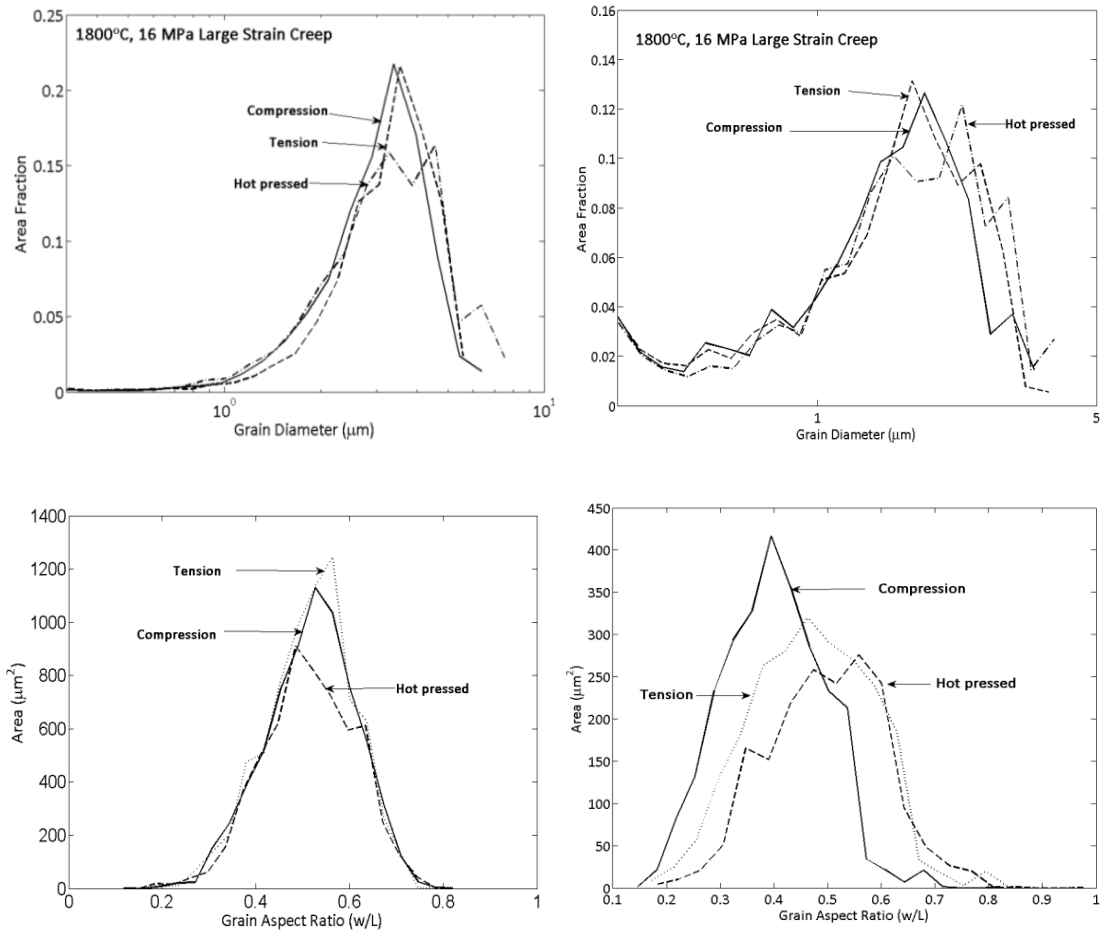

Figure 5-16: Grain size (top) and Grain aspect ratio (Bottom) for ZrB2 (left) and SiC (right) grains measured using EBSD method for compressive and tensile deformation regions.

EBSD microscopy was completed for compression and tension regions of the same crept specimen and compared to initial, hot-pressed, conditions of a different specimen. The equivalent strains are 13.72+/-0.62% and -4.60+/-0.62% for the tensile and compressive zone, respectively. General grain shape, size and crystallographic orientation statistics were compiled for each location and are shown in Figure 5- 16. The EBSD method, ZrB_2 grain sizes of 3.15 +/- 1.10 μm and 3.38 +/- 1.04 μm for the compressive and tension regions, respectively. Additionally, SiC grain sizes of 1.608 +/- 0.760 μm and 1.55 +/- 0.734 μm for the compressive and tension regions, respectively. These grain sizes show a negligible and statistically

insignificant change from the hot-pressed condition having grain sizes of 3.47 +/- 1.46 μm and 1.75 +/- 0.86 μm for ZrB_2 and SiC, respectively. Furthermore, ZrB_2 grain aspect ratios of 0.527 +/- 0.109, 0.519 +/- 0.108 and 0.518 +/- 0.111 were measured for the tensile, compressive and hot-pressed regions, respectively. The corresponding SiC grain aspect ratios of 0.472 +/-0.116, 0.463 +/- 0.116, and 0.498 +/- 0.107 were measured for the tensile, compressive and hot-pressed regions, respectively. Although, no statistical change of the ZrB_2 grain shape is detected due to the tensile and compressive loading, the differences in SiC grain shape indicate a gradual shift to elongated grains with the compressive side having a lower aspect ratio despite the lower creep strain as compared to the tensile zone.

Observed crystallographic texture appears minimal with creep strain, Figure 5- 17. From the inverse pole (IPF) map no distinct preferred orientation for both ZrB_2 and SiC, along the stress axis, is observed with respect to the standard crystallographic triangle for hexagonal materials. For both ZrB_2 and SiC, apparent random grain orientation was preserved with increasing creep strain. However, Limited texture development from the un-crept (Hot-pressed) to the crept (Compressive and Tensile zones) condition is evident, however, the times random magnitude are considered small compared to most texture analysis problems, Figure 5-18. “Micro texturing” was apparent in both ZrB_2 and SiC having dominant peak texture fiber orientations (Greek symbols) parallel to the bending stress axis, relative to the primary basal plane, (0001) pole and $[2\ \bar{1}\ \bar{1}\ 0]$ directions. We indicate these EBSD texture fiber orientation results graphically on Figure 5- 18 and as (ϕ, λ) slip plane pole and direction angle pairs in tabular form for reference throughout the forthcoming sections.

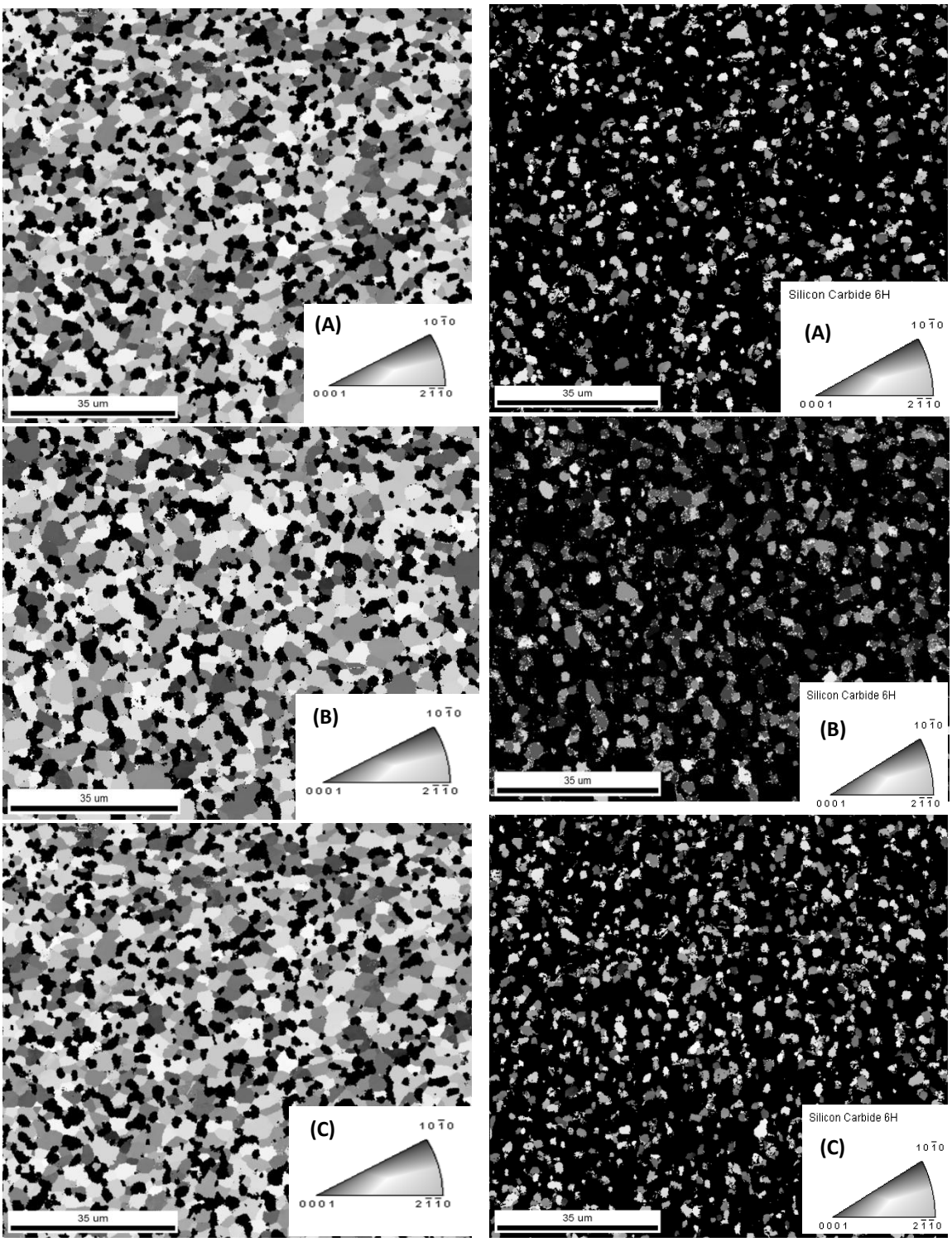

Figure 5-17: Inverse pole figure (IPF) maps of the tensile (a), Hot-pressed (b) and compression (c) deformation zones of a Z20SB crept composite for ZrB2 (left) and SiC (right). The Hot-pressed condition is provided as a reference for the initial conditions.

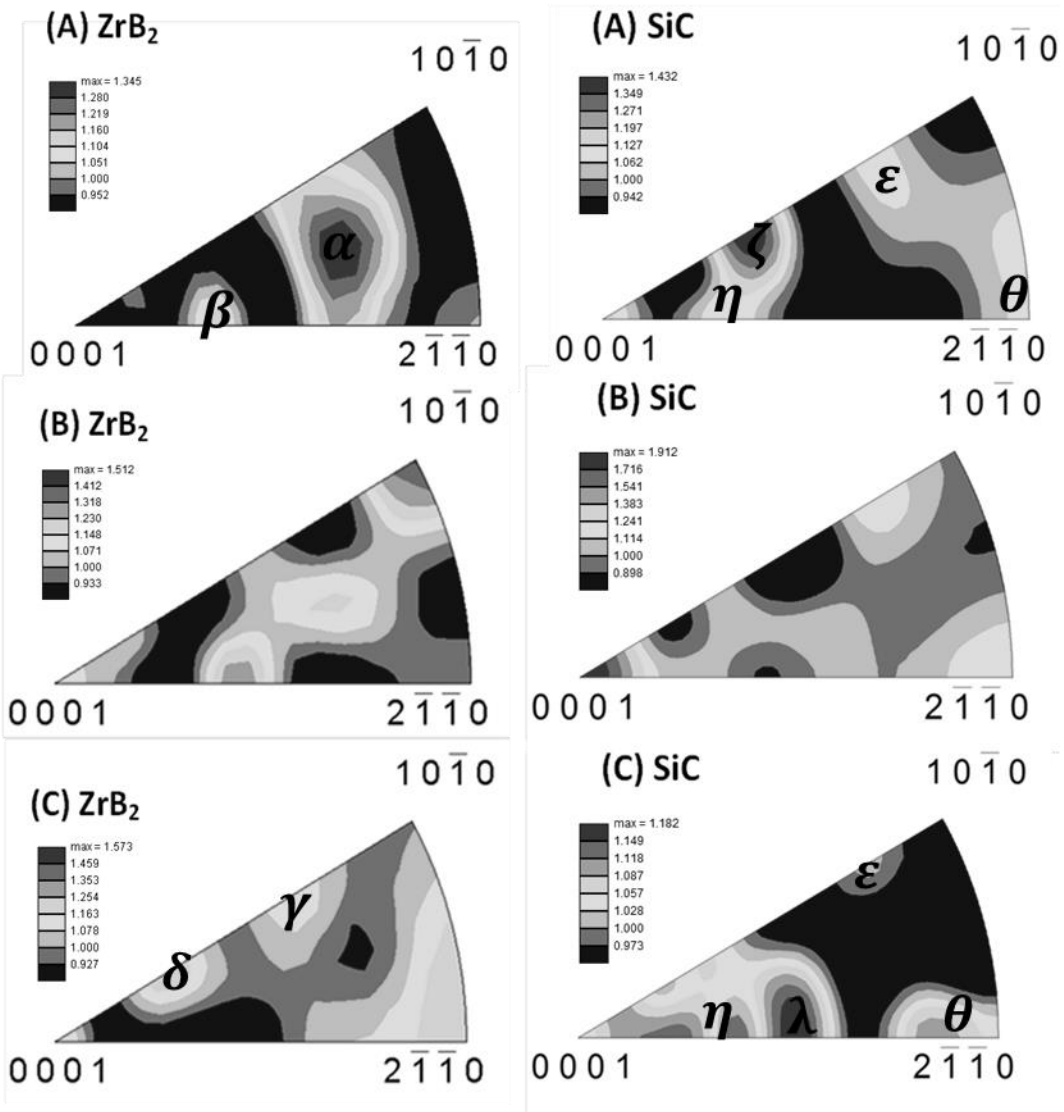

Figure 5-18: Inverse Pole Figure (IPF) texture plots for ZrB2 (left) and SiC (right) for the tension (a), hot-pressed (b) and compression (c) bending zones. Greek letters correspond to Schmid angle pairs for predominant fiber texture orientations.

Table 5- 5: Fiber Texture Directions from Figure 5- 18 and the equivalent stress vector positions relative to the (0001)-Pole and $[2\ \bar{1}\ \bar{1}\ 0]$ crystallographic directions.

		Fiber	Crystallographic Fiber Orientation Angle (+/- 1 deg)	
		Direction//Stress	(0001)-Pole (deg)	$[2\ \bar{1}\ \bar{1}\ 0]$ (deg)
Phase	Stress	Axis	ϕ	λ
ZrB2	Tension	α	69	25
	Tension	β	39	51
	Compression	γ	66	36
	Compression	δ	32	60
SiC	Tension	ε	64	36
	Tension	ζ	32	55
	Tension	η	22	68
	Tension	θ	90	0
	Compression	λ	49	41
	Compression	η	22	68
	Compression	ε	64	36
	Compression	θ	90	0

High Resolution Electron Backscatter Diffraction (HREBSD) post-processing of the fine scans were completed and reconstructed for detailing the quantitative and spatial GND density, Figure 5- 19 and Figure 5- 20. The following two observations were made: The SiC phase shows the highest GND density of ~$1x10^{12}$ cm^{-2}. Of critical importance to the present case however, the two grain boundary mantle types (ZrB2 and SiC-ZrB_2) demonstrate densities one to two orders of magnitude above the core. That of the mantle is $1x10^{11}$-$1x10^{12}$ cm^{-2} while the core is found to be $1x10^{9}$-$5x10^{10}$ cm^{-2}. The total GND density qualitatively follows the mantle-core hypothesis for both compression and tension zones.

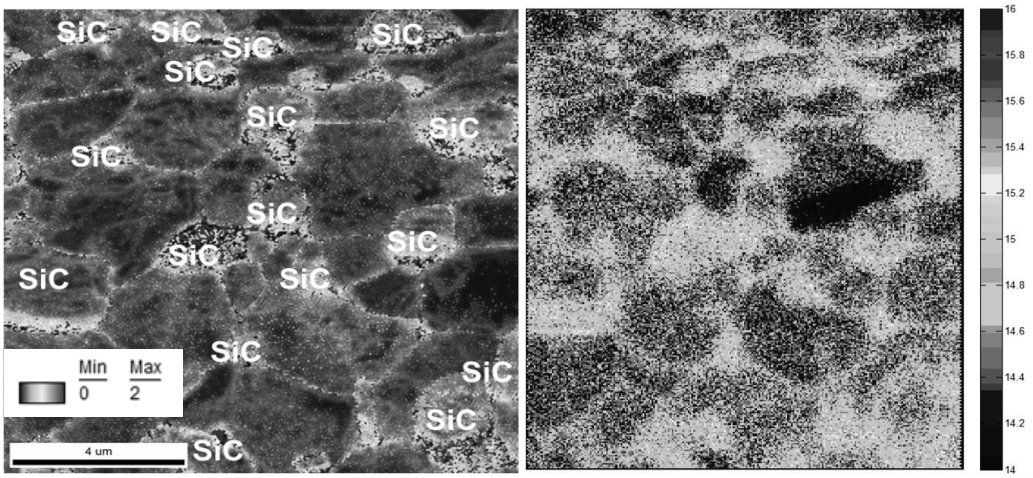

Figure 5- 19: Compression bending region KAM (left) and HREBSD GND concentration rendering (right) regions. SiC particles are labeled for reference and the GND color map is in log10 m-2 units.

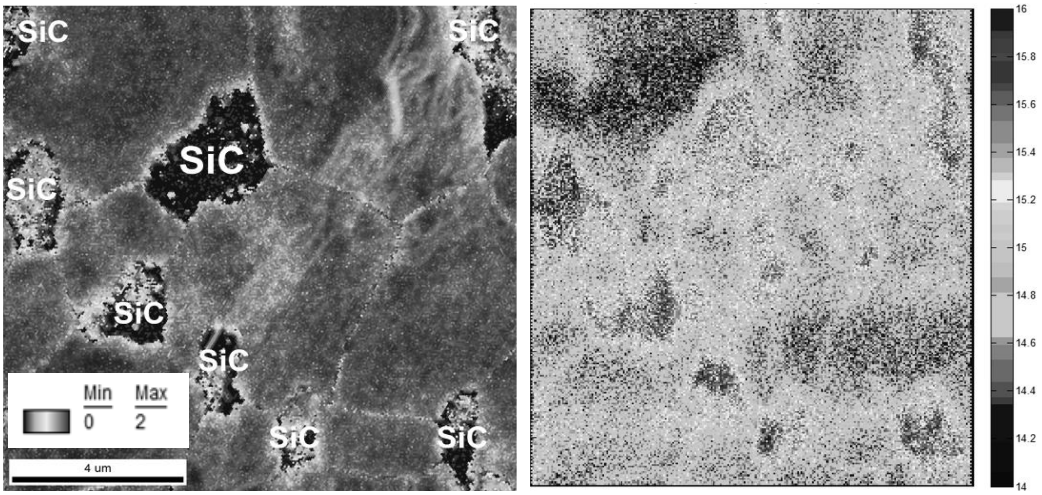

Figure 5-20: Tension bending region KAM (left) and HREBSD GND concentration rendering (right) regions. SiC particles are labeled for reference and the GND color map is in log10 m-2 units.

An indentation marking method for experimentally tracking grain deformation offers further insight into local ZrB_2 grain response to creep strains and local accommodation mechanisms, thereby linking local micro-mechanisms to the macroscopic behavior. We sampled all grains to determine a representative distribution of both intra- and inter-granular strains as shown in, Figure 5- 21. For comparison with the global creep strain, we consider the average strain of 0.080 +/- 0.064 , in good agreement with the optical measurements. The limited

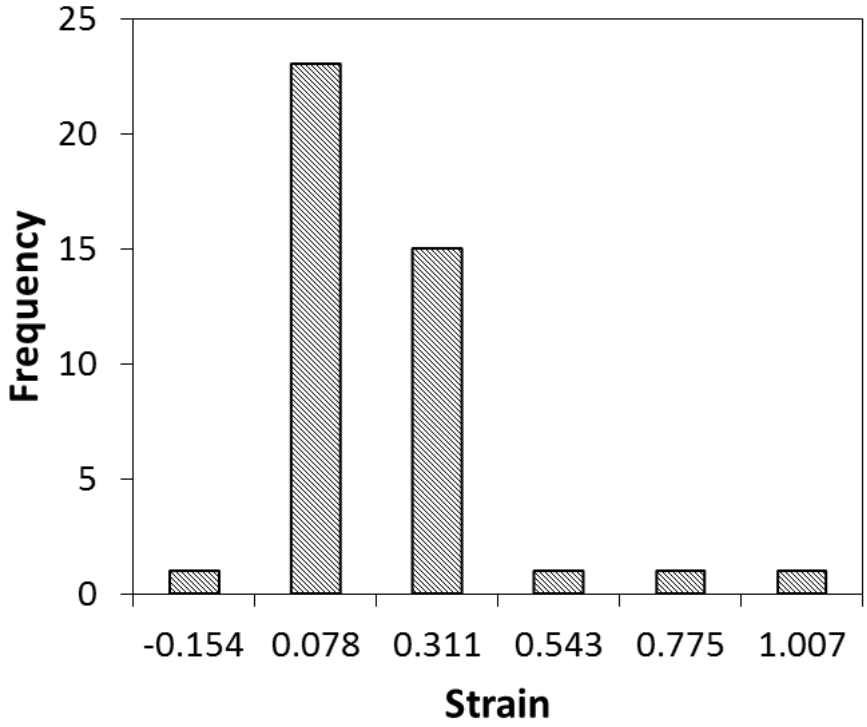

Figure 5-21: Local creep strain distribution based on indent-to-indent horizontal creep displacement changes from the un-crept reference frame.

compressive creep strain in these specimens precluded our gathering any compressive creep data. The total strain distribution was further partitioned into individual strains labeled rotational, translational and grain interior strains. For example, the angular position of two indents, within a single grain, was measured with respect to the horizontal axis of the micrograph. From this information, and comparing the angular misalignment between indents in the un-crept condition, the strains due to grain rotation were measured, Figure 5- 22. Furthermore, displacement changes between indents in the same grains were measured as deformation strains (Figure 5- 22) and purely translational strains, developed from horizontal displacement between indents of different grains, were measured (Figure 5- 22).

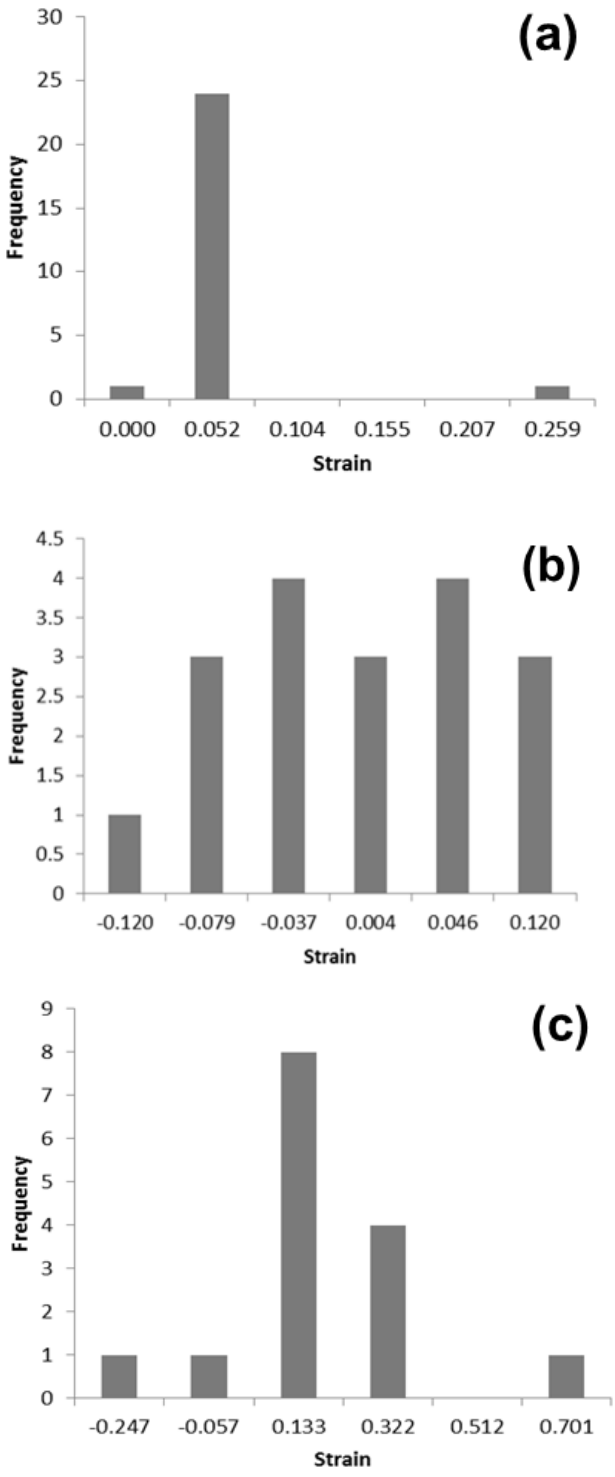

Figure 5-22: Partitioned strain distributions for (a) Rotational, (b) Grain interior and (c) Translational.

Probability distribution functions (PDFs) were fit for each distribution in Figure 5- 23 with an unbounded non-parametric PDF having a normal kernel bandwidth of 0.075 (The MathWorks, Inc. 2009). The contributions of individual strains (i.e. rotational, translation and grain interior) were determined from the probability fractions outlined, Figure 5- 23. Summation of the fractional areas pertaining to each individual creep strain compares well with the local creep probability of 1.07 and 1.00, respectively. These observations, coupled with EBSD measurements allows for local grain deformation mapping providing the necessary insights to the governing creep mechanisms.

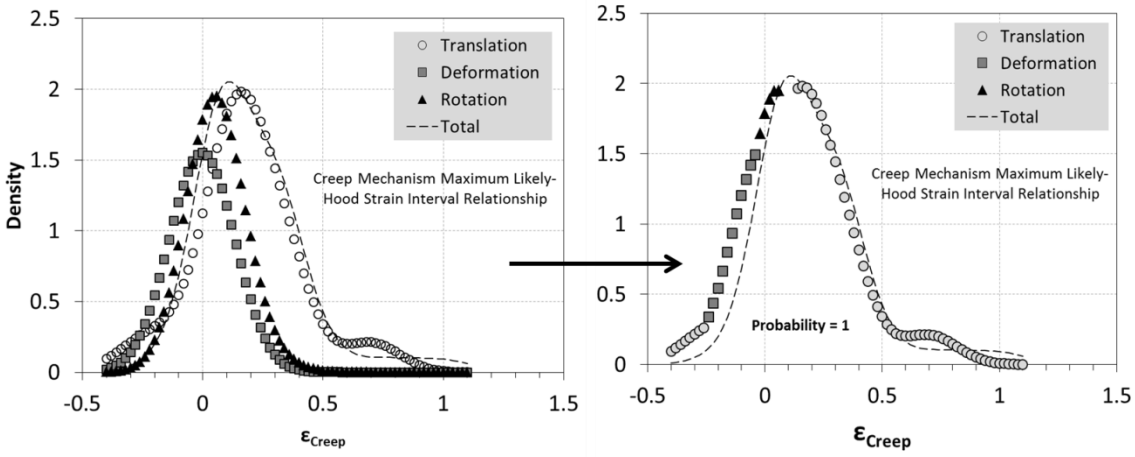

Figure 5-23: Local creep strain probability (dashed line) and PDF's (left) and maximum likelihood (right). The fractional probability of individual strains (i.e. rotational, translation and grain interior) identify the local creep contributions (shapes).

The IDM experiment was attempted for measuring local grain deformations of the ZWC3HT alloy. The experiment was conducted at 30 and 40MPa dead load on the same sample under inert conditions at 1800°C. Therefore, the creep time was extended beyond the 5 hr time-frame for the Z20SB composite. The creep strains compared favorably with the protective atmosphere creep experiments showing negligible strain precluding optical strain

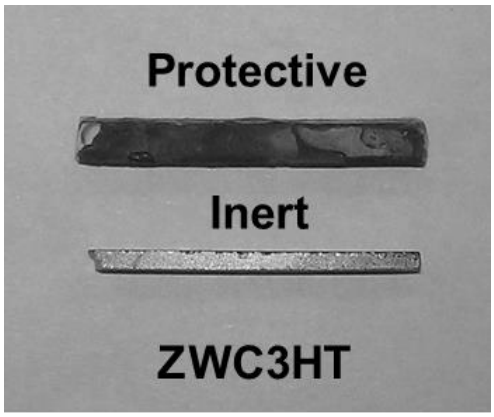

Figure 5-24: IDM crept specimen comparison with those conducted in the flowing argon setup. Creep experiments were conducted at 1800°C and stresses of 30 MPa and 30 and 40MPa for the protective and inert conditions, respectively.

measurements, Figure 5- 24. However, the alloy creep behavior was substantially reduced compared to the Z20SB composite. Indentation displacements measurements revealed negligible local strains. Grain rotations and translations were not observed as the deformations are well within the method uncertainty, Figure 5- 25. However, cavitation was observed near the indentation array suggesting small relative grain movements during creep.

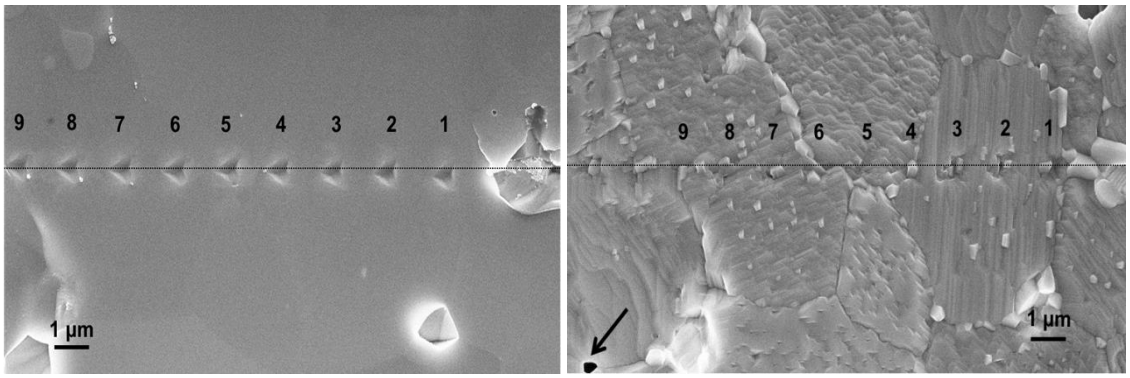

Figure 5-25: IDM results for the crept (right) and un-crept (left) condition. The solid arrow highlights a cavity formed during creep.

5.2. Analysis and Discussion

The Norton constants derived from our creep experiments conducted on the Z20SB composite suggest two dominant mechanisms separated by ~ 100°C and over a 2 decade

increase in creep rate. At low temperatures a diffusion controlled creep mechanism corresponds to n=1 and for high temperatures additional mechanisms are expected for n>2.

5.2.1. Low Temperature

At 1400°C and 1500°C and all stress levels, we determined a stress exponent of n = 1, and observed no cavitation along the tensile or compressive zones suggesting diffusion creep mechanisms operating. Classical diffusion mechanisms include vacancy diffusion from grain boundaries perpendicular to the applied stress, coupled with the slowest atomic species finding the most likely diffusion path (i.e., grain boundary or lattice). Grain elongation accounts for accumulated strain while grain boundary sliding accommodates this process as suggested by Coble (R. Coble 1963), Nabarro (F. R. Nabarro 1948), Herring (C. Herring 1950) and Cannon (Cannon and Langdon 1988). Creep rates are defined by' (Cannon and Langdon 1988)' (C. Herring 1950), (F. R. Nabarro 1948), (Hynes and Doremus 1996)

$$\dot{\varepsilon} = \frac{AbG^n D}{KT}\left(\frac{b}{d}\right)^p \left(\frac{\sigma}{G}\right)^n, \tag{5-2}$$

where A, n and p are constants, *b* the Burger's vector, *D* the respective diffusion coefficient (D_{gb} for grain boundary and D_l for lattice), *G* is shear modulus, *d* grain size, σ applied stress and *KT* has the usual significance. For grain boundary diffusion creep (Coble) (R. Coble 1963), (Cannon and Langdon 1988), (Hynes and Doremus 1996) creep n = 1, p=3 and $D=D_{gb}$ where for lattice diffusion creep n=1, p =2 and $D=D_l$. Grain size dependence (p) and numerical constant differ between both diffusion mechanisms where Coble creep is favored at low temperature and fine grain sizes contrasting with high temperatures and large grain sizes favoring Nabarro (1948) and Herring (1950) creep. However, under constant grain size conditions, the transition to Nabarro (1948) and Herring(1950) creep can occur because of lower grain boundary diffusion activation energy.

Additional linear models exist, particularly, Lifshitz (1963), Raj and Ashby (1971), Harper-Dorn and solution precipitation creep through viscous intergranular phase. Raj and Ashby (1971) and Lifshitz (1963) depicted accumulated strain from grain boundary sliding accommodated by diffusion. The accommodation process is considered a mechanism contributing least to the overall creep rate and therefore vacancy diffusion occurs in response to grain boundary sliding. However, considering both classical diffusion and diffusion accommodated grain boundary sliding models, both are coupled, if the microstructure is to remain continuous. Ashby and Verrall (1973) suggested diffusion accommodated flow dominating at low temperatures and stresses and predicted creep rates 7 fold faster than those predicted by Coble (1963) and Narbarro (1948) and Herring (1950). From this work Harper-Dorn creep is described by n=1 and p=0 predicting creep rates 1000 times those predicted by diffusion processes. For this model dislocation glide into barriers and subsequent escape by climb is assumed rate-controlling ((Hynes and Doremus 1996), (T. Langdon 2002)). Typically materials with large grain sizes (D>400 μm), owing to p = 0, are subject to Harper-Dorn creep ((Hynes and Doremus 1996), (T. Langdon 2002)). Solution precipitation falls within this category for diffusion creep; however, a viscous phase must be present in sufficient quantity ((Hynes and Doremus 1996), (Raj and Chyung 1981)). Solution-precipitation creep reportedly dominates under compression in glass containing silicon nitride ceramics where vacancy diffusion through an amorphous inter-phase becomes rate-controlling ((Wiederhorn, Hockey and French 1999), (D. S. Wilkinson 1998) and (Krause Jr., et al., 1999)). Intragranular amorphous phases have been reported for ZrB_2 based UHTC's (Jayaseelan, et al., 2011) however, unless purposefully alloyed with glass-forming sintering aids ((Monteverde, Guicciardi and Bellosi 2003) and (Sciti, et al., 2011)), the majority of like and unlike phase boundaries have been reported to be glass free at room temperature (Jayaseelan, et al., 2011). Therefore, our focus is on grain boundary and or

lattice diffusion at T≤1500°C.

Comparisons between the experimental data and creep theory reveals grain boundary creep as the dominant creep mechanisms over the measured stress interval. Lattice diffusion paths may be considered as presented by Cannon and Langdon (1983). Because deformation of the structure depends upon deformation of three competing boundary types, SiC – SiC (S-S), ZrB_2 – SiC (Z-S) and ZrB_2 – ZrB_2 (Z-Z), each grain boundary diffusion path must operate sequentially where the slowest controls creep. If Nabarro (1948) and Herring (1950) creep is included, the deformation and hence vacancy flow must also follow a sequential order. The Z20SB composite contains 1:1 balance of Z-S and Z-Z grain boundaries with < 10% S-S creating two preferential vacancy diffusion paths with differing diffusion properties. Each diffusion mechanism behaves non-sequentially and independently. The following relationships are developed accounting for each boundary type where *Z, S* and *ZS* are ZrB_2- ZrB_2, SiC- SiC, and ZrB_2-SiC boundaries respectively. However, owing to a lack of grain size-creep rate data, the relative amounts of each diffusion mechanism were assessed using the measured activation

$$\frac{1}{\dot{\varepsilon}_{Coble}} = \frac{1}{\dot{\varepsilon}_Z} + \frac{1}{\dot{\varepsilon}_S} + \frac{1}{\dot{\varepsilon}_{ZS}}, \tag{5-3}$$

$$\frac{1}{\dot{\varepsilon}_{N-H}} = \frac{1}{\dot{\varepsilon}_Z} + \frac{1}{\dot{\varepsilon}_S} \tag{5-4}$$

and

$$\dot{\varepsilon}_{Total} = \dot{\varepsilon}_{Coble} + \dot{\varepsilon}_{N-H} \tag{5-5}$$

energy comparison and theoretical comparisons with measured creep data.

Assuming Coble (1963) creep is preferred at low temperatures and fine grain sizes, Z-Z or Z-S grain boundary diffusion appears as a limiting path. Variations in ZrB_2 grain boundary

activation energy have been reported including derived ZrB_2 polycrystalline diffusion creep energies (Talmy, et al., (2008) and Kats, et al., *(*1981)) and shear viscosity energies (Kuzenkova and Kislyi 1966) of 130-186 and 242-590 KJ/mol, respectively. Additionally, activation energies, derived from creep experiments, for ZrB_2-25% SiC and ZrB_2-20% ZrC of 276 KJ/mol and 272 KJ/mol, respectively, have been reported. Kislyi and Kuzencova (1966) reported activation energy of 379 +/- 46 KJ/mol for 15% Mo-ZrB_2 monolith based on shear viscosity measurements. Both the composite and monolithic polycrystalline activation energies reported represent grain boundary diffusion as the dominant creep deformation or sintering mechanism. Considering Nabarro (1948) and Herring (1950) creep, the activation energy would correlate with the self-diffusion energy of 678 ± 114 KJ/mol (Kuzenkova and Kislyi 1966). The measured apparent activation energy of 364 ± 93 KJ/mol agrees well with those reported by Kislyi and Kuzencova (1966), Talmy, et al., (2008) and Kats, et al., (1981) suggesting either Z-S and/or Z-Z grain boundaries are the preferred path and rate-controlling From diffusion data provided by Datta (Datta, Bandyopadhyay and Chaudhuri 2002), α-SiC polycrystalline diffusion yields an activation energy ~ 490 KJ/mol and $D_{gb} \sim 10^{-10}$-10^{-9} cm^2/s between 1400-1500°C; ZrB_2 grain boundary diffusion of 10^{-11}- 10^{-12} cm^2/s were derived from sintering data ((Kuzenkova and Kislyi 1966), (R. L. Coble 1970)), and compared to values derived from Kaufman and Claugherty (1963). There appears to be a 1-3 decade difference in ZrB_2 and SiC grain boundary diffusion coefficients indicating ZrB_2 grains restrain S-S grain boundary sliding resulting from faster SiC cation/anion diffusion along the limited number of S-S boundaries. The creep rate predicted by the Coble (1963) formulation for the SiC particulate predicts a creep rate 3 decades faster than those observed, Figure 5- 26.

Table 5- 6: Low temperature grain boundary diffusion model inputs for 1400°C and 1500°C creep.

	ZrB2		SiC	
b, (Å)	3.16		3.1	
d, (μm)	3.1		1.5	
k, $(Jmol^{-1})$	$1.381\text{x}10^{-23}$		$1.381\text{x}10^{-23}$	
Ω, (Å^3)	21.5		21.7	
δ , (Å)	6.32		6.2	
	1400°C	**1500°C**	**1400°C**	**1500°C**
G, (GPa)	183	179	176	174
D_l,(cm^2s^{-1})	$4.08\text{x}10^{-15}$	$3.08\text{x}10^{-14}$	$1.55\text{x}10^{-14}$	$4.66\text{x}10^{-13}$
D_{gb}, (cm^2s^{-1})	$2.56\text{x}10^{-12}$	$1.00\text{x}10^{-11}$	$3.64\text{x}10^{-10}$	$2.74\text{x}10^{-09}$

Theoretical model considerations provide additional support for the low temperature grain boundary creep deformation of this Z20SB composite; model inputs are shown in Table 5-6 for ZrB_2 and SiC at 1400 and 1500°C. Figure 5- 26 illustrate the creep-rate prediction for the Coble formulations and show the sequential nature of the phase contributions to creep. As mentioned earlier, Nabarro (1948) and Herring (1950) creep may contribute as suggested by Cannon and Langdon (1983) and shown in Equation (5-6).

$$\dot{\varepsilon} = 9.3\frac{bGD_l}{KT}\left(\frac{b}{d}\right)^2\left(\frac{\sigma}{G}\right)\left[1 + 3.6\frac{D_{gb}}{D_l}\left(\frac{\delta}{d}\right)\right] \tag{5-6}$$

combines grain boundary (D_{gb}) and lattice (D_l) diffusion vacancy transport paths with δ representing the grain boundary width. Creep rate prediction based on Equation (5-6) yields a decade increase in creep-rate over those experimentally observed. Considering only Nabarro (1948) and Herring (1950) creep, predictions show a ½ decade faster predicted creep rate contrasting with the Coble (1963) format within a factor of three for ZrB_2 grain boundary diffusion. From the activation energy argument, the apparent activation energy scales with those measured for grain boundary controlled diffusion. Application of the Ashby-Verrall (1973) diffusion model reveals similar results as those predicted by Equation (5-6) despite the this model historically predicting faster creep-rates by a factor of seven (Ashby and Verrall

1973). In the limit of small strains Ashby and Verrall (1973) suggest their formulation reduces to Equation (5-3) and only at large strains does their model differentiate from diffusion creep proposed by Coble (1963), Nabarro (1948), Herring (1950), Raj and Ashby (1971) and Lifshitz (1963). Invoking the sequential nature of diffusion creep between the three boundary types (Equation (5-2)) encountered in the Z20SB composite predicts the creep rate within a factor of two.

Discrepancies in apparent activation energy and predicted creep rate may arise due to impurity solute effects on diffusion or grain boundary misorientation and coherency ((Cannon and Langdon 1988), (Hynes and Doremus 1996), (Lane, Carter Jr. and Davis 1988). The Z20SB composite is known to have W impurities in solid solution with ZrB_2 phase, impeding solute diffusion, thereby increasing the activation energy. It is not understood whether tungsten diffuses to grain boundaries during sintering, however, we assume an effect on either lattice or grain boundary diffusion. Z-S coherent and incoherent interfaces (Jayaseelan, et al., 2011) have been reported for similar composites and would suggest sluggish ZrB_2 cation/anion coherent boundary diffusion. It is assume the atomic mobility along Z-S and Z-Z high angle special and coherent boundaries are rate limiting and may contribute towards an increasing activation energy. It is not possible to calculate strain rate contributions without knowledge of Zr^{2+} and B^- self diffusion data through ZrB_2 and ZrB_2-SiC interfaces. Therefore, the proposed low temperature creep-rate prediction assumes the Z-S and Z-Z boundaries contribute equally to the creep rate.

5.2.2. High Temperature

An apparent creep mechanism shift is evident when approaching temperatures greater than 1500°C. From the Arrhenius plot (Figure 5- 6) and Table 5- 1 there exists two transitions with increasing temperature beyond 1500°C: (1) increasing activation energy between 1500 -

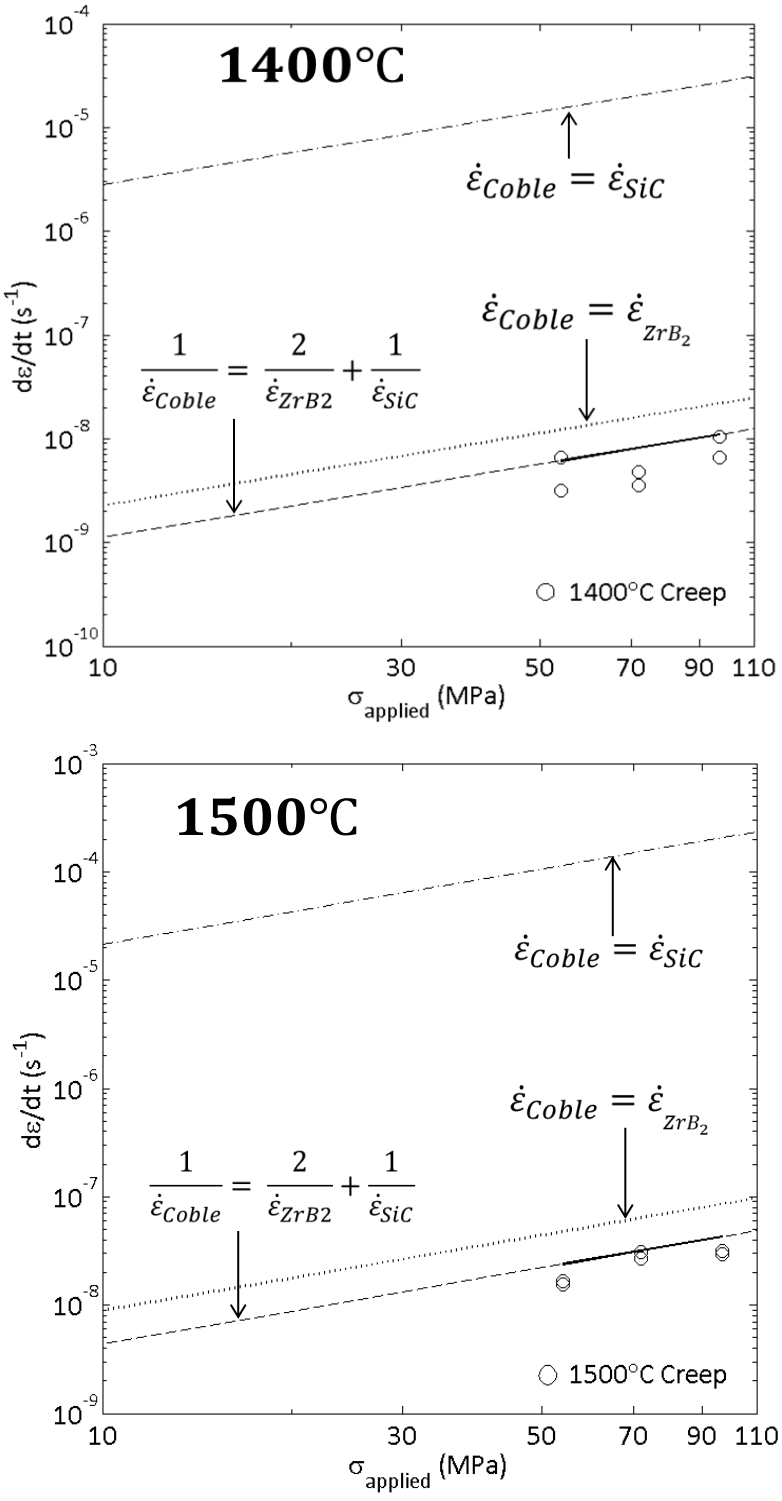

Figure 5-26: Low temperature creep models with the open circles representing experimental data, the solid line represents known prediction range and the hashed line indicates model predicted intervals.

1600°C and (2) reaching an intermediate value beyond 1600°C. The former case suggests non-sequential creep mechanisms may account for the abrupt non-linear stress dependency while the subsequent shift to lower activation energy suggests a transition to sequential creep mechanisms (Hynes and Doremus 1996). Above 1500°C creep behavior becomes non-linear and is accompanied by a two decade strain-rate increase.

Ceramics and metals research have shown multiple sources for creep non-linearity where either grain boundary sliding, cavitation/damage and/or intragranular dislocation creep may dominate. Reference to the various models have been tabulated and discussed to length in Chapter 2. However, the forth coming sections attempt to explain the creep deformation behavior of the Z20SB composite in the context of cavitation, grain deformation and grain boundary sliding prior to presentation of the theoretical creep deformation description. A creep model is presented based on existing theory, derived from the aforementioned creep deformation categories.

5.2.2.1. Cavitation

Controversy surrounds cavitation creep as a source for non-linear stress responses where the exponent has been reported over a range of values $n \geq 1$. Porter, et al., (1981) modeled alumina creep as a cavitating material for equilibrium shaped cavities and corresponding stress exponent of n =1; it wasn't until cavity growth into wedge ("crack-like")-shaped cavities where stress non-linearity was achieved with maximum n-value of 2 (Porter, Blumenthal and Evans 1981). In contrast, silicon nitride is best modeled using an exponential strain rate function due to the large increases in stress exponent over decades of applied stress ((Wiederhorn, Hockey and French 1999) and (Krause Jr., et al., 1999)). Viscous flow phenomena, as modeled by Lange (1975) and Dryden (1989), show linear stress dependence and are associated with transient or "exhaustion" creep mechanisms (D. S. Wilkinson 1998). Evans and

Rana (1979), concluded cavitation strain rate contribution is inherently a non-linear process where cavity nucleation and growth are a result of un-accommodated grain boundary sliding.

Since, cavitation does not scale linearly with strain as found for other ceramic materials we look to other mechanisms for a dominant creep strain contribution.. The fraction of total strain attributable to cavitation, Figure 5- 27, clearly trends toward ~ 5% for steady state creep, with those experiments within the primary regime showing larger cavitation fractions (> 10%). This particular data point of Figure 5- 27 represents creep at 1600°C and 16-20 MPa , which we found to be primary creep, consistent behavior with the results outlined by Leucke, et al., (1995). Tensile silicon nitride creep studies found cavitation participates at the onset of creep load application as a transient tensile creep mechanism (Yoon, Wiederhorn and Luecke 2000). Additionally, such cavitation is responsible for bending stress redistribution owing to creep behavior differences under compression and tension ((Chadwick, Jupp and Wilkinson 1994), (Chen, Wiederhorn and Chuang 1991)). From residual plastic strain measurements, the tensile

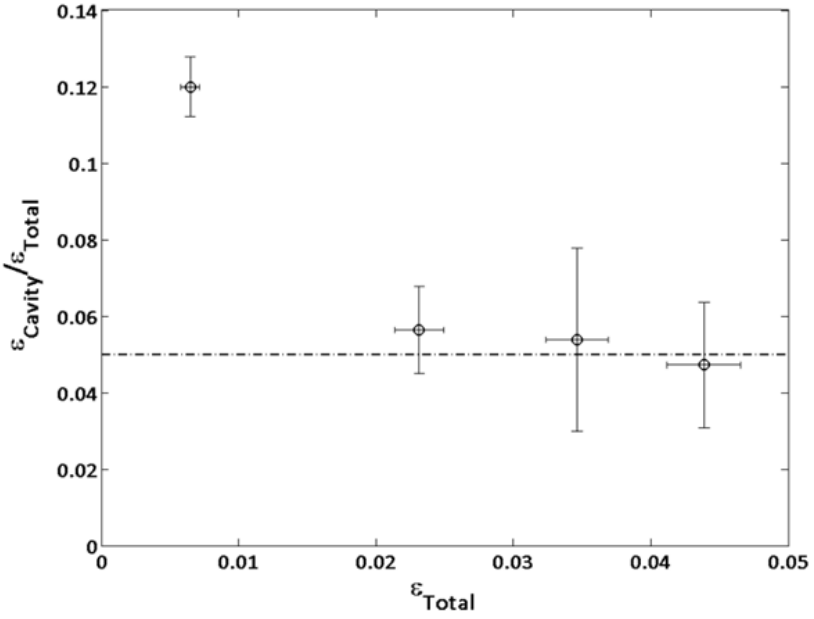

Figure 5-27: Strain due to cavitation (%) contribution to overall creep strain independent of temperature. Vertical error bars show standard deviations for all creep experiments; horizontal error bars show error in creep strain measurement.

and compressive curvature radii suggest a neutral axis shift toward the compressive surface. Shift ratios increase from 0.60 to 0.75, from the tensile side, with corresponding cavity volume fractions of 0.0010 and 0.0028, respectively. However, unlike glass-containing ceramics, creep strain appears minimally dependent upon cavitation and would expect creep behavior differences between compression and tension sides. For example, polycrystalline alumina creep showed a non-linear stress dependence suggesting a strong dependence on interface activity such as grain boundary sliding (Porter, Blumenthal and Evans 1981). In this material cavitation represented less than 30% of the strain.

Cavitation size and number density results indicate a possible change in cavity nucleation and growth kinetics during steady state creep, where growth may dominate under 30 MPa and nucleation may control above ~ 30 MPa. From Figure 5- 28, the stress-dependent (temperature independent) cavity number density shows minimal change in cavity number through 30 MPa and a 3.5 fold number increase above 30 MPa. Additionally, cavity size (Figure 5- 28) statistics show a rising trend in average (temperature independent) cavity volume with an increasing distribution through 30 MPa and a size and distribution reduction beyond 30 MPa. The stress dependent behavior indicates the cavity number does not significantly increase while cavity size appears to increase through 30 MPa contrasting with an increasing cavity number density and negligible size and distribution change indicating growth and nucleation dominant stress regimes. Figure 5- 29 illustrates low stress full facet cavity growth contrasting with isolated triple point cavities at high stresses. ZrB_2 cavitation was modeled using a cohesive zone micromechanics (Yu, Huang, et al., 2012) approached showing stress dependent cavity nucleation and growth kinetics (Yu, Huang, et al., 2013). Normalized cavity sizes and spacing linearly decreased ~25% between 50-100 MPa corresponding to the linear trending average cavity size reduction for creep stresses greater than 30 MPa.

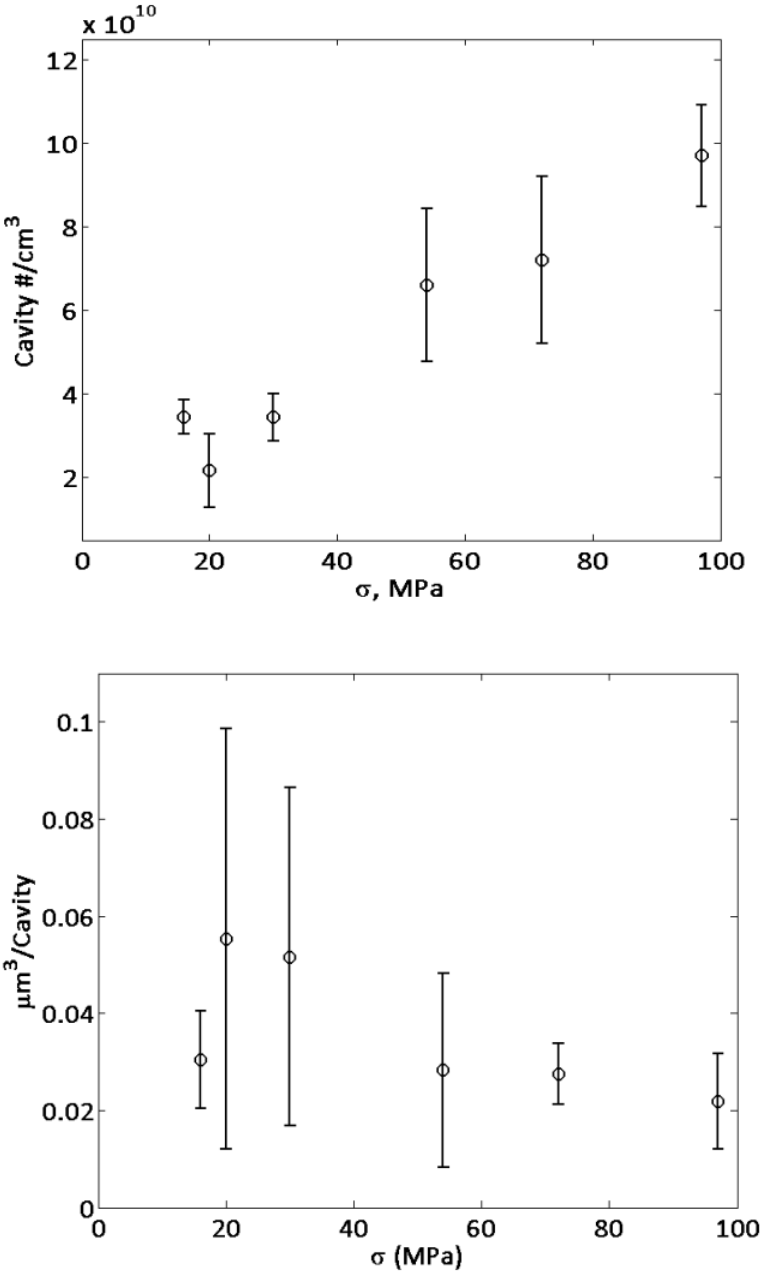

Figure 5-28: Cavity number density, independent of temperature, as a function of stress for T>1500°C (Left). Vertical error bars are standard deviations for 1600 -1800°C creep experiments.

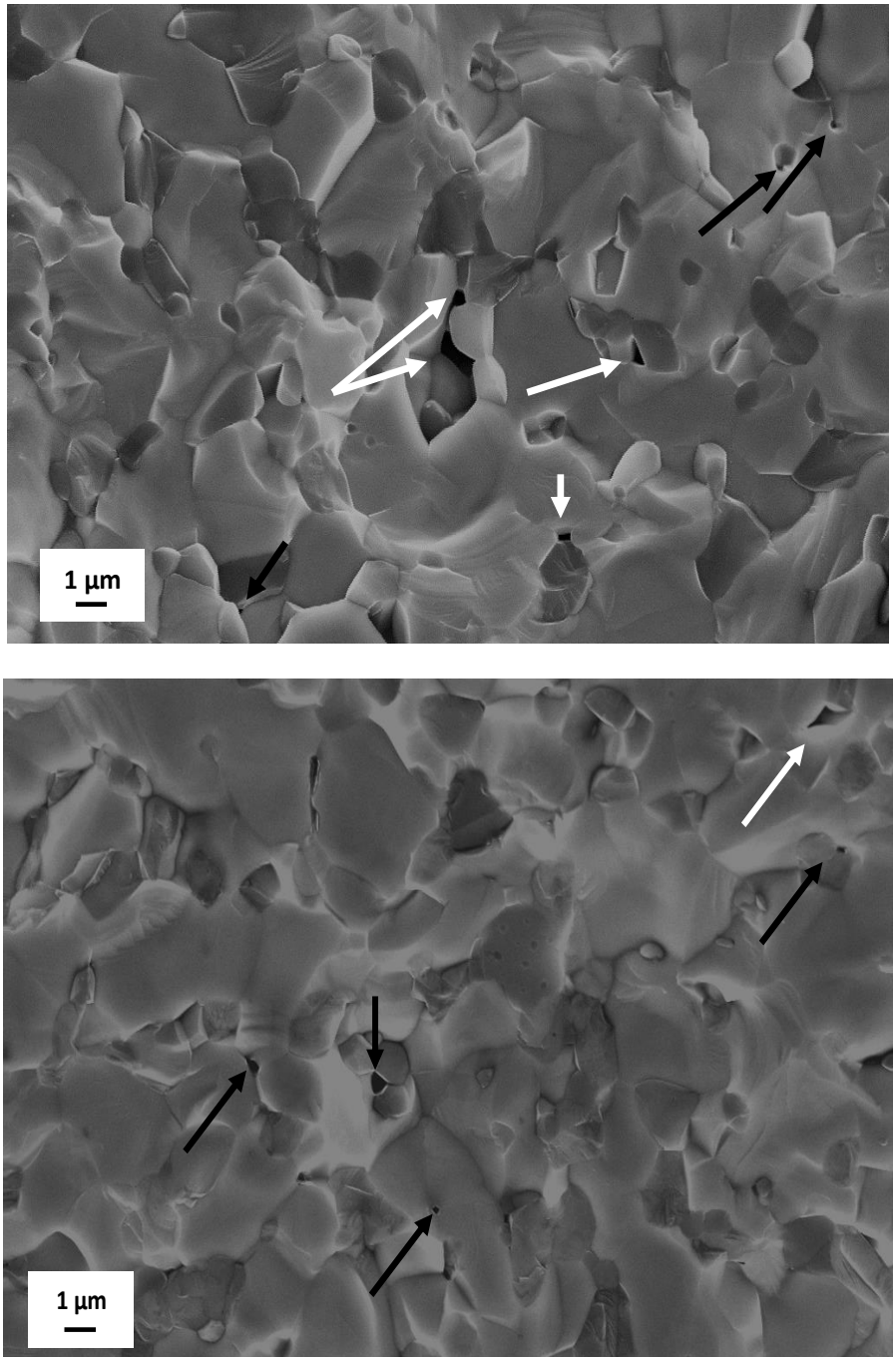

Figure 5-29: 1600C 16 MPa (left) and 97 MPa (right) post creep fracture faces showing cavitation primarily at Z-S boundaries. White arrows indicate Z-S full facet cavitation and black arrows indicate isolated triple point cavitation.

5.2.2.2. Grain Deformation

Grain shape change can occur by diffusion and dislocation assisted deformation modes associated with ZrB_2 and SiC following the creep event. Both mechanisms directly contribute to the macroscopic creep strain resulting in grain elongation parallel to the applied stress direction. For the present case, texture analysis quantifies the lattice rotations from deformation manifested by dislocation flow. Under the assumption of insufficient lattice deformation strains, with observed grain elongation, diffusion mechanism must prevail accounting for the shape change. The forthcoming analysis probes the SiC and ZrB_2 grain deformation using single crystal slip and texture theories for describing grain shape change.

Grain deformation is a result of lattice-dominated creep mechanisms involving either dislocation glide or climb, or a combination of the two. Weertman (1957) proposed two creep mechanisms that are climb and glide rate controlling have stress exponents of n =5 (Weertman 1957) and n=3 (Weertman 1957), respectively. Nabarro (1967) and Cannon and Sherby (1967) proposed a lattice model based on dislocation climb from Bardeen-Herring sources resulting in an n=3. Intragranular dislocation creep mechanisms typically require large homologous stress and temperatures where dislocation climb is rate-controlling (T. G. Langdon, Grain Boundary Sliding as a Deformation Mechanism during Creep 1970). However, all intragranular mechanisms require generation and flow of dislocations which are difficult in most ceramic systems, even at elevated temperatures, owing to high Peierls force and onset of cavitation and fracture prior to large dislocation strain contributions (Hull and Bacon, Strength of Crystalline Solids 2001). Haggerty and Lee (1971) observed ZrB_2 single crystal to slip along prismatic $\{10\bar{1}0\}$ and basal $\{0001\}$planes with a Burger's vector parallel to $< 11\bar{2}0 >$ for room temperature and 2025°C, respectively. Prismatic slip along the $\{10\bar{1}0\}$ planes with a Burger's vector parallel to the $< 11\bar{2}0 >$ lattice direction was later confirmed on polycrystalline ZrB_2 using nano-indentation

(Ghosh, Subhash and Bourne 2009) . Therefore, dislocation dominated mechanisms are plausible for ZrB_2 based ceramics.

The high-strain creep experiments revealed the average SiC particle spacing scales with the macroscopic creep strain. SiC grains were observed to elongate with creep strain, however, more grain deformation was observed for the compression zone rather the tensile zone despite the reduced total accumulated creep strain. Considering a simplistic deformation model, based on a single crystal shape, for determining the average grain strain according to

$$\varepsilon = \frac{\left[\frac{AR_f w_0}{\left(1+AR_f\right)AR_0} - \frac{w_0}{\left(1+AR_f\right)}\right]}{l_0}, \tag{5-7}$$

where AR_f and AR_0 are the crept and un-crept grain aspect ratios, respectively, defined by the grain width, *w*, and length, *l*, as the ratio *w/l*. The maximum single SiC crystal deformation strains of 0.017 and 0.024 for tensile and compression zones, respectively, were calculated using the average hot-pressed aspect ratio (AR_0) and either the tensile or compressive aspect ratio (AR_f). Apparently SiC grain deformation contributes to the Z20SB creep.

Apparently SiC grain deformation contributes to the Z20SB composite compressive creep. Considering SiC grain shape change in the context of dislocation mechanisms, a first approximation for determining the feasibility of dislocation glide was made by assessing the Schmid factor distribution relative to the calculated texture plots, Figure 5- 18. The most probable slip system(s) were determined and paired with the hexagonal closed pack crystallographic triangle, Figure 5- 30; only Schmid Factors > 0.400 are considered and overlaid on the hexagonal crystallographic triangle with respect to the bending stress axis. The orientation of dominant texture fibers along favorable slip plane poles and directions allow for determining the feasibility of glide. Figure 5- 31, illustrates the fiber rotations, from the

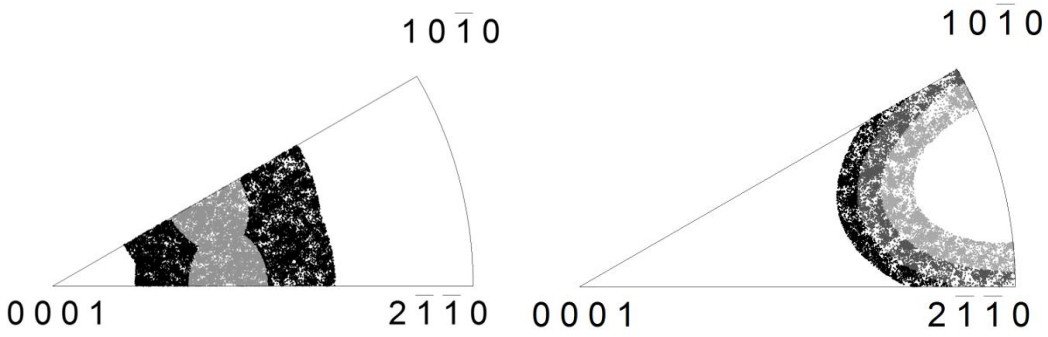

Figure 5-30: (0001) $< 11\bar{2}0 >$ or $< 10\bar{1}0 >$ slip systems (Left) with Schmid factors 0.488-0.500 (light grey) and 0.400-0.488 (black) and $\{10\bar{1}0\} < 11\bar{2}0 >$ system (right) with Schmid factors 0.488-0.500 (white) and 0.400-0.488 (light grey to black).

uncrept condition (light grey regions in Figure 5- 31), during deformation, suggesting that both (0001) $< 11\bar{2}0 >$ or $< 10\bar{1}0 >$ basal slip preferred for the SiC phase. Lane, et al., (1988) observed dislocation glide, during compression creep between 1400°C and 1800°C and 138-414MPa, in sintered α-SiC, of extended dislocations along the (0001) $< 11\bar{2}0 >$ basal slip plane. Glide of Shockley partials, bounding a stacking fault ribbon, of Burger's vectors parallel to $\frac{a}{3} < 1\bar{1}00 >$ and the companion partial $\frac{a}{3} < 01\bar{1}0 >$ were determined as parallel mechanism with Nabarro (1948) and Herring (1950) creep. Other slip systems have been observed for sintered SiC along the $\{4\,\bar{4}\,0\,1\}$ and $\{1\,\bar{1}\,0\,1\}$ planes, however, dislocation glide during creep was not a rate controlling mechanism (Lane, Carter Jr. and Davis, 1988). Thus, (0001) $< 11\bar{2}0 >$ or $< 10\bar{1}0 >$ basal slip was considered for texture analysis of the SiC phase. An apparent shift of texture fiber peaks, towards favored (0001) basal plane slip, occurs for both tension and compression zones.

Texture analysis was completed applying random grain orientation theory outlined in, Appendix C, for assessing large strain (<15% for the present case) creep deformation. The characteristic strain was calculated based on the un-crept and crept pole plot orientation data $\left(\frac{dP/d\psi}{\sin\psi}\right)$ representing a measure of the average lattice deformation strain relative to the fixed

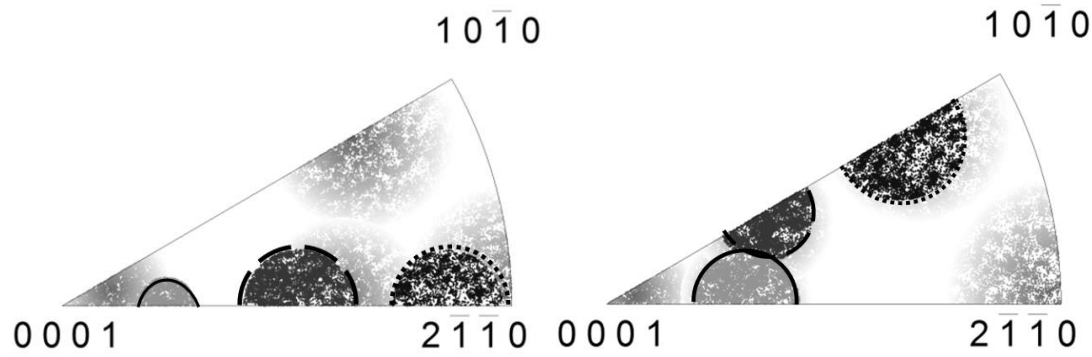

Figure 5-31: SiC IPF plots; compression creep (left) having solid (22°, 68°), dotted (90°, 0°) and dashed (49°, 41°) orientations. Tension creep (right) having solid (22°,68°), dotted (64°,36°) and dashed (32°,55°) orientations.

Table 5- 7: SiC Texture Strain Results for fiber texture peaks developed in the hot-pressed (HP), tension (T) and compression (C) deformation configurations.

Fiber-Stress Orientation	0-90° ε_{HP}	0-90° ε_{T}	0-90° ε_{C}
(22°,68°)//Stress	-0.0004	0.0059	0.0029
(49°,41°)Stress	0.0008	0.0001	-0.0124
(32°,55°)//Stress	-0.0013	0.0064	0.0159
(64°,36°)//Stress	0.0009	0.0009	-0.0084
Average	0.0000	0.0033	-0.0005
Stdev	0.001	0.0033	0.0127
95% CI	0.0008	0.0052	0.0202

reference axis with orientation angles $0 \leq \psi \leq 90°$. The SiC phase texture orientation models for the un-crept and crept configurations, using Equations (C1) and (C3), A = 1.9007 ± 0.0046 and numerically solving for the strain are shown in Table 5- 7. The reference crystallographic directions were parallel to the maximum fiber orientation represented in Figure 5- 18. The average lattice deformation strain, in the tensile region, accounts for ~20% of the 1.71% strain calculated, based on grain shape change, indicating a combination of lattice and diffusion deformation. This combined creep behavior has been observed by Lane, et al., (1988) and Wiederhorn, et al., (1999) for sintered SiC when creep temperatures approach 1700°C.

Additionally, the dominant observed texture directions are aligned favorably with the (0001) $< 11\bar{2}0 >$ or $< 10\bar{1}0 >$ basal glide systems. Review of the compression data shows ~2% contribution to the maximum calculated grain deformation strain and was statistically indistinguishable from the hot-pressed condition. This is direct evidence that SiC grain elongation, under compression, deforms by diffusion mechanisms. Therefore, within the tensile and compressive bending regions, SiC deformation accounts for <5% and <20% of the creep strain.

A similar analysis was conducted for ZrB_2 grain deformation with additional local deformation mapping, using nano-indentation markings, for the tensile region. The ZrB_2 grain shapes were shown to remain constant through deformation in both tension and compression, Figure 6. This priority suggests both lattice and diffusion dominated mechanisms according to Weertman (1957) and Lifshitz (1963) are not occurring, but rather Rachinger (1952) sliding. Although the microstructure gives little warning of any grain shape/size change, the texture

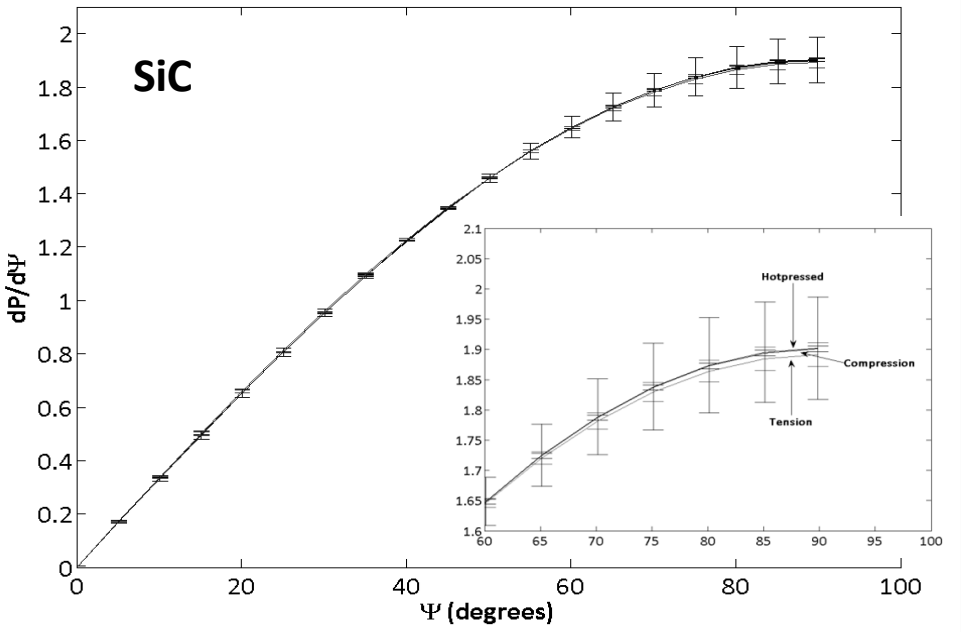

Figure 5- 32: SiC texture orientation distribution change.

plots suggest some degree of lattice reorientation and the indentation mapping confirms that local grain deformation contributes as either an accommodation or a rate-controlling mechanism. Therefore, the calculated theoretical grain deformation strains, using Equation (2), illustrate the range of possible local ZrB_2 grain deformation, Figure 5- 33. Additionally, the directly measured grain deformation strains and final aspect ratios are overlaid displaying the agreement between EBSD based grain deformation calculations and direct measurements (square shapes in Figure 5- 33). From this configuration, the IDM and EBSD grain deformation suggest local ZrB_2 grain deformation being compressive in nature despite the applied tensile stress. Additionally, some grains deformed with positive strains partially offsetting the compressively deformed grains resulting in a statistically insignificant net difference in aspect ratio between the crept and un-crept conditions. The compressive bending zone was considered to behave similarly as the tensile region based on the lack of grain shape change with strain.

ZrB_2 grain deformation was apparent within both the tensile and compressive bending regions. The calculated Schmid factors further confirm the development of fiber texture along more favorably orientated slip systems, Figure 5- 34. Both basal $(0001) < 11\bar{2}0 >$ and first order prismatic $\{10\bar{1}0\} < 11\bar{2}0 >$ slip has been observed from single crystal and polycrystalline ZrB_2 indentation and compression creep experiments ((T. G. Langdon 1994) and (Ghosh, Subhash and Bourne 2009)). Specifically, high temperature compression creep deformation was controlled by $(0001) < 11\bar{2}0 >$basal slip despite a Schmid factor of 0.324 compared to 0.437 for prismatic slip. Haggerty and Lee (1971) discuss the shift in deformation behavior explaining a reduction in the critical resolved shear stress for basal slip with temperature. The compressive bending zone shows a shift towards basal slip with either the $< 11\bar{2}0 >$ or $< 10\bar{1}0 >$ glide directions**.** Similarly, we only observed deformation for those loading conditions where the

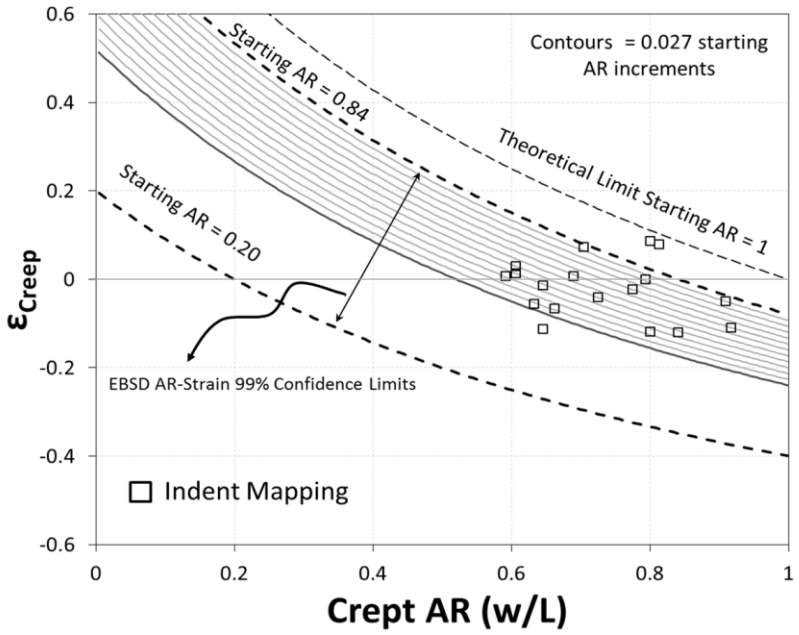

Figure 5-33: Strain limits for starting grain shapes of 0.20≤AR<1.0. The bold dotted line represents the 99% confidence interval from ZrB_2 EBSD grain shape measurement intervals and the outer dotted line representing a starting aspect ratio of 1.

Schmid factor exceeded 0.4. However, Prismatic slip was not eliminated as a possibility as a Schmid factor of 0.437, for the $(39°, 51°)$ crystal direction, was calculated and planar packing density is greater than (0001) basal plane (T. G. Langdon 1994). The $(69°, 25°)$ stress direction lies between both basal and prismatic slip with an assumed Burger's vector parallel to $< 11\bar{2}0 >$ having equal schmid factors, suggesting that both systems may operate during deformation provided the critical resolved shear stresses are equal. Haggerty and Lee (1971) suggest this was likely not the case, as their contrast experiments indicated slip along the basal plane. The ZrB_2 EBSD lattice positions were favorably oriented for dislocation glide along the $(0001) < 11\bar{2}0 >$ basal slip directions with increasing compressive and tension strain based on the negligible changes in plan pole alignment with the $\{10\bar{1}0\} < 11\bar{2}0 >$ prismatic slip system.

Texture plot analysis based on Equations (C1)-(C3) revealed quantitative ZrB_2 deformation evolution with creep strain. Table 5- 8 lists the average lattice deformation strains

from an orientation change with respect to tensile and compressive fiber peak directions. Lattice deformation was compressive for both the tensile and compressive bending regions. These texture strains correlate with the indentation mapping analysis having select grains compressing along the axis of the applied tensile stress. The magnitude of the texture strains are less than the measured local strains confirming our previous observation that large local grain shape changes are infrequent.

From two independent methods, the magnitude of grain deformation and its contribution to the creep process has been demonstrated. The indentation mapping experiment directly assesses this element of deformation, suggesting lattice deformation operates largely as an accommodation process in support of grain rotation and sliding. In the following section, we will show that grain boundary sliding processes (i.e. rotation and translation) account for 80% of the creep strain, with much less than the remainder accountable to grain deformation.

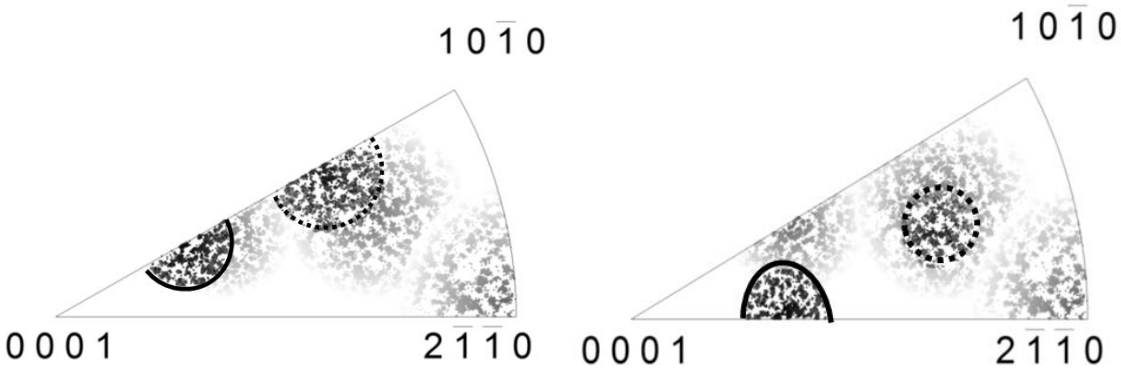

Figure 5-34: ZrB_2 IPF plots; Compression creep (left) having solid (32°,60°) and dotted (66°,36°) orientations. Tension creep (right) having solid (39°,51°) and dotted (69°,25°) orientations.

Table 5- 8: Texture Strain Results for fiber texture peaks developed in the hot-pressed (HP), tension (T) and compression (C) deformation configurations.

Direction-Axis Orientation	0-90° ε_{HP}	0-90° ε_{T}	0-90° ε_{C}
(69°,25°)//Stress	0.0010	-0.0200	-0.0139
(39°,51°)//Stress	-0.0010	-0.0139	-0.0051
(66°,36°)//Stress	-0.0010	-0.0139	-0.0069
(32°,60°)//Stress	0.0010	-0.0200	-0.0144
Average	0.0000	-0.0169	-0.0101
Stdev	0.0011	0.0035	0.0048
95% CI	0.0009	0.0056	0.0076

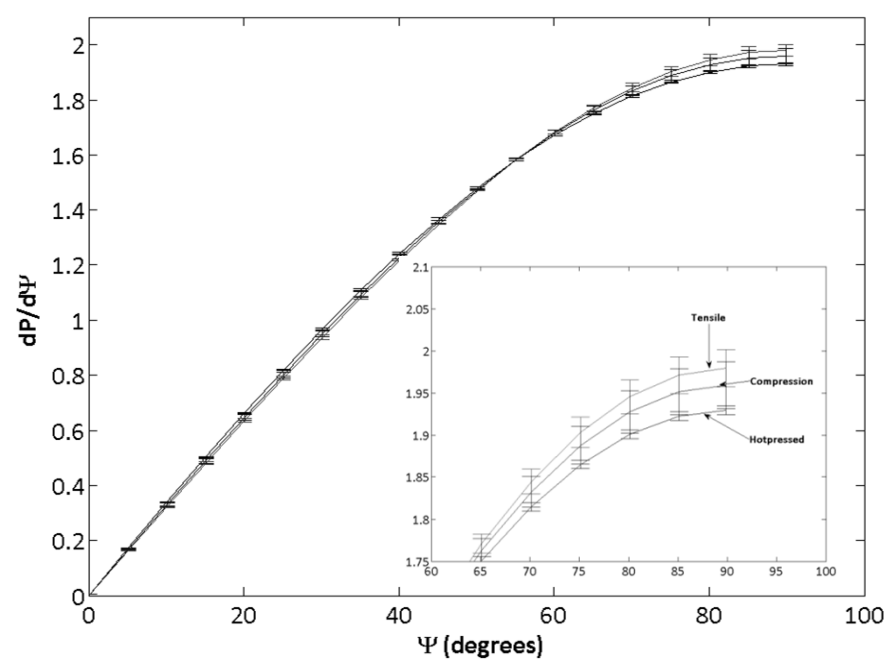

Figure 5-35: ZrB_2 texture orientation distribution change.

5.2.2.3. Grain Boundary Sliding

Grain boundary sliding, has been suggested by many authors as a dominant creep mechanism in metal and ceramic systems with stress exponents n = 2. Langdon (1970) proposed this mechanistically as alternating dislocation glide and climb within the grain boundary dislocation network or along adjacent zones controlled by dislocation climb. Ball and Hutchinson (1968) considered grain deformation of four-grain groups where accommodation may require dislocation glide deformation of unfavorably oriented grains. Mukherjee (1971)

proposed a similar deformation mechanism without the requirement of grain group sliding. Gifkens (1976) later proposed a sliding event similar to Ashby and Verrall' s (1973) sliding model where grain mantles deform in response to neighbor translation and concomitant grain rotation leaving the grain cores relatively dislocation free. Later Langdon (1994) unified the theories of grain boundary sliding into two groups of sliding based on the dislocation substructure stability corresponding to a grain size transition. In all grain boundary sliding models the grain shapes remain constant throughout the deformation process and microstructures remain continuous. Dislocation flow, activated by glide and/or climb, accommodates the sliding event during deformation.

Indentation deformation mapping clearly shows grain boundary sliding to (Figure 5- 24) account for ~80% of the total creep strain, with the balance assigned to a combination of ZrB_2 grain deformation, SiC grain deformation and cavitation. The latter two combine for <10% of the total creep rate along the tensile region. We have shown the sliding components, namely translations and rotations contribute 56% and 24%, respectively, to the total strain. Grain boundary misorientation angle and interphase boundary type determine sliding mobility. A qualitative assessment of ZrB_2 and ZrB_2-SiC grain boundaries, from the EBSD data, reveals >95% are high angle random boundaries suggesting highly mobile boundaries. SiC grain boundaries are <10% of all grain boundaries, present in the composite, suggesting minimal influence from the SiC-SiC boundaries. Kokawa and coworkers (Kokawa, Watanabe and Karshima 1983) observed grain boundary sliding rate dependency on lattice dislocation absorption rate into and along grain boundary networks for aluminum metals. Their work concluded crystallographic dis-registry between aluminum grains (i.e., low energy coincident vs. high angle grain boundaries) affected dislocation absorption and subsequent sliding rate. Under such conditions high angle

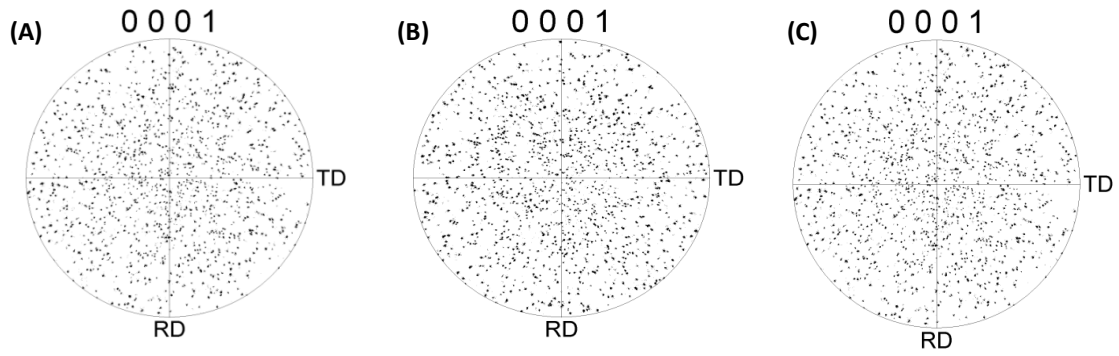

Figure 5-36: Pole figures of the (0001) pole projection for the tensile (a), Hot-pressed (b) and Compression (c) ZrB_2 zones. The ND direction is normal to the polish plane. The TD and RD directions are parallel and normal to the bending stress axis.

Z-Z grain boundaries and high angle incoherent Z-S interfaces should possess faster sliding rates compared to "clean" Z-S coherent/semicoherent interfaces. A qualitative assessment of ZrB_2 and ZrB_2-SiC grain boundaries, from the EBSD data, reveals >95% are high angle random boundaries suggesting highly mobile boundaries. Jayaseelan, et al., (2011) has observed predominantly non-coherent interfaces with coherent interphase boundaries present. These observations and low cavitation fractions lead to the assumption the Z-S boundary mobility to be equivalent to that of the Z-Z boundaries. The ratio of Z-Z to Z-S boundaries is close to unity for the Z20SB composite. ZrB_2 pole figures (Figure 5- 36) suggest the microstructure consists of predominantly randomly orientated crystallographic vectors with increasing strain suggesting grain movement. Direct observation of grain rotation was manifested as intragranular indentation pair misalignment with the micrograph horizontal, Figure 5- 37. The starting microstructure shows negligible deviation from horizontal for all combinations of indentations within the observable row contrasting with the deformed state. Biner (1995) modeled the effects of grain boundary sliding on cavitation for particulate composites. Our composite shows negligible cavitation, however, large non-uniform displacement fields from anisotropic sliding behavior between matrix and reinforcement, caused substantial grain rotations and cavity nucleation at triple points (Biner 1995). This is

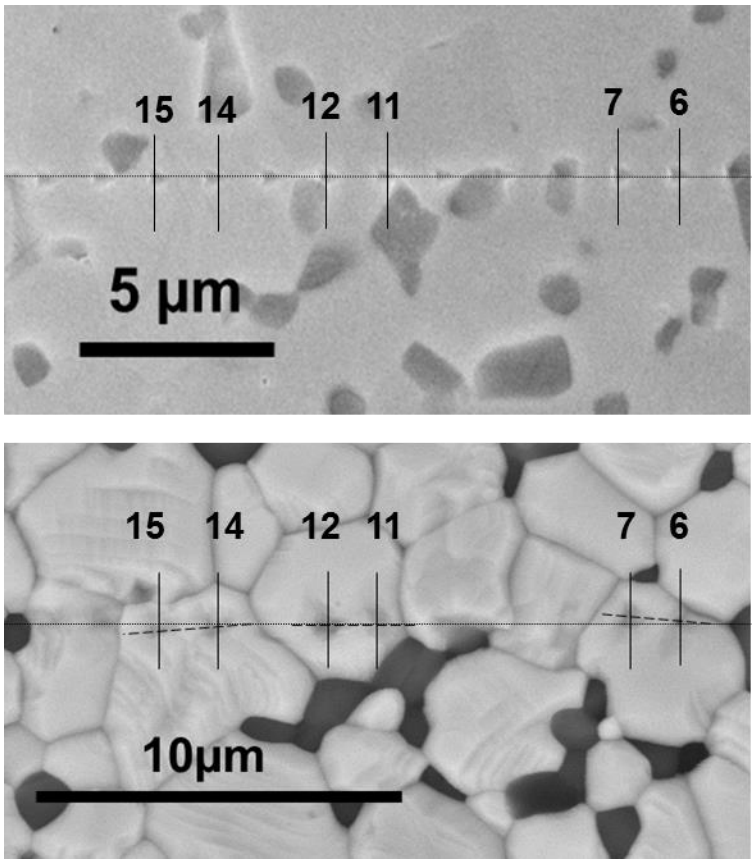

Figure 5-37: As-crept micrograph of observed grain rotation (Top) and un-crept condition (Bottom). Indent alignments, between grains, noticeably deviate from the un-crept array positions.

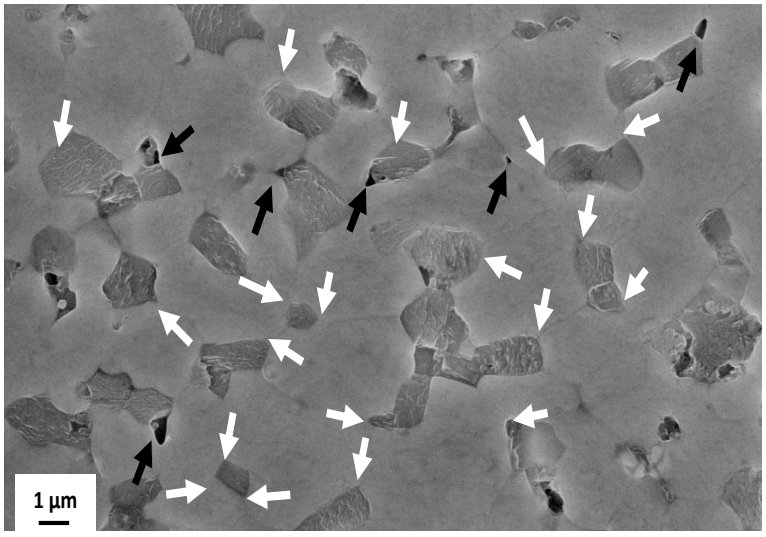

Figure 5-38: 1800°C and 54 MPa outer-fiber tensile creep zone on polished and etched surface. Black arrows indicate Z-S triple point cavitation and white arrows indicate the appearance of damage free Z-S triple points.

consistent with our observations of cavitation at the Z-S triple points in the high strain creep specimen, Figure 5- 38.

Considering Ashby and Verrall' s (1973) model for grain boundary sliding creep, grain translations occur by neighbor switching while maintaining an equiaxed grain structure. The deformation model superimposes diffusion and dislocation creep mechanisms as a viable creep description. For our research we add SiC particles to the idealized ZrB_2 grain edges and the conceptual model fits the high strain observations found from the linear intercept and EBSD analysis. However, this model takes into account grain group neighbor switching without appreciable grain rotation. A similar model was proposed by Gifkens (1976) and incorporated a core-mantle region of low and high dislocation density, respectively, for explaining the neighbor switching event. The creep model requires grain rotation as a response to stress relaxation ahead of a dislocation pileup at grain boundary triple points. The heavily deformed mantle region was a requirement for accommodating these rotations and translations and preserving microstructural continuity. Therefore, dislocations dominate the creep *accommodation* step based on the forthcoming analysis.

Mantle-core deformation behavior were modeled using a revised GND rendering (Figure 5- 39) and single crystal deformation theory following the Orowan equation (Hull and Bacon 2001)

$$\varepsilon = \rho_m b \bar{x}, \tag{5-8}$$

where the plastic strain, ε, describes the total number of mobile dislocations, ρ_m (density), moving on a slip plane an average distance $\bar{x}$ and b the Burgers vector. SiC GNDs were ignored because of distorted EBSD patterns from polishing damage artificially inflated the total dislocation concentration. Evidence supports, from application of Equation (5-8), the equivalent deformation strain possible from a GND concentration of 1×10^{12} cm^{-2} is 460% assuming a grain

size of 1.5 µm. The EBSD texture analysis suggests SiC deformation contributes < 5% of the macroscopic tensile creep strains. Therefore, SiC deformation was not included on the basis of negligible creep strain contributions along the tensile zone in the forthcoming analysis.

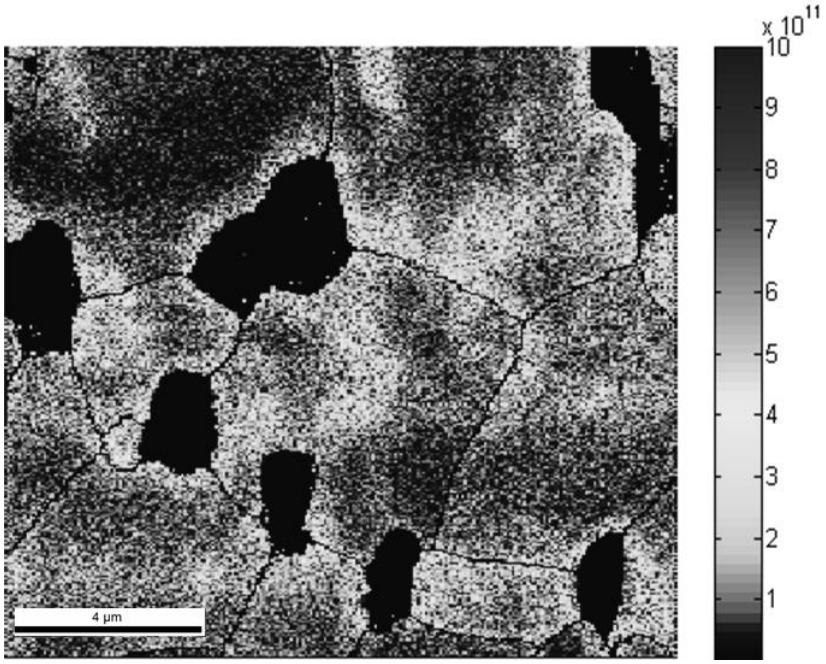

Figure 5-39: Revised tensile zone featuring ZrB_2 GND density spatial distributions.

The observed GND density changes with distance from the interphase and ZrB_2 grain boundaries may be shown to follow the Orowan (Hull and Bacon 2001) approach by rewriting Equation (5-8) in the form of

$$\rho_m = \frac{\varepsilon}{b\bar{x}}, \tag{5-9}$$

where $\bar{x}$ is taken as the distance away from a grain boundary and ρ_m the total GND density in this gradient zone. Using linear regression, the Orowan model was fit to the calculated GND-distance relationship from a series of random line profiles overlaid on the HREBSD rendering, Figure 5- 40, assuming the total GND density population is mobile (Ashby 1970). Although, the two slopes are not perfectly matched, this comparison with the Orowan model suggests a mantle thickness of about ~ 250 nm. TEM research on ZrB_2 powders and fully dense compacts

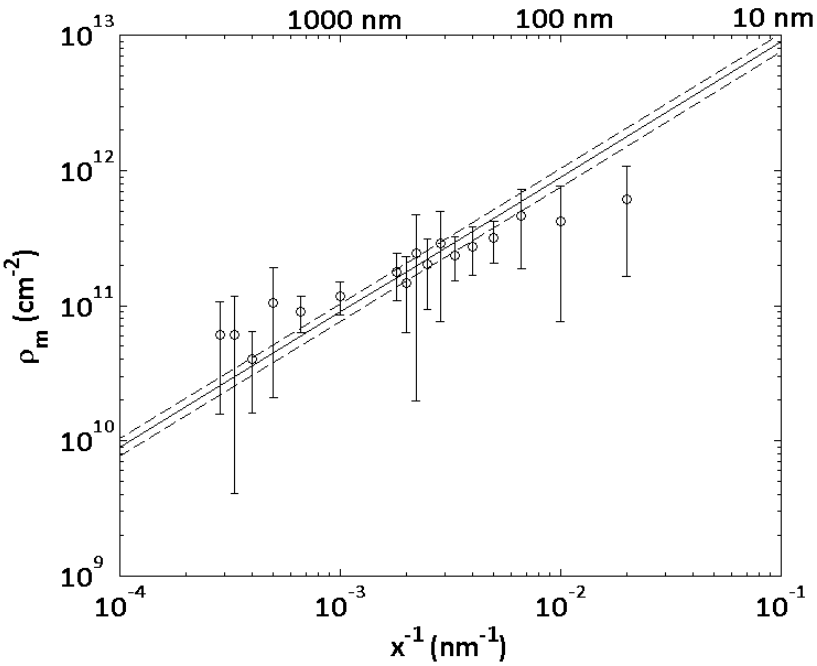

Figure 5-40: Orowan model (solid line) with the 95% confidence bounds (dashed lines) overlaid with GND-distance quantities calculated using HREBSD rendering (circles). Error bars represent the standard deviations.

show a wide range of dislocation densities. Goutier, et al., (2008) observed significant plastic deformation, within ZrB_2 grains, accommodating the thermal strain developing from spark plasma sintering of ZrB_2-ZrC composites. In the presence of large thermal gradients, a dislocation density of approximately 10^{-9}-10^{-10} cm^{-2} was found for deformed ZrB_2 grain cores neighboring ZrC grains (Goutier, et al., 2008). Mishra, et al., (2004) investigated the ZrB_2 powder defect structures for three powder processing routes. Dislocation densities of ~10^8 cm^{-2} were measured for 20% of particles for traditional carbothermic and replacement reaction powder processing techniques. For the highly exothermic self-propagating high temperature synthesis, 80% of particles had grain core dislocation densities of 10^{12} cm^{-2} suggesting accommodation plasticity within ZrB_2 particles due to thermal gradients (Mishra, Das and Pathak 2004). Other ZrB_2 – SiC and ZrB_2-$MoSi_2$ TEM studies have shown large isolated interphase dislocation densities contrasting with low dislocation density grain cores ((Mizuguchi, Guo and

Kagawa 2009), (Mizuguchi, Guo and Kagawa 2010)). Haggerty and Lee (1971) observed easy glide and subsequent work hardening during compression experiments at 2050°C, for single crystal ZrB_2, suggesting low initial dislocation densities followed by increasing statistically stored dislocations (SSD) density. It is recognized these dislocations differ from the GND-type, however, the presence of grain boundaries in otherwise low-dislocation grain core regions would generate the necessary deformation strain gradients and, therefore, promote the increased GND density and subsequently the total dislocation density near the grain boundary (Ashby 1970). The present HREBSD method likely provides a reasonable approximation of the GND population within those reported for ZrB_2.

Local measurements of grain movements show that both grain deformations and rotations result from the sliding event. The creep model requires grain rotation as a response to stress relaxation ahead of a dislocation pileup at grain boundary triple points or flow along sliding interphase boundaries (Gifkins 1976). Therefore, assuming hexagonal grain geometry and the presence of ledges, along the sliding boundary, a minimum mantle thickness accommodating the deformation follows (Gifkins and Langdon 1978)

$$y = \frac{d}{2}(1 - \cos\theta), \tag{5-10}$$

where the mantle thickness, y, is proportional to the grain size, d, for ideal hexagonal grain shapes rotating at an angle θ. The maximum mantle thickness approaches $y_{max} \approx 0.067d$ with a 30° grain rotation (Gifkins 1978). The present IDM experiments find average ZrB_2 grain rotations of 4.9° with maximum rotations of 37° and 0°, corresponding to average mantle thicknesses of 19 nm with a range falling between 154 nm and 0.40 nm. Mantle thicknesses below one Burger's vector correspond to ~ 1° of grain rotation, for our ZrB_2 grain sizes confining slip accommodation within the grain boundary plane.. The distribution of mantle thicknesses suggests varying degrees of local mantle deformation in response to macroscopic stress. For the

present case, grains having core strains greater than 8% are outnumbered 4:1 over those exhibiting lower core defect contents. Applying the Orowan model to the IDM results allows for characterization of the deformed mantle region at thicknesses < 50 nm and core deformation based on the average grain strain. Mantle mobile dislocation densities were calculated following

$$\varepsilon = \frac{2y}{d} = 1 - \cos\theta \,, \tag{5-11}$$

where ε, y, d and θ hold the usual significance. If we assume $\bar{x} = y$ Equation (5-11) reduces to

$$\rho_m = \frac{2}{bd} \,. \tag{5-12}$$

Application of Equation (5-12) suggests the mobile dislocation density should not significantly change, under a normal grain size distribution, defining y_{max} as the limit for the maximum expected mobile dislocation range. The mobile dislocation densities for the IDM rotations are shown with the Orowan model, Figure 5- 41. Below y_{max} the calculated mobile dislocation density deviates from Orowan model plateauing at ~2x10^{11} cm^{-2} for an average grain size ~ 4μm. This agrees with the lower bound GND density from the HREBSD analysis. Grain core mobile dislocation evidence for the few select grains exhibiting large deformations followed single crystal behavior according to Figure 5- 39, for $\bar{x} = d$, Figure 5- 41. This behavior was confirmed using a pseudo Fourier analysis (Appendix D) on the KAM and HREBSD sinusoidal local misorientation (GND) spectra, across random grains, for determining the Fourier distance (Frequency= 1/λ) or subgrain size, λ. For the present case, the Fourier distance (λ) of 4.11±1.61μm and 3.35±1.23μm scales with the measured grain size, following the Orowan model above. Additionally, dislocation substructure has been experimentally correlated with stress based on the following relationship ((Bird, Makherjee and Dorn 1969))

$$\frac{\lambda}{b} = \xi \left(\frac{\sigma}{G}\right)^{-1} \,, \tag{5-13}$$

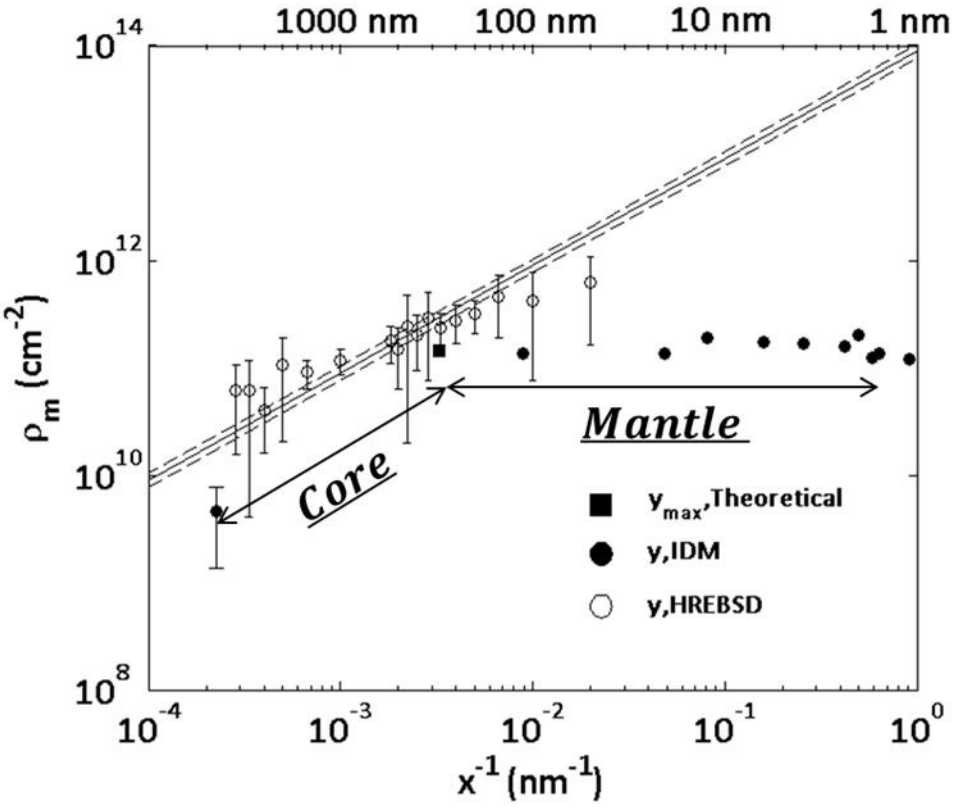

Figure 5-41: Orowan model (solid line) with the 95% confidence bounds (dashed lines). IDM calculated and theoretical GND densities (filled shapes). HREBSD GND densities (open circles). Error bars represent the standard deviations.

where λ is the dislocation cell size normalized by, b, the Burger's vector; ξ is a constant of magnitude ~20 for metals and 20-30 for ceramics (T. G. Langdon, Grain Boundary Sliding as a Deformation Mechanism during Creep 1970) and σ is the applied stress normalized by the shear modulus G. For the Z20SB composite, the equivalent subgrain size of $\lambda \approx 86$ μm at 1800°C and 13 MPa, for b = 3.167Å, $\xi = 20$ (T. G. Langdon, 1970) and G = 177 GPa (Okamoto, et al., 2010), exceeds the measured grain size. Therefore, core slip distances are assumed equivalent to the grain diameter, following the Orowan model presented, having a lower dislocation density than the mantle region.

Comparison between the IDM and HREBSD results show similar dislocation densities where the mantle exceeds that of the core by a factor of 13 and 12, respectively. From Figure

5- 41, our two experimental methods predict a transition from mantle to core dominated deformation and the slopes agree well with single crystal behavior for both HREBSD and IDM, thereby assuming low-defect single crystal behavior in the core (Ashby 1970). Dislocation densities peak within the mantle region as a consequence of excess GND's generated to satisfy the grain deformation gradient. However, varying the grain size would yield a change in the deformation gradient and hence the mantle dislocation density. For example, transitioning from 2 μm to 20μm grain sizes decreases the theoretical mantle dislocation density by an order of magnitude, from $3x10^{11}$ cm^{-2} to $3x10^{10}$ cm^{-2}. Therefore, the transition from mantle-dominated (fine grain) to core-dominant (coarse-grain) behavior is marked by the theoretical mantle dislocation density limit approaching that of the core.

The present case, creep accommodation by mantle deformation suggests the cores remain rigid-plastic and continuity is preserved by additional shear displacement accommodated by emitting dislocations from the grain boundary into parallel adjacent zones (Ashby 1970). Additionally, normal displacements are accommodated through formation of dislocations pairs across the boundaries penetrating the mantle, into the core (Ashby 1970). The former accommodation process follows the requirement for minimizing the mantle-core dislocation interactions proposed by Gifkens (1976) and promotes grain rotations from shear displacements ((Gifkins 1978), [(Biner 1995)]). Prior to Gifken's (1976) model, Ashby (1970), observed a grain size dependence, supporting the role of the mantle regions described by Gifkens (1976) and Equation (5-12). Core dominated deformation infrequently occurs compared with predominately low defect grains with mantle accommodation.

5.2.2.4. Theoretical Interpretation

Creep results, from the transition region, show that independent, non-sequential creep mechanisms are operating. Based on the measured stress exponent and the microstructure

analysis the following creep formulations are proposed for describing the creep rate

$$\dot{\varepsilon}_{Total} = \dot{\varepsilon}_{Diff} + \dot{\varepsilon}_{gbs} + \dot{\varepsilon}_{g\ or\ c}\ , \tag{5-14}$$

$$\dot{\varepsilon}_{gbs,1} = \frac{\beta G b^2 D_l}{dKT}\left(\frac{\sigma}{G}\right)^2\ , \tag{5-15}$$

$$\dot{\varepsilon}_{gbs,2} = \frac{\beta G b^3 D_{gb}}{d^2 KT}\left(\frac{\sigma}{G}\right)^2, \tag{5-16}$$

and

$$\dot{\varepsilon}_c = \left[3\beta\sigma^{(n+1)}/_{4G}\right]\exp\left(-\frac{Q}{RT}\right), \tag{5-17}$$

where b, d, , D, β , G, Q, R, and T are the Burger's vector, grain size, diffusion coefficient representing either grain boundary (gb) or lattice (l), numerical constant, shear modulus, surface activation energy, gas constant and absolute temperature, respectively High temperature diffusion creep includes both grain boundary and lattice diffusion mechanisms consistent with low temperature creep findings.

As can be seen in Figure 5- 42, the strain rate and stress range may be identified with each non-sequential (Equation (5-14)) creep mechanism within 1500°C <T≤1600°C. Through 1600°C, cavitation strain rate (Equation (5-17)) increases as the applied stress increases with a corresponding decrease in diffusion (Equation (5-3)) contribution near 97 MPa applied stress. Grain boundary sliding (Equation (5-16)) dominates with minimal contributions from both diffusion and cavitation at intermediate stress levels. The degree of non-linear stress contributions to the total creep rate agrees well with those predicted by statistical fitting procedures.

The activation energy reduction above 1600°C suggests the creep behavior may operate in sequence (Hynes and Doremus 1996). The total creep behavior would follow the sequential

relationship of

$$\frac{1}{\dot{\varepsilon}_{Total}} = \frac{1}{\dot{\varepsilon}_{gbs}} + \frac{1}{\dot{\varepsilon}_{c}} + \frac{1}{\dot{\varepsilon}_{g}}, \tag{5-18}$$

having contributions from grain boundary sliding creep, gbs, cavitation, c, and lattice deformation, g. From the grain deformation and grain boundary sliding analysis, we assert that grain boundary sliding is rate-controlling with additional contribution from cavitation promoting a stress exponent n>2; lattice deformation is considered an accommodation process not directly contributing to the creep strain and strain-rate. Equations (5-15)-(5-17) are plotted with the 1800°C flexure creep data (Figure 5- 43) for comparison and the model parameters shown in Table 5- 9. Both grain boundary sliding models show excellent agreement, within a factor of 2,

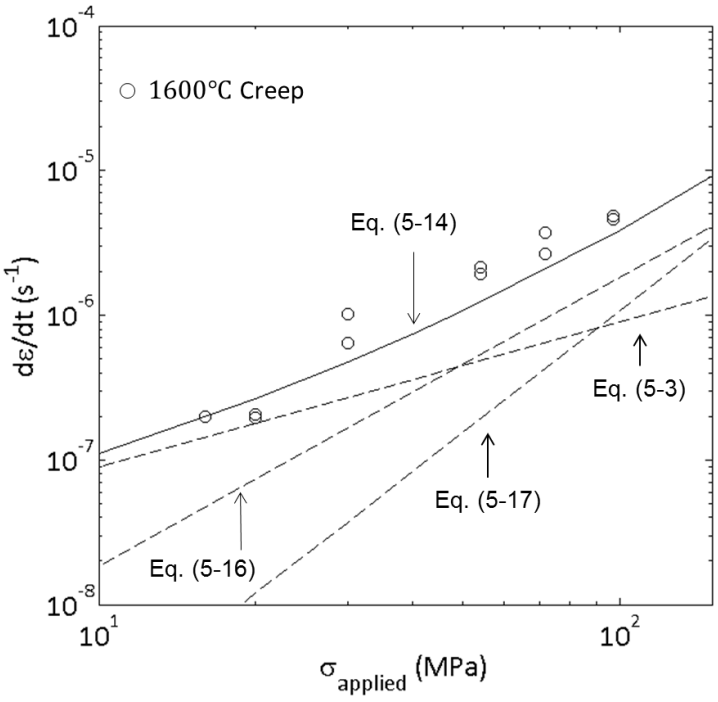

Figure 5-42: 1600°C creep model comparison for diffusion and grain boundary sliding creep at low stresses. Intermediate stresses: grain boundary sliding accounts for majority of creep. High stress: grain boundary sliding and cavitation dominate.

despite the grain size dependence and the diffusion path dependence differences. The grain size exponent was not determined from a lack of available microstructures, however, inferences can be made for determining the operating creep model based on the activation energy. An observed activation energy reduction, with stress, was defined for the low (< 30 MPa) and high stress (≥ 30 MPa) stress regimes having energies of 568 +/- 10 KJ/mol and 639 +/- 1 KJ/mol, respectively. The shift in activation energy with stress appears to scale with a shift in the dominate vacancy diffusion path. At lower stresses the activation energy begins to correlate with the range of ZrB_2 grain boundary activation energies following the ZrB_2 polycrystalline creep work of Talmy (2008), Kats, et al., (1981) and the shear viscosity measurements conducted by Kuzenkova and Kislyi (1966). With increasing stress the measured activation energy correlates with those for Zr/ZrB_2 bulk diffusion. Cannon and Langdon (1988) suggest that vacancy diffusion may occur along either path simultaneously. Additionally, Ball and Hutchinson (1968) argue most activation energies correlate with the grain boundary diffusion activation energy; however, this is not a priority. Therefore, we assume both diffusion paths operate simultaneous thus resulting in a total grain boundary sliding creep rate of

$$\dot{\varepsilon}_{gbs} = \frac{b^3\sigma^2}{d^2GKT} D_{gb}\left[64 + \frac{D_l}{D_{gb}}\left(\frac{d}{b}\right)\right]. \tag{5-19}$$

Here, increasing the applied stress favors bulk diffusion paths contrasting with lower stresses where grain boundary diffusion is favored. This agrees with the activation energy reduction observed with creep stress.

A conceptual model according to Ashby and Verrall (1973) was suggested based upon the SiC interparticle spacing scaling with the creep strain. Incorporating Gifkens (1976, 1978) assumptions, introduces, the grain neighbor switching event as an independently operating

Table 5- 9: Grain boundary sliding and cavitation model parameters.

Parameters	Equation (5-15)	Equation (5-16)	Equation (5-17)
b, m	3.13E-10	3.13E-10	---
G, GPa	171.5	171.5	171.5
d, m	3.10E-06	3.10E-06	3.10E-06
k, J/K	1.38E-23		
D_l, m^2/s	6.6E-15	2.417E-12	---
β	1	64	0.192
Q , KJ/mol	550-792	242-590	580-634
n	2	2	3.2

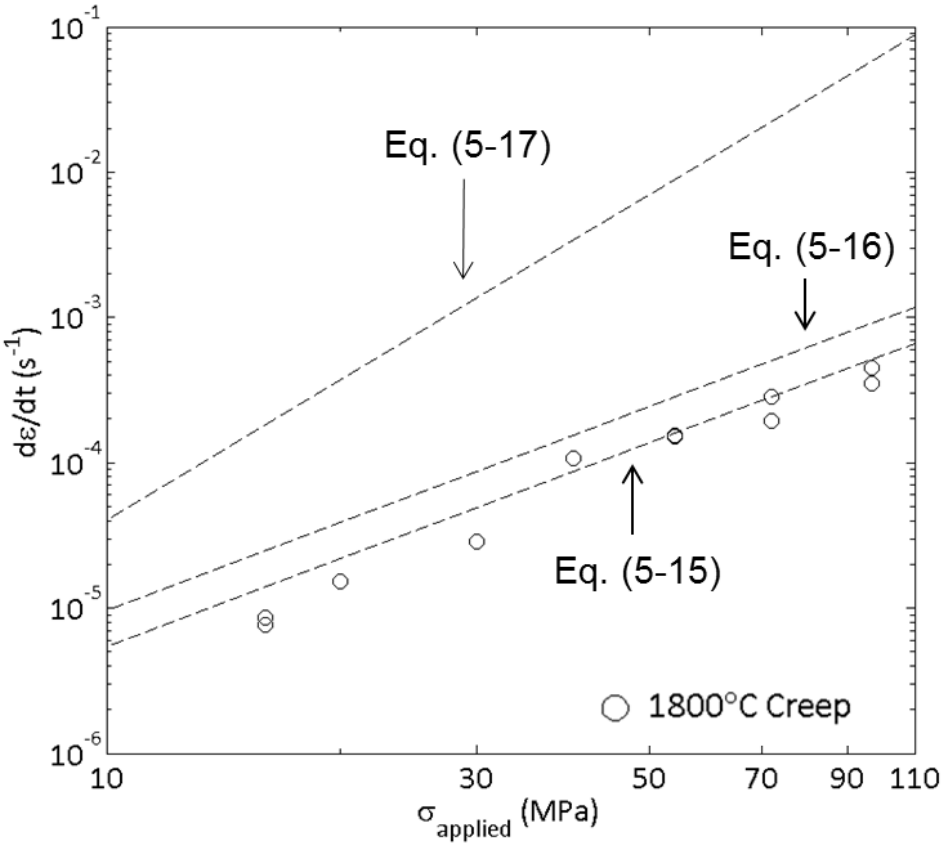

Figure 5- 43: 1800°C Z20SB flexure creep comparisons with existing creep theory.

mechanism. Applying Ashby and Verrall' s (1973) superposition model using Coble's[2] (1963) equation,

$$\dot{\varepsilon}_{diff} = \frac{48b\Omega D_{gb}\sigma}{d^3 KT}, \tag{5-20}$$

for diffusion accommodation and Nabarro' s (1967) equation,

$$\dot{\varepsilon}_G = \frac{\beta G b D_l}{\pi KT}\left(\frac{\sigma}{G}\right)^3, \tag{5-21}$$

for rate-controlling dislocation climb the Region II limits can be calculated and shown with the proposed Z20SB creep model, Figure 5- 44. According to Figure 2-6, grain boundary sliding was described as Region II creep deformation, bounding the current experimental results. Assuming sequential creep behavior (Equation (5-18)) and substituting for the modified grain boundary sliding model (Equation (5-19)), the proposed creep model predicts those measured within the Region II deformation region. Furthermore, the superposition of Equations (5-20) and (5-20) creep models deviate at low and high stresses. Based on the analysis, creep deformation of the Z20SB composite follows a deformation path described by Ashby and Verrall (1973) through mechanisms detailed by Gifkens (1976, 1978) and Langdon (1970), Figure 5- 45. The development of a deformed ZrB_2 grain mantle region accommodates grain boundary sliding.

5.2.2.5. Creep Strengthening by Solid Solution

Evidence supports rate-controlling dislocation flow accommodated grain boundary sliding within the ZrB_2 matrix above 1600°C. From these observations WC based solid solution alloys were prepared in effort for probing the solute effect on reducing the *accommodating* mechanism with anticipation of reducing the creep rate. The ZWC3 as-sintered and heat-

[2] Ashby and Verrall (1973) diffusion accommodated flow reduces to Coble (1963) and Nabarro (1948) and Herring (1950) diffusion creep at strains less than 0.5.

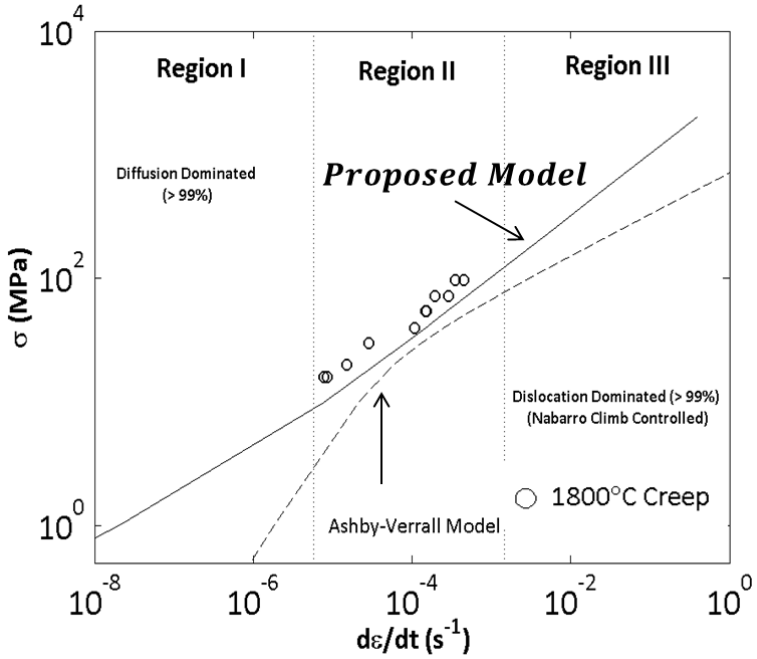

Figure 5-44: Flexure creep model comparison at 1800°C. The hashed line represents Equation (5-17) and (5-19) operating sequentially. The black hashed line represents Ashby and Verrall (1973) creep model.

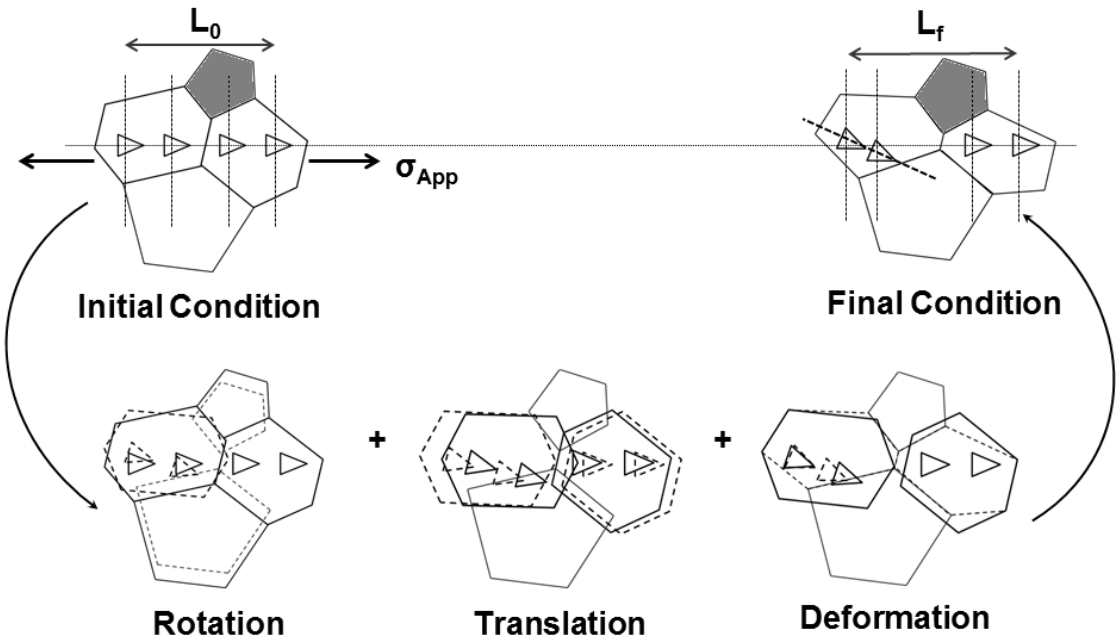

Figure 5-45: Deformation Mechanism Schematic for Z20SB composite. Grey grain represents a place holder for a SiC or ZrB_2 grain.

treated microstructures were used for the preliminary study on the solute constitution effect on creep rate. Limited ZrB_2 alloy creep experiments suggest a solid solution effect on creep rate having an ~1.2 -10 fold creep rate reduction over an average solid solution concentration of 1.1 mol% W in ZrB_2. Because of a limited number of creep experiments, only qualitative trends were considered based loosely on the apparent stress exponent. A review of the strain-rate – stress relationship reveals a decade creep rate difference between the tests conducted at 97MPa. Stress exponents of 1.3 +/- 1.0 and 2.7 +/- 1.0 were not statistically different, based on an analysis of covariance, for the AR and HT alloys, respectively. However, these relative magnitudes coupled with the cavitation microscopy provide valuable insights to the operating creep mechanisms. For the present alloys, the formation of cavities suggests some degree of grain boundary sliding occurring as an independent creep mechanism. The apparent stress exponents suggest the non-linear response may include both grain boundary sliding and cavitation. Diffusion creep cannot be rule out based on these findings, however, experience with ZrB_2 composites suggests the ZrB_2 matrix deforms by grain boundary sliding at these elevated temperatures and fine grain sizes. Furthermore a 10 fold decrease in the observed macroscopic creep strain and strain-rate, at 30 MPa, with similar final microstructures and increasing W-concentration, indicates a solute effect on creep behavior despite a 1 μm average grain size increase.

Solute hardening and softening effects have been studied to some length in the $MoSi_2$ and ZrC ceramic systems ((Sharif, et al., 2001), (Misra, et al., 2000) and (Harada, Murata and Morinaga 1998)). Harada, et al., (1998) conducted a comprehensive study on solid solution softening and hardening of $MoSi_2$ using group 5 and 6 transition metals and Zr and Re for substitution with Mo on the body centered tetragonal lattice sites. Temperature dependent microhardness measurements indicated solid solution hardening over the entire test

temperature range for W and Re additions of 16-32 and 3-32 mol%, respectively. A separate study showed ≤ 2.5 mol% Re additions increased the flow stress ~700% at 1600°C beyond that of the unalloyed $MoSi_2$ (Misra, et al., 2000). ZrC-WC solid solution alloys were studied in compression creep by Kats, et al., (1979) for understanding the low W-concentration effects ranging from 1-7 mol% WC dissolution. A decreasing creep rate of one decade was observed over all temperature ranges with increasing WC dissolution. Stress exponents ranged from n ≈ 1 and 2.75 for testing temperatures 2650-2800°C and 2450-2650°C, respectively. Assessment of the grain size exponent showed a weak dependence of 0<m<1 suggesting mechanisms other than diffusion were rate-controlling over all temperature ranges (e.g., m=2 or 3 for diffusion). From these findings and activation energy measurements close to the Zr/ZrC self-diffusion coefficient suggested slip dominated mechanisms. They considered solute drag on dislocations promoting dislocation climb as a rate-controlling mechanism despite a stress exponent less than 3 (Kats, Ordan'yan and Gorin, et al., 1979). Furthermore, solute interaction on retarding grain boundary sliding was suggested for the ceramics having n=1-2 as the dislocation flow occurs adjacent to the grain boundaries similar to the matrix creep behavior of the Z20SB composite. An independent ZrC-WC study of 0-0.3 mol% solid solution found negligible influence on creep rate, flexure strength, microstructure or lattice constants. The brittle-to-ductile transition temperature increased with WC composition by ~100°C as a result of increasing covalent bonding and interatomic reaction (Gurevich, et al., 1981).

Solute constitution effects on dislocation glide were modeled by Cottrell and Jaswon (1949) for metals exhibiting micro-creep. Their approach considers both the hydrostatic stress field of a single dislocation and the atomic misfit strains *dependent* on concentration. Later Rickman, et al., (2003) included probabilistic terms to a similar interaction potential proposed by Cottrell and Jaswon (1949) for two interaction types: Quasiparticle interactions and stationary

solute traps. The former pertains to fast diffusing solute species dragging low velocity dislocations in the form of solute atmospheres and the latter as low mobility solute acting as stationary traps with short range interactions on high velocity dislocations (Rickman, LeSar and Srolovitz 2003). Under creeping conditions, dislocation glide is considered sufficiently slower than time-independent plasticity allowing sufficient time for solute diffusion to the dislocation (time-dependent) (Cottrell and Jaswon 1949). Therefore, the speed of slow dislocation glide is limited by the rate of migration of the solute atoms defining the rate-controlling creep mechanism commonly found in substitutional solid solutions having n=3 (Mohamed and Langdon 1974). Mohamed and Langdon (1974) suggested preference to Cottrell and Jaswon (1949) formulation for including a composition *dependence* on creep rate contrasting with the composition *independent* model proposed by Friedel (1964). Cannon and Sherby (1973) proposed the importance of the misfit strain on alloy classification and dislocation based creep behavior suggesting $r_{cation}/r_{anion} > 2$ indicates n=3 creep of non-metals. For the present case, the concentration dependence on creep rate is desired using a form of the Cottrell and Jaswon (1949) solute drag model having the following form

$$\frac{\dot{\varepsilon}_{wc}}{\dot{\varepsilon}_0} = \left(\frac{D_{wc}}{D_0}\right)\left(\frac{c_0}{c_{wc}}\right). \tag{5-22}$$

The creep rate ratio, $\frac{\dot{\varepsilon}_{wc}}{\dot{\varepsilon}_0}$, for a *WC* composition, normalized by a reference state strain rate and D and c are the diffusivities and concentrations, respectively, for the alloy and reference state; the complete model derivation is provided in Appendix E. Application of Equation (5-22) to the experimental compression creep, from Kats, et al., (1979), is shown in Figure 5- 46 for the 1 mol% WC reference composition. The W-composition dependence is clearly observed and suggests solute interaction with dislocation creep similar to the conclusions of Kats, et al., (1979). Furthermore, the composition plateau approaches a WC composition of 5-6 mol% WC

coinciding with the experimental lower limit of ~4 mol% WC. The increasing creep rate with WC composition beyond the 4-6 mol% range corresponds to an increasing homologous temperature as a result of the melting point reduction proposed by Y.N Vil'k, et al., (1972).

For the present alloys, assuming grain boundary sliding as an independently operating mechanisms the observed ZWC3AR and HT strain-rates were normalized using Langdon's formula (Equation (5-15)) accounting only for the non-constitution dependent terms with exception to the assumed b=a* lattice constant (Table 5- 10):

$$\frac{\dot{\varepsilon} d K T}{\sigma^2 b^2} = \frac{D_l}{G}, \tag{5-23}$$

where d and a* are the average grain size and basal plane lattice constant reported in Chapter 4 for the AR and HT alloy. These normalized strain-rates, for the 1.4 mol% WC reference composition, are overlaid with the Equation (5-23) and the ZrC-WC data illustrating the qualitative model agreement.

The observed W-constitution effect on creep in the ZrB_2 alloys apparently follows the solute drag model over the 2.5 mol% W composition range. However, these data points are limited and only qualitative trends are considered. An attempt was made to qualitatively assess the effectiveness of W constitution on creep properties by examining the dislocation "break away" stress marking a behavior transition from viscous drag to solute trap behavior (Rickman, LeSar and Srolovitz 2003). Friedel (1964) proposed the dislocation breakaway shear stress follows

$$\tau_B = \frac{\beta W^2 c_0}{K T b^3}, \tag{5-24}$$

where the breakaway shear stress , τ_B, scales with the average solute concentration, c_0, the interaction potential, W, constant $\beta = 0.1$ (Endo, Shimada and Langdon 1984) and K, T and b the usual significance. Cottrell and Jaswon (1949) report a similar breakaway stress model and

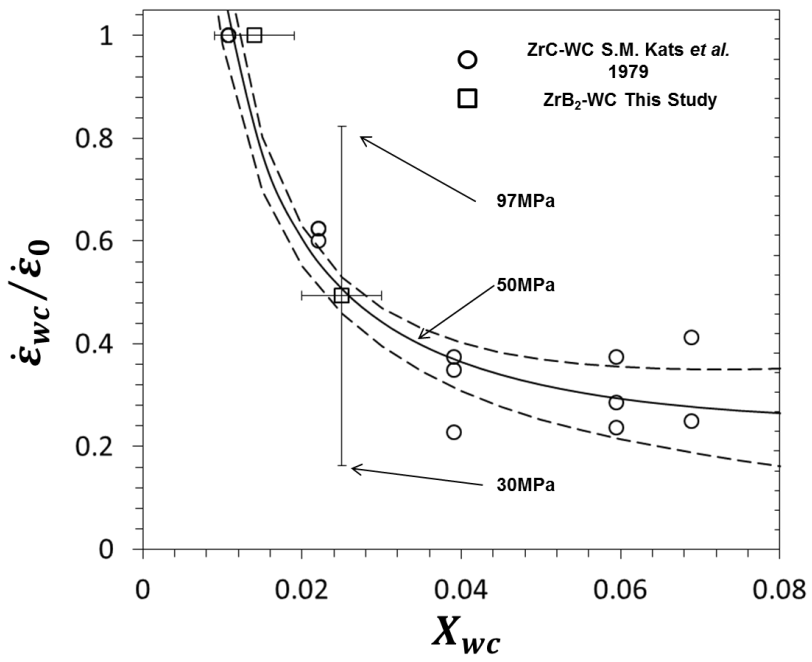

Figure 5-46: Solute drag model derived by Cottrell and Jaswon (solid line) with 95% CI bounds (hashed lines) compared with normalized creep rates for the ZrC-WC (circles) and ZrB_2-WC (Squares).

the interaction potential differences between Equation (5-24) of which the details are summarized in Appendix E. A comparison of Equation (5-24) with material properties of ZrC-WC and ZrB_2-WC suggests a larger W constitution effect on dislocation interaction within the ZrB_2 lattice at the same homologous temperature, Figure 5- 47. For reference, single and polycrystalline Al_2O_3 breakaway stresses are provided illustrating the magnitude of the lattice stress for hexagonal ceramics at $T/T_m = 0.66$ (Ota and Pezzotti 1996). These stresses indicate the reference lattice stress for moving a dislocation in the limit the solute concentration goes to zero. Binary Sn-Bi constitution dependence on the breakaway strengths are shown for $T/T_m = 0.55$ (Mitlin, Raeder and Messler, Jr. 1999). Considering the model validity, the yield point drop observed by Haggerty and Lee (1971) corresponds to an equivalent "breakaway" shear stress of ~34 MPa (Figure 5- 47) exceeding the theoretical solute-dislocation stress of ~2 MPa for nominally pure ZrB_2. The yield point drop was a result of dislocation interactions with ZrB_2

Table 5- 10: Normalized experimental creep rates for ZWC3AR (1.4 mol% WC) and HT (2.5 mol% WC)

$WC_{mol\%}$	$\sigma_C\ (MPa)$	$\dot{\varepsilon}\ (s^{-1})$	$d\ (\mu m)$	$b\ (\text{Å})$	$D_l G^{-1}$
1.4	97	1.75E-06	4.64	3.167	2.46E-16
1.4	97	1.21E-05	4.64	3.167	1.71E-15
1.4	30	1.04E-06	4.64	3.167	1.53E-15
2.5	97	7.98E-06	5.63	3.1663	1.36E-15
2.5	97	1.23E-06	5.63	3.1663	2.11E-16
2.5	30	1.30E-07	5.63	3.1663	2.32E-16

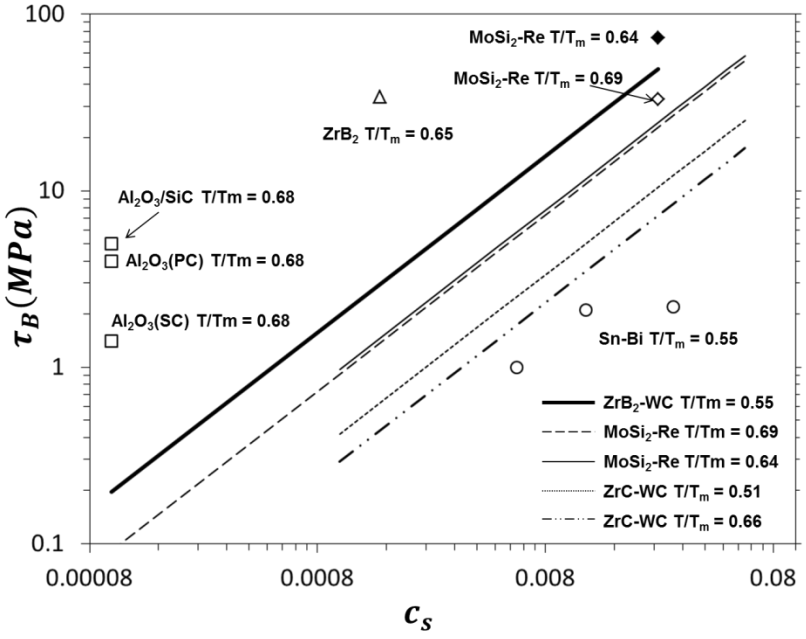

Figure 5- 47: Breakaway stress model illustrating alloy constitution, cs, effectiveness.

precipitates based on the shear stress correlations with the precipitate spacing. $MoSi_2$-Re alloy system compares favorably with the Equation (5-24) at $T/T_m = 0.69$. A behavior transition occurs over a 100°C reduction suggesting yield phenomena differing from the traditional solute-dislocation interactions, Figure 5- 47. Misra, et al., (2000) considered complex solute-vacancy point defect interactions with dislocations for the observed flow stress increases at the lower temperatures (T<1400°C) in the $MoSi_2$-2.5% Re alloy system. Si constitution vacancies, in addition to thermal vacancies, were expected to migrate near the Re substitution sites, as

charge compensating defects for the higher electron valence (Re^{+7}), forming irregular stress fields. These vacancy-solute complexes enhance lattice straining beyond those predicted for solute-solvent volume differences and shear moduli changes (Misra, et al., 2000). Deviations from the breakaway model represent dislocation interaction phenomena different from the traditional spherical strain field assumed for the aforementioned solute-dislocation interaction models. Therefore, the present model provides qualitative insights to the solute-dislocation interaction.

The ZrB_2 break away stresses of 27 MPa and 49 MPa were calculated for the 1.4 and 2.5 mol% composition correlating with the observed macroscopic creep strain differences, between the AR and HT alloys, as the applied stress falls below the breakaway stress. For the condition of $\tau_B > \sigma_{App}$, solute pinning may dominate with small dislocation perturbations overcome by short range solute diffusion as a result of slow dislocation velocities. The resulting creep or accommodation response is dominated by the solute drag on the dislocation (Rickman, LeSar and Srolovitz 2003). The $\tau_B \leq \sigma_{App}$ condition promotes solute-dislocation interactions in the form of stationary traps as the solute mobility is relatively low to that of the freely moving dislocation (Rickman, LeSar and Srolovitz 2003). The drag hypothesis qualitatively agrees with the small macroscopic creep strains observed for the HT alloy. Evidence supports grain boundary sliding creep occurring in both the AR and HT alloys manifested by the presence of cavities at multigrain junctions despite a one decade creep-rate reduction. Therefore, the increased W composition correlates with the creep rate reduction presumably by solute interaction with dislocation accommodating mechanisms at 30 MPa. Increasing the creep stress to 97 MPa shows little macroscopic creep strain contradicting the $\tau_B \leq \sigma_{App}$ condition. It is recognized that uneven loading likely caused pre-mature rupture, beneath the inner span loading pin, prior to sufficient creep strain accumulation despite the high W-concentration.

The W alloying effectiveness was apparent between the ZrB_2 and ZrC systems having breakaway shear stresses of 49 and 7 MPa, respectively, for a 2.5mol% W concentration and T/T_m = 0.51-0.55. The increased effectiveness of W in the ZrB_2 system correlates with the observed one decade normalized creep rate reduction between 1 to 2.5 mol% W for 30 MPa ZrB_2 creep contrasting with a half decade decrease for the ZrC-WC system. The observed difference may follow the same solute interaction arguments on the basis of the $\tau_B \leq \sigma_{App}$ condition for ZrC-WC system. Comparing the formation enthalpies of -207 KJ/mol (Baker, Storms and Holley 1969) and -322 KJ/mol (ref) for ZrC and ZrB_2, respectively, reveals the highly angle dependent covalent bonding between Zr-C and Zr-B. Moreover, the bonding differences between the two systems are reflected in the shear modulus differences of 220 and 168GPa for ZrB_2 and ZrC, respectively, at room temperature owing to the larger calculated ZrB_2 breakaway lattice stress. Apparently, the substitution of W atoms at Zr lattice sites in ZrB_2 preserves the bonding state, at low concentrations, maintaining the increased lattice stress required for moving a dislocation, from its atmosphere, enhancing creep resistance. Evidence supports W constitution affects the low stress creep-rate of ZrB_2 beyond those from grain size.

Chapter 6

Conclusions and Future Work

The conclusion section comprises of both the processing, room temperature properties and preliminary alloy development and creep behavior programs. Each will be addressed in its own section with the subsequent future work combining the findings for addressing UHTC microstructure improvements for long duty cycle aerospace applications.

6.1. Processing and Room Temperature Mechanical Behavior

ZrB_2-SiC and alloys were hot-pressed to ~100% theoretical density at 2100°C despite select densities exceeding the theoretical density. Milling impurities and residual sintering aids were observed and final densities adjusted using a law of mixtures. Density measurements proved useful for verifying the nominal composite and alloy chemistry based on accurate knowledge of the initial powder charge and control of introducing milling impurities. Attrition milling procedures were observed having significantly higher milling impurity concentration as a result of excessive milling media wear. Although, ball milling introduced milling impurities, the approximated WC concentrations were 14% of those introduced from attrition milling.

ZrB_2-WC solid solution alloys were successfully developed for improved creep resistance having limited W-constitution in ZrB_2. The calculated WC solubility of ~4 mol% at 2100°C was an overestimate for the 1.4-3.5 mol% measured for the hot-pressed condition. Increasing the temperature through 2300°C accompanied an increasing W composition of 2.5-4.2 mol% compared with calculated value of 9.25mol%. A monotonic decreasing lattice parameter was observed with increasing WC constitution confirming solid solution formation. Reaction equilibria were proposed describing the thermodynamic competition between WC dissolution

and formation of WB at multigrain junctions. Apparently the presence of excess carbon promotes WC dissolution as a result of a thermodynamically favorable reaction. Although, WB was observed in all alloys, there exists a kinetic interplay such that reducing starting particle sizes increases WC dissolution and decreases WB formation as a result of shorter diffusion distances and higher interfacial energies. WC-dissolution was described in the context of an excess carbon factor dependent on the desired WC constitution, temperature and grain size. However, residual carbon concentrations proved deleterious upon solution treating at 2300°C. Excessive discontinuous grain growth was observed as a result of solution precipitation mechanism in the presence of a boron-carbon rich melt. Control of the final residual carbon concentration inhibits liquid phase formation, at high temperatures, stabilizing the ZrB_2 microstructures.

Composites and alloy room temperature mechanical properties were within those reported in prior studies. Composite and alloy MOR and SENB results showed strength limiting correlations with the maximum inclusion size based on an intrinsic Griffith flaw size. The carbon containing microstructures showed evidence of crack initiation at the partially de-bonded high aspect ratio carbon inclusions. ZWC1 alloy had a strength and fracture toughness of 486 +/- 101 MPa and 3.8 +/-0.5 MPa√m despite the presence ZrO_2 and fine matrix grain size. ZCWC strengths and toughness of 371 +/- 39 MPa and 2.7 +/- 0.5 MPa√m , respectively, highlight the inherently low toughness of the ZrB_2 matrix. Room temperature MOR and SENB results for the ZSB material showed strength and fracture toughness of 456 ± 66 MPa and 3.92 ± 0.24 MPa√m, respectively. Similar tests of the ZS material resulted in average strength and fracture toughness of 734 ± 60 MPa and 4.48 ± 0.91 MPa√m, respectively. ZSB composite strength is limited by maximum Boron-rich carbide (B_xC_y) inclusions, while the ZS composite is likely limited by SiC grains. Predominately transgranular fracture was observed for each alloy with exception

to the ZWC3 having increasing intergranular fracture path. ZWC3 strength and toughness of 401 +/- 61 MPa and 4.2 +/- 0.2 MPa√m, respectively, did not correlate with the calculated flaw size suggesting additional toughening mechanisms operating. Process zone crack deflection and wake zone grain bridging were presumed responsible for the ~1 MPa√m toughness increase based on improved crack face communication and thermal expansion anisotropy. Elastic modulus and hardness properties were within the reported limits for all materials and heat treatments. Solid solution room temperature strengthening, over the limited composition range, was masked by ZrB_2 crystal plasticity anisotropy.

6.2. Creep Behavior

ZrB_2-20 vol% SiC flexure creep behavior was investigated through 1800°C under constant stress through 97 MPa. Creep rate increased with applied stress and temperature revealing two distinct creep behavior regimes (1) Low temperature (1400-1500°C) and (2) High temperature (> 1500°C). Stress exponent n=1 and activation energy of 364±92 KJ/mol represents low temperature and $1.7<n<2.2$ and activation energy between 598±72 KJ/mol and 670±23 KJ/mol for stresses ≤ 30MPa and >30MPa, respectively, represents high temperature.

Low temperature creep behavior is dominated by ZrB_2 grain or ZrB_2-SiC interphase boundary sliding accommodated diffusion with ZrB_2 lattice diffusion likely contributing to the overall creep-rate. Microstructural continuity and a stress exponent of unity suggest diffusion dominated creep behavior. Calculated activation energies are within the ranges of those measured and reported for other composites exhibiting similar creep behavior. A transition to higher temperatures ($1600<T\leq1800$°C) accompanies a creep mechanism shift with 1.5 decade increase in strain rate. From the directly observed creep deformation and applied texture theory, rate-controlling ZrB_2 grain boundary sliding creep operates in sequence with cavitation for bending creep of a ZrB_2-20% SiC composite. The ZrB_2 matrix grain boundary sliding was

comprised of matrix grains translating and rotating in response to the accumulated creep strain maintaining a relatively constant grain shape. Grain deformation, presumably by dislocation flow, was observed for unfavorably orientated grains restricted from sliding. Although, ZrB_2 lattice deformation was found as an *accommodation* mechanism for the grain sliding event. The ZrB_2 grains were modeled having a mantle and core region of high and low dislocation density, respectively. The HREBSD and IDM methods probed the deformation characteristics of the mantle and core regions in the context of a single crystal deformation. Mantle dislocation densities were larger than those residing in the core by a factor of 13. The transition from core to mantle deformation deviates from single crystal behavior as a result of extra geometrically necessary dislocations accommodating the grain deformation gradient. A final deformation model was presented including grain boundary translation, rotation and deformation accounting for the >90% tensile creep strain contribution. Composite cavitation and SiC deformation contribute <10% of the macroscopic tensile creep strain contrasting with an increase in SiC grain deformation of <20% for the compressive strain.

Contrary to traditional ceramic creep deformation cavitation contributes little to the deformation event. SEM observations suggest two distinct stress dependent cavitation models. $\sigma \leq 30$MPa, high temperature cavitation occurs with a constant number density suggesting preferred cavity growth contrasting with 3.5 fold cavity number density increase suggesting nucleation kinetics. These findings were supported by a cohesive zone cavitation model illustrating these kinetic trends at stresses beyond 50MPa.

Preliminary alloy creep experiments show improved creep resistance over 1.1 mol% increasing W concentration in ZrB_2 monoliths and a two decade creep rate reduction from the ZrB_2-20%SiC composite. Evidence supports grain boundary sliding was operating in both the AR and HT alloys with the presence of equilibrium shaped cavities located at ZrB_2 multigrain

junctions despite a one decade creep rate reduction at 30MPa creep stress. Although, these findings are limited, a condition was imposed hypothesizing a solute-dislocation interaction transition when the applied stress approaches the theoretical dislocation "breakaway" stress. For the $\tau_B \leq \sigma_{App}$ condition, solute atmospheres act as stationary traps interacting with freely gliding dislocations. Below the breakaway stress, gliding dislocations presumably drag solute atmospheres as a result of low dislocation velocities. The observed creep strain for the former condition correlates with the proposed behavior contrasting with negligible creep strain over extended creeping times for the latter case. The alloying effectiveness of W appears greater for ZrB_2 compared with the known ZrC system as a result of a higher bonding energy. The predicted dislocation breakaway stress for ZrB_2 exceeds those of ZrC lattice by a factor of ~7, at similar homologous stress, supporting this observation.

6.3. Future Work

These ZrB_2 based composites and ceramics are candidates for long duty cycle aerospace applications. The current research indicates structure-property relationships aiding the design of these functional ceramics for low and high temperature applications. Typically, high temperature materials design includes a compromise of room temperature strength properties. For the current applications this leaves structural components susceptible to foreign body impact damage initiating or propagating pre-existing flaws below design stresses. However designing for creeping conditions over long exposure times requires increasing grain sizes, grain boundary pinning by precipitation and solid solutions. The former two render low room temperature strengths contrasting with the latter having little influence on linear elastic failure. Therefore, careful consideration of microstructure design and the end application are required for these extreme environment applications.

The current research has identified the dominant creep mechanisms and a promising alloy design having improved properties including favorable room temperature mechanical behavior, Table 6- 1. However, the final application microstructure may likely differ from those presented in this study, a few key microstructure components need further understanding for improved high temperature behavior: Particle reinforcement, matrix grain size, and quasi-binary alloying constitution effects on low and high temperature mechanical behavior.

Table 6- 1: ZrB_2 based composite and alloy property comparison.

Property	ZrB_2-20SiC	ZrB_2-1.5WC	ZrB_2-2.5WC
ZrB_2 Grain Size (μm)	3.1 +/- 0.9	4.6 +/- 0.7	5.6 +/-1.0
Relative Density %	99.8	99.9	99.9
Modulus (GPa)	492 +/- 41	478 +/- 38	514 +/- 57
ZrB_2 Hardness (GPa)	21.6 +/- 0.7	20.7 +/- 0.5	20.6 +/-2.0
Strength (MPa)	456+/- 66	401 +/- 61	-----
K_{IC} $(MPa\sqrt{m})$	3.9 +/- 0.2	4.2 +/- 0.2	-----
$\dot{\varepsilon}_{97\ MPa}$ (s^{-1})	4 x 10^{-4}	7 x 10^{-6}	5 x 10^{-6}
$\dot{\varepsilon}_{30\ MPa}$ (s^{-1})	3 x 10^{-5}	1 x 10^{-6}	1 x 10^{-7}

Particle reinforcement strength and toughness properties are well studied for SiC particles, although, limited data exists for other non-reacting reinforcements. Temperatures exceeding 2300°C favor eutectic liquid formation limiting both process annealing and application temperatures. Candidate high temperature oxide materials such as ZrO_2 and HfO_2 may likely have the required phase stability as a result of large formation free energies near these high temperatures. Mechanical property considerations include: the effect of martensitic phase transformation on the thermal shock behavior, transformation toughening and creep behavior. The former reviews the tetragonal –to – monoclinic transformation accompanying a volume expansion in the temperature range of 850<T<900°C and 1500<T<1600°C for ZrO_2 and HfO_z, respectively. These volume expansions may cause matrix cracking upon quenching resulting in poor thermal shock performance. However, these matrix-particle interactions are not well

known, specifically, at temperatures where stress relaxation may promote improved mechanical stability. The spatial and volume fraction of these reinforcement phases are important for boosting strength and toughness. Particle agglomeration and particle size are factors easily controlled and need consideration for improving flexure strength and toughness. A survey of the effects on SiC particle size and volume fraction show an apparent particle/agglomerate size threshold of ~6 µm defining a ~250 MPa change in room temperature strength, Figure 6- 1. Additionally, the reinforcement volume fraction effect on strength was confirmed in the present study. Others have observed 10 vol% reinforcement phase as a tentative lower bound for improved strength and toughness (Leohman, et al., (2006), and Fahrenholtz, et al., (2007)). Creep experiments have revealed a reducing volume fraction favors a reduction in creep rate; therefore, experiments are needed for determining the optimum composite reinforcement composition.

Extreme environment target creep rates are ~10^{-8} s^{-1} (Courtright, et al., 1992) can be achieved by increasing the matrix grain size, reducing the reinforcement volume fraction, decorating grain boundaries with precipitates and solid solution strengthening. The present work shows a creep rate reduction from 10^{-5}- 10^{-4} s^{-1} to 10^{-7}-10^{-6} s^{-1} with 1-2 µm grain size increase, removal of SiC phase and solid solution creep strengthening. Increasing matrix grain size is straight forward, however, large reductions in room temperature strength are expected and including particle reinforcements may offset these strength reductions. Understanding the interplay between matrix grain size and particle reinforcement provides an opportunity for optimizing both low and high temperature mechanical behavior. Grain boundary precipitates are likely to reduce room temperature strength and fracture toughness. Additionally, microstructure stability is then controlled by the melting point, solubility and aging characteristics during prolonged high temperature exposure. The present study showed

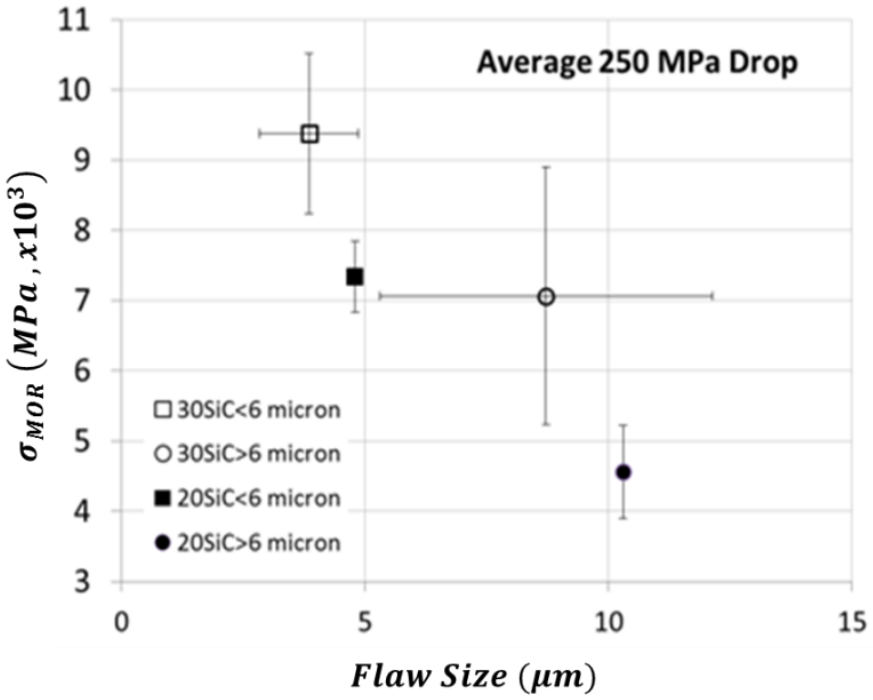

Figure 6-1: ZrB_2-SiC composite strength assessment illustrating volume fraction reinforcement and critical grain/agglomerate size relationships.

promise of small WC alloying (<2.5 mol%) reducing the creep rate one decade from the reference composition. Although, the present work includes insights to phase stability, additional experiments are needed for probing the extent and rate of WC solubility in ZrB_2 and the constitution effects on creep rate. Such effects include: starting particle size effects on WC dissolution, the maximum temperature of which the solute-dislocation drag mechanism may operate and melting point determination. Reducing starting ZrB_2 particle size was correlated with improved WC dissolution from the small diffusion distances and improved starting WC distribution. The attrition milling provides a grinding method suitable for particle size reduction (average size 1μm) and reducing particle agglomeration satisfying the room temperature strength and toughness requirements. Additionally, annealing at temperature greater than 2300°C increases the driving force for WC dissolution and homogenization. Combining the milling and the high temperature post sintering (hotpressing) anneal favors grain growth from

the increased thermal and interfacial driving forces. Annealing experiments would determine the optimum time and temperature for promoting controlled grain growth, extended solubility and homogenization (if applicable).

Clearly one example of an optimum microstructure includes the following: a WC-ZrB_2 solid solution alloy having large ZrB_2 grain sizes and less then 10vol% oxide reinforcement. The relative amounts of each category should reduce steady state creep rates approaching the 10^{-8} s^{-1} while maintaining strengths above ~500 MPa and $K_{IC} > 4$ $MPa\sqrt{m}$.

References

Adams, B L. "Orientation Imaging Microscopy: Emergin and Future Applications." *Ultramicroscopy* 67 (1997): 11-17.

Anderson, T L. "Linear Elastic Fracture Mechanics." In *Fracture Mechanics Fundamentals and Applications Third Addition*, by T L Anderson, 25-101. Boca Raton: CRC Press, 2005.

Ashby, M F. "The Deformation of Plastically Non-homogenous Materials." *Philosophical magazine* 21, no. 170 (1970): 399-424.

Ashby, M F, and R A Verrall. "Diffusion-Accommodated Flow and Superplasticity." *Acta Metallurgica* 21 (February 1973): 149-63.

Ashby, M F, R Raj, and R C Gifkins. "Diffusion-Controlled Sliding at a Serrated Grain Boundary." *Scripta Metallurgica*, 1970: 737-742.

ASTM, B962-13. "Standard Test Methods for Density fo Compacted or Sintered Powder Metallurgy (PM) Products Using Archimedes' Principle." In *ASTM B962 02.05*, by ASTM International. West Conshohocken, PA, 2013.

Aune, R P. "Flexural Creep of ZrB_2-SiC Ultra-High Temperature Ceramic." Master's Thesis, Houston, 2011.

Baker, F B, E K Storms, and Jr., C E Holley. "Enthalpy of Formation of Zirconium Carbide." *Journal of Chemical and Engineering Data*, 1969: 244-246.

Ball, A, and M M Hutchinson. "Superplasticity in the Aluminum-Zinc Eutectoid." *Metal Science Journal*, 1968: 1959-1969.

Barin, I, F Sauert, E Shultze-Rhonhof, and W S Sheng. *Thermochemical Data of Pure Substances, Part II La-Zr Secon Edition.* New York, NY: VCH, 1992.

Becher, P F. "Microstructural Design of Toughened Ceramics." *Journal of the American Ceramic Society*, 1991: 255-269.

Bell, R L, and T G Langdon. "An Investigation of Grain-Boundary Slding During Creep." *Journal of Materials Science*, 1967: 313-323.

Benson, H. "University Physics." In *University Physics Revised Edition*, by Harris Benson, 662-667. New York: John Wiley & Sons, Inc., 1995.

Biner, S B. "The Role of Grain Boundary Sliding on Creep Deformation Characteristics of Discontinuous Reinforced Composites." In *Plastic Deformation of Ceramics*, edited by R.C. Bradt, C A Brookes, J L Routbort, 495-505. New York: Plenum Press, 1995.

Bird, J E, A K Makherjee, and J E Dorn. "Quantitative Relation Between Properties and Microstructure, Edited by Brandon, D G, Rosen, A." *Proceedings of an International Conference.* Haifa, Isreal: Israel Universities Press, 1969. 255.

Bird, M W, P F Becher, and K W White. "Grain Rotation and Tranaslation Contribute Substantially to Flexure Creep of a Zirconium Diboride Silicon Carbide Composite." *In-Press*, 2013.

Bird, M W, R P Aune, A F Thomas, P F Becher, and K W White. "Temperature-Dependent Mechanical and Long Crack Behavior of Zirconium Diboride-Silicon Carbide Composite." *Journal of the European Ceramic Society* In Press (2012): 3453-3462.

Bird, M W, R P Aune, F Yu, P F Becher, and K W White. "Creep Behavior of a Zirconium Diboride-Silicon Carbide Composite." *Journal of the European Ceramic Society*, 2013.

Bunge, H. *Texture Analysis in Materials Science.* London: Butterworths, 1982.

Cannon, R W, and O D Sherby. "Third-Power Stress Dependence in Creep of Polycrystalline Nonmetals." *Journal of the American Ceramic Society*, 1973: 157-160.

Cannon, R W, and T G Langdon. "Review Creep of Cermaics Part 1 Mechanical Characteristics." *Journal of Materials Science*, 1983: 1-50.

Cannon, W R, and T G Langdon. "Review: Creep of Ceramics: Part 2 An Examination of Flow Mechanisms." *Journal of Materials Science* 23 (1988): 1-20.

Chaboche, J L, and J Lemaitre. "Viscoplasticity." In *Mechanics of Solid Materials*, by J. Lemaitre J.L Chaboche, 253-345. New York: Cambridge University Press, 1990.

Chadwick, M M, R S Jupp, and D S Wilkinson. "Creep Behavior of a Sintered Silicon Nitride." *Journal of the American Ceramic Society*, 1993: 385-396.

Chamberlain, A L, W G Fahrenholtz, G E Hilmas, and D T Ellerby. "High-Strength Zirconium Diboride-Based Ceramics." *Journal of the American Ceramic Society*, 2004: 1170-1172.

Chang, Y A. *Part II. Ternary Systems. Volume IX. Zr-W-B System and the Pseudobinary System TaB_2-HfB_2.* AFML-TR-65-2, Wright-Patterson Air Force Base: 1-26, 1966.

Chang, Y A. *Ternay Phase Equilibria in Transition Metal-Boron-Carbon-Silicon Systems.* AFML-TR-65-2 Part II, Vol IX, Wright-Patterson Air Force Base, OH: Air Force Materials Laboratory, 1966.

Change, R. "Creep of Al_2O_3 Single Crystals." *Journal of Applied Physics* 31 (1960): 484-487.

Chauvenet, W. *Appendix: The Method of Least Squares.* Vol. II Theory and Use of Astronomical Instruments, in *Manual of Spherical and Practiacl Astronomy Vol II. Theory and Use of Astorno*, by W Chauvenet, 558-566. Philadephia, PA: L.B. Lippincott & Co., 1868.

Chen, C-F, S M Wiederhorn, and T-J Chuang. "Cavitation Damage during Flexural Creep of SiAlON-YAG Ceramics." *Journal of the American Ceramic Society,* 74, no. 7 (1991): 1658-62.

Coble, R L. "A Model for Boundary Diffusion Controlled Creep in Polycrystalline Materials." *Journal of Applied Physics* 34 (1963): 1679-1682.

Coble, R L. "Diffusion Models for Hot Pressing with Surface Energy and Pressure Effects as Driving Forces." *Journal of Applied Physics*, 1970: 4798-4807.

Coble, R.L. "A Model for Boundary Diffusion Controlled Creep in Polycrystalline Materials." *Journal of Applied Physics* 34 (1963): 1679-1682.

Cottrell, A H, and M A Jaswon. "Distribution of Solute Atoms Round a Slow Dislocation." *Proceedings of the Royal Society of London. Series A, Mathematical and Physical Sciences*, 1949: 104-114.

Courtright, E L, H C Graham, A P Katz, and R J Kerans. *Ultrhigh Temperature Assessemnt Study-Ceramic Matrix Composites.* WL-TR-91-4061, Writgh-Patterson Air Force Base, Ohio: Materials Directorate Wright Laboratory, 1992.

Cullity , B D, and S R Stock. *Elements of X-ray Diffraction (3rd Edition).* Upper Saddle River, NJ: Prentice Hall, 2001.

Datta, M S, A K Bandyopadhyay, and B Chaudhuri. "Sintering of Nano Cyrstalline a Silicon Carbide by Doping With Boron Carbide." *Bulleting Material Science* 25, no. 3 (2002): 181-89.

de Graeff, Marc. *Introduction to Conventional Transmission Electron Microscopy.* Cambridge University Press, 2003.

Dryden, J R, D Kucerovsky, D S Wilkinson, and D F Watt. "Creep Deformation Due to a Viscous Grain Boundary Phase." *Acta Metallurgica*, 1989: 2007-2015.

Dunne, F. "Finite Element Formulatin for Plasticity." In *Introduction to Computational Plasticity*, by N. Petrinik F. Dunne, 133-136. New York: Oxford University Press, 2005.

Dunne, F, and N Petrinic. "Viscoplasticity and Creep." In *Introduction to Computational Plasticity*, by N. Petrinic F. Dunne, 38-45. New York: Oxford University Press, 2005.

Dunne, F, and N Petrinik. "Implicit and Explicit Integration." In *Introduction to Computational Plasticity*, by N. Petrinik F. Dunne, 143-168. New York: Oxford University Press, 2005.

Eckert, T E. *Ternary Phase Equilibira in Transition Metal-Boron-Silicon Systems Part II. Ternary Systems Volume XII. Ti-Zr-B System Investigation of Pseudo-Binary Systems ZrB_2-NbB_2, ZrB_2-TaB_2, and HfB_2-NbB_2.* Wright Patterson Air Force Base: RTD Technical Report, 1966.

EDAX. "TSL Orientation Imagaing Microscopy Anslysis 6 Manual." Software Manual, Materials Analysis Division, AMETEK, Inc., 2011.

Ekbom, L B, and C O Amundin. *Science of Ceramics*, 1981: 237-243.

Endo, Takao, Takashi Shimada, and T G Langdon. "The Deviation From Creep by Viscous Glide in Solid Solution Alloys at High Stresses - I. Characteristics of the Dragging Stress." *Acta Metallurgica*, 1984: 1991-1999.

Evans, A G, and A Rana. "High Temperature Failure Mechanisms in Ceramics." *Acta Metallurgica* 28 (1979): 129-41.

Fahrenholtz, W G, G E Hilmas, I G Talmy, and J A Zaykoski. "Refractory Diborides of Zirconium and Hafnium." *Journal of the American Ceramic Society* (Journal of the American Ceramic Society) 90 (2007): 1347-1364.

Fahrenholtz, W G, G E Hilmas, S C Zhang, and S Zhu. "Pressureless Sintering of Zirconium Diboride: Particle Size and Additive Effects." *Journal of the American Ceramic Society* 91 (2008): 1398-1404.

Finnie, I. "Method for Predicting Creep in Tension and Compression from Bending Tests." *J. Am. Ceram. Soc.* 49, no. 4 (1966): 218-20.

Friedel, J. "Dislocations." *Pergamon Press*, 1964: 410.

Gangireddy, S, J W Halloran, and Z N Wing. "Non-Contact Mechanical Property Measurements at Ultrahigh Temperatures." *Journal of the European Ceramic Society* 30 (2010): 2183-89.

Gardner, C J, B L Adams, and D T Fullwood. "EBSD-Based Continuum Dislocation Microscopy." *International Journal of Plasticity* 26 (2010): 1234-1247.

Gaskell, D R. *Introduction to the Thermodynamics of Materials, Fourth Edition.* New York, NY: Taylor and Francis, 2003.

Ghosh, D, G Subhash, and G R Bourne. "Room-Temperature Dislocation Activity During Mechanical Deformation of Polycrystalline Ultra-High-Temperature Ceramics." *Scripta Materialia* 61 (2009): 1075-1078.

Gifkins, R C. "Grain Rearrangements During Superplastic Deformation." *Journal of Materials Science*, 1978: 1926-1936.

Gifkins, R C. "Grain-Boundary Sliding and its Accommodation During Creep and Superplasticity." *Metallurgical Transactions A*, 1976: 1225-1232.

Gifkins, R C, and T G Langdon. "Comments on Theories of Structural Superplasticity." *Materials Science and Engineering*, 1978: 27-33.

Gogotsi, G A. "Crack Resistance of Modern Ceramics and Ceramic Composites. I. SEVNB-Method." *Powder Metallurgy and Metal Ceramics*, 2004: 372-382.

Gouissem, Afif. "Un-Published ." 2013.

Goutier, F, G Trolliard, S Valette, A Maitre, and C Estournes. "Role of Impruities on Spark Plasma Sintering of ZrC_x-ZrB_2 Composites." *Journal of the European Ceramic Society* 28 (2008): 671-678.

Grimes, R E, G P Kelkar, L Guazzone, and K W White. "Elevated-Temperature R-Curve Behavior of a Polycrystalline Alumina." *Journal of the American Ceramic Society* 73, no. [5] (1990): 1399-1404.

Guo, S-Q. "Densification of ZrB_2-Based Composites and Their Mechanical and Physical Properties: A Review." *Journal of the European Ceramic Society*, 2009: 995-1011.

Guo, W-M, and G-J Zhang. "Oxidation Resistance and Strength Retention of ZrB_2-SiC Ceramics." *Journal of the European Ceramic Society*, 2010: 2387-2395.

Guo, W-M, G-J Zhang, and H-T Lin. "High-Temperature Flexural Creep of ZrB_2-SiC Ceramics in Argon Atmosphere." *Ceramics International*, 2012: 831-835.

Guo, W-M, Z-G Yang, and G-J Zhang. "High-Temperature Deformation of ZrB_2 Ceramics with WC Additive in Four-Point Bending." *International Journal of Refractory Metals and Hard Materials*, 2011: 705-709.

Gurevich, B D, et al., "Effect of Small Amounts of Tungsten Carbide on the Strength, Creep and Brittle-to-Ductile Transition Temperature of Zirconium Carbide." *Poroshkovaya Metallurgiya*, 1981: 39-42.

Haggerty, J S, and D W Lee. "Plastic Deformation of ZrB_2 Single Cyrstals." *J. Amer. Ceram. Soc.* 54, no. 11 (1971): 572-576.

Harada, Y, Y Murata, and M Morinaga. "Solid Solution Softening and Hardening in Alloyed $MoSi_2$." *Intermetallics*, 1998: 529-535.

Hay Jr., J.C. "High Temperature Characterization of Microstructural Mechanisms Affecting Grain Bridging in Monolithic Structural Ceramics." PhD Thesis, University of Houston, Houston, TX, 1995.

Hay, J C, and K W White. "Effect of Thermoelastic Anisotropy on the R-curve Behavior of Monolithic Alumina." *J. Am. Ceram. Soc.* 77, no. [9] (1994): 2283-88.

Herring, C. "Diffusional Viscosity of a Polycrystalline Solid." *Journal of Applied Physics* 21 (1950): 437-445.

Hertzberg, R W. "High-Temperature Deformation Response of Cyrstalline Solids." In *Deformation and Fracture Mechanics of Engineering Materials*, by R. W. Hertzberg, 157-205. New York: John Wiley & Sons, Inc., 1996.

Hollenberg, G W, G R Terwilliger, and R S Gordon. "Calculation of Stresses and Strains in Four-Point Bending Creep Tests." *Journal of the American Ceramic Society* 54 (1971): 196-199.

Hosford, W F. *The Mechanics of Crystals and Textured Polycrystals.* Edited by A L Cullen and L C Woods. New York: Oxford University Press, 1993.

Hsueh, C H, and A G Evans. "Creep Fracture in Ceramic Polycrystals -II Effects of Inhomogeneity on Creep Rupture." *Acta Metallurgica*, 1981: 1907-1917.

Hu, P, and Z Wang. "Flexure Strength and Fracture Behavior of ZrB_2-SiC Ultra-High Temperature Ceramic Composite at 1800°C." *Journal of the European Ceramic Society* 30 (2010): 1021-26.

Hualong, Li, Hsu Emilie, and Jerzy Szpunar. "Deformation Mechnaims and Texture and Microstructure Evolution During High-Speed Rolling of AZ31B Mg Sheets." *Journal of Material Science* 43 (2008): 7148-7156.

Hull, D, and D E Rimmer. "The Growth of Grain Boundary Voids Under Stress." *Philosophical Magazine*, 1959: 673-687.

Hull, D, and D J Bacon. "Strength of Crystalline Solids." In *Inroduction to Dislocations Fourth Edition*. Elsevier, 2001.

Humphreys, F J. "Characteristion of Fine-Scale Microstrcutures by Electron Backscatter Diffaction (EBSD)." *Scripta Materiallia* 51 (2004): 771-776.

Hynes, A, and R Doremus. "Theories of Creep in Ceramics." *Ciritical Reviews in Solid State and Materials Sciences* 21, no. 2 (1996): 129-187.

Jakus, K, and S Wiederhorn. "Creep Deformation of Ceramics in Four-Point Bending." *Journal of the American Ceramic Society* 71, no. 10 (1988): 832-36.

Jana, A K. *Chemical Process Modelling and Computer Simulation.* New Delhi, India: PHI Learning Pvt. Ltd. , 2008.

Jayaseelan, D.D., Y. Wang, G.E. Hilmas, W. Fahrenholtz, P. Brown, and W.E. Lee. "TEM Investigation of Hot Pressed-10 vol.% SiC-ZrB_2 Composite." *Advances in Applied Ceramics* 110, no. 1 (2011): 1-7.

Jou, Z C, and A V Virkar. "High-temperature Creep and Cavitation of Polycrystalline Aluminum Nitride." *Journal of the American Ceramic Society* 73, no. 7 (1990): 1928-35.

Jou, Z C, S-Y Kuo, and A V Virkar. "Elevated-Temperature Creep of Silicon Carbide-Aluminum Nitride Ceramics: Role of Grain Size." *Journal of the American Ceramic Society* 69, no. 11 (1986): C-279-C-281.

Kacher, J, C Landon, B L Adams, and D T Fullwood. "Bragg's Law Diffraction Simulations for Electron Backscatter Diffraction Analysis." *Ultramicroscopy* 109 (2009): 1148-1156.

Kanninen, M F. "A Dynamic Analysis of Unstable Crack Propagation and Arrest in the DCB Specimen." *Int. J. Fracture* 10 (1974): 415-430.

Kats, S M, S S Ordan'yan, A I Gorin, S S Semenov, and L V Kudraysheva. "Influence of Tungsten Carbide on Creep of Zirconium Carbide." *Inorganic Materials*, 1979: 1775-1778.

Kats, S M, S S Ordan'yan, and V I Unrod. "Compressive Creep of Alloys of the ZrC-ZrB_2 and TiC-TiB_2 Systems." *Soviet Powder Metallurg Metal Ceram.* 20, no. 12 (1981): 886-90.

Kaufman, L. *Calculation of Multicomponent Refractory Composite Phase Diagrams.* NSWC TR 86-242, Cambridge: Manlabs, Inc., 1986.

Kaufman, L, and E V Clougherty. *Investigation of Boride Compounds for very High Temperature Applications.* RTD-TDR-63-4096 Part 2, ManLabs Inc., Cambridge: Manlabs Inc, 1965.

Kaufman, L, and E V Clougherty. *Investigation of Boride Compounds for Very High Temperature Applications.* RTD-TDR-63-4096 Part 1, ManLabs Inc., Cambridge: Manlabs Inc., 1963.

Kaufman, L., and H. Nesor. "Coupled Phase Diagrams and Termochemical Data for Transition Metal Binary Systems - IV*." *CALPHAD* 2, no. 4 (1978): 293-318.

Kaufman, L., B. Uhrenius, D. Birnie, and K. Taylor. "Coupled Pair Potential, Thermochemical and Phase Diagram Data for Transiton Metal Binary Systems - VII*." *CALPHAD* 8, no. 1 (1984): 25-66.

Kaysser, W A, M Sprissler, C A Handwerker, and J E Blendell. "Effect of a Liquid Phase on the Morphology of Grain Growth in Alumina." *Journal of the American Ceramic Society*, 1987: 339-343.

Kelkar, G.P. "Fracture Behavior of Monolithic Alumina and Magnesium Aluminate Spinel." MS Thesis, University of Houston, Houston, TX, 1989.

Kim, J, and S Kang. "First Principles Investigation of Temeprature and Pressure Dependent Elastic Properties of ZrC and ZrN Using Debye-Gruneisen Theory." *Journal of Alloys and Compounds*, 2012: 94-99.

Kislyi, P S, and M A Kuzenkova. "Regularities of Sintering of Zirconium Diboride-Molybdenum Alloys." *Poroshkovaya Metallurgiya*, 1966: 16-23.

Kokawa, H, T Watanabe , and S Karashima. "Sliding Behavior and Dislocation Structures in Aluminium Grain Boundaries." *Philosophical Magazine A* 44, no. 6 (1981): 1239-1254.

Kokawa, K, T Watanabe, and S Karshima. "Dissociation of Lattice Dislcoation in Coincidence Boundaries." *Journal of Materials Science* 18 (1983): 1183-1194.

Krause Jr., R F, W E Luecke, J D French, B J Hockey, and S M Wiederhorn. "Tensile Creep and Rupture of Silicon Nitride." *Journal of the American Ceramic Society* 82, no. 5 (1999): 1233-41.

Kroner, E. "Continuum Theory of Dislocations and Self-Stresses." *Ergebnisse der Angewandten Mathematik* 5 (1958): 1327-1347.

Kurihara, J K, T Tomimatsu, Y F Liu, S Q Guo, and Y Kagawa. "Mode I Fracture of SiC Particle-dispersed ZrB_2 Matrix Composite Measured Using DCDC Specimen." *Ceramics International*, 2010: 381-384.

Kuzenkova, M A, and P S Kislyi. "The Mechanism of Shrinkage of Zriconium Diboride During Sintering." *Poroshkovaya Metallurgiya*, 1966: 46-55.

Landes, J D, and J A Begley. "ASTM STP 590." 1976: 128-148.

Landon, C, B Adams, and J Kacher. "High Resolution Rethods for Characterizing Mesoscale Dislocation Structures." *Journal of Engineering Materials and Technology* 130 (2008): 40-45.

Lane, J E, C H Carter Jr., and R F Davis. "Kinetics and Mechanisms of High-Temperature Creep in Silicon Carbide: III, Sintered a-Silicon Carbide." *Journal of the American Ceramic Society* 71, no. 4 (1988): 281-95.

Langdon, T G. "A Unified Approach to Grain Boundary Sliding in Creep and Superplasticity." *Acta Metallurgica Materiala* 42, no. 7 (1994): 2437-2443.

Langdon, T G. "Grain Boundary Sliding as a Deformation Mechanism during Creep." *Philosophical Magazine* 22 (1970): 689-700.

Langdon, T G. "Grain Boundary Sliding Revisited: Developments in Sliding Over Four Decades." *Journal of Material Science*, 2006: 597-609.

Langdon, T G. "Grain-Boundary Sliding During Creep of MgO." *Pacific Coast Regional Meeting, The American Ceramic Society.* San Francisco, 1974. 92-93.

Langdon, T.G. "Creep at Low Stresses: An Evaluation of Diffusion Creep and Harper-Dorn Creep as Viable Creep Mechanisms." *Metallurgical and Materials Transactions A* 33A (2002): 249-259.

Lange, F F. "Non-Elastic Deformation of Polycrystals with a Liquid Boundary Phase." In *Deformation of Ceramic Materials*, by R C Brandt and R E Tressler, 361-381. New York: Plennum Press, 1975.

Lawson, J W, M S Daw, T H Squire, and C W Baushlicher, Jr. "Computational Modeling of Grain Boundaries in ZrB_2: Implications for Lattice Thermal Conductivity." *Journal of the American Ceramic Society*, 2012: 3971-3978.

Le Claire, A D. "Solute Diffusion in Dilute Alloys." *Journal of Nuclear Materials*, 1978: 70-96.

Le Claire, A D. "Solute Effects in Diffusion." *Thin Solid Films*, 1975: 1-14.

Lee, S K, and D N Lee. "Calculation of Phase Diagrams using Partial Phase Diagram Data." *CALPHAD* 10, no. 1 (1986): 61-76.

Leohman, R, E Corral, H P Dumm, P Kotula, and R Tandon. *Ultra High Temperature Ceramics for Hypersonic Vehicle Applications.* SAND 2006-2925, Sandia National Laboratories, Albuquerque: Sandia National Laboratory, 2006.

Levine, S R, E J Opila, M C Halbig, J D Kiser, M Singh, and J A Salem. "Evaluation of Ultra-High Temperature Ceramics for Aeropropulsion Use." *Journal of the European Ceramic Society*, 2002: 2757-2767.

Li, Z, and R C Bradt. "Thermal Expansion of Hexagonal (6H) Polytype of Silicon Carbide." *Journal of the American Ceramic Society* 69, no. [12] ((1986)): 863-66.

Lifshitz, L M. "On the Theory of Diffusion-Viscous Flow of Polycrystalline Solids." *Soviet Physics JETP* 17 (1963): 909-920.

Lim, L C. "Cavity Nucleation at High Temperatures Involving Pile-Ups of Grain Boundary Dislocations." *Acta Metallurgica* 35, no. 7 (1987): 1663-1673.

Lofaj, F, and S M Wiederhorn. "Creep Process in Silicon Nitride Ceramics." *Journal of Ceramic Processing Research* 10, no. 3 (2009): 269-277.

Luecke, W E, S M Wiederhorn, B J Hockey, R F Krause Jr., and G G Long. "Cavitation Contributes Substantially to Tensile Creep in Silicon Nitride." *Journal of the American Ceramic Society* 78, no. 8 (1995): 2085-96.

Migliori, A, and J D Maynard. "Implementation of a Modern Resonant Ultrasound Spectroscopy System for the Measurement of the Elastic Moduli of Small Solid Samples." *Review of Scientific Instruments*, 2005: 121301-121306.

Mishra, S K, and L C Pathak. "Effect of Carbon and Titanium Carbide on Sintering Behavior of Zirconium Diboride." *Journal of Alloys and Compounds*, 2008: 547-555.

Mishra, S K, S Das, and L C Pathak. "Defect Structure in Zirconium Diboride Powder Prepared by Self-Propagating High-Temperature Synthesis." *Materials Science and Engineering* A364 (2004): 249-255.

Mishra, S K, S K Das, A K Ray, and P Ramachandrarao. "Effect of Fe and Cr Addition on the Sintering Behavior of ZrB_2 Produced by Self-Propagating High-Temperature Synthesis." *Journal of the American Ceramic Society*, 2002: 2846-2848.

Misra, A, A A Sharif, J J Petrovic, and T E Mitchell. "Rapid Solution Hardening at Elevated Temperatures by Substitutional Re Alloying in $MoSi_2$." *Acta materilia*, 2000: 925-932.

Mitlin, D, C H Raeder, and R W Messler, Jr. "Solid Solution Creep Behavior of Sn-xBi Alloys." *Metallurgical and Materials Transactions A*, 1999: 115-122.

Mizuguchi, T, S Guo, and Y Kagawa. "Transmission Electron Microscopy Characterization of Spark Plasma Sintered ZrB_2 Ceramic." *Ceramics International* 36 (2010): 943-46.

Mizuguchi, T, S-Q Guo, and Y Kagawa. "Transmission Electron Microscopy Characterization of Hot-Pressed ZrB_2 with $MoSi_2$ Additive." *Journal of the American Ceramic Society* 92, no. 5 (2009): 1145-48.

Mohamed, F A, and T G Langdon. "The Transition From Dislocation Climb To Viscous Glide in Creep of Solid Solution Alloys." *Acta Metallurgica*, 1974: 779-788.

Monteverde, F, A Bellosi, and S Guicciardi. "Processing and Properties of Zirconium Diboride-Based composites." *Journal of the European Ceramic Society*, 2002: 270-288.

Monteverde, F, and A Bellosi. "Beneficial Effects of AlN as Sintering Aid on Microstructure and Mechanical Properties of Hot-pressed ZrB_2." *Advanced Engineering Materials*, 2003: 508-512.

Monteverde, F, S Guicciardi, and A Bellosi. "Advances in Microstructure and Mechanical Properties of Zirconium Diboride Based Ceramics." *Materials Science and Engineering* A346 (2003): 310-319.

Monteverde, F., A. Bellosi, and L. Scatteia. "Processing and Properties of Ultra-High Temperature Ceramics for Space Applications." *Materials Science and Engineering A* 485 (2008): 415-421.

Mukherjee, A K. "The Rate Controlling Mechanism in Superplasticity." *Materials Science and Engineering*, 1971: 83-89.

Nabarro, F R N. "Deformation of Crystals by the Motion of Single Ions." *Report of a Conference on the Strength of Solids.* London: Physical Society, 1948. 75-90.

Nabarro, F R N. "Steady-state Diffusional Creep." *Philisophical Magazine*, 1967: 231-237.

Nakano, K, T Imura, and S Takeuchi. "Hardness Anisotropy of Single Crystals of IVa-Diborides." *Japanese Journal of Applied Physics*, 1973: 186-189.

Needleman, A, and J R Rice. "Plastic Creep Flow Effects in the Diffusive Cavitation of Grain Boundaries." *Acta Metallurgica* 28 (1980): 1315-1332.

Neumann, G, and C Tuijn. *Self-Diffusion and Impurity Diffusion in Pure Metals: Handbook of Experimental Data.* San Diego, CA: Pergamon, 2009.

Nikolic, Z S. "Computer Simulation of Grain Growth by Grain Boundary Migration During Liquid Phase Sintering." *Journal of Materials Science*, 1999: 783-794.

Norton, F H. *The Creep of Steel at High Temperatures.* New York: McGraw-Hill, 1929.

Nye, J F. "Some Geometrical Relations in Dislocated Crystals." *Acta Metallurgica* 1 (1953): 153-162.

Okamoto, N L, M Kusakario, K Tanaka, H Inui, and S Otani. "Anisotropic Elastic Constants and Thermal Expansivities in Monocrystal CrB_2, TiB_2, and ZrB_2." *Acta Materialia* 58 (2010): 76-84.

Oliver, W C, and G M Pharr. "Measurement of Hardness and Elastic Modulus by Instrumented Indentation: Advances in Understanding and Refinements to Methodology." *Journal of Materials Research*, 2004: 3-20.

Opeka, M M, I G Talmy, and J A Zaykoski. "Oxidation-Based Materials Select for 2000°C + Hypersonic Aerosurfaces: Theoretical Considerations and Historical Experience." *Journal of Material Science* 29 (2004): 5887-5904.

Opeka, M M, I G Talmy, E J Wuchina, J A Zaykoski, and S J Causey. "Mechanical, Thermal and Oxidation Properties of Refractory Hafnium and Zirconium Compounds." *Journal of the European Ceramic Society* 19 (1999): 2405-2414.

Ota, Ken'ichi, and Giuseppe Pezzotti. "Dislocation Damping in Sapphire, Al_2O_3 Polycrystal and Al_2O_3/SiC Nanocomposite." *Journal of Materials Science Letters* , 1996: 966-969.

Pantleon, W. "Resolving the Geometrically Necessary Dislocation Content by Convental Electron Backscattering Diffraction." *Scripta Materialia* 58 (2008): 994-997.

Park, J-H, Y-H Koh, H-E Kim, and C S Hwang. "Densification and Mechanical Properties of Titanium Diboride with Silicon Nitride as a Sintering Aid." *Journal of the American Ceramic Society*, 1999: 3037-3042.

Park, J-H, Y-H Lee, Y-H Koh, and H-E Kim. "Effect of Hot-Pressing Temperature on Densification and Mechanical Properties of Titanium Diboride with Silicon Nitride as a Sintering Aid." *Journal of the American Ceramic Society*, 2000: 1542-1544.

Petrov, R, L Kestens, A Wailkowska, and Y Houbaert. "Microstructure and Texture of Lightly Deformed TRIP-Assisted Steel Characterized by Means of the EBSD Technique." *Materials Science and Engineering A* 447 (2007): 285-297.

Pharr, G M, and M F Ashby. "On Creep Enhanced by a Liquid Phase." *Acta Metallurgica*, 1983: 129-138.

Porter , D A, and K E Easterling. "Diffusion." In *Phase Transformations in Metals and Alloys Second Edition*, by D A Porter and K E Easterling, 60-106. Boca Raton: CRC Press, 2004.

Porter, J R, W Blumenthal, and A G Evans. "Creep Fracture in Ceramic Polycrystals-I. Creep Cavitation Effects in Polycrystalline Alumina." *Acta Metallurgica* 29 (1981): 1899-1906.

Rachinger, W A. "Relative Grain Translations in the Plastic Flow of Aluminum." *Journal of the Institute of Metals* 81 (1952): 33-41.

Raj, R, and C K Chyung. "Solution-Precipitation Creep in Glass Ceramics." *Acta Metallurgica* 29 (1981): 159-186.

Raj, R, and M F Ashby. "On Grain Boundary Sliding and Diffusional Creep." *Metallurgical Transactions* 2 (1971): 1113-1127.

Rana, A.G. Evans A. "High Temperature Failure Mechanisms in Ceramics." *Acta Metallurgica* 28 (1979): 129-141.

Redlich, O, and A T Kister. "Thermodynamics of Non-Electrolyte Solutions, X-Y-T Relations in a Binary System." *Industrial Engineering Chemistry*, 1948: 341-345.

Reed-Hill, R E, and R Abbaschian. "Dislocations and Plastic Deformation." In *Physical Metallurgy Principles*, 124-167. Boston, MA: PWS Publishing Company , 1994.

Reed-Hill, R E, and R Abbaschian. "Darken's Equations." In *Physical Metallurgy Principles Third Edition*, by R E Reed-Hill and R Abbaschian, 369-373. Boston, MA: PWS Publishing Company, 1994.

Rezaie, A, W G Fahrenholtz, and G E Hilmas. "Effect of Hot Pressing Time and Temperature on the Microstructure and Mechanical Properties of ZrB_2-SiC." *Journal of Material Science*, 2007: 2735-2744.

Rezaie, A, W G Fahrenholtz, and G E Hilmas. "Evolution of Structure during the Oxidation of Zirconium Diboride-Silicon Carbides in Air up to 1500°C." *Journal of the European Ceramic Society* 27 (2007): 2495-2501.

Rice, J R. "Constraints on the Diffusive Cavitation of Isolated Grain Boundary Facets in Creeping Polycrystals." *Acta Metallurgica* 29 (1980): 675-681.

Rickman, J J, R LeSar, and D J Srolovitz. "Solute Effects on Dislocation Glide in Metals." *Acta Materialia*, 2003: 1199-1210.

Riedel, H. "Creep Crack Growth." *ASTM STP 1020*, 1989: 101-126.

Riley, K F, M P Hobson, and S J Bence. "Integral Transformations." In *Mathematical Methods for Physics and Engineering, Third Edition*, by K F Riley, M P Hobson and S J Bence, 433-453. Cambridge, UK: Cabridge University Press, 2006.

Rudy, E. *Ternary Phase Equilibria in Transition Metal-Boron-Carbon-Silicon Systems Part V. Compendium of Phase Diagram Data.* AFML TR 65-2, Wright Patterson Air Force Base: RTD Technical Publications, 1969.

Rudy, E. *Experimental Phase Equilibria of Selected Binary, Ternary and Higher Order Systems.* AFML-TR-69-117, Part V, Wright-Patterson Air Force Base, OH: Air Firce Materials Laboratory, 1970.

Ruggles, T J, and D T Fullwood. "Estimations of Bulk Geometrically Necessary Dislocation Density Using High Resolution EBSD." *Ultramicroscopy* 133 (2013): 8-15.

Santoro, C J. "Effect of Silver on Diffusion in Zinc." *The Physical Review*, 1969: 593-600.

Sarin, P, P E Driemeyer, R P Haggerty, D-K Kim, J L Bell, Z D Apostolov, W M Kriven, "In Situ Studies of Oxidation of ZrB_2 and ZrB_2-SiC Composites at High Temperatures." *Journal of the European Ceramic Society*, 2010: 2375-2386.

Schwartz, A J, and M Kumar. *Electron Backscatter Diffraction in Materials Science.* 2nd. New York, NY: Springer, 2009.

Sciti, D, L Silvestroni, V Medri, and S Guicciardi. "Pressureless Sintered In Situ Toughened ZrB_2-SiC Platelets Ceramics." *Journal of the European Ceramic Society* 31 (2011): 2145-53.

Shackelford, J F, W Alexander, and J S Park. *CRC Practical Handbook of Materials Selection.* Boca Raton, FL: CRC Press Inc., 1995.

Sharif, A A, A Misra, J J Petrovic, and T E Mitchell. "Solid Solution Hardening and Softening in $MoSi_2$ Alloys." *Scripta Materialia*, 2001: 879-884.

Song, H, and R L Coble. "Origin and Growth Kinetics of Platelike Abnormal Grains in Liquid-Phase-Sintered Alumina." *Journal of the American Ceramic Society*, 1990: 2077-2085.

Spivak, I I, R A Andrievskii, V V Klimenko, and V D Lazarenko. "Creep in the Binary Systems TiB_2-TiC and ZrB_2-ZrN." *Soviet Powder Metallurg Metal Ceram.* 13, no. 8 (1974): 617-20.

Squire, T H, and J Marschall. "Material Property Requirements for Analysis and Design of UHTC Components in Hypersonic Applications." *Journal of the European Ceramic Society* (doi: 10.1016/j.jeurceramsoc.2010.01.026.), 2010: 2239-2251.

Steinbrech, R W, A Reichl, and W Shaarwachter. "R-Curve Behavior of Long Cracks in Alumina." *Journal of the American Ceramic Society* 73, no. [7] (1990): 2009-2015.

Stojakovic, D. "Electron Backscatter Diffraction in Materials Characterization." *Processing and Application of Ceramics*, 2012: 1-13.

Swain, M V, and B R Lawn. "A Study of Dilsocation Arrays at Spherical Indentations in LiF as a Function of Indention Stress and Strain." *physica status solidi*, 1969: 909-923.

Tabor, D. *Hardness of Metals.* Oxford University Press, 2000.

Talmy, I G, J A Zaykoski, and C A Martin. "Flexural Creep Deformation of ZrB_2/SiC Ceramics in Oxidizing Atmosphere." *Journal of the American Ceramic Society* 97 (2008): 1441-1447.

Teatum, E, K Gschneidner, Jr., and J Waber. *Compilation of Calculated Data Useful in Predicting Metallurgical Behavior of the Elements in Binary Alloy Systems.* LA-2345, Los Alamos, NM: Los Alamos Scientific Laboratory, 1960.

The MathWorks, Inc. *Matlab User Guide.* V7.9.0. Vol. R2009b. The MathWorks, Inc., 2009.

Thomas, A F. "Temperature-Dependent Fracture Behavior of Zirconium-Diboride-Silicon Carbide Ultra High Temperature Ceramic." Master Thesis, Houston, 2011.

Troost, K Z, P V D Sluis, and D J Gravesteijn. "Microscale Elastic-Strain Determination by Backscatter Kikuchi Diffraction in the Scanning Electron Microscope." *Applied Physics Letters* 62 (1993): 1110-1112.

Tvergaard, V. "On the Creep Constrained Diffusive Cavitation of Grain Boundary Facets." *Journal of Mechanical Physics and Solids* , 1984: 373-393.

Underwood, E E. *Quantitative Metallography.* Vol. 9, in *ASM Handbook Metallography and Microstrcutures*, edited by J R Davis and J D Destefani, 123-134. Materials Park, Ohio: ASM International, 1995.

Vil'k, Y N, S S Ordan'yan, and A I Avgustinik. "The Possible Formation of Isothermal Sections of Zr-W-C at 2200°C and 2600°C." *Inorganic Materials*, 1972: 1245-1248.

Wakai, F. "Step Model of Solution-Precipitation Creep." *Acta metallurgica*, 1994: 1163-1172.

Watanabe, T, and S Kouno. "Mechanical Properties of TiB_2-CoB-Metal Boride Alloys." *The American Ceramic Society Bulletin* 61, no. 7 (1982): 970-973.

Watts, J, W G Hilmas, W G Fahrenholtz, D Brown, and B Clausen. "Measurement of Thermal Residual Stresses in ZrB_2-SiC Composites." *Journal of the European Ceramic Society* 31 (2011): 1811-1820.

Weertman, J. "Steady State Creep of Crystals." *Journal of Applied Physics*, 1957: 1185-1189.

Weertman, J. "Steady State Creep Through Dislocation Climb." *Journal of Applied Physics*, 1957: 362-364.

Wei, G C, and P F Becher. "Improvements in Mechanical Properties in SiC by the Addition of TiC Particles." *Journal of the American Ceramic Society*, 1984: 571-574.

Wiederhorn, S M. "Brittle Fracture and Toughening Mechanisms in Ceramics." *Annual Review Material Science*, 1984: 374-403.

Wiederhorn, S.M., B.J. Hockey, and J.D. French. "Mechanisms of Deformation of Silicon Nitride and Silicon Carbide at High Temperature." *Journal of the European Ceramic Society,* 78 (1999): 2273-2284.

Wilkinson, A J, G Meaden, and D J Dingley. "High-Resolution Elastic Strain Measurement Form Electron Backscatter Diffraction Patterns: New Levels of Sensitivity." *Ultramicroscopy* 106 (2006): 307-313.

Wilkinson, D S. "Creep Mechanisms in Multiphase Ceramic Materials." *Journal of the American Ceramic Society* 81 (1998): 275-299.

Wolten, G M. "Diffusionless Phase Transformations in Zirconia and Hafnia." *Journal of the American Ceramic Society*, 1963: 418-422.

Xuan, Yi, C-H Chen, and S Otani. "High Temeprature Microhardness of ZrB_2 Single Crystals." *Journal of Physics D: Applied Physics*, 2002: L98-L100.

Yoon, K J, S M Wiederhorn, and W E Lueke. "Comparison of Tensile and Compressive Creep Behavior in Silicon Nitride." *Journal of the American Ceramic Society* 83, no. 8 (2000): 2017-22.

Yoon, K J, S M Wiederhorn, and W E Lueke. "Comparison of Tensile and Compressive Creep Behavior in Silicon Nitride." *Journal of the American Ceramic Society* 83, no. 8 (2000): 2017-22.

Yu, C-H, C-W Huang, C-S Chen, Y Gao, and C-H Hsueh. "A Micromechanics Study of Competing Mechanisms for Creep Fracture of Zirconium Diboride Polycrystals." *Journal of the European Ceramic Society*, 2013: 1625-1637.

Yu, C-H, C-W Huang, C-S Chen, Y Gao, and C-H Hsueh. "Effects of Grain Boundary Heterogeneities on Creep Fracture Studied Rate-Dependent Cohesive Model." *Engineering Fracture Mechanics*, 2012: 48-64.

Zhang, G-J, Z-Y Deng, N Kondo, J-F Yang, and T Ohji. "Reactive Hot Pressing of ZrB_2-SiC Composites." *Journal of the American Ceramic Society*, 2000: 2330-2332.

Zhang, S C, G E Hilmas, and W G Fahrenholtz. "Oxidation of Zirconium Diboride with Tungsten Carbide Addition." *Journal of the American Ceramic Society* 94, no. 4 (2011): 1198-1205.

Zhang, S C, G E Hilmas, and W G Fahrenholtz. "Pressureless Densification of Zirconium Diboride with Boron Carbide Additions." *Journal of the American Ceramic Society*, 2006: 1544-1550.

Zhang, X-H, P Hu, and J-C Han. "Structure Evolution of ZrB_2-SiC During Oxidation in Air." *Journal of Materials Research* 23 (2008): 1961-1972.

Zhu, S, W G Fahrenholtz, and G E Hilmas. "Influence of Silicon Carbide Particle Size on the Mircostructure and Mechanical Properties of Zirconium Diboride-Silicon Carbide Ceramics." *Journal of the European Ceramic Society*, 2007: 2077-2083.

Zhu, S, W G Fahrenholtz, G E Hilmas, and S C Zhang. "Pressureless Sintering of Carbon-Coated Zirconium Diboride Powders." *Materials Science and Egnineering A*, 2007: 167-171.

Zou, J, Zhang, G-J, Hu, C-F, Nishimura, T., Sakka, Y., Vleugels, J., Van der Biest, O., "Strong ZrB_2-SiC-WC Ceramics at 1600°C." *Journal of the American Ceramic Society* 95, no. 3 (2012): 874-878.

Appendix A

Thermochemical Formulations and Data

The thermochemical behavior of quasi-binary ZrB_2-WC alloys and the equilibrium phase stability is not well known due to the complexity of the system (e.g. 4-component solution). At the present, no published phase diagram was found for the quaternary system. An attempt was made for constructing the solvus curve between ZrB_2-WC assuming sub-regular solution behavior despite the intermetallic nature of the bounding binaries. Extension to the Zr-B and W-C binary systems reveals these phase equilibria were described by interaction parameters based on sub-regular behavior ((L. Kaufman 1986), (Lee and Lee 1986)). The Gibb's free energy of a phase follows the form

$$G^{\theta} = X_1 \Delta G_1^{0-\theta} + (1 - X_1)\Delta G_2^{0-\theta} + \Delta G_{id}^{\theta} + \Delta G_{xs}^{\theta}, \quad \text{(A-1)}$$

where G^{θ} is the total Gibb's free energy of phase θ for the mole fractional quantities of components 1 and 2 (Gaskell 2003). The unmixed free energy terms, $\Delta G_i^{0-\theta}$, represent the lattice stability of component, i, for phase θ with respect to the standard state of the pure component. ΔG_{id}^{θ} denotes the ideal mixing free energy change due to atomic configurational changes only and ΔG_{xs}^{θ} is the excess mixing free energy dependent upon composition and temperature from the binary chemical interactions (Gaskell 2003). A four component system ideal mixing and excess free energy terms follow

$$\Delta G_{id}^{\theta} = RT[X_1 \ln X_1 + X_2 \ln X_2 + X_3 \ln X_3 + X_4 \ln X_4] \quad \text{(A-2)}$$

and

$$\Delta G_{xs}^{\theta} = X_k X_l (G^{XS})_{ij} + Ternary\ Interactions, \quad \text{(A-3)}$$

where X_k, and X_l are the mole fraction quantities for a given binary pair in the quaternary alloy system (Redlich and Kister 1948). For example, the present research considers six binary interactions including: Zr-B, Zr-C, Zr-W, W-B, WC and B-C each having. $(G^{XS})_{ij}$ is the excess binary mixing free energy having the form of (Redlich and Kister 1948)

$$(G^{XS})_{ij} = \left(\frac{X_k}{X_{k+}X_l}\right)\left(\frac{X_l}{X_{k+}X_l}\right)\left[\Omega_{ij}^{i}\left(\frac{X_k}{X_{k+}X_l}\right) + \Omega_{ji}^{j}\left(\frac{X_k}{X_{k+}X_l}\right)\right], \qquad \text{(A-4)}$$

where Ω_{ij}^{i} and Ω_{ji}^{j} are the chemical interaction parameters of the ith and jth component for the i-j interaction, respectively. Ternary interaction terms were ignored for the present case as a result of inadequate knowledge of the higher order interaction parameters. Kaufman (1986) showed the significance of ternary Zr-B-C interaction parameter illustrating a ~ 200°C reduction in the calculated eutectic temperature from that calculated ignoring the higher order term. The importance of these higher order terms is recognized for accurately predicting phase stability. The present research confirms the above approach provides WC solubility insights important for the preliminary alloying study.

Applying Equations (A-1) – (A-4) for the HCP phase of both the ZrB_2 and WC binary components yields a series of molar free energy curves as a function of the WC mol fractions for the tabulated lattice stability and excess free energy terms, Figure A- 1 and Table A- 1. The standard state for lattice stability was taken as the liquid state (Kaufman (1986), (Kaufman and Nesor 1978) and (Kaufman, Uhrenius, et al., 1984)); $\Delta G_{ZrB_2}^{L-\theta_{WC}}$ and $\Delta G_{WC}^{L-\theta_{ZrB_2}}$ were assumed zero for the present case. The WC-ZrB_2 solubility was assessed by fitting a common tangent to each free energy curve using a least squares approach under the assumption of 0% solubility of ZrB_2 in WC. Final construction of the ZrB_2-rich solvus line illustrates the limited WC solubility at typical sintering temperatures below 2100°C, Figure A- 2. The experimentally measured solid solutions confirmed by lattice parameter measurements are overlaid for reference. The present

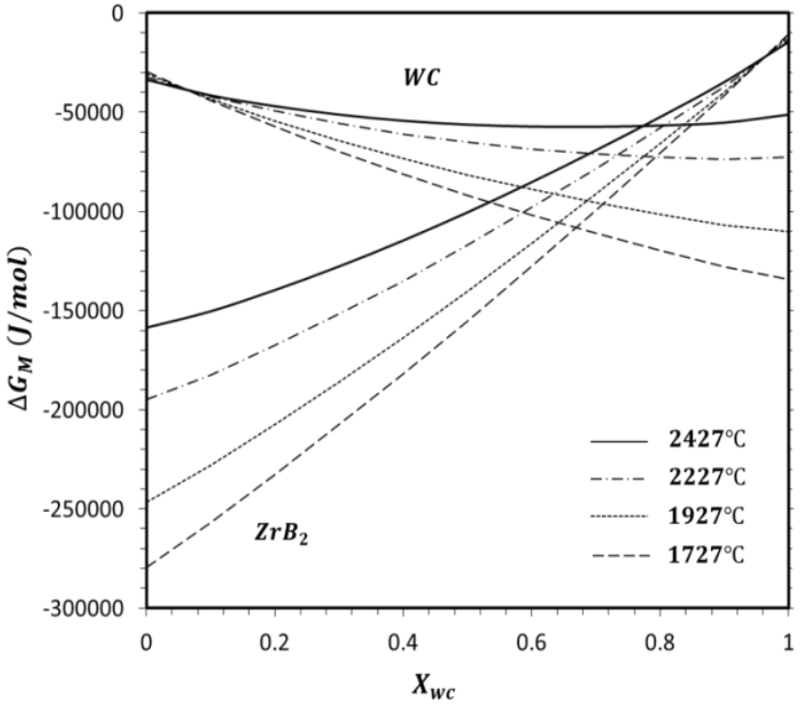

Figure A- 1: Calculated molar free energy-composition curves for the ZrB_2 and WC phases.

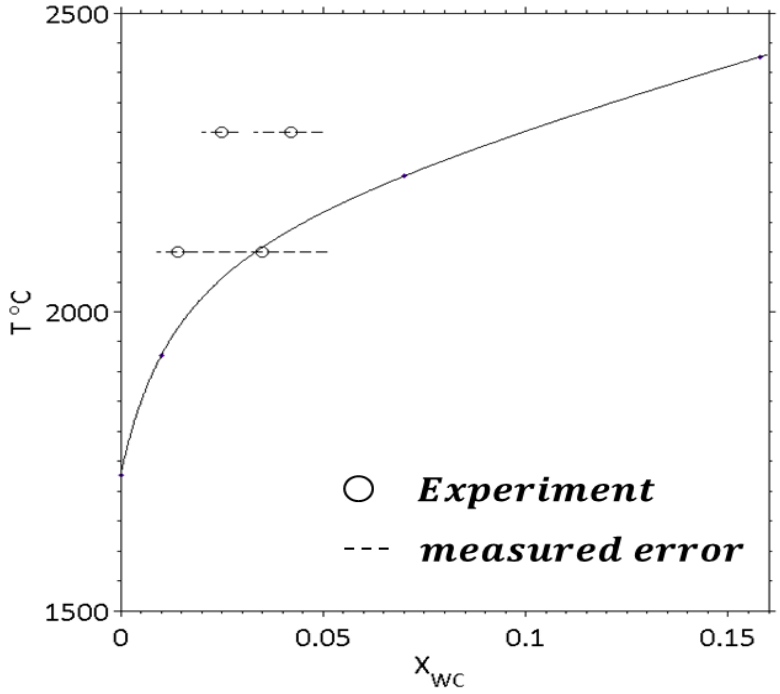

Figure A-2: Calculated ZrB_2-WC solvus line with temperature. Experimental WC solute concentrations (circles) and the composition variation (hashed line) are shown for reference.

calculated solubility limit correlates with the observed solid solutions defining a minimum solubility of WC in ZrB_2. Reaction phase equilibria was assessed assuming standard state compounds (e.g., WC, WB , ZrB_2 etc.) were reacting with non-standard state Boron and Carbon in solution with ZrB_2. Reaction free energies were calculated using the following relationships, for the hypothetical reaction

$$aA + bB = cC + dD, T, P = 1atm \tag{A-5}$$

and

$$\Delta G_{rxn} = \sum \Delta G_{products} - \sum \Delta G_{reactants}. \tag{A-6}$$

Reaction components following standard state behavior consider only the free energy formation (e.g. $\Delta G = \Delta G_f$). Non-standard state components follow the relationship (Gaskell 2003)

$$\Delta G_i = RT \ln a_i \tag{A-7}$$

and

$$a_i = \gamma_i X_i, \tag{A-8}$$

where a_i is the activity defined by the activity coefficient, γ_i, and the mole fraction of component i. For simplicity, only the Zr-W-B and Zr-B-C ternaries were used for calculating the activity coefficients of the each component following Margules model (Jana 2008)

$$\ln \gamma_1 = \Omega_{12} X_2^2 + \Omega_{13} X_3^2 + (\Omega_{12} + \Omega_{13} - \Omega_{23}) X_2 X_3, \tag{A-9}$$

$$\ln \gamma_2 = \Omega_{12} X_1^2 + \Omega_{23} X_3^2 + (\Omega_{12} + \Omega_{23} - \Omega_{13}) X_1 X_3, \tag{A-10}$$

and

$$\ln \gamma_3 = \Omega_{13} X_1^2 + \Omega_{23} X_2^2 + (\Omega_{13} + \Omega_{23} - \Omega_{12}) X_1 X_2. \tag{A-11}$$

The above assumption considers dilute solid solutions of WC in ZrB_2 neglecting the W-C bonds in solution as a result of the low configuration probability of forming these bonds. Applying this

simplistic model, and ignoring ternary interaction terms, provides insights to the non-linear behavior of each component in the solution. Binary Zr-B activities were also calculated from (Gaskell 2003)

$$\ln \gamma_B = \frac{\Omega_{Zr-B}}{RT} X_{Zr}^2. \qquad \text{(A-12)}$$

The activities of all three components with respect to the respective binary or ternary system are shown in Figure A- 3.

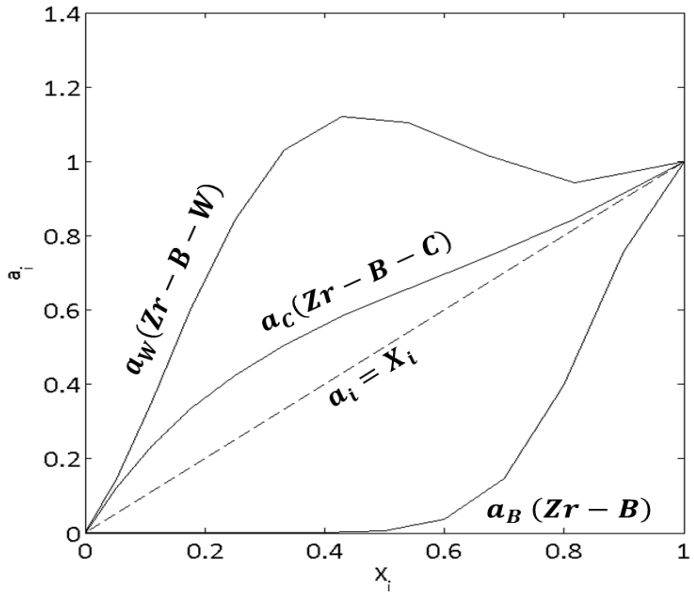

Figure A-3: Activity coefficients for non-standard state W, C and B in solution with either a ternary or binary Zr based solution.

Over the small composition ranges boron in solution exhibits exothermic behavior suggesting a strong tendency to form a solution contrasting with the carbon and tungsten in solution. However, despite the positive deviation from Raoult's law, both the carbon and tungsten activities promote solid solution formation over the dilute concentrations of interest. Activity coefficients used for the current study are given in Table A- 2.

Table A- 1: Thermochemical data used for phase diagram and reaction equilibria development

$^{1}\Delta^{0}G$	$KJ/_{mol}$	T, K
$G^{L} - G_{ZrB_2}^{HCP}$	$\Delta G = 0.1741T - 595.16$	1500<T<3000
$G^{L} - G_{WC}^{HCP}$	$\Delta G = 0.1222T - 256.99$	1500<T<3000
ΔG_{i-j}^{xs}	$J/_{mol}$	T, K
[2]Zr-B	$-X_{Zr}X_B\left((X_{Zr}430115 + X_B314218) + (X_{Zr}41.84 - X_B41.84)T\right)$	1100<T<2700*
[3]W-C	$-X_WX_C(16736)$	600<T3700
[4]W-B	$-X_WX_B\left((X_W123520 + X_B33890) + (X_W50.2 - X_B33.5)T\right)$	300<T<3700
[2]Zr-C	$-X_{Zr}X_B(253509 + 20.92T)$	1100<T<2700*
[2]B-C	0	300<T<4200
[5]Zr-W	$X_{Zr}X_{WC}\left((39140 - X_{Zr}48556) + (7.43 + X_{Zr}19.96)T\right)$	300<T<2700

*Extrapolated to 2700K

1 (Barin, et al., 1992)

2 (L. Kaufman 1986)

3 (Kaufman and Nesor 1978)

4 (Kaufman, Uhrenius, et al., 1984)

5 (Lee and Lee 1986)

Table A- 2: Activity coefficients for select ternary and binary Zr based systems for T= 2500 and 2700K.

T=2700K	Zr-B-C	Zr-W-B	Zr-B	
X_C or X_W	γ_C	γ_W	X_B	γ_B
0	2.560	2.298	0	2.786E-08
0.053	2.325	2.780	0.1	7.593E-07
0.111	2.102	3.175	0.2	1.461E-05
0.176	1.892	3.395	0.3	0.0002
0.25	1.697	3.374	0.4	0.0019
0.333	1.519	3.094	0.5	0.0130
0.429	1.359	2.615	0.6	0.062
0.538	1.222	2.050	0.7	0.209
0.667	1.110	1.529	0.8	0.450
0.818	1.032	1.153	0.9	0.840
1	1	1	1	1
T=2500K	**Zr-B-C**	**Zr-W-B**	**Zr-B**	
0	2.280	3.431	0	7.921E-09
0.053	2.066	3.769	0.1	2.742E-07
0.111	1.864	3.885	0.2	6.535E-06
0.176	1.676	3.731	0.3	0.0001
0.25	1.504	3.320	0.4	0.0012
0.333	1.350	2.734	0.5	0.0094
0.429	1.216	2.100	0.6	0.051
0.538	1.107	1.544	0.7	0.187
0.667	1.031	1.155	0.8	0.474
0.818	1	1	0.9	0.830
1	1	1	1	1

Appendix B

Electron Backscatter Diffraction (EBSD)

Polycrystalline materials are plastically inhomogeneous, causing incompatible deformation between grains oriented with different critical resolved shear stresses or the presence of a second phase (Ashby 1970)) GND's are required for microstructure compatibility in addition to the accumulating SSD's. Both SSD and GND dislocations can be individually inspected using transmission electron microscopy (de Graeff 2003). However, such studies typically cover a tiny specimen area, and sample preparation can remove or modify many of the defects being studied. At a higher length scale-ray techniques and electron microscopy are traditionally used for quantifying the GND densities of a plastically deformed polycrystalline. These methods rely upon a continuum field of dislocations. At a given length scale, the net effect of GNDs within a virtual Burgers circuit distorts the crystal lattice. The rotational component of this distortion is then measured, and the GND content inferred; SSD's provide no net contribution to the distortion. Electron Backscatter Diffraction (EBSD) and post processing Orientation Imaging Microscopy (OIM) routines have been developed for quantifying the total GND density ((Adams 1997), (Gardner, Adams and Basinger, et al., 2010), (Wilkinson, Meaden and Dingley 2006) and (Pantleon 2008)).

An EBSD system consists of an SEM electron beam accelerating electrons, at a particular sample point, and diffracting them from sets of crystallographic planes, Figure B- 1. These diffraction patterns are captured from the intersection of wide diffraction cones with the phosphor screen, attached to the CCD camera, forming a Kikuchi pattern having bands corresponding to unique crystallographic plane orientations, Figure B- 1. Conventional EBSD utilizes the Hough Transform for accurately detecting Kikuchi bands by locating the Hough

transformed peak of maximum intensities (Stojakovic 2012). Further computations are required for measurement of the band intersections, widths, and angle orientations which are computed based on comparisons with tabulated theoretical diffraction intersections and orientations. Finally, a unique set of Euler angles are calculated specifying the lattice orientations, within the diffracted volume, with respect to the sample reference coordinates (Stojakovic 2012). The maximum spatial and angular resolution is controlled by the SEM beam conditions. For example, for a 15-30 KV accelerating voltage and 15-20 nA probe current the maximum spatial and angular resolutions of 15 nm and 0.5-1.0°, respectively, can be obtained (Humphreys 2004). For the present case, the conventional method appears suitable for measuring microtexturing and general grain statistics. However, the maximum angular resolution appears insufficient for accurately calculating the elastic distortion tensor and hence quantifying the GND density.

High resolution EBSD techniques have led to improvements in angular resolution by implementing cross-correlation procedures, in place of the Hough transformation technique, by

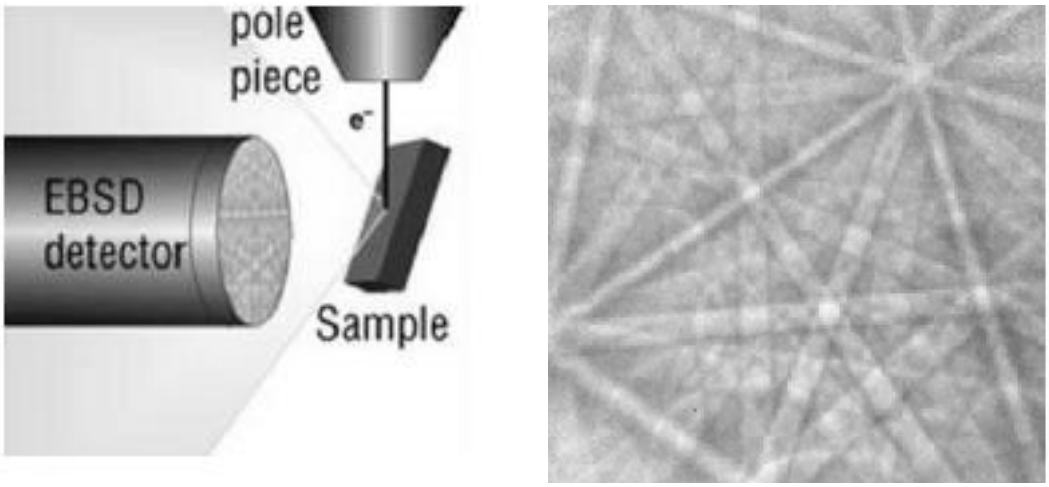

Figure B-1: EBSD setup in an SEM chamber illustrating the sample, beam and diffraction camera positions (left) and a representative Kikuchi diffraction pattern produced from an accelerating voltage (right). Images taken from EDAX (2011).

comparing measured patterns with the theoretical, strain-free patterns having equivalent orientations. J. Kasher, et al., (2009) proposed sampling regions of interest (ROIs) for determining the pattern center relative to the strain free state resulting in an average angular resolution of 0.037°,Figure B- 2. Reducing the step size to 20 nm, angular resolution experiments showed lattice curvature resolution through 0.003° for grain boundary misorientations (Gardner, Adams and Basinger, et al., 2010). Coupling the enhanced angular resolution and capturing the change in pattern displacement provides the necessary information for calculating the derivatives of the elastic distortion tensor. The present research applies the HREBSD method using methods and code developed at Brigham Young University for quantitative estimates of the GND density.

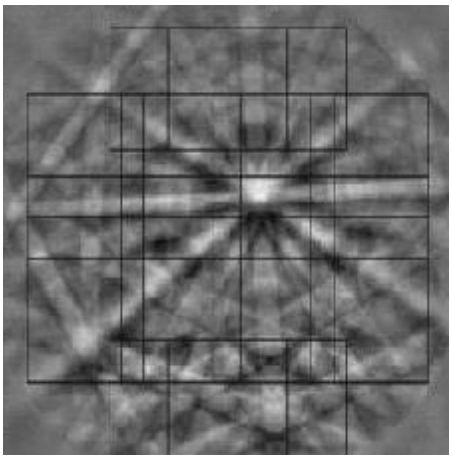

Figure B-2: ROI selections (rectangles) illustrating the approach for determining the Kikuchi pattern center.

Estimates of GND density from EBSD data result from the work of Nye (1953), and Kroner (1958) who connected GND densities to the lattice elastic distortion tensor, β, following Nye's tensor ((Nye 1953), (Kroner 1958))

$$\alpha = \nabla \times \beta, \tag{B-1}$$

where the dislocation tensor α, defined by the curl of the elastic distortion tensor $\beta = \frac{\partial u_j}{\partial x_i}$,

includes the rigid rotation and strain tensors ((Gardner, Adams and Basinger, et al., 2010) and (Pantleon 2008)). The dislocation density, $\rho^{(m)}$, on a given slip system contributes to the total Nye tensor by

$$\alpha_{ij} = \sum_m \rho^{(m)} b_i^{(m)} v_i^{(m)}, \tag{B-2}$$

where b is the Burgers vector, and v is the corresponding unit vector in the dislocation line direction. By definition, Nye's tensor requires derivatives of the elastic distortion tensor which are obtained by comparing the relative distortion between two neighboring scan point EBSD patterns (Gardner, Adams and Fullwood 2010). Therefore, Equation (B-2) has the form

$$\alpha_{ij} = \begin{bmatrix} - & \alpha_{12} & \alpha_{13} \\ \alpha_{21} & - & \alpha_{23} \\ - & - & \alpha_{33} \end{bmatrix}, \tag{B-3}$$

Illustrating the determinable tensor components reside parallel to the sample surface as a result of the two dimensional nature of the experiment. The incomplete Nye tensor suggests an underestimation of the GND tensor requiring a summation and appropriate scaling of known components to compensate for the missing components (Ruggles and Fullwood (2013)). Therefore, using high-resolution EBSD techniques the elastic distortion tensor may be derived from the comparison of two EBSD patterns of the two structures using convolution techniques ((Troost, Sluis and Gravesteijn 1993), (Wilkinson, Meaden and Dingley 2006), (Landon, Adams and Kacher 2008) and (Kacher, et al., 2009)).

Appendix C

Random Orientation Texture Analysis

Random grain orientation theory was used for assessing lattice deformation strains as a result of creep. Pole orientation data along any average crystallographic direction, acquired by EBSD patterns, was used for calculating the creep deformation strains using texture deformation theory, Figure C- 1.

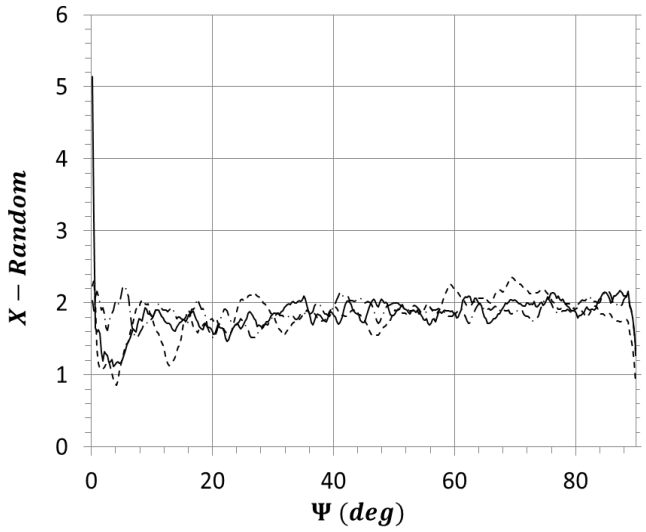

Figure C-1: Pole plot orientation data from EBSD pattern analysis along three arbitrary crystallographic directions.

Assuming uniform grain deformation, under a uniaxial displacement, from an initially random grain orientation distribution, the probability, *P*, of a plane pole lying between an orientation angle, Ψ, and $\Psi + \Delta\Psi$ within a single hemisphere relative to a fixed arbitrary axis is given by (Hosford 1993)

$$\frac{dP}{d\psi} = \sin\psi. \qquad \text{(C-1)}$$

With increasing deformation, $\frac{dP}{d\psi}$ varies with increasing tension or compressive strain, ε, with

respect to the orientation distribution by (Hosford 1993)

$$\frac{dP}{d\psi} = \left[\frac{Ac^2 \sin\psi}{(\cos^2\psi + c^2 \sin^2\psi)^{3/2}}\right] \quad \text{(C-2)}$$

and

$$c = exp\left[\frac{3}{2}\varepsilon\right]. \quad \text{(C-3)}$$

In the limit that ε approaches zero, Equation (C-2) reduces to Equation (C-1) and the proportionality constant A = 2 is only necessary if experimental pole plot data includes both southern and northern hemispheres. However, realistic microstructures are not ideally random in the un-crept condition as a result of hot pressing. Therefore, A is scaled by the factor c^2, which is dependent of the initial permanent strain accumulated during processing. Considering the Z20SB-SiC and Z20SB-ZrB_2 hot-pressed texture data, A is reduced to 1.9007 ± 0.0046 and 1.9296 ± 0.0052, respectively, as the EBSD pole plot information includes both southern and northern hemisphere pole projections. Under positive extension, increasing ε results in a general orientation shift to small ψ as grains begin to rotate towards and align parallel with the stress axis, Figure C- 2, contrasting with compression strains where an opposite shift to larger misorientation angles would be expected ((Hosford 1993) and (Reed-Hill and Abbaschian 1994)). A characteristic strain can be calculated based on the un-crept and crept pole plot orientation data $\left(\frac{dP/d\psi}{\sin\psi}\right)$ representing a measure of the average lattice deformation strain relative to the fixed reference axis with orientation angles $0 \leq \psi \leq 90°$. For example, EBSD pole plot data are represented with the deformation theory calculations for a lattice deformation of ε = -1.40%. A representation of experimental and model calculations are shown for a characteristic deformation strain of ε = -1.40%, Figure C- 3.

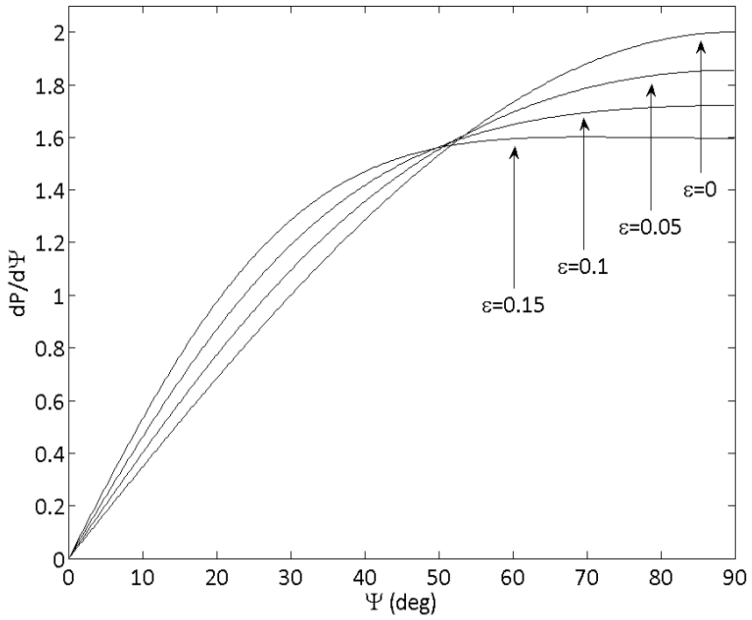

Figure C-2: Theoretical orientation distribution profiles for tensile strains illustrating lattice rotations towards the stress axis indicated by small misalignment angle peak development recreated from ref ((Hosford 1993)).

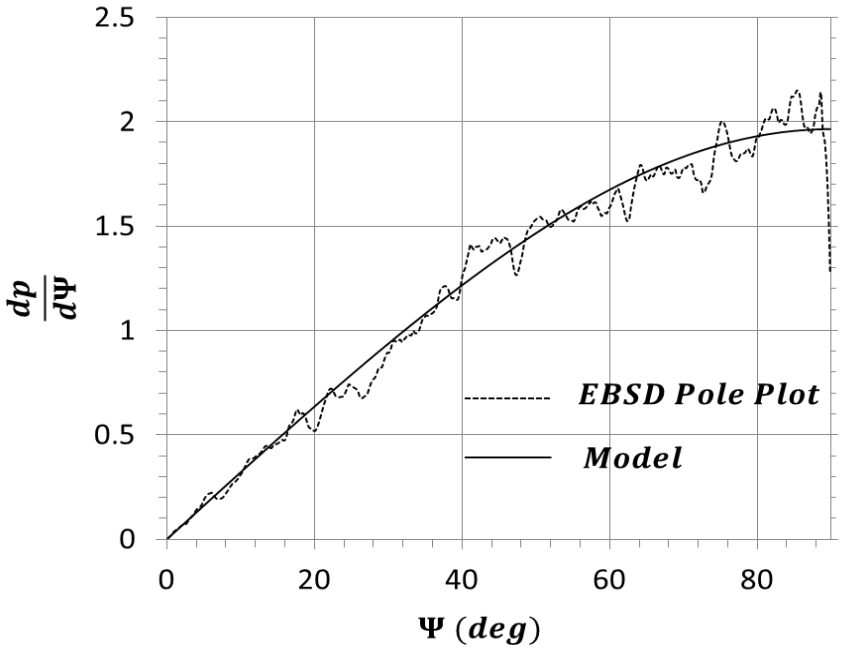

Figure C-3: Experimental orientation distribution plot compared with the model fit for an average lattice deformation strain of -1.40%. The stress axis is oriented 69° and 25° from the (0001) pole and [11$\bar{2}$0] crystal direction.

Appendix D

Pseudo Fourier Transform Method

An analysis technique was used for non-objectively comparing lattice misorientation and geometrically necessary dislocation density profiles with the microstructure. The primary objective was to measure the ZrB_2 sub-grain size development (if applicable) in the post crept specimen using the EBSD Kernel Average Misorientation (KAM) and GND density plots, Figure D-1. A typical output from a distance- misorientation (GND density) profile was inherently harmonic along the profile length, therefore, a discrete Fourier transform was used following (Riley, Hobson and Bence 2006)

$$F(x) = \sum_{r=-\infty}^{\infty} C_r e^{-i\omega x}, \qquad \text{(D-1)}$$

where C_r are the Fourier coefficients for an integer, r, over a profile distance, x, Figure D- 2.

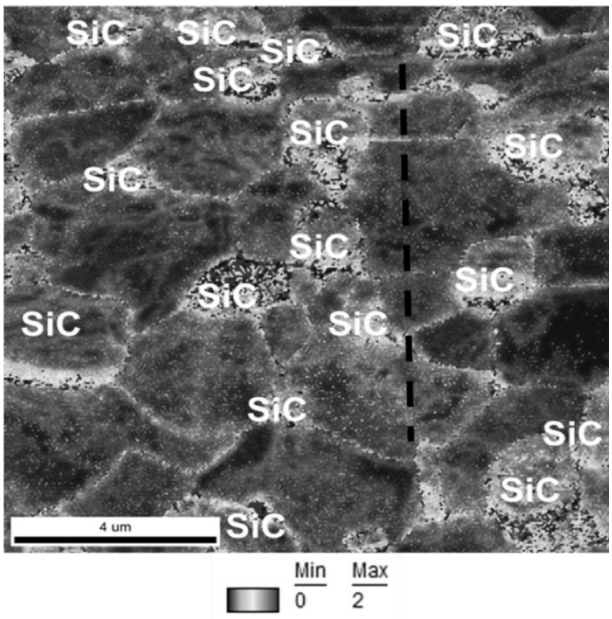

Figure D-1: Example KAM image with a profile line overlaid.

The pseudo frequency ω is related to the spectrum period by (Riley, Hobson and Bence 2006)

$$\omega = \frac{2\pi r}{d}, \tag{D-2}$$

where d is the spectrum period corresponding to the distance between maximum regions of misorientation (GND density). For example, considering sub-grain formation, the Fourier length, d, would scale with a fraction of the ZrB_2 grain size. Implementing Equation (D-1) using the Fast Fourier Transform (FFT) approach converges on a solution using N $\log_2$(N) floating point operations contrasting with the $2N^2$ operations; N is the sample number of length 2^n (Riley, Hobson and Bence 2006). The frequency having the maximum amplitude was correlated with the observed microstructure grain size, Figure D- 3. The non-objectivity of this analysis provides valuable insights to the development of low-angle grain boundaries and regions of low and high dislocation densities during creep deformation.

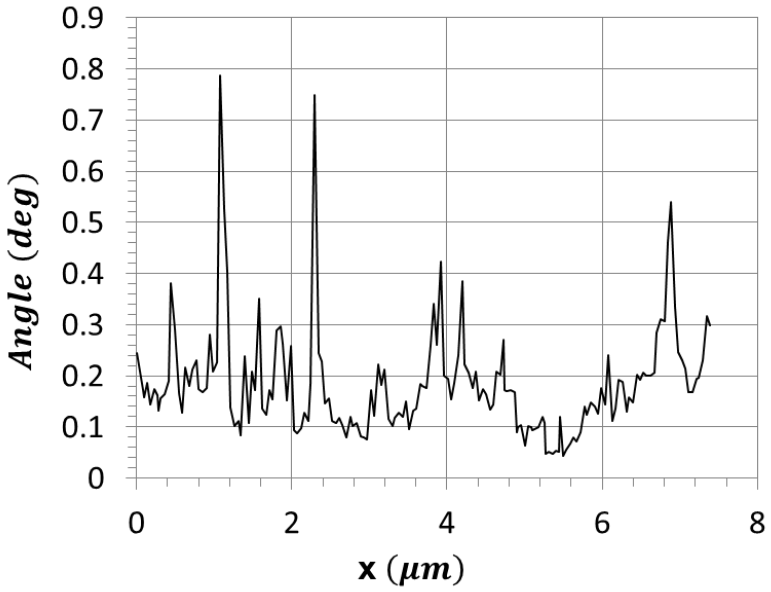

Figure D-2: Example lattice misorientation-distance profile across the ZrB_2 grain structure illustrating the harmonic signal nature.

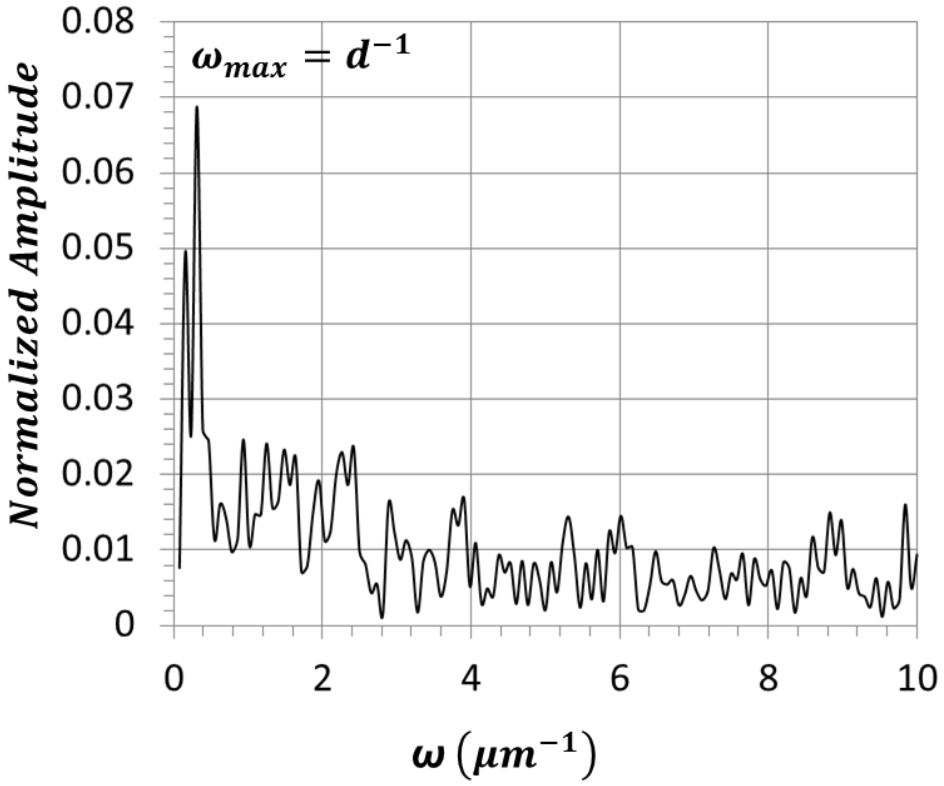

Figure D-3: FFT plot illustrating the maximum frequency corresponding to the profile Fourier length, d.

Appendix E

Solute-Dislocation Interaction Model

Considering a substitutional solid solution with solute atoms relieving local hydrostatic stress field, from a dislocation located at the origin, follows the potential (Cottrell and Jaswon 1949)

$$U = A\frac{\sin\theta}{r} \tag{E-1}$$

and

$$A = \frac{4}{3}G\varepsilon r_a^3 b\left(\frac{1+\nu}{1-\nu}\right), \tag{E-2}$$

where G is the shear modulus, ν the Poisson's ratio, b, Burger's vector, r_a and $r_a(1+\varepsilon)$ the atomic radii of the solvent and solute, respectively and θ and r are the solute coordinates relative to the dislolcation. *A* is the interaction potential accounting for the concentration and solute-solvent size difference. The equilibrium concentration of solute in the vicinity of the point θ, r is defined

$$c(r,\theta) = c_0\exp\left(-\frac{U(r,\theta)}{KT}\right), \tag{E-3}$$

where c_0 is the average atomic concentration. Therefore, Equations (E-1) - (E-3) adequately describe viscous drag dislocation creep based on salient compositional and atomic size interactions. The macroscopic creep strain follows the general form (Mohamed and Langdon 1974)

$$\dot{\varepsilon} \propto \frac{1}{A'}\left(\frac{\sigma}{G}\right)^3 \tag{E-4}$$

and

$$A' \simeq \frac{e^2 c b^5 G^2}{KT\widetilde{D}} \ , \tag{E-5}$$

where *e* is the solute-solvent size difference, *c* is the solute atomic concentration and $\widetilde{D}$ is Darken's interdiffusivity coefficient for a binary alloys (Reed-Hill and Abbaschian 1994). For the present case, the solute composition dependent terms (e.g. c, b, G, $\widetilde{D}$) provide the necessary insight for creep-rate- solute constitution effects assuming equal grain sizes and applied stresses. For example, taking a reference composition of c_0 and the solid solution composition c_{WC} one can define the strain rate change by the following form

$$\frac{\dot{\varepsilon}_{wc}}{\dot{\varepsilon}_0} = \left(\frac{D_{wc}}{D_0}\right)\left(\frac{c_0}{c_{wc}}\right)\left(\frac{b_0}{b_{wc}}\right)^5\left(\frac{G_0}{G_{wc}}\right)^5. \tag{E-6}$$

For the present case solute composition and diffusivity terms appear dominant despite the fifth power dependence of the remaining two. Experimentally determined lattice parameter values suggests $\left(\frac{b_0}{b_{wc}}\right)^5 \approx 1$ for the maximum average W-composition of 4.2 mol%. Furthermore the $\left(\frac{G_0}{G_{wc}}\right)^5 \approx 1$ based on the assumption the low solid solution concentrations (<4 mol%) have a negligible change of the shear modulus. Atomistic calculations for 4 mol% W, in ZrB_2, have a Bulk modulus reduction of 1.6% corresponding to a maximum $\left(\frac{G_0}{G_{wc}}\right)^5 \approx 1.1$ (Gouissem 2013). This finding confirms the original assumption of unity for the present compositions. Therefore, Equation (E-6) reduces to the form

$$\frac{\dot{\varepsilon}_{wc}}{\dot{\varepsilon}_0} = \left(\frac{D_{wc}}{D_0}\right)\left(\frac{c_0}{c_{wc}}\right), \tag{E-7}$$

where compositional variations in the interdiffusivity coefficients have been modeled using the form of ((Santoro 1969), (Le Claire 1975))

$$D_{WC} = D_{WC,0}\exp(b * c_{WC}), \tag{E-8}$$

where $D_{WC,0}$ is the interdiffusivity coefficient of W in ZrB_2 at infinite dilution and b and c_{WC} are a

solute enhancement factor and solute concentration, respectively. Substitution of Equation (E-8) into (E-7) yields the final solute creep model

$$\frac{\dot{\varepsilon}_{wc}}{\dot{\varepsilon}_0} = \left(\frac{D_{wc,0}\, exp(bc_{wc})}{D_0}\right)\left(\frac{c_0}{c_{wc}}\right), \tag{E-9}$$

with D_0 representing the self-diffusion coefficient of Zr/ZrB_2 at infinitely small reference solute composition (i.e., pure state). Equation (E-9) eloquently describes the composition dependence on creep rate for various solid solutions provided the solute diffusion coefficients are known for the solid solution.

The 1 mol% W-ZrC or 1.4 mol% W-ZrB_2 reference compositions eliminates the need for knowing the self-diffusion coefficients of Zr/ZrB_2 or Zr/ZrC and, therefore,

$$D_0 = D_{WC,0}\exp(0.01b), \tag{E-10}$$

resulting in

$$\frac{\dot{\varepsilon}_{wc}}{\dot{\varepsilon}_0} = \left(\frac{exp(bc_{wc})}{\exp(0.01b)}\right)\left(\frac{0.01}{c_{wc}}\right). \tag{E-11}$$

Following the custom form of Equation (E-11) and using non-linear regression for determining the constant, *b*=9.36 +/-6.29 for the W-concentration effects on the interdiffusivity of W through ZrC. The resulting solute enhancement factor suggests increasing W-concentration increases the W/ZrC diffusion coefficient by a factor of 1-1.5 depending on the solid solution concentration. Le Claire (1975) suggests solute compositions which lower the melting point of the solvent generally increase the diffusion coefficients. Vil'k, et al., (1972) showed a ZrC melting point reduction of ~900°C with W-concentrations of >10 mol%. Additionally, W has a higher valence than Zr suggesting vacancy attraction because of an increasing electron/atom ratio ((Porter and Easterling 2004) and (Misra, et al., 2000)). Impurity diffusion coefficients for W/Zr (BCC) are ~36x those of Zr/Zr (BCC) (Neumann and Tuijn 2009). The present regression coefficients qualitatively agree with general trends in diffusion behavior, rendering Equation (E-

11) a viable model for expressing the solute constitution effects on creep rate.

Break away stress was used to assess the solute-dislocation interactions, between ceramic systems. A breakaway stress was proposed by Cottrell and Jaswon (1949) following

$$\tau_B = \frac{\beta \mu A^2 c_0}{KTb^2}, \tag{E-12}$$

where μ is the molecular volume of solute and β a numerical constant defining the solute-dislocation stress field geometry ≈ 0.68. Similarly, Friedel proposed the breakaway stress as

$$\tau_B = \frac{\beta W^2 c_0}{KTb^3} \tag{E-13}$$

and

$$W = -\frac{1}{2\pi}\left(\frac{1+\nu}{1-\nu}\right) G|\Delta V| , \tag{E-14}$$

where W is the interaction potential scaled by the volumetric change, ΔV, between the solute and solvent atom and the constant β taken as unity. Both equations assume the same perturbation force geometry exerted by the solute atmosphere on the dislocation. Taking $\varepsilon = \frac{\Delta V}{V}$, $r^3 = \frac{3}{4\pi}V$ and $\mu = \frac{1}{b^3}$, from Equation (E-2), shows the Cottrell and Jaswon model overestimates the Friedel stress by a factor of ~3. Furthermore, Endo, et al., (1984) compared measured dislocation velocities for a Al-5%Mg alloy showing Equation (E-13) accurately predicts these stresses with a value of $\beta = 0.1$. Similar breakaway stresses were predicted applying the same $\beta = 0.1$ for Sn-Bi binary alloys (Mitlin, Raeder and Messler, Jr. 1999). Equation (E-12) overestimates the breakaway stress by a factor of ~27 agreeing with the model comparisons made by Mitlin, et al., (1999) reporting a one decade increase in the Cottrell and Jaswon (1949) breakaway stress prediction. Therefore, Equation (E-13) apparently predicts the actual breakaway stress for solid solution alloys having low concentrations.

Table E- 1: Model parameters for the breakaway stress calculation.

	ZrB_2	ZrC
$G\ (GPa)$	188[1]	*150[2]
ν	0.14[1]	0.19[2]
$r_{Zr}\ (10^{12}m)^3$	160	160
$r_W\ (10^{12}m)^3$	140	140
$b\ (10^{10}m)$	3.1687[4]	4.698[5]
$T\ (K)$	2073	2073

* Estimated from the room temperature value.

1 Okamoto, et al., (2010)

2 (Kim and Kang 2012)

3 (Teatum, Gschneidner, Jr. and Waber 1960)

4 (Kaufman and Clougherty 1965)

5 (Kats, Ordan'yan and Gorin, et al., 1979)